NASA TECHNICAL NOTE

NASA TN D-7092

NASA TN D-7092

THE BEHAVIOR OF A COMPRESSIBLE TURBULENT BOUNDARY LAYER IN A SHOCK-WAVE-INDUCED ADVERSE PRESSURE GRADIENT

by William C. Rose

Ames Research Center
Moffett Field, Calif. 94035

NATIONAL AERONAUTICS AND SPACE ADMINISTRATION • WASHINGTON, D. C. • MARCH 1973

1. Report No.	2. Government Accession No.	3. Recipient's Catalog No.
NASA TN D-7092		

4. Title and Subtitle	5. Report Date
THE BEHAVIOR OF A COMPRESSIBLE TURBULENT BOUNDARY LAYER IN A SHOCK-WAVE-INDUCED ADVERSE PRESSURE GRADIENT	March 1973
	6. Performing Organization Code
7. Author(s)	8. Performing Organization Report No.
William C. Rose	A-4554
	10. Work Unit No.
9. Performing Organization Name and Address	501-06-08-00-21
University of Washington Seattle, Wash. 98195 and NASA Ames Research Center Moffett Field, Calif. 94035	11. Contract or Grant No.
	13. Type of Report and Period Covered
12. Sponsoring Agency Name and Address	Technical Note
National Aeronautics and Space Administration Washington, D.C. 20546	14. Sponsoring Agency Code

15. Supplementary Notes

Submitted to University of Washington as partial fulfillment of Ph.D. degree, August 1972.

16. Abstract

The results of an experimental investigation of the mean- and fluctuating-flow properties of a compressible turbulent boundary layer in a shock-wave-induced adverse pressure gradient are presented. The turbulent boundary layer developed on the wall of an axially symmetric nozzle and test section whose nominal free-stream Mach number and boundary-layer thickness Reynolds number were 4 and 10^5, respectively. The adverse pressure gradient was induced by an externally generated conical shock wave.

Mean and time-averaged fluctuating-flow data, including the complete experimental Reynolds stress tensor and experimental turbulent mass- and heat-transfer rates are presented for the boundary layer and external flow, upstream, within, and downstream of the pressure gradient. The mean-flow data include distributions of total temperature throughout the region of interest. The turbulent mixing properties of the flow were determined experimentally with a hot-wire anemometer. The calibration of the wires and the interpretation of the data are discussed.

From the results of the investigation, it is concluded that the shock-wave - boundary-layer interaction significantly alters the turbulent mixing characteristics of the boundary layer.

17. Key Words (Suggested by Author(s))	18. Distribution Statement
Turbulence Compressible boundary layer Hot-wire anemometer Reynolds stresses Shock-wave - boundary-layer interaction	Unclassified - Unlimited

19. Security Classif. (of this report)	20. Security Classif. (of this page)	21. No. of Pages	22. Price*
Unclassified	Unclassified	236	$3.00

* For sale by the National Technical Information Service, Springfield, Virginia 22151

TABLE OF CONTENTS

SYMBOLS

A_w	overheating parameter, $\frac{1}{2}\frac{\partial \ln R_w}{\partial \ln I}$
a_w	overheating parameter, $\frac{R_w - R_r}{R_r}$
c_f	skin friction coefficient
c_p	specific heat at constant pressure
d	diameter of hot wire
E	bridge voltage
f	frequency
H	heat loss from wire
h	enthalpy
I	current
K	wire parameter, $\frac{d \ln R_w}{d \ln T_w}$
k	thermal conductivity
ℓ	wire length
ℓ_{sep}	length of separated flow
M	Mach number
$\dot{m}$	boundary-layer mass flow
Nu	Nusselt number
n_x	direction cosine of sound wave
p	pressure
p_{tp}	pitot pressure
Q_i	total heat-transfer rate
q_i	molecular heat-transfer rate
R_s	resistance in series with wire (includes cable resistance)
R_w	resistance of wire

Re	Reynolds number
Re_t	wire Reynolds number, $\rho ud/\mu_t$
r	coordinate defined in figure 2
r	fluctuating diagram parameter
S	fluctuating diagram parameter
S*	fluctuating diagram parameter
T	temperature
T_{ij}	total stress tensor
t	time
u	velocity component defined in figure 2
$\vec{V}$	total velocity, $u\vec{i} + v\vec{j} + w\vec{k}$
v	velocity component defined in figure 2
W	power to wire
w	velocity component defined in figure 2
x	coordinate defined in figure 2
y	coordinate defined in figure 2
α	$1/\{1 + [(\gamma-1)/2]M^2\}$
β	$(\gamma-1)M^2\alpha$
γ	ratio of specific heats (1.40 for present study)
δ	boundary-layer thickness
δ^*	boundary-layer displacement thickness
$\Delta e_{()}$	fluctuation sensitivity
η	recovery factor, T_r/T_t
π	sound pressure mode amplitude, 100 $p'/\gamma\bar{p}$
θ	overheating parameter, T_w/T_t; or coordinate defined in figure 2
ρ	density
λ	wavelength
σ	vorticity mode amplitude, 100 $u'/\bar{u}$

τ entropy mode amplitude, $100\ T'/\bar{T}$

τ_{ij} molecular stress tensor

τ_{wr} overheating parameter, $\frac{T_w - T_r}{T_r}$

ϕ yaw angle of wire relative to local flow angle

μ absolute viscosity

μ_1 second coefficient of viscosity

ω local flow angle relative to nozzle center line

ω_1 flow turning angle across incident shock wave

Subscripts

c convected in direction of flow

e edge of viscous effects

r recovery conditions

t local total conditions

wall evaluated at the wall

w pertaining to wire

∞ conditions ahead of incident shock wave

Superscripts and Other Symbols

$()'$ fluctuating quantity

$(\bar{})$ time-averaged quantity

$\langle() \rangle$ rms of fluctuating quantity

THE BEHAVIOR OF A COMPRESSIBLE TURBULENT BOUNDARY LAYER IN A SHOCK-WAVE-INDUCED ADVERSE PRESSURE GRADIENT

William C. Rose

Ames Research Center

SUMMARY

A review of previous analytical and experimental investigations of the behavior of a compressible, turbulent boundary layer in a shock-wave-induced adverse pressure gradient is presented. This review led to the following assessment of the present status of research on such boundary-layer flows:

1. Present analytical methods for describing flow in such pressure gradients are incapable of properly accounting for the turbulent mixing properties in the boundary layer.

2. These mixing properties change throughout the flow and they significantly affect the boundary-layer flow downstream of the shock-wave - boundary-layer interaction.

3. Data on which to base improved models of the turbulent mixing characteristics for such compressible flows are not available.

The purpose of the present investigation was to obtain mean- and fluctuating-flow data, including the complete Reynolds stress tensor and turbulent mass- and heat-transfer rates, upstream of, within, and downstream of a severe adverse pressure gradient induced by an externally generated shock wave. This body of data can be used to assess the validity of analytical prediction methods, and to aid in formulating improved turbulent mixing models.

The differential conservation equations of mass, momentum, and thermal energy are written in terms of mean and fluctuating quantities and then time averaged. These equations yield the turbulent transport terms that affect the

time-averaged (mean) flow. The present work reports the results of an experimental investigation to determine each of these turbulent transport terms.

The experimental investigation was conducted in an axially symmetric flow at a nominal free-stream Mach number of 4 and a Reynolds number based on boundary-layer thickness of 10^5. An externally generated, conical shock wave of a strength near that required for separation of the boundary layer was used to impose the adverse pressure gradient. Mean- and fluctuating flow data are presented for this case.

The mean-flow data consist of pitot and static pressures and total temperatures throughout the flow region of interest. In addition, incipient separation data obtained from surface flow patterns of alcohol and pressure readings from a small orifice dam are presented. These mean-flow data are used in conjunction with an existing analytical method to infer the complete mean-flow properties including static pressures and flow angles within the boundary layer throughout the interaction. The mean-flow measurements serve primarily to define the flow in which the fluctuating-flow measurements are obtained; however, new information relative to the behavior of the mean flow is presented.

The fluctuating-flow data consist of the turbulent transport terms in the conservation equations of mass, momentum, and thermal energy. These quantities were determined experimentally with the aid of a hot-wire anemometer using both normal and yawed wires. Techniques for the calibration of the wires and the interpretation of the hot-wire data are discussed in detail.

Important conclusions derived from the present investigation are summarized below:

1. The pressure rise to incipient separation is less than previously obtained in axially symmetric flow and is much less than corresponding planar, two-dimensional flow.

2. There are significant static-pressure and flow-angle variations across the boundary layer within and downstream of the interaction.

3. The adverse pressure gradient significantly affects the total temperature distribution.

4. The experimental turbulent stresses agree qualitatively with data obtained in incompressible flows with adverse pressure gradients.

5. The Reynolds normal-stress term normally neglected in boundary-layer analyses is important within and just downstream of the interaction.

6. The turbulent mixing rates are strongly out of equilibrium with the mean flow as a result of the interaction.

7. Because of 6, nonequilibrium modeling of the turbulent mixing rates is required, even far downstream of the interaction.

INTRODUCTION

The behavior of compressible, turbulent boundary layers in strong adverse pressure gradients, particularly those gradients induced by oblique shock waves in supersonic flows, is of prime current interest. One major source of this interest stems from the desire to predict the behavior of a turbulent boundary layer in both internal and external aerodynamic flows on aircraft that are to fly at supersonic and hypersonic Mach numbers. Shock waves are always present at these Mach numbers; generally, when they interact with the boundary layer (whether in an internal flow such as the engine inlet system or an external flow such as a deflected control surface), a strong, retarding (adverse) pressure gradient acts on the boundary layer. This gradient causes a modification of the boundary layer itself, as well as of the flow external to the boundary layer. The modifications to the boundary-layer flow through the shock-wave - boundary-layer interaction region (figure 1) include changes in mean profile shape (possibly including separation) and changes in the

turbulent mixing properties of the layer. Deviations of the flow external to the boundary layer from the classical gasdynamic-discontinuity concept of a shock wave include the existence of broad regions of compression and/or expansion. For internal aerodynamic flows, the modifications of the external flow field are of paramount importance, since the characteristics of the reflected compression and expansion waves originating on one wall will determine the character of the flow field that interacts with the boundary layer on the opposite wall.

A primary goal of fluid mechanics research today is to develop computing techniques that take advantage of recent developments in computer hardware. If these computing techniques are to provide realistic solutions for interaction phenomena, a basic understanding of such phenomena (e.g., turbulent transport rates) is required. The interaction phenomena may be broadly divided into two categories denoted here by "mean" and "fluctuating." The mean quantities, such as velocity profiles, shock-wave locations, and extent of separated regions, are the ones most frequently studied. The fluctuating quantities, such as those related to turbulent mixing rates, have been investigated to a much lesser extent, in spite of their important role in determining the mean quantities.

Existing analytical efforts toward predicting the effects of shock waves incident on turbulent boundary layers can be classified into two groups: The first considers the interaction phenomenon to be a boundary-layer problem; the second considers the interaction phenomenon to be one requiring a separate modeling that includes the effects of shock waves. An example of the first group is the analysis of Lynes, Nielsen, and Kuhn (ref. 1), which is based on the turbulent boundary-layer equations. The effects of turbulence are taken

into account through an effective eddy viscosity transport model. The agreement between this method and data obtained in interaction regions becomes poorer with increasing streamwise pressure gradients. This may be due to the fact that large transverse pressure gradients exist in the interaction region (ref. 2), or it may result because the turbulence modeling is not valid for these flows. Another example of the first group is the control volume analysis such as that of Seebaugh et al. (ref. 3) or the improved version by Mathews (ref. 4). In this analysis, the boundary layer is assumed to be confined to a control volume, which is subjected to the conditions of satisfying the streamwise momentum balance and continuity relationship. This technique has been shown to give reasonable agreement with data for which the pressure gradients do not cause large regions of separated flow (ref. 4); however, the agreement becomes poorer with increasing pressure gradients. Again, the assumption in these methods concerning turbulent mixing and the neglect of transverse pressure gradients may cause the poor agreement where pressure gradients are strong. Methods in the first group generally yield little information concerning the flow external to the boundary layer.

A highly developed method in the second group is given in reference 5. This method assumes that the turbulent boundary layer in the interaction region can be divided into two portions: one that responds inviscidly to the pressure rise and includes transverse pressure gradients, and one (near the wall) that responds as a viscous laminar shear layer with no transverse pressure gradients. The inviscid portion is computed with a rotational method of characteristics program and the viscous portion by a laminar boundary-layer program. These two programs are coupled, and the resulting scheme is capable of predicting static pressures, total pressures, and flow angles in the

interaction region. The method gives results that are in good agreement with the observed external flow field and portions of the boundary-layer flow even for separated interactions; however, the results derived from the viscous portion diverge from data when extensive separation is present (ref. 6). Possible reasons for this divergence are discussed in reference 6.

Both the control-volume and the two-layer methods have their advantages and disadvantages; they are both ad hoc approximations to the actual physical phenomena. These methods have been brought to reasonably "polished" forms only within the last three years, and further comparisons with mean-flow data are required to assess how good the approximations of each method actually are. These two methods treat only modifications to the mean flow and neglect changes in the turbulent mixing properties of the boundary layer. However, observations (made during the present investigation) of two interactions occurring in proximity in the same boundary layer indicate that the modification of the turbulent mixing properties due to the upstream interaction alters the mean flow characteristics of the downstream interaction. This alteration could not be accounted for in either of the methods of references 4 or 5, because they consider the entire "transfer function" of the interaction to be one of momentum removal subject to mass conservation.

The purpose of the present investigation was to obtain a body of mean- and fluctuating-flow data, including the complete Reynolds stress tensor and turbulent mass- and heat-transfer rates, upstream, within, and downstream of a shock-wave - boundary-layer interaction. As a means of determining which of the turbulent transport quantities primarily affect the mean flow, the differential conservation equations of mass, momentum, and thermal energy were written in terms of mean and fluctuating quantities and then time averaged. The

present work reports the results of an experimental investigation to determine each of the turbulent transport quantities and, thereby, to determine which of the quantities must be known (or modeled) to predict the changes in the mean flow throughout the interaction.

The measurements were obtained in the turbulent boundary on the wall of an axially symmetric nozzle and test section. The nominal free-stream Mach number was $M = 4$ and the Reynolds number based on boundary-layer thickness was $Re_\delta = 10^5$. The adverse pressure gradient was imposed on the boundary layer by a conical shock wave generated by a 9° half-angle cone placed in the center of the circular test section. The shock strength for this cone was near that required for separation of the boundary layer. This experimental arrangement produces a steep pressure rise in the immediate region of the interaction followed by an almost linear, but shallower pressure rise in the downstream flow. Mean- and fluctuating-flow data were taken throughout these regions of pressure rise. The techniques used for calibration of the wires and interpretation of both the mean- and fluctuating-flow measurements are discussed.

REVIEW OF PREVIOUS WORK

Mean Flow

Measurements of mean-flow properties of compressible turbulent boundary layers in strong adverse pressure gradients induced by shock waves have been made by several investigators (refs. 2, 4, 7-18). These investigations and their primary contributions to the understanding of shock-wave - boundary-layer

interaction phenomena have been summarized in references 2, 4, 14, and 15. Since mean measurements are made with the intent of improving our understanding of flow in the interaction region, the simplest configurations are chosen for investigation. Thus, the investigations of references 2, 4, and 7 through 18 have been performed in two-dimensional flows, either planar or axially symmetric. The planar-flow studies (refs. 2, 7-14) were conducted either on the turbulent boundary layer on one wall of a rectangular wind-tunnel test section or on the boundary layers developing on flat or curved planar surfaces held in a supersonic stream. The studies for axially symmetric flows (refs. 4, 15-18) were conducted either on circular wind-tunnel walls or on circular center bodies in a supersonic stream. It was tacitly assumed that there was no difference in the axially symmetric and planar two-dimensional flows except for a coordinate transformation. However, a problem exists in obtaining exactly two-dimensional flow on a planar configuration. One such configuration was investigated by Lewis (ref. 19) for the case of laminar boundary layers. He showed that using planar models with side walls ("boundary-layer fences") did not necessarily lead to two-dimensional flow. He also showed that simply checking spanwise surface pressure distribution to ensure no large variation of pressure across the model at a given longitudinal station is not sufficient to guarantee two-dimensional flow. He concluded that an axially symmetric model is the only way that an actual two-dimensional flow can be realized. Recently, Green (ref. 20) has shown oil-flow photographs of a planar shock-wave - turbulent-boundary-layer interaction that indicated a highly three-dimensional flow. Similar highly three-dimensional results have been found in a supersonic rectangular channel by Reda and Murphy (ref. 21). The effect of these three-dimensional flows on the interpretation of data, presumed to be nominally two-dimensional, is unknown. However, it now appears that the only practical way to achieve a flow that remains two-dimensional throughout a

strong adverse pressure gradient is to use an axially symmetric configuration. Thus, data obtained in axially symmetric environments are given primary consideration in comparisons with "two-dimensional" theoretical predictions.

The studies cited above have mapped the behavior of the mean-flow properties in shock-wave - boundary-layer interactions as functions of Mach number, Reynolds number, and shock-wave strength. However, three areas of interest relative to the mean-flow properties remain unsettled: (1) the detection of separated flow near a wall; (2) the accurate measurement of static pressures in boundary layers with large transverse and streamwise pressure gradients; and (3) the accurate measurement of total temperature in such boundary layers.

The existence of separated flow is usually detected by pitot tube measurements (as in ref. 8, 14, or 15). However, a problem with the pitot tube arises when it is used near a solid wall. For small separated regions, the height of separation can be less than the probe height. For this case, a portion of the probe is influenced by the impact pressure from the flow external to the separation bubble and causes the pitot to read higher than the actual pressure that would exist in the absence of the probe. This error causes underestimation of the extent of separation. When one is looking for the pressure rise to the condition of incipient separation, the rise will be overestimated. To avoid this problem, Reda and Page (ref. 22) used orifice dams that in essence determine if the flow next to the wall is moving upstream or downstream.

Static-pressure measurements have been made in shock-wave - boundary-layer interactions (e.g., refs. 2 and 18). However, when static-pressure probes are used in regions containing shock waves, the presence of these shocks severely affects the probe readings, and as shown in reference 23, the magnitude of the error can be nearly as large as the static-pressure change across the shock wave. Thus, it would seem highly unlikely that such a probe

could accurately detect the pressure gradients in the boundary layer in an interaction region. In fact, even the behavior of the static probe in a boundary layer known to have little or no normal pressure gradient (and, of course, no shock waves) is not clear. For example, figure 8(a) of reference 2 indicates a change of approximately 10 percent in pressure from the indicated free-stream level as the probe is brought through the boundary layer. In the present study, no attempt was made to make direct static-pressure measurements in the flow.

The mean total temperature of a free-stream supersonic flow can be made readily by triple-shielded thermocouples. Measurements in boundary layers, however, require small probes, and single-shielded or bare-wire probes are generally considered. Two types of single-shielded probes have been used. The first is the self-aspirated type (ref. 24 or 2) in which the flow through the probe, and hence over the thermocouple bead, is governed by the flow conditions present at the front and rear of the probe. The second is a controlled-aspirated type (ref. 25) in which the mass flux past the thermocouple bead is predetermined by a system of orifices. Since the output of the thermocouple depends on its cooling (mass flux past the bead) and on the difference between the mean total temperature and the recovery temperature for the bead, the advantage of the second type is clear. Both the controlled-aspirated probe and some bare-wire probes require a relatively large holder and thus may not provide the necessary spatial resolution.

Fluctuating Flow

Many investigations of the fluctuating properties of compressible turbulent flows have been made (e.g., refs. 14, 26-36). The investigations cited date back only to about 1950 when electrical compensation networks were applied to constant-current anemometers to make them a serious research tool

in high-speed turbulence. Kovasznay (ref. 37) summarizes the development of constant-current equipment leading to frequency responses in excess of 50 kHz. Constant-temperature anemometers that at least double or triple this frequency range are now more or less "off-the-shelf" items. Methods other than the hot-wire anemometer for making fluctuating measurements - for example, the electron-beam technique studied by Wallace (ref. 32) - have been investigated recently. However, Kovasznay (ref. 38) concludes that the hot-wire anemometer is, at present, the best instrument for this purpose, and it was used in the present study.

The now classic works of Kovasznay (refs. 28 and 30) and Morkovin (ref. 27) led to the relatively sophisticated present status of signal interpretation in high-speed flow (summarized by Morkovin, in ref. 39). All the cited references use these hot-wire signal-interpretation techniques to separate the fluctuations in mass flux and total temperature. The wire is operated at at least three different wire temperatures (so-called "over-heat" ratios). The sensitivity of the wire to the various fluctuations changes with the over-heat ratio, and the wire thus may be used to obtain the desired fluctuations in an unknown field. In addition to the normally predominant entropy and vorticity fluctuations in a boundary layer, there are pressure fluctuations ("sound" mode or "aerodynamic noise") that usually become significant external to a viscous boundary layer. Investigations of this sound mode and its interaction with shock waves and the other modes have been investigated (refs. 14, 27, 33, 36, 40-44). Again, the techniques of reference 27, 28, or 30 are used to separate the sound from the entropy and vorticity. These techniques have been in existence for over 15 years and are not discussed here in detail; Grande (ref. 14) gives an excellent review of this work.

The results of these investigations are reviewed here as they apply to the determination of fluctuations in the turbulent boundary layer and near-field external flow.

Kistler (ref. 29) has shown distributions of $\langle(\rho u)'\rangle$, $\langle T_t'\rangle$, and $\overline{(\rho u)' T_t'}$ across a zero-pressure-gradient turbulent boundary layer at Mach numbers of 1.71, 3.56, and 4.67 for a single streamwise location. Laufer (ref. 36) has measured the mass-flux and total-temperature fluctuations external to a zero-pressure-gradient turbulent boundary layer and concluded that they were produced solely by pressure fluctuations radiated from it. These two investigations were carried out using a single, normal wire. However, none of the measurements was converted to a form that could be used to assess relative magnitudes of the turbulent stresses, such as $\bar{\rho}\overline{u'^2}$ or $\bar{u}\overline{\rho' u'}$, in the momentum equations. Morkovin and Phinney (ref. 26) considered the use of a yawed wire to determine the $\overline{v'^2}$-like fluctuations and the shear-stress-like term $\overline{u'v'}$. They present the shear-stress measurement at one point in a zero-pressure-gradient turbulent boundary layer. After 14 years, this apparently is still the only data point of its kind.

Grande (ref. 14) used a single normal wire to obtain fluctuating flow measurements in the turbulent boundary layer and external flow in an oblique shock-wave (turning angles of 6°, 8°, 10°, and 12°) - turbulent-boundary-layer interaction at a Mach number of 2.5. This is certainly the most detailed survey of the most general flow configuration studied to date. He presented values of $\langle(\rho u)'\rangle$, $\langle\tau\rangle$, $\langle\sigma\rangle$, and $\langle\pi\rangle$, and the fluctuating pitot pressure $\langle\pi_t\rangle$, obtained with a Kulite sensor, at several points throughout the interaction. However, most of the data were obtained outside the boundary layer. He showed that the fluctuations downstream of an interaction were significantly changed due to the interaction. These findings are summarized schematically in figure 100 of reference 14.

Grande used an anemometer system whose upper frequency response was at most 40 kHz and, therefore, his measurements only encompass fluctuations whose scales are larger than about δ. This system is probably inadequate for studies of boundary-layer turbulence but may have been adequate for his purposes. In spite of the limitations of Grande's system, he was able to show that existing signal-interpretation techniques for hot-wire anemometers using normal wires could be used with assurance in very complicated flow fields.

As noted previously, the turbulent mixing properties of compressible, turbulent boundary layers have been investigated to a much lesser extent than the mean-flow properties. Furthermore, turbulent shear stresses, which could likely play an important role in altering the boundary-layer flow downstream of an interaction, have never been experimentally investigated.

ANALYTICAL CONSIDERATIONS

We will consider the flow of air (a compressible, viscous, heat-conducting medium) at pressures and temperatures for which the continuum flow assumptions are valid and no dissociation of the gas takes place. In addition, we assume the gas behaves as a Newtonian fluid (i.e., a linear stress - rate-of-strain relationship is an adequate assumption for the flow process involved) and that Stokes' hypothesis is valid for these processes ($\mu_1 = -2/3\mu$; i.e., the relaxation times for energy transfer from translational to rotational or vibrational modes in the molecules are essentially zero). Further, we consider only flow without body forces. We will consider the equations of motion in cylindrical coordinates and make the assumption of axially symmetric flow. Of course, these equations reduce to the equations of planar, two-dimensional flow in the limit as $r \to \infty$. The coordinate-system nomenclature used throughout this work is shown in figure 2. The axial coordinate is denoted by x; the radial, r; and circumferential, θ. The velocities in these directions are

denoted by u, v, and w, respectively. In addition, y denotes the direction negative to that of r and is measured from the wind-tunnel wall rather than the centerline.

Using these coordinates, the governing equations, which apply instantaneously to the local flow field, may be written for the flow as follows:

Continuity:

$$\frac{\partial \rho}{\partial t} + \frac{\partial \rho u}{\partial x} + \frac{1}{r}\frac{\partial r \rho v}{\partial r} = 0$$

Momentum:

x:
$$\frac{\partial \rho u}{\partial t} + \frac{\partial \rho uu}{\partial x} + \frac{1}{r}\frac{\partial r \rho vu}{\partial r} = -\frac{\partial p}{\partial x} + \frac{\partial \tau_{xx}}{\partial x} + \frac{1}{r}\frac{\partial r \tau_{rx}}{\partial r}$$

r:
$$\frac{\partial \rho v}{\partial t} + \frac{\partial \rho vu}{\partial x} + \frac{1}{r}\frac{\partial r \rho vv}{\partial r} - \frac{\rho ww}{r} = -\frac{\partial p}{\partial r} + \frac{\partial \tau_{xr}}{\partial x} + \frac{1}{r}\frac{\partial r \tau_{rr}}{\partial r} - \frac{\tau_{\theta\theta}}{r}$$

θ:
$$\frac{\partial \rho w}{\partial t} + \frac{\partial \rho wu}{\partial x} + \frac{1}{r}\frac{\partial r \rho vw}{\partial r} + \frac{\rho wv}{r} = \frac{\partial \tau_{x\theta}}{\partial x} + \frac{1}{r^2}\frac{\partial r^2 \tau_{r\theta}}{\partial r}$$

Energy:

$$\frac{\partial \rho h}{\partial t} + \frac{\partial \rho uh}{\partial x} + \frac{1}{r}\frac{\partial r \rho vh}{\partial r} = u\frac{\partial p}{\partial x} + v\frac{\partial p}{\partial r} + \frac{\partial}{\partial x}\left(k\frac{\partial T}{\partial x}\right) + \frac{1}{r}\frac{\partial}{\partial r}\left(rk\frac{\partial T}{\partial r}\right) + \mu\Phi$$

State:

$$p = \rho RT$$

where

$$\tau_{xx} = \mu\left[2\frac{\partial u}{\partial x} - \frac{2}{3}(\nabla \cdot \vec{V})\right]$$

$$\tau_{rr} = \mu\left[2\frac{\partial v}{\partial r} - \frac{2}{3}(\nabla \cdot \vec{V})\right]$$

$$\tau_{\theta\theta} = \mu\left[2\frac{v}{r} - \frac{2}{3}(\nabla \cdot \vec{V})\right]$$

$$\tau_{rx} = \tau_{xr} = \mu\left[\frac{\partial u}{\partial r} + \frac{\partial v}{\partial x}\right]$$

$$\tau_{r\theta} = \tau_{\theta r} = \mu\left[r\frac{\partial w/r}{\partial r}\right]$$

$$\tau_{x\theta} = \tau_{\theta x} = \mu \frac{\partial w}{\partial x}$$

$$\vec{V} = u\vec{i} + v\vec{j} + w\vec{k}$$

$$\nabla \cdot \vec{V} = \frac{\partial u}{\partial x} + \frac{1}{r}\frac{\partial rv}{\partial r}$$

and

$$\Phi = 2\left[\left(\frac{\partial v}{\partial r}\right)^2 + \left(\frac{v}{r}\right)^2 + \left(\frac{\partial u}{\partial x}\right)^2\right] + \left[r\frac{\partial w/r}{\partial r}\right]^2 + \left[\frac{\partial w}{\partial x}\right]^2 + \left[\frac{\partial v}{\partial x} + \frac{\partial u}{\partial r}\right]^2 - \frac{2}{3}(\nabla \cdot \vec{V})^2$$

We now examine explicitly the "turbulence" and use the Reynolds substitutions

$$u = \bar{u} + u' \quad \rho = \bar{\rho} + \rho' \quad h = \bar{h} + h'$$

$$v = \bar{v} + v' \quad p = \bar{p} + p' \quad \mu = \bar{\mu} + \mu'$$

$$w = \bar{w} + w' \quad T = \bar{T} + T' \quad \Phi = \bar{\Phi} + \Phi'$$

where the time average of any fluctuating quantity is zero (e.g., $\overline{u'} = 0$). When these quantities are substituted in the previous equations, the time average taken, and the flow under consideration is assumed to be steady in the mean (i.e., $\partial\overline{\rho u}/\partial t$, etc.= 0) with $\bar{w} = 0$ for axially symmetric, two-dimensional flow, we obtain the following system:

Continuity:

$$\frac{\partial \bar{\rho}\bar{u}}{\partial x} + \frac{1}{r}\frac{\partial r\bar{\rho}\bar{v}}{\partial r} + \frac{\partial \overline{\rho' u'}}{\partial x} + \frac{1}{r}\frac{\partial r\overline{\rho' v'}}{\partial r} = 0 \qquad (1)$$

Momentum:

x:
$$\frac{\partial \bar{\rho}\bar{u}\bar{u}}{\partial x} + \frac{1}{r}\frac{\partial r\bar{\rho}\bar{u}\bar{v}}{\partial r} = -\frac{\partial \bar{p}}{\partial x} + \frac{\partial}{\partial x}[\overline{\tau_{xx}} - (\overline{\rho u'u'} + 2\bar{u}\overline{\rho' u'})]$$

$$+ \frac{1}{r}\frac{\partial}{\partial r} r[\overline{\tau_{rx}} - (\overline{\rho u'v'} + \bar{u}\overline{\rho' v'} + \bar{v}\overline{\rho' u'})] \qquad (2a)$$

r:
$$\frac{\partial \bar{\rho}\bar{u}\bar{v}}{\partial x} + \frac{1}{r}\frac{\partial r\bar{\rho}\bar{v}\bar{v}}{\partial r} = -\frac{\partial \bar{p}}{\partial r} - \frac{1}{r}[\overline{\tau_{\theta\theta}} - \overline{\rho w'w'}]$$

$$+ \frac{\partial}{\partial x}[\overline{\tau_{xr}} - (\overline{\rho u'v'} + \bar{u}\overline{\rho' v'} + \bar{v}\overline{\rho' u'})] + \frac{1}{r}\frac{\partial}{\partial r} r[\overline{\tau_{rr}} - (\overline{\rho v'v'} + 2\bar{v}\overline{\rho' v'})] \qquad (2b)$$

$$\theta: \qquad 0 = \frac{\partial}{\partial x}\left[\overline{\tau_{x\theta}} - \left(\overline{\rho u'w'} + \bar{u}\overline{\rho'w'}\right)\right] + \frac{1}{r^2}\frac{\partial}{\partial r} r^2\left[\overline{\tau_{r\theta}} - \left(\overline{\rho v'w'} + \bar{v}\overline{\rho'w'}\right)\right] \tag{2c}$$

Energy:

$$\frac{\partial \bar{\rho}\bar{u}\bar{h}}{\partial x} + \frac{1}{r}\frac{\partial r\bar{\rho}\bar{v}\bar{h}}{\partial r} = \bar{u}\frac{\partial \bar{p}}{\partial x} + \bar{v}\frac{\partial \bar{p}}{\partial r} + \overline{u'\frac{\partial p'}{\partial x}} + \overline{v'\frac{\partial p'}{\partial r}} + \overline{\mu\Phi}$$

$$+ \frac{\partial}{\partial x}\left[\overline{k\frac{\partial T}{\partial x}} - \left(\overline{\rho u'h'} + \bar{u}\overline{\rho'h'} + \bar{h}\overline{\rho'u'}\right)\right]$$

$$+ \frac{1}{r}\frac{\partial}{\partial r} r\left[\overline{k\frac{\partial T}{\partial r}} - \left(\overline{\rho v'h'} + \bar{v}\overline{\rho'h'} + \bar{h}\overline{\rho'v'}\right)\right] \tag{3}$$

State:

$$\bar{p} = R\left(\bar{\rho}\bar{T} + \overline{\rho'T'}\right) \tag{4}$$

where the $\overline{\tau_{ij}}$, $\overline{k(\partial T/\partial x)}$, and $\overline{k(\partial T/\partial r)}$ terms still contain correlations between μ' and $\partial u'/\partial x$-like terms and the k' and $\partial T'/\partial x$-like terms.

We now consider some of the individual terms in equations (2) through (4) together with experimentally observed features of supersonic flows to reduce (slightly) the complexity of this governing system of equations. First, consider the following definitions:

$$T_{xx} = \overline{\tau_{xx}} - \left(\overline{\rho u'u'} + 2\bar{u}\overline{\rho'u'}\right)$$

$$T_{rr} = \overline{\tau_{rr}} - \left(\overline{\rho v'v'} + 2\bar{v}\overline{\rho'v'}\right)$$

$$T_{rx} = \overline{\tau_{rx}} - \left(\overline{\rho u'v'} + \bar{u}\overline{\rho'v'} + \bar{v}\overline{\rho'u'}\right)$$

$$T_{\theta\theta} = \overline{\tau_{\theta\theta}} - \overline{\rho w'w'}$$

Now, if the stress tensor is to remain symmetric, we must have $T_{xr} = T_{rx}$. We also have

$$T_{\theta x} = T_{x\theta} = \overline{\tau_{x\theta}} - \left(\overline{\rho u'w'} + \bar{u}\overline{\rho'w'}\right)$$

$$T_{\theta r} = T_{r\theta} = \overline{\tau_{r\theta}} - \left(\overline{\rho v'w'} + \bar{v}\overline{\rho'w'}\right)$$

Thus (2c) may be written:

$$0 = \frac{\partial T_{x\theta}}{\partial x} + \frac{1}{r^2}\frac{\partial}{\partial r} r^2 T_{r\theta}$$

Now, for an axially symmetric flow (e.g., ref. 45), or, for that matter, a planar, two-dimensional flow (e.g., ref. 26), $T_{x\theta}$ must be identically zero. We then have: $0 = (\partial/\partial r)r^2T_{r\theta}$. Integrating from $r = 0$ to r we see:

$$0 = \int_{r=o}^{r} \frac{\partial}{\partial r} r^2T_{r\theta}dr = r^2T_{r\theta} - r^2T_{r\theta}\Big|_{r=o} + f(x)$$

Assuming the physical variables in $T_{r\theta}$ to be bounded, we have $r^2T_{r\theta}\big|_{r=o} = 0$ and thus $T_{r\theta}$ must also be identically zero. With this result, the θ momentum equation is degenerate.

Thus, we may write the equations describing axially symmetric, turbulent flow in the following form:

Continuity: equation (1)

Momentum:

x:
$$\frac{\partial\bar{\rho}\bar{u}\bar{u}}{\partial x} + \frac{1}{r}\frac{\partial r\bar{\rho}\bar{u}\bar{v}}{\partial r} = -\frac{\partial\bar{p}}{\partial x} + \frac{\partial T_{xx}}{\partial x} + \frac{1}{r}\frac{\partial rT_{xr}}{\partial r} \tag{5a}$$

r:
$$\frac{\partial\bar{\rho}\bar{u}\bar{v}}{\partial x} + \frac{1}{r}\frac{\partial r\bar{\rho}\bar{v}\bar{v}}{\partial r} = -\frac{\partial\bar{p}}{\partial r} + \frac{\partial T_{rx}}{\partial x} + \frac{1}{r}\frac{\partial rT_{rr}}{\partial r} - \frac{T_{\theta\theta}}{r} \tag{5b}$$

θ:
$$T_{r\theta} = T_{x\theta} = 0 \tag{5c}$$

Energy: equation (3)

State: equation (4)

These equations are exact in that no order-of-magnitude approximations or any other assumptions relative to the size of the terms have been invoked. We now make use of existing knowledge of the size of some of these terms to reduce the complexity of equations (3) and (5), and thereby see which terms in these equations are significant in altering the mean flow. First consider the term

$$\overline{\tau_{xx}} = \bar{\mu}\left[2\frac{\partial\bar{u}}{\partial x} - \frac{2}{3}(\overline{\nabla\cdot\vec{V}})\right] + \overline{\mu'\left[2\frac{\partial u'}{\partial x} - \frac{2}{3}(\nabla\cdot\vec{V})'\right]}$$

where

$$\overline{\nabla\cdot\vec{V}} = \frac{\partial\bar{u}}{\partial x} + \frac{1}{r}\frac{\partial r\bar{v}}{\partial r}$$

and

$$(\nabla \cdot \vec{V})' = \frac{\partial u'}{\partial x} + \frac{1}{r}\frac{\partial rv'}{\partial r}$$

To simply neglect the second part of $\overline{\tau_{xx}}$ is inconsistent with a nonzero h', since μ' is a (weak) function of h'. However, indications are (see Laufer, ref. 46, or Favre, ref. 47) that gradients of the fluctuating viscosity-velocity gradient correlations are usually much smaller than the gradients in the mean terms so that in all the $\overline{\tau_{ij}}$ terms we need only retain the terms involving the mean viscosity and velocities. Thus, we write the explicit relations:

$$T_{xx} = \bar{\mu}\left[2\frac{\partial \bar{u}}{\partial x} - \frac{2}{3}\overline{(\nabla \cdot \vec{V})}\right] - (\overline{\rho u'u'} + 2\bar{u}\overline{\rho' u'}) \tag{6a}$$

$$T_{rr} = \bar{\mu}\left[2\frac{\partial \bar{v}}{\partial r} - \frac{2}{3}\overline{(\nabla \cdot \vec{V})}\right] - (\overline{\rho v'v'} + 2\bar{v}\overline{\rho' v'}) \tag{6b}$$

$$T_{\theta\theta} = \bar{\mu}\left[2\frac{\bar{v}}{r} - \frac{2}{3}\overline{(\nabla \cdot \vec{V})}\right] - \overline{\rho w'w'} \tag{6c}$$

$$T_{rx} = \bar{\mu}\left[\frac{\partial \bar{u}}{\partial r} + \frac{\partial \bar{v}}{\partial x}\right] - (\overline{\rho u'v'} + \bar{u}\overline{\rho' v'} + \bar{v}\overline{\rho' u'}) \tag{6d}$$

$$T_{x\theta} = -(\overline{\rho u'w'} + \bar{u}\overline{\rho' w'}) \tag{6e}$$

$$T_{r\theta} = -(\overline{\rho v'w'} + \bar{v}\overline{\rho' w'}) \tag{6f}$$

Now, considering the energy equation (3), we first examine the nature of the terms

$$\overline{u'\frac{\partial p'}{\partial x}} \quad \text{and} \quad \overline{v'\frac{\partial p'}{\partial r}}$$

Based on measurements by Kistler (ref. 29) and the discussion by Laufer (ref. 46) for flows below a Mach number of 5, one would expect that $\overline{u'(\partial p'/\partial x)}$ and $\overline{v'(\partial p'/\partial r)}$ are small compared to their mean counterparts $\bar{u}(\partial \bar{p}/\partial x)$ and $\bar{v}(\partial \bar{p}/\partial r)$, and may be neglected. Next we write the terms:

$$\overline{k\frac{\partial T}{\partial x}} = \bar{k}\frac{\partial \bar{T}}{\partial x} + \overline{k'\frac{\partial T'}{\partial x}}$$

and

$$\overline{k \frac{\partial T}{\partial r}} = \bar{k} \frac{\partial \bar{T}}{\partial r} + \overline{k' \frac{\partial T'}{\partial r}}$$

Again, based on arguments similar to those that lead to neglecting $\overline{\mu'(\partial u'/\partial x)}$, etc., we assume that $\overline{k'(\partial T'/\partial x)}$ and $\overline{k'(\partial T'/\partial r)}$ are small. Finally we consider the term $\overline{\mu\Phi}$. Recalling the definition of $\mu\Phi$ as the tensor product

$$\mu\Phi = \tau : \nabla\vec{V} = \tau_{ij} \frac{\partial u_i}{\partial x_j}$$

we may write

$$\overline{\mu\Phi} = \overline{\tau_{ij}} \frac{\partial \bar{u}_i}{\partial x_j} + \overline{\tau'_{ij} \frac{\partial u'_i}{\partial x_j}}$$

The terms τ'_{ij} contain fluctuating terms such as μ' and $\partial u'/\partial x$, which are then correlated in the term $\overline{\tau'_{ij}(\partial u'_i/\partial x_j)}$. This term contains double and triple correlations of the viscosity and velocity gradients, which we have previously neglected. Therefore, it is not inconsistent to neglect the term $\overline{\tau'_{ij}(\partial u'_i/\partial x_j)}$ and simply write $\overline{\mu\Phi} = \bar{\mu}\bar{\Phi}$. In view of the foregoing argument, equation (3) may be cast in the following form:

$$\frac{\partial \overline{\rho u h}}{\partial x} + \frac{1}{r} \frac{\partial r \overline{\rho v h}}{\partial r} = \bar{u} \frac{\partial \bar{p}}{\partial x} + \bar{v} \frac{\partial \bar{p}}{\partial r} + \bar{\mu}\bar{\Phi} + \frac{\partial Q_x}{\partial x} + \frac{1}{r} \frac{\partial r Q_r}{\partial r} \tag{7}$$

where

$$Q_x = \bar{k} \frac{\partial \bar{T}}{\partial x} - (\overline{\rho u' h'} + \bar{u}\overline{\rho' h'} + \bar{h}\overline{\rho' u'})$$

and

$$Q_r = \bar{k} \frac{\partial \bar{T}}{\partial r} - (\overline{\rho v' h'} + \bar{v}\overline{\rho' h'} + \bar{h}\overline{\rho' v'})$$

We now consider the terms such as $\overline{\rho u' v'}$ and $\overline{\rho v' h'}$ that contain triple correlations; for example,

$$\overline{\rho u' v'} = \bar{\rho}\overline{u' v'} + \overline{\rho' u' v'}$$

Laufer (ref. 46) gives reasonable arguments that lead to

$$\frac{\overline{\rho'u'v'}}{\bar{\rho}\overline{u'v'}} < \sim 5 \text{ percent}$$

In addition, Way and Libby (ref. 31) have recently reported measurements of the triple correlation $\overline{\rho'u'u'}$ in a low-velocity flow that contained significant density fluctuations. Their reported data indicate

$$\frac{\overline{\rho'u'u'}}{\bar{\rho}\overline{u'u'}} < 5 \text{ percent}$$

Considering the expected accuracy to which quantities such as $\bar{\rho}\overline{u'u'}$ or $\bar{\rho}\overline{u'v'}$ can be measured, it thus seems reasonable to neglect the triple correlations. We had previously considered the correlations

$$\overline{u' \frac{\partial p'}{\partial x}} \quad \text{and} \quad \overline{v' \frac{\partial p'}{\partial r}}$$

to be small. For weak (either unseparated or weakly separated) shock-wave - boundary-layer interactions, such as considered in this study, Grande (ref. 14) has shown that the pressure fluctuations themselves induced by the interaction are small in comparison with the boundary-layer turbulence. Now we examine the consequence of assuming the fluctuations p' to be zero. This assumption is also an important basis for the hot-wire anemometer data reduction procedure discussed later. For $p' = 0$, it can be shown by logarithmically differentiating the equation of state:

$$\frac{\rho'}{\bar{\rho}} = -\frac{T'}{\bar{T}} = -\frac{h'}{\bar{h}}$$

this is used in the following. The effect of neglecting the triple correlations and pressure fluctuations on the turbulent heat-transfer terms is discussed below. First, neglecting triple correlations, we have:

$$Q_x = \bar{k} \frac{\partial \bar{T}}{\partial x} - (\overline{\rho u' h'} + \overline{u\rho' h'} + \overline{h\rho' u'}) \tag{8a}$$

$$Q_r = \bar{k}\frac{\partial \bar{T}}{\partial r} - (\overline{\rho v' h'} + \overline{v\rho' h'} + \overline{h\rho' v'}) \tag{8b}$$

Consider, for example, the first term inside the parentheses of Q_x and employ the relationship $\rho'/\bar{\rho} = -h'/\bar{h}$ based on the assumption of zero pressure fluctuation. We have:

$$\overline{\rho u' h'} = -\overline{\rho u' \rho'}\frac{\bar{h}}{\bar{\rho}} = -\bar{h}\overline{\rho' u'}$$

and similarly:

$$\overline{\rho v' h'} = -\bar{h}\overline{\rho' v'}$$

Thus we see that, for the form of the convective terms (left-hand side) used in equation (7), the expressions for the heat-transfer rates reduce to:

$$Q_x = \bar{k}\frac{\partial \bar{T}}{\partial x} - \overline{u\rho' h'} \tag{9a}$$

$$Q_r = \bar{k}\frac{\partial \bar{T}}{\partial r} - \overline{v\rho' h'} \tag{9b}$$

Making use of the above assumptions, we obtain the conservation equations and the equation of state in the forms given below:

Continuity:

$$\frac{\partial \bar{\rho}\bar{u}}{\partial x} + \frac{1}{r}\frac{\partial r\bar{\rho}\bar{v}}{\partial r} + \frac{\partial \overline{\rho' u'}}{\partial x} + \frac{1}{r}\frac{\partial r\overline{\rho' v'}}{\partial r} = 0 \tag{10}$$

Momentum:

x:
$$\frac{\partial \bar{\rho}\bar{u}^2}{\partial x} + \frac{1}{r}\frac{\partial r\bar{\rho}\bar{u}\bar{v}}{\partial r} = -\frac{\partial \bar{p}}{\partial x} + \frac{\partial T_{xx}}{\partial x} + \frac{1}{r}\frac{\partial rT_{rx}}{\partial r} \tag{11a}$$

r:
$$\frac{\partial \bar{\rho}\bar{u}\bar{v}}{\partial x} + \frac{1}{r}\frac{\partial r\bar{\rho}\bar{v}^2}{\partial r} = -\frac{\partial \bar{p}}{\partial r} + \frac{\partial T_{rx}}{\partial x} + \frac{1}{r}\frac{\partial rT_{rr}}{\partial r} - \frac{T_{\theta\theta}}{r} \tag{11b}$$

θ:
$$T_{r\theta} = T_{x\theta} = 0 \tag{11c}$$

where

$$T_{xx} = \bar{\mu}\left[2\frac{\partial \bar{u}}{\partial x} - \frac{2}{3}\overline{(\nabla \cdot \vec{V})}\right] - (\overline{\rho u'^2} + 2\bar{u}\overline{\rho' u'}) \tag{12a}$$

$$T_{rr} = \bar{\mu}\left[2\frac{\partial \bar{v}}{\partial r} - \frac{2}{3}\overline{(\nabla \cdot \vec{V})}\right] - (\overline{\rho v'^2} + 2\bar{v}\overline{\rho' v'}) \tag{12b}$$

$$T_{\theta\theta} = \bar{\mu}\left[2\frac{\bar{v}}{r} - \frac{2}{3}\overline{(\nabla \cdot \vec{V})}\right] - (\overline{\rho w'^2}) \tag{12c}$$

$$T_{rx} = \bar{\mu}\left[\frac{\partial \bar{u}}{\partial r} + \frac{\partial \bar{v}}{\partial x}\right] - (\overline{\rho u'v'} + \overline{u\rho'v'} + \overline{v\rho'u'}) \tag{12d}$$

$$T_{x\theta} = -(\overline{\rho u'w'} + \overline{u\rho'w'}) \tag{12e}$$

$$T_{r\theta} = -(\overline{\rho v'w'} + \overline{v\rho'w'}) \tag{12f}$$

Energy:

$$\frac{\partial \overline{\rho u h}}{\partial x} + \frac{1}{r}\frac{\partial r\overline{\rho v h}}{\partial r} = \bar{u}\frac{\partial \bar{p}}{\partial x} + \bar{v}\frac{\partial \bar{p}}{\partial r} + \overline{\mu\Phi} + \frac{\partial Q_x}{\partial x} + \frac{1}{r}\frac{\partial rQ_r}{\partial r} \tag{13}$$

where Q_x and Q_r are given by equation (9).

State:

$$\bar{p} = R(\bar{\rho}\bar{T} + \overline{\rho'T'}) = R\bar{\rho}\bar{T}\left(1 - \frac{\overline{\rho'^2}}{\bar{\rho}^2}\right) \tag{14}$$

An experimental investigation was conducted to measure the mean-flow properties and each of the turbulent transport terms in equations (10) through (14) in a shock-wave - boundary-layer interaction. The remainder of the thesis reports the results of that investigation.

EXPERIMENTAL INVESTIGATION

The experimental investigation was conducted in an axially symmetric flow facility to minimize three-dimensional effects. Figure 3 is a schematic diagram of the experimental facility used in the investigation. A complete description of the experimental apparatus is given in appendix A.

The turbulent boundary layer under investigation was the one that developed on the nozzle and test section wall. The boundary layer upstream of the interaction is referred to as the "undisturbed" boundary layer. At the beginning of the interaction it had a history of both a favorable and a slight adverse pressure gradient (appendix A). The Mach number for the core flow in the test section was 3.88 ± 0.02. The Reynolds number based on the thickness of the undisturbed boundary layer was 8.7×10^4. The total temperature was

540° R (300° K), and the wall temperature was near that of the adiabatic wall temperature for the test section Mach number.

The boundary layer was subjected to an adverse pressure gradient generated by a cone placed on the centerline of the test section. The resulting wall static pressure distribution is depicted in figure 3. Three rather distinct pressure gradients are evident: the nominally zero pressure gradient ahead of the incident shock wave, and two adverse pressure gradients, both of which are studied in the present investigation. The second gradient is a rather steep one induced directly by the incident-reflected shock-wave system, while the third (downstream of the second) is a less severe, nearly constant gradient induced by the conical flow field.

The magnitude of the pressure gradients can be varied by using different half-angle, straight cones. It was decided that a flow for which the imposed pressure gradient was near that for incipient separation should be investigated. As a preliminary step in the experimental investigation, then, the pressure gradient required to just separate the boundary-layer flow had to be determined. This was done by a technique using surface flow patterns of alcohol in conjunction with pressure measurements from a miniature orifice dam (appendix B). With the use of this more sensitive technique, the incipient separation pressure rise was found to be much lower than that reported for comparable Mach and Reynolds numbers in reference 15. The results of the incipient separation study showed that a cone of 9° half-angle produced a pressure gradient that was very near that required for incipient separation, so the 9° cone was used in the present study.

The results of the experimental investigation consist of mean- and fluctuating-flow data obtained throughout the boundary layer and external flow at the locations shown in figure 4. The mean-flow data consist of pitot and surface-static pressures and total temperatures. The pitot pressures were

obtained with a pitot probe, and the total temperatures were obtained by using a hot wire as a resistance thermometer. The fluctuating-flow data consist of the turbulent transport terms for mass, momentum, and thermal energy. The turbulent terms were obtained by using a constant-temperature hot-wire anemometer. Both normal and yawed wires were used. A detailed discussion of the instrumentation is given in appendix A.

The experimental operating procedures and data-reduction techniques for both mean- and fluctuating-flow measurements are given in appendix C. Special attention is given to describing the theory and interpretation of the hot-wire-anemometer data in appendix D, and the data accuracy is discussed in appendix E.

RESULTS AND DISCUSSION

The principal experimental results are shown in figures 5 through 17. The data are also presented in tabular form to facilitate the use by others who may wish to examine aspects of the data which are different from those discussed below. The mean-flow data are listed in table 1 and the fluctuating-flow data in table 2.

Mean-Flow Data

Mean-flow data were obtained at a single Mach number and Reynolds number ($M = 3.88$; $Re_\delta = 8.7 \times 10^4$) and a single shock-wave strength (cone half-angle of 9°). The pitot pressures and total temperatures obtained through the region of interest (fig. 4) are shown in figure 5. The incident shock wave is evident in plots of the pitot pressures given in figure 5(b) through (d), and the reflected shock-wave system is evident in figure 5(g) through (j). The temperature profiles have the shape expected for an adiabatic flow. The temperatures are lower near the wall than in the free stream and higher than the

free-stream value in the outer part of the boundary layer. These profiles are qualitatively the same as those found in reference 48. The wall temperature is the adiabatic wall temperature for $M = 3.88$, assuming a recovery factor of 0.90. The height at which the temperature becomes essentially that of the free stream is denoted by δ_{T_t}, the boundary-layer thickness based on the total-temperature profile. The pitot-pressure profiles reveal a well-defined boundary-layer thickness $\delta_{p_{tp}}$ ahead of the incident shock wave. Downstream of the incident wave, however, the Mach number in the inviscid flow is no longer uniform, so that a boundary-layer thickness based on Mach number profiles is not reliable. Thus, the term "boundary-layer thickness" used in the present study refers to δ_{T_t}, which agrees with the $\delta_{p_{tp}}$ upstream of the incident shock and which remains clearly definable throughout the interaction and downstream flow.

The data presented in figure 5 can be combined to give the representation of the mean-flow field shown in figure 6. The incident shock wave is shown as a single line (discontinuity in the flow) even though from pitot-pressure profiles alone the shock appears as a band. The hot-wire anemometer was used, as discussed in appendix C, to locate the shock more accurately. The line representing the incident shock wave has been drawn through the experimental points obtained by the hot-wire technique. These points are located approximately in the center of the band given by the pitot-pressure survey. The reflected shock-wave system is shown as two separate compression bands. The presence of two compression bands could not be shown conclusively based on the pitot-pressure profiles alone; however, with the use of the hot-wire anemometer it was found that two bands were present. Since the shock wave used to generate the pressure rise is believed to have been insufficiently strong to separate the boundary layer, the term "separation shock wave" probably should not be used to describe the upstream (first) reflected compression band. (Even if

there were a small separation present, the well-developed, two-compression configuration could probably not be explained on the simple basis of the existence of a region of separation.) This upstream band is denoted by the term "induced shock wave," indicating that it is probably induced from the turning of the supersonic flow within the boundary layer due to a thickening of the subsonic portion of the layer caused by the forward feeding of the pressure rise. Also indicated in the flow field is the edge of the boundary layer determined from total-temperature measurements. The induced wave merges with the reflected wave soon after leaving the boundary layer. The boundary-layer thickness is reduced by about 35 percent in passing through the incident-reflected shock system. The thickness of the layer downstream of the reflected shock remains constant even though the pressure is rising.

The experimental surface-static-pressure distribution is shown in figure 7. A region of nominally zero-pressure-gradient flow exists upstream of the incident shock. This region is followed by a steep pressure rise caused by the incident-reflected shock system and then by a shallower rise associated with the conical flow field. No attempt was made to measure static pressures in the flow field because of the large uncertainty present in interpreting results of static-pressure-probe data when shock waves are present (see Review of Previous Work). However, a technique is outlined below that allowed reasonable estimates of the static pressure throughout the flow field.

The static pressure can be computed from the Rayleigh pitot formula using the measured pitot pressure if the actual total pressure is known. Within the boundary layer, the total pressure is what we seek to find and is, of course, unknown. However, outside the boundary layer the total pressure may be known (e.g., from inviscid-flow calculations). In the particular case of a shock wave generated by a 9° half-angle cone, the total pressure behind the incident shock is 99.6 percent of the tunnel stagnation pressure. The reflected

compression system consists of two broad compression bands (and not a single shock wave) so that there is probably very little further loss in total pressure. Therefore, it is reasonable to estimate that the total pressure loss across the shock system is at most 0.5 percent. (Even if the incident shock were reflected as a single shock, there would be a net loss in total pressure of only 0.7 percent.) In view of the almost negligible losses across the shock systems, the static pressures in the flow field external to the boundary layer were computed from the Rayleigh pitot formula assuming no total pressure loss. These pressures are shown in figure 8, where they have been normalized with respect to the measured value of the local wall static pressure. Also shown in figure 8 are the static pressures as computed by the method of reference 5, which was discussed in the Introduction. The calculation procedure of reference 5 was started at station 2.60 in. (6.60 cm) (fig. 8(b)) where p/p_{wall} was taken to be 1.00 across the boundary layer. The static pressures determined in this manner agree to within 2 percent of those computed from pitot pressures except in the vicinity of the reflected compression system (e.g., fig. 8(g)). Here, the method of reference 5 predicts a shock wave rather than the broad compression indicated by the experimental data. It can be seen from figure 8 that there are large static pressure gradients normal to the flow within the boundary layer. In figure 8(ℓ), the expansion from the aft corner of the shock-wave generator is evident. At this station (x = 4.60 in. (11.68 cm)), the expansion is still outside the boundary layer so that the data discussed should be free of expansion effects.

The predictions for static pressure below δ_{T_t} seem to be reasonable; however, a check on the credibility of these predictions is needed. To this end, the method of reference 5 was used to predict pitot pressures. These were then compared directly with the pitot pressures measured in the interaction region below δ_{T_t} (fig. 9). The starting profile at x = 2.60 in. (6.60 cm)

is shown in figure 9(a). Experimental data were used for points within the boundary layer and below the shock wave, while points above the wave were obtained from a theoretical conical flow solution. Profiles are also shown for x = 3.00 in. (7.62 cm), 3.20 in. (8.13 cm), and 3.60 in. (9.14 cm) (figs. 9(b) through (d)). At x = 3.60 in. (9.14 cm), the reflected compression is just outside the boundary layer. The predictions agree quite well with the data, with the largest difference of about 10 percent observed to occur near δ_{T_t} at x = 3.60 in. (9.14 cm) (fig. 9(d)); in most instances, the predictions are within 5 percent of the measured values. In view of the agreement between predicted and measured values of pressure, it was decided that the method of reference 5 provided reasonable estimates of the static pressure below δ_{T_t}. These values have been used for points within the boundary layer, while at the wall and outside the boundary layer the experimentally determined values have been used.

Estimates of the flow angles throughout the flow field were also obtained from the method of reference 5. Flow angles must be input at the initial station; however, no attempt was made to obtain them by measurement. Above the incident shock wave, the flow angles were taken to be those determined from the theoretical conical flow solution. At δ_{T_t} the flow angle was estimated from the continuity equation by assuming planar flow in a zero pressure gradient and integrating the continuity equation to give $v_e/u_e = d\delta^*/dx$. The flow angle was then assumed to vary linearly from the value at δ_{T_t} to zero at the wall. Experimental values of δ^* in the undisturbed boundary-layer flow are shown in figure 10. The rate of change of δ^* indicates a flow angle of about -0.4° at δ_{T_t}. Using this initial set of flow angles, the method of reference 5 predicts the angles throughout the flow field shown in figure 11. As an approximate check of the predicted values, estimates were made of flow direction at the boundary-layer edge in downstream flow (fig. 11(g) through (ℓ)) by

use of the continuity equation. Since, as noted previously, the boundary-layer thickness does not change downstream of station 3.60 in. (9.14 cm) (fig. 11(g)), the flow angle at δ_{T_t} can be estimated by using the values of the mass flow entrained into the boundary layer. The mass flow in the boundary layer, normalized with respect to the undisturbed boundary-layer flow (x = 2.40 in. (6.10 cm)), is shown in figure 12. The flow angles determined in this manner are shown in figure 11(g) through (ℓ). The agreement between the predicted flow angle and the angle determined from mass entrainment is quite good at x = 3.60 in. (9.14 cm). Further downstream, however, the predicted values become successively larger than those based on entrainment. Since the angles determined by entrainment are only estimates (probably accurate to within only 1°, if that) it was decided that the predicted values should be used for the mean radial velocity $\bar{v}$. As can be seen in figure 11, flow angles within the boundary layer may be quite large.

The total-temperature data can also be used to examine the effect of a strong adverse pressure gradient on the temperature profile. To this end, the temperature data are plotted in figure 13 on the nondimensional temperature versus velocity coordinate. The linear relationship for zero-pressure-gradient, unity-Prandtl-number flow (the so-called Crocco relationship) is shown along with the data for four streamwise stations. The entering profile (x = 2.60 in. (6.60 cm)) has a behavior typical of nozzle-wall (favorable pressure gradient) temperature distributions (see ref. 48). However, a rather pronounced change in the profile occurs after the flow encounters a region of adverse pressure gradient (x = 3.20 in. (8.13 cm)). The profiles continue to change as the flow moves into regions of higher and higher pressure. Thus, the departure of the temperature from the Crocco relationship is substantial, just as it is for flows undergoing sustained favorable gradients (e.g., the nozzle wall).

One final topic relative to the mean flow can be discussed with the aid of figure 12. The analytical method described in reference 4, for example, assumes that the mass addition to the boundary layer throughout the incident-reflected shock system is negligible. The data of the present study indicate that this condition is true as can be seen from figure 12. The rate of mass addition up to station $x = 3.60$ in. (9.14 cm) is essentially the same as in the undisturbed boundary layer; however, downstream of this station the rate of mass addition is more than an order of magnitude larger than that in the undisturbed flow.

Fluctuating-Flow Data

The fluctuating-flow data consist of the turbulent mass-transfer, momentum-transfer (Reynolds stress), and heat-transfer terms discussed in relation to equations (8) and (10) through (13). Only the data relative to the continuity and momentum equations are discussed here. However, all the fluctuating-flow data (including the heat-transfer term $\overline{\rho v' T'}$, which appears in eq. (8), but not eq. (9)) are presented in table 2. We examine the continuity and momentum equations to determine which of the fluctuating terms are significant in altering the mean flow throughout the interaction region.

The turbulent mass-transfer terms $\overline{\rho' u'}$ and $\overline{\rho' v'}$ in the continuity equation (10) are shown in figure 14. The values of $\overline{\rho' v'}$ actually go to zero at δ_{T_t}, while those of $\overline{\rho' u'}$ have a small but positive value in the free stream. The wall values are assumed to be zero, consistent with ρ', u', and v' each being zero at the wall. The shape of the $\overline{\rho' v'}$ profiles remains qualitatively the same throughout the interaction and in the downstream flow, attaining maxima near $\delta_{T_t}/2$. The profile of $\overline{\rho' u'}$, however, changes qualitatively throughout the interaction. The maximum exists near the wall in the upstream (zero pressure gradient) flow. Within the interaction, this maximum near the wall is washed out. However, the downstream flow appears to be relaxing to a

profile (with a maximum near the wall) similar to that of the upstream flow.

In addition to the observable qualitative changes, significant quantitative changes are evident in figure 14. There are significant increases in both $\overline{\rho'u'}$ and $\overline{\rho'v'}$ downstream of the incident shock and within the boundary layer (fig. 14 (d)). Further increases are evident downstream of the reflected shock system. These increases persist in the downstream flow to the last measuring station (x = 4.60 in. (11.68 cm)). The slight increases in the magnitudes of $\overline{\rho'u'}$ and $\overline{\rho'v'}$ evident near the reflected shock system (fig. 14(g) and (h)) are probably due to pressure fluctuations associated with the reflected shock system. These pressure fluctuations are neglected in the present study as discussed in the Analytical Considerations Section. We now turn directly to the derivatives of $\overline{\rho'u'}$ and $\overline{\rho'v'}$ in equation (10). Figure 15 shows the experimental values of $\partial\overline{\rho'u'}/\partial x$ and $(1/r)(\partial r\overline{\rho'v'}/\partial r)$ at four streamwise stations. Figure 15(a) shows data at an upstream station (x = 2.40 in. (6.10 cm)), 15(b) at a station within the interaction (x = 3.20 in. (8.13 cm)), 15(c) at a station just downstream (x = 3.80 in. (9.65 cm)), and 15(d) at a station far downstream (x = 4.60 in. (11.68 cm)). The derivatives were obtained from the data shown in figure 14 by first smoothing the data and then differentiating the smoothed data as discussed in appendix C.

It is clear from figure 15 that the term $\partial\overline{\rho'u'}/\partial x$ is almost everywhere at least one order of magnitude less than $(1/r)(\partial r\overline{\rho'v'}/\partial r)$. Furthermore, the difference between the two derivatives becomes more pronounced as the flow goes through the adverse pressure gradient. Thus, for flows similar to the one in the present study, it appears that the term $\partial\overline{\rho'u'}/\partial x$ may safely be neglected in analytical descriptions of such flows. Invoking this assumption, equation (10) may be written as:

$$\frac{\partial\bar{\rho}\bar{u}}{\partial x} + \frac{1}{r}\frac{\partial r\bar{\rho}\bar{v}}{\partial r} + \frac{1}{r}\frac{\partial r\overline{\rho'v'}}{\partial r} = 0$$

or

$$\frac{\partial \overline{\rho u}}{\partial x} + \frac{1}{r} \frac{\partial \overline{r \rho v}}{\partial r} = 0$$

which is just the usual continuity equation obtained by employing the boundary-layer approximation.

All the turbulent momentum-transfer terms (Reynolds stresses) that appear in equation (11) except $T_{r\theta}$ were measured in the present study and are shown in figure 16. All values of T_{ij}, except T_{rx} at the wall, are taken to be just the turbulent components of the stresses. This was justified by calculating the molecular contribution to T_{rx} from the mean-flow velocity data. At measuring stations away from the wall, the molecular portion of the total shear stress was found to be less than the turbulent portion by at least two orders of magnitude. At the wall, all the T_{ij} are assumed to be zero, except T_{rx}. The wall values for T_{rx} were calculated from the value of c_f derived from a fit of the mean-flow velocity profile to a compressible form of the law of the wall (ref. 4).

The qualitative behavior of these profiles can be discussed in light of known results obtained for incompressible, adverse-pressure-gradient flows (e.g., Sandborn and Slogar, ref. 50, or Bradshaw, ref. 51).

The general behavior of the T_{rx} profiles does not significantly change throughout the interaction. The values go to zero at the edge of the boundary layer, have a maximum near $\delta/2$, and have approximately constant values from the wall to the first data point away from the wall. However, the magnitude of T_{rx} increases markedly as the flow goes through the interaction. This is in qualitative agreement with results shown in references 50 and 51 for incompressible flows in adverse pressure gradients. The behavior of T_{rx} in the undisturbed flow (e.g., x = 2.40 in. (6.10 cm), fig. 16(a)) is similar to that shown in references 50 and 51 for a mild adverse pressure gradient. As

noted in appendix A, the present "undisturbed" flow has, in fact, gone through a slight adverse gradient.

The behavior of T_{xx}, T_{rr}, and $T_{\theta\theta}$ are also similar to their incompressible analogs. The values of T_{xx} are larger than either T_{rr} or $T_{\theta\theta}$ in the lower part of the layer; T_{rr} is less than $T_{\theta\theta}$ near the wall, while T_{rr} is greater than $T_{\theta\theta}$ in the outer portion of the boundary layer.

The value of $T_{\theta x}$ was measured in the present study. As was shown for a flow that is exactly two-dimensional, this term must be zero. It can be seen that the values of $T_{\theta x}$ are at least one order of magnitude lower than those of T_{rx} over nearly the entire flow. Although the values of $T_{\theta x}$ are small, they are not zero. Furthermore, the values of $T_{\theta x}$ exhibit a systematic pattern at all the measuring stations. The values are positive in the portion of the layer near the wall, and negative in the outer portion. The pattern is accentuated as the flow passes through the adverse pressure gradient (and as the boundary layer becomes thinner). This behavior might possibly be explained by the presence of streamwise (Goertler) vortices that are approximately the scale of the boundary-layer thickness. No definite conclusion relative to this possibility could be drawn from the present data and further work is required before the cause of these patterns can be confirmed. One can conclude, however, that the flow remained nominally two-dimensional throughout the adverse pressure gradient.

With a view toward determining which of the stresses play a significant role in altering the mean flow in equation (11), we turn directly to the gradients of the stresses. The gradients of mean pressure also appear in the momentum equations. Thus, to determine which gradients alter the mean flow, it is necessary to compare the turbulent stress gradients with themselves and with the pressure gradients.

The derivatives that appear on the right-hand side of the x-momentum equation (eq. (11a)) are shown in figure 17. These derivatives were obtained from the data shown in figure 16 by the same technique used to obtain the derivatives shown in figure 15. The same four stations as shown in figure 15 are used to show representative data for the entire flow. These are upstream (fig. 17(a)), within (fig. 17(b)), just downstream (fig. 17(c)), and far downstream (fig. 17(d)) of the interaction.

In the upstream, or undisturbed, flow (fig. 17(a)) $\partial\bar{p}/\partial x$ is nominally zero, while $\partial T_{xx}/\partial x$ is about 10 percent of $(1/r)(\partial r T_{rx}/\partial r)$. Thus, the upstream flow conforms reasonably well to the boundary-layer approximation (in which $\partial T_{xx}/\partial x$ is assumed to be zero). The behavior is sharply altered within the interaction region as is evident in figure 17(b), where the value of $\partial\bar{p}/\partial x$ is larger in magnitude than either turbulent stress term in the lower half of the boundary layer, while in the upper half $\partial\bar{p}/\partial x$ and $(1/r)(\partial r T_{rx}/\partial r)$ are of approximately the same magnitude. Thus, the flow becomes more heavily influenced by the pressure gradient than by the turbulence gradients. In contrast with the situation for the upstream flow, the term $\partial T_{xx}/\partial x$ in the downstream flow becomes more significant. Over most of the boundary layer, the magnitude of $\partial T_{xx}/\partial x$ is about 20 percent of that for $\partial\bar{p}/\partial x$, while it is about 25 to 30 percent of $(1/r)(\partial r T_{rx}/\partial r)$ in the lower half of the layer.

The value of $\partial T_{xx}/\partial x$ is still about 20 to 25 percent of $\partial\bar{p}/\partial x$ at the downstream station (fig. 17(c)); while the shear stress gradient $(1/r)(\partial r T_{rx}/\partial r)$ tends to dominate nearly all of the boundary-layer flow. We see that the flow within and just downstream of the interaction is definitely not boundary-layer-like in that $\partial T_{xx}/\partial x$ is not negligible; and, further, that the value of $\partial\bar{p}/\partial x$ varies substantially across the boundary layer.

At the far downstream station (fig. 17(d)), the flow is more typical of that for a boundary layer, in that $\partial T_{xx}/\partial x$ has become quite small over most of the layer.

Two additional points relative to the fluctuating flow can be made. In the Introduction, the susceptibility to separation when two interactions in the same boundary layer occur in proximity was noted. Two interactions were produced by a double cone similar to those used in reference 16. The interaction resulting from the first shock wave produced boundary-layer separation. The second shock wave would also have been strong enough to produce separation of the undisturbed layer. However, when the second interaction occurred just downstream of the first (so that there were two distinct interactions), the second interaction did not produce a boundary-layer separation. This phenomenon could not be predicted by either of the methods of reference 4 or 5, but it may be explained with the aid of figure 16 as follows. It can be seen that the wall shear stress, T_{rx} at the wall, continually increases throughout the region of adverse pressure gradient. This occurs because all of the turbulent mixing rates (e.g., T_{xx} and T_{rx}) have been increased so much as a result of the shock-wave - boundary-layer interaction that the momentum added to the flow near the wall exceeds that removed in passing through the pressure rise. Therefore, if another shock-wave - boundary-layer interaction followed closely downstream of the one considered here, the boundary layer could sustain a larger pressure gradient than the initial layer without separating.

Another point that is quite significant in the modeling of turbulent transport terms can be investigated with the aid of the shear stress T_{rx} presented in figure 16. For so-called "equilibrium boundary layers," a unique relationship exists between the shear stress and the mean velocity gradient $\partial\bar{u}/\partial y$. The constant of proportionality between these two quantities is termed an "eddy viscosity" or a "mixing length." We consider for simplicity here the

eddy viscosity model of the shear stress. The eddy viscosity ε is defined as:

$$\varepsilon = \frac{T_{rx}/\bar{\rho}}{\partial\bar{u}/\partial y}$$

One relationship proposed for ε for flow points away from the wall region (Clauser, ref. 52) is

$$\varepsilon = \text{const}\ \bar{u}_e \delta^*$$

which implies

$$T_{rx}/\bar{\rho} = \text{const}\ \bar{u}_e \delta^* \frac{\partial\bar{u}}{\partial y}$$

From the data in figure 16 and the behavior of δ^* (see fig. 10) and $\bar{u}_e$ through the shock interaction region, we can assess the validity of this general type of modeling. We first note from table 1 that $\bar{u}_e$ decreases by only about 10 percent between stations just upstream and just downstream of the interaction. From figure 10 we see that δ^* decreases by about 40 percent. We may estimate that the average value of $\partial\bar{u}/\partial y$ over the layer goes up by about 35 percent since $\bar{u}$ remains essentially unchanged and δ decreases by about 35 percent. This would indicate that the quantity $\bar{u}_e \delta^* (\partial\bar{u}/\partial y)$ downstream is about 70 percent of its value upstream. On the other hand, $\bar{\rho}$ increases by about a factor of 2 across the interaction. Therefore, if the equilibrium-shear-stress model were applicable, we would find T_{rx} increasing by a factor of less than 2. We see from figure 16, however, that T_{rx} is nearly an order of magnitude larger over most of the boundary layer, even far downstream of the interaction (approximately nine downstream-boundary-layer thickness after the reflected shock system leaves the boundary layer). On the basis of this, we can conclude that boundary-layer flow downstream of the interaction is strongly out of equilibrium with the mean flow, a situation that should be accounted for by the shear-stress modeling used in analytic methods to describe this flow. Such a modeling has been proposed for use in compressible flows by Bradshaw and Ferris (ref. 53).

CONCLUSIONS

The important conclusions derived from the present investigation are summarized below:

1. The pressure rise to incipient separation is less than previously obtained in axially symmetric flow and is much less than corresponding planar two-dimensional flow.

2. There are significant static-pressure and flow-angle variations across the boundary layer within and downstream of the interaction.

3. The adverse pressure gradient significantly affects the total temperature distribution.

4. The experimental turbulent stresses agree qualitatively with data obtained in incompressible flows with adverse pressure gradients.

5. The Reynolds normal-stress term normally neglected in boundary-layer analyses is important within and just downstream of the interaction.

6. The turbulent mixing rates are strongly out of equilibrium with the mean flow as a result of the interaction.

7. Because of 6, novel modeling of the turbulent mixing rates is required, even far downstream of the interaction such as that proposed by Bradshaw and Ferris (ref. 53).

Ames Research Center

National Aeronautics and Space Administration

Moffett Field, Calif. 94035, August 18, 1972

APPENDIX A

EXPERIMENTAL APPARATUS

The experimental investigation was conducted in the Heat-Power Laboratory of the Mechanical Engineering Building at the University of Washington, Seattle, Washington. The experimental apparatus used in this investigation consists of the supersonic wind tunnel (nozzle plus test section) and the instrumentation used to measure the flow within the test section. Figure 3 is a diagram of the test facility.

The supersonic wind-tunnel apparatus is similar to that used by Seebaugh (ref. 15), Mathews (ref. 4), and Teeter (ref. 16). However, significant improvements have been made in the ease of operation of the facility and in the actual aerodynamic components. A line sketch of the experimental facility is shown in figure 18. The wind tunnel is a continuous-flow facility using air supplied by two teflon-ring compressors capable of delivering in excess of 1 lbm/s (2.2 kg/s) of dried and filtered air at 540° R (300° K) and 70 psia (4.82×10^5 N/m^2). The air passes through the first of two pressure regulators, through an electric heater to vary the air temperature, an additional dryer consisting of approximately 25 ft^3 (0.7 m^3) of silica gel, a cartridge filter, the second pressure regulator, a quick-opening valve, a small gate valve, and into the tunnel plenum chamber. The pressure regulators allow continuous variation of tunnel plenum (operating total) pressures from zero to the maximum pressure, depending on the size of tunnel in operation and the pressure level desired. The plenum chamber has a volume of approximately 3 ft^3 (0.08 m^3) and contains several screens and four 2-in. (5.07 cm) thicknesses of 1/4-in. (0.635 cm) cell honeycomb straightener, which ensures that the swirl is negligible when the flow contracts from the plenum to the nozzle throat (area ratio approximately 150:1).

The plenum provides for the interchanging of the axially symmetric, plexiglass nozzle and test sections. The nozzle-test section facility that was used in the present study is shown in figure 19. The nozzle is 5.8 in. (14.7 cm) long and the constant-diameter test section is 6.5 in. (16.5 cm) long. Also shown is the probe drive mechanism (the same one used by Grande, ref. 14) that drives either pitot probes or hot-wire anemometer probes in both the longitudinal (x) and radial (r) directions. The x and r locations can be set to the nearest 0.0005 in. (0.00127 cm) with the dial adjustments. The aft portion of the test section contains a 2.2-in.-long (5.6 cm) by 0.2-in.-wide (0.51 cm) slot to allow for insertion and longitudinal translation of the probes. The contour of the nozzle is the same as that used by Seebaugh (ref. 15) with the addition of a correction for the boundary-layer-displacement thickness. The coordinates of the nozzle are given in table 3. The downstream end of the test section attaches to the movable diffuser and model-support sting mechanism. An overall view of this test site, including plenum and diffuser, is shown in figure 20.

The diffuser is supported by, and rigidly attached to, the carriage of a lathe bed. The carriage can be moved axially fore and aft to facilitate model changes in the tunnel and can be locked in position during operation. Also, the lathe bed is used to ensure precise alignment of the entire tunnel-diffuser combination each time the tunnel is opened and closed. The diffuser also contains the sting (see fig. 20) and sting translation mechanism. The sting is a case-hardened 1/2-in.-diam. (1.27 cm) steel shaft running in three Thompson linear ball bushings. The axial motion of the sting is controlled externally by a pinion gear driving a rack gear on the sting. A counter indicates the sting location to within 0.005 in. (0.013 cm).

The cone models used for generating the incident shock waves are mounted on the sting and may then be positioned anywhere on the centerline of the

tunnel. The cones themselves are straight cones turned from brass so that the base diameter is 1.30 in. (3.30 cm). The diffuser exhausts into a 150-ft^3 (4.25 m^3) vacuum tank maintained at a pressure of approximately 5 in. Hg (1.7×10^4 N/m^2) absolute, at maximum plenum pressure, by four Worthington Model 24D steam ejectors. A view of the facility with the wind tunnel installed is shown in figure 21.

A detailed survey of the flow within the nozzle and test section was conducted to define the mean-flow environment in which the boundary-layer investigation took place and in which the hot-wire anemometer calibrations (appendix C) were made. This survey consisted of pitot-pressure measurements on the centerline from the nozzle throat through the test section, off-centerline pitot measurements in the test section, and surface-static pressures in the test section.

The Mach number on the centerline deduced from these pitot pressure measurements is shown in figure 22. It can be seen that there is an overexpansion in the nozzle above the design value of 3.95. Recompression from this overexpansion then reduces the Mach number below the design value. Further expansions and compressions are evident.

The surface-static-pressure distribution in the absence of a cone (fig. 23) also indicates an overexpansion followed by a recompression. Near the origin of the test section, the wall pressure is low, and a definite rise occurs about 2 in. (5.1 cm) downstream. The off-centerline pitot measurements also confirm the presence of a recompression wave in this vicinity (about 1 in. (2.5 cm) ahead of the region studied in the present investigation).

Thus, the boundary layer on the nozzle-test section wall has a history of the favorable pressure gradient in the expansion section and of the slight adverse gradient induced by a recompression wave.

The off-centerline pitot measurements in the test section indicate that the Mach number external to the boundary layer has a value of 3.88 ± 0.02 over the length of the test section used in the present study.

The static pressure taps used in this study were constructed as shown in figure 24(a). There are 33 taps located at 0.10-in. (0.254 cm) intervals in the main line of taps, plus nine symmetry taps located at 90° intervals around the periphery of the tunnel at longitudinal intervals of 1.00 in. (2.54 cm). These taps were used to confirm the symmetry of the flow when the conical shock generator was installed.

The pitot pressures were measured with the probe shown in figure 24(b). The tip of the probe was made from 0.025-in. (0.063 cm) stainless steel tube with 0.006-in. (0.015 cm) walls. This tube was flattened and filed to produce a probe tip approximately 0.010 in. (0.025 cm) high with a 0.004-in. (0.010 cm) opening. The remainder of the probe is constructed of telescoping stainless tube as shown.

The orifice dam used in the detection of incipient separation (appendix B) was located 1 in. (2.54 cm) downstream of one of the last symmetry taps. The dam itself was constructed as shown in figure 25. The dam is 0.010 in. (0.025 cm) wide and 0.005 in. (0.013 cm) high and extends along the tunnel periphery for 1/2 in. (1.27 cm). These dimensions give a length-to-height ratio of 100:1 so that the flow near the center of the dam where the pressure taps are located can be expected to be reasonably two-dimensional.

The static pressures and the orifice dam pressures were measured with a CEC Model 4-312-0002, 0- to 10-psi absolute-pressure transducer. The absolute zero calibration point was obtained by a vacuum pump holding a pressure of approximately 60 to 80 μm Hg. The pitot pressures were measured with a CEC Model 4-312-0001, 25-psi differential-pressure transducer, with atmospheric pressure as reference. A Model J9D Scanivalve was used to aid in reading the

static pressures. All millivolt readings from the pressure transducers were obtained on a Dynasciences Model 440 digital multimeter whose lowest digit is 1 μV.

The instrumentation used for the fluctuating flow measurements consisted of the hot-wire probes and the anemometer system itself. A normal wire probe, used as a resistance thermometer, was used to measure total temperature.

The hot-wire probes were constructed as shown in figure 26. The wire itself was of 5-μm diam., etched tungsten wire supplied by the Sigmund Cohn Corporation, Mt. Vernon, New York. The wire supports (prongs) were made from high carbon steel, five-sided jeweler's broaches. They were tapered from approximately 50 μm at the tip to approximately 200 μm 1/4 in. (0.63 cm) from the tip. These prongs were set in a ceramic twin-conductor holder with epoxy resin so that approximately 1/8 in. (0.32 cm) of the prongs were exposed. The holder was approximately 0.040 in. (0.10 cm) in diameter and was wedge-shaped to minimize the influence of the probe support. Small twin-lead wire was used to connect the probes to the anemometer's coaxial cable. The resulting probes had a distance between the probe tips of approximately 500 μm, and, thus, an $\ell/d = 100$. This is a lower value of ℓ/d than is generally used and is the reason that individual calibration of each wire was required (see appendix C). The length was chosen to be small in order to obtain data as close to the wall as possible when the probe is in the r-x plane. With such a small distance between the probe tips, it was not feasible to use copper-plated wire ends (resulting in an even smaller sensing length of wire) similar, for example, to those used by Grande (ref. 14). Since tungsten cannot be soldered, the wires had to be arc welded to the prongs. During the present study, a micro-arc welder (fig. 27) was constructed and considerable time was spent learning how to attach wires without destroying the wire (and, at times, the entire prong!). The technique that was finally successful was to place the welding rod (a

0.003-in. (0.008 cm) silver wire) on top of the wire and in contact with the prong. The weld button was then depressed, causing a fine (roughly 10 μm) layer of silver to be deposited on the prong. Microscope examination of the weld showed that the wire was firmly embedded in the silver.

The sketches of the probes shown in figure 26 indicate that the wires were mounted slack. This was done to prevent inordinate amounts of strain-gaging in the wire. No quantitative measure of the slackness can be given except to say that the two wires used for the final results of the present study contained strain-gage signals that were always less than 2 percent of the rms voltage. The only way found in the present study to ensure that the wires did not produce too much strain-gage signal was simply to construct and try them. Wires that appeared visually identical could give entirely different extraneous signals. Although the wires were mounted in a somewhat arbitrary manner, the individual calibration of each wire allowed for any possible adverse effect of wire slack.

The probes constructed as above, one a normal wire and the other yawed, lasted the entire test. The normal wire had a nominal cold (540° R (300° K)) resistance of 1.03 Ω and was run for 30 hr in the supersonic stream. The yawed wire had a nominal cold resistance of 1.26 Ω and was run for 46 hr in the supersonic stream. During these run times the cold resistance changed only by about 3 percent (probably due to oxidation of the tungsten). Approximately 25 hot-wire probes were constructed and run during the preliminary phase of the present study; one should not get the impression that he need only construct two wires!

The anemometer was a Disa model 55D01, constant-temperature system. The manufacturer's quoted upper frequency response is 200 kHz, which corresponds to a decay time on the backside of a step input to the system of 0.80 μs. The decay-time oscilloscope traces for the wires constructed in the present study

are shown in figure 28. Figures 28(a) and (b) show decay traces for the normal wire at the minimum and maximum mass flows encountered in the study. Figure 28(c) shows the decay trace for the yawed wire at minimum mass flow. It can be seen that the decay time (the time required for the signal to decrease to within 1/e of its final value) was always less than or equal to 1 μs, indicating that the frequency response was in excess of 200 kHz throughout the range of flow. The blip in these time traces at about 3 to 4 μs indicates a slight overcompensation of the anemometer. The traces are shown for an overheat ratio $a_w = 0.8$. The frequency response decreases with decreasing overheat ratio; however, for the range of overheats used in the present study the frequency response was at least 200 kHz.

This high value of frequency response permits resolution of disturbances in the boundary layer whose streamwise dimensions are greater than $\delta/5$ in the outer part of the layer and greater than $\delta/8$ in the lower part of the layer. Consider a "chunk" of self-correlated fluid moving in the boundary layer at a velocity u_c. For a turbulent boundary layer, u_c is approximately $0.6u_e$ (Kistler and Chen, ref. 34), while in the inner part, the observed convection speeds may be as low as $0.4u_e$ (Vrebalovich, ref. 35). We may then use the equation relating u_c and the upper frequency response f_o to find the minimum size of disturbance resolved by a given system:

$$\lambda_{min} = u_c/f_o$$

Taking f_o to be 200 kHz and $u_e \approx 2200$ ft/sec (670 m/s), $\lambda_{min} \approx 0.0066$ ft (0.20 cm) in the outer part of the layer, while in the lower part $\lambda_{min} \approx 0.0044$ ft (0.13 cm).

To resolve a "chunk" of fluid passing the wire we need only consider $\lambda/2$ from the above equation. Thus, we can resolve disturbances larger than 0.0033 ft (0.10 cm) in the outer part of the layer and 0.0022 ft (0.06 cm) in the

inner part. These values correspond, respectively, to $\delta/5$ and $\delta/8$. Kistler (ref. 29) estimates that 90 percent of the turbulent energy is contained in disturbances larger than $\delta/4$, so that using the present anemometer and hot-wire combinations we should have been able to resolve over 90 percent of the turbulent energy.

APPENDIX B

DETECTION OF INCIPIENT SEPARATION

The strength of the shock wave used to generate the adverse pressure gradient imposed on the boundary layer was near that required for incipient separation of the layer. This strength was chosen for two reasons. It is low enough that the large pressure fluctuations found in highly separated flows would not be present (such fluctuations significantly affect the interpretation of the hot-wire anemometer signals). It is high enough to produce a pressure gradient that is realistic in terms of gradients that will exist in both internal and external flows for supersonic aircraft applications.

Before a final decision was reached as to the strength of the shock (i.e., the cone generator angle), a brief experimental investigation was made of the incipient separation pressure rise for the flow of the present study. Seebaugh (ref. 15) concluded from his experimental results that the pressure rises for incipient separation in axially symmetric flow were much lower than those found by Kuehn (ref. 9, and substantiated by others) for planar two-dimensional flow. This appendix presents information on incipient separation pressure rise that confirms and/or extends the conclusions reached by Seebaugh (ref. 15) for axially symmetric flows.

The flow conditions used in the present study were nearly the same as those used by Seebaugh (ref. 15). The Mach number was slightly higher, 3.88 versus 3.78; and the boundary-layer-thickness Reynolds number Re_δ slightly larger, 8.7×10^4 versus 6.2×10^4. Both studies were conducted in nominally 2-in.-diam. (5.08 cm) wind tunnels with the shock waves being generated by various angle cones placed in the center of the tunnel.

Several methods for detecting the incipient separation condition have been proposed and used in the past. Six of these methods are listed below:

1. Determine whether a "knee" or "hump" occurs in the surface static pressure distribution.

2. Determine whether the indicated reading of a pitot probe held on the surface becomes less than the surface static pressure in the absence of the pitot probe.

3. Use measurements of pitot pressure near the wall and surface static pressure to find Mach number and then extrapolate curves of Mach number versus y to zero Mach number (ref. 14 or 15).

4. Use a light coating of oil on the surface and observe whether ridges of accumulation are present that could be associated with the stagnation points of separation and reattachment.

5. Compare the static pressures observed just upstream and just downstream of a small obstruction on the surface (the so-called orifice dam).

6. Determine whether two reflected waves are present in the reflected shock system.

Methods 2 and 3 are similar in that they neglect disturbance effects of the pitot probe as it is brought near the surface. A problem with this assumption was discussed in the Review of Previous Work.

Methods 1, 2 (and essentially 3), 5, and 6 were investigated in the present study. Another method based on the introduction of alcohol at a minute rate into the boundary layer through a surface-static-pressure tap also was investigated. The physical principles involved with this technique are in some respects similar to the oil-flow technique (4); however, it is sufficiently different to consider it a new method. The alcohol injection method is discussed below.

A tiny stream of alcohol is allowed to enter a surface-static-pressure tap at negligibly low velocity while the cone (and the shock-wave - boundary-layer interaction region) is positioned well ahead of the tap. The cone is

then moved aft (see appendix C for details on motion of the conical generator) until the interaction region is quite close to the tap. On entering the tunnel, the alcohol turns and flows downstream along the tunnel surface. Now, if the flow is separated, when the cone is moved just slightly further aft, the flow of alcohol will reverse and the alcohol will proceed entirely upstream. Without further motion of the cone, a well-developed ring of alcohol will propagate around the periphery of the tunnel wall.

This change from downstream to upstream flowing alcohol is termed the "reattachment behavior," since the downstream-to-upstream change occurs at or very near what is most surely the reattachment point. So visually striking is the behavior that it is taken as the absolute criterion for the existence of separated flow. If no reattachment behavior can be observed, the boundary layer is assumed to have remained attached. The observed reattachment behavior is depicted schematically in figure 29. The location of the reattachment point can be determined quantitatively with a fair degree of certainty by the above procedure, since the presence of the alcohol itself probably alters the downstream to upstream behavior very little.

The location of the separation point, however, cannot be quantitatively located with certainty since the ring of alcohol that forms in the upstream portion of the separated flow most likely alters the separation point from that which would exist with no alcohol ring present. The location of the upstream edge of the alcohol ring is probably farther forward than the separation point in the absence of alcohol due to the buoyancy effect discussed in reference 10.

Using the alcohol-injection technique, it was found that cones whose half-angles were 10° or larger separated the boundary layer, but that a 9° cone did not. In order to quantify this result somewhat, the results obtained

using the orifice dam (see appendix A) were compared with the results from the alcohol-injection study.

The results of the orifice dam surveys made in the present study are shown in figure 30. The data were taken at x intervals of 0.015 in. (0.038 cm) ($\Delta x/\delta \approx 0.07$). The pressures from the upstream orifice and downstream orifice on the orifice dam are shown in comparison with the undisturbed static pressure (i.e., the surface static pressure in the absence of the dam). Also shown for the cases with separation are the locations of the reattachment point and the position of the leading edge of the alcohol ring.

Figure 30(a) shows the orifice dam results for a 12° half-angle cone. The reattachment point from the alcohol-injection technique matches exactly the point where the downstream pressure crosses the undisturbed pressure. There is some uncertainty in the location of reattachment due to uncertainty in the positioning of the cone relative to the pressure taps. An error band is indicated for the reattachment point. The position of the leading edge of the alcohol ring is also indicated. As previously noted, this is probably the farthest forward position at which separation could be occurring. Just downstream of this location, the upstream and downstream orifice dam pressures cross. This indicates that the orifice dam is located in a region of total backflow - that is, a separated region. Thus the separation point must lie upstream of this crossover point. The leading edge of the alcohol is at the same location as the crossover between the downstream and undisturbed pressures. The separation point was chosen to be at the center of the extremes indicated above. This is shown in figure 30(a). The length of separation ℓ_{sep} is indicated.

Similar results are indicated for the 10° cone in figure 30(b). For this case, a crossover of the upstream and downstream pressures does not occur.

The uncertainty in the separation point is assumed to be the same as in figure 30(a). With this assumption, the value of ℓ_{sep} for the 10° cone is as shown.

The results for the 9° cone are shown in figure 30(c). Reattachment behavior from the alcohol injection method was not observed for this case, so no alcohol locations are shown. The reattachment point (if any) was taken as the location of the downstream crossover point between the undisturbed and downstream pressures. The separation point was located by assuming that the forwardmost possible upstream location corresponds to the upstream crossover of the undisturbed and downstream pressures, and applying the uncertainty band as in figures 30(a) and (b). A range of no separation to slight separation is indicated for the 9° cone.

These separation lengths and their related uncertainties are shown in figure 31 as a function of cone half-angle. This plot indicates that a zero separation length (i.e., the incipient separation case) could occur anywhere between 8.1° and 9.3°, the most likely value being 8.9°. This is in agreement with results from the alcohol injection, which showed that a 9° cone was the incipient separation case. Thus, flow with the 9° cone has been considered the incipient separation case in the present study.

This value of incipient separation cone angle is lower than that found by Seebaugh (ref. 15) and corresponds to much lower pressure rises than Kuehn's (ref. 9) planar values. These values are compared in figure 32.

As noted earlier, other methods for determining incipient separation were investigated. Method 1, determining whether a hump occurs in the surface-static-pressure distribution, can be examined with the aid of figure 30(a). For this case, a separated region existed but no hump in the undisturbed pressure distribution is evident. Thus, separation may occur without producing a hump in the pressure distribution. This was further confirmed in the 10°

interaction by taking undisturbed static-pressure data at every 0.0015 in. (0.0038 cm), or one-tenth the spacing used in figure 30.

Method 2, and essentially method 3, can be tested by a comparison of the pitot pressure reading when the probe tip is at the wall with the undisturbed static pressure through an interaction known to be separated. The comparison for the 10° cone is shown in figure 33. Over the approximate separation length indicated, the pitot pressure might be expected to be less than the static pressure. This is not the case, however, so methods of detecting incipient separation based on pitot-pressure measurements near the wall are probably inaccurate.

Finally, method 6, which bases the existence of separated flow on whether two reflected waves are present in the reflected shock system, was studied. As noted in the main body of the thesis, a well-developed, two-wave reflected shock system existed for the 9° cone interaction. For this interaction the flow was very near the condition for incipient separation. It is doubtful that this well-developed shock system could have suddenly appeared due to the presence of a slight (if any) separated region. Therefore, the two-wave shock-system criterion should not be used without some reservation.

APPENDIX C

EXPERIMENTAL OPERATING PROCEDURES AND DATA REDUCTION

The procedures followed in obtaining the mean-flow and fluctuating-flow data and in reducing these data are given in this appendix. Several preliminary steps were taken before data were obtained. The diffuser was retracted and the desired conical shock generator installed on the sting. The diffuser was then locked in place and the downstream vacuum tank was evacuated. While the tunnel was under a vacuum, all the static-pressure instrumentation was checked to ensure against leaks. The pressure-transducer excitation voltage was set and the transducers zeroed to their respective reference pressures. The pressure regulators were set to give the desired operating total pressure (53.7 psia (3.7×10^5 N/m^2), nominally). The quick-opening valve to the plenum was then opened and supersonic flow established in the test section.

The cone was then moved to a position that would cause the peak pressure rise to occur near a set of symmetry pressure taps. The sting-bearing supports were then adjusted on the basis of symmetry of the wall static pressures to ensure that the cone was on the tunnel centerline and at zero incidence angle.

The streamwise variations of the data obtained in the present study were obtained by two techniques. First, for the undisturbed boundary-layer studies, the cone was moved to the aft end of the tunnel. Data were obtained from the static pressure ports at locations 2.60, 2.80, and 3.00 in. (6.60, 7.11, and 7.62 cm) downstream of the test section origin. The pitot pressures, total temperatures, and hot-wire data for the undisturbed boundary layer were also obtained at these stations.

The second method for obtaining streamwise variation was to hold the instrumentation at a fixed x station and move the cone (and interaction region) past the instrumentation. This fixed instrumentation station was

located 3.00 in. (7.62 cm) downstream of the test section origin. Moving the cone in this manner allowed data to be obtained over a length of 2.2 in. (5.7 cm) or approximately 11 boundary-layer thicknesses. An advantage of this technique was that the profile measurements could be made 1 in. (2.54 cm) ahead of the probe entry slot in the tunnel wall so that no interference from the slot was likely. When the cone was moved and the instrumentation held fixed, the flow entered the interaction at a slightly different value of Re_δ; however, this effect is quite small.

A check on these two procedures was made to ensure that the data were essentially the same whether the cone was moved relative to one fixed static-pressure tap, or whether the cone was fixed and the various static-pressure taps were used to obtain the static-pressure distribution. The surface static pressures obtained by these two techniques agreed to within 2 percent everywhere in the region in which data were obtained.

All of the x stations referred to in the main body of the thesis were measured relative to the cone tip. A cone tip x station of 2.80 in. (7.11 cm) corresponds to the tunnel x station of 3.00 in. (7.62 cm) (measured from the test section origin). The undisturbed boundary-layer data taken at tunnel x stations of 2.60 and 2.80 in. (6.60 and 7.11 cm) then correspond to cone tip x stations of 2.40 and 2.60 in. (6.10 and 6.60 cm), respectively. Thus, data obtained at cone tip stations 2.40, 2.60, and 2.80 in. (6.10, 6.60, and 7.11 cm) provide information on the actual boundary-layer development ahead of the interaction, while data for cone-tip stations from $x = 3.00$ in. (7.62 cm) to $x = 4.60$ in. (11.68 cm) show the effect of the interaction on the boundary layer holding the instrumentation station fixed and moving the cone.

The correspondence between tunnel x station and cone-tip x station was obtained by sighting across the plastic tunnel along peripheral scribe

lines located at 1-in. (2.54 cm) intervals starting at the test section origin. The accuracy of this procedure was estimated to be ±0.002 in. (0.005 cm).

As a means of stabilizing the operating total pressure and temperature, the wind tunnel was allowed to run for at least 30 min before data were taken. All electronic equipment, including the pressure transducers and the hot-wire anemometer units, was allowed to warm up at least 1 hr before data were taken.

The pitot pressures were taken at each of the 12 stations indicated in figure 4. The probe tip was first brought to the wall, so that the midplane of the probe was 0.005 in. (0.013 cm) from the wall (half of the probe height). The probe was then moved 0.005 in. (0.013 cm) toward the center of the tunnel and the first data point obtained. Successive points were obtained at 0.010 in. (0.025 cm) increments. The probe could be positioned in the y direction to within 0.0005 in. (0.0013 cm). The longitudinal position of the pitot probe was determined by sighting across the peripheral scribe lines to within an estimated accuracy of ±0.002 in. (0.005 cm).

Total temperatures were obtained in the present study by using a normal wire, constructed exactly as the normal hot-wire probe shown in figure 26(a), as a resistance thermometer. The wire probe was placed in a holder similar to that used to hold the pitot probe tip and was positioned with the same probe drive apparatus. The location of the wire in the flow was determined in a manner similar to that described for determining the pitot tip location, and to within about the same accuracy.

The wire was calibrated in the wind tunnel with the cone retracted to its farthest aft position. The calibration was accomplished by using established recovery factor r versus Mach number curves for various Reynolds numbers and changing the total temperature of the stream with the electric heater (fig. 18) and changing the total pressure. The recovery curves obtained from the data summarized in reference 54 are shown in figure 34. The wire temperature could

then be calculated for each Reynolds number. At the same time, the wire resistance was measured. These measurements yielded a thermal coefficient of resistivity α_1 that was valid for the probe in the presence of flow. The value obtained for the linear coefficient α_1 in the expression

$$\frac{R}{R_{ref}} = 1 + \alpha_1(T_w - T_{ref})$$

was 1.95×10^{-3} per °R (3.5×10^{-3} per °K) for $T_{ref} = 540°$ R (300° K). With this coefficient and measurements of the wire's resistance at each point in the flow field, T_t was calculated from the information in figure 34.

The fluctuating properties of the flow were obtained by a hot-wire anemometer. The hot-wire probes were installed on a probe shaft that was similar to that for the pitot probe. Positioning of the hot wires was accomplished by sighting across the peripheral scribe lines. The position of the yawed wire was taken to be at the center of the wire.

The Disa 55D01 constant-temperature anemometer unit was operated as suggested by the manufacturer. The input bias was adjusted to achieve a stable bridge operation over the range of overheat ratios used. The gain setting was set at position 9 for all cases. The high-frequency filter was set at position 2. The low-frequency gain was set to the high position. The bridge ratio was 20:1.

For each point in the flow, the wire's cold (recovery) resistance was read, the overheat ratio ($0.1 \leq a_w \leq 1.0$) selected, and the operating resistance of the wire was set on the anemometer. Data were obtained at five overheat ratios for each wire position used. At a given point in the flow, the normal wire was operated in only one position; however, the yawed wire was operated in four positions - two in the r-x plane and two in the x-θ plane. Fluctuating measurements were taken at a total of 137 flow-field points. Thus, just over 3400 data points were taken.

For each of these 3400 points, a square-wave frequency-response check was made by adjusting the inductance and capacitance controls in the anemometer to insure a high upper frequency response (see appendix A).

After the frequency response check, the value of the mean bridge voltage $\tilde{E}$ and the rms of the fluctuating voltage $\langle E' \rangle$ were recorded. The next operating resistance was then set and the process repeated.

Each wire was individually calibrated before being used to obtain data. From appendix D we see that to obtain fluctuations of the flow properties from the voltage fluctuations for the normal wire, two sensitivities are required: the sensitivity to mass fluctuations $\Delta e_{\rho u}$ and the sensitivity to total temperature fluctuations Δe_{T_t}. For the yawed wire, the sensitivity to the v component Δe_v also is required. Direct calibrations of the required sensitivities were made over the range of Mach and Reynolds numbers encountered in the study. This range is shown in figure 35. In the calibration process, the wires were mounted on the sting on the centerline of the supersonic nozzle. The Mach number seen by the wire was varied by moving the probe into various centerline stations in the nozzle. The Reynolds number (and thus ρu) was varied by changing the total pressure. To obtain the Δe_v sensitivity, a holder that could position the wire at -10°, -5°, 0°, +5°, +10° incidence angles to the free-stream flow direction was mounted on the sting.

The calibration of the normal wire was done as follows. The wire was positioned in the nozzle to give one of the desired calibration Mach numbers. For this position, the mean bridge voltage was read for various total pressures with constant total temperature. The results of these readings were then plotted as shown for two example Mach numbers in figure 36. The derivative $\partial \ln E / \partial \ln \rho u$ is needed to obtain $\Delta e_{\rho u}$. From figure 36, $\partial \ln E / \partial \ln p_t$ may be obtained. At a fixed Mach number and total temperature, $\partial \ln p_t = \partial \ln \rho u$. Thus, the desired term can be obtained directly

from plots similar to that of figure 36. The logarithmic relationship between E and p_t is not linear, so the slope must be determined as a function of Reynolds number. There was no significant effect of Mach number or overheat on $\partial \ln E/\partial \ln \rho u$. The values of $\partial \ln E/\partial \ln \rho u$ for the normal wire as a function of the Reynolds number are shown in figure 37.

An attempt was made to obtain Δe_{T_t} by direct calibration of the quantity $\partial \ln E/\partial \ln T_t$. This attempt was not successful, since when T_t was changed the total pressure also had to be changed to hold ρu constant (as required). The total pressure simply could not be controlled accurately enough to ensure that the change in voltage was produced solely from a change in total temperature.

The method used to calculate Δe_{T_t} is based on the expression for Δe_{T_t} given in appendix D. The sensitivity Δe_{T_t} is made up of $\Delta e_{\rho u}$ plus two physical constants of the gas and one of tungsten, which are well known, plus a term involving $\partial \ln E/\partial \ln R_w$ and R_w itself. The terms E and R_w, which were found at the time of the actual data acquisition, are then curve fit as suggested by Grande (ref. 14) to give $\partial \ln E/\partial \ln R_w$. Thus, all the information used in calculating Δe_{T_t} was either obtained ahead of time, known from physical constants, or obtained in place. The Δe_{T_t} obtained in this manner is considered to be directly calibrated.

The yawed-wire sensitivities to ρu and T_t were calibrated in the same manner as for the normal wire. The values obtained for $\partial \ln E/\partial \ln \rho u$ for the yawed wire were 0.65 of those for the normal wire over the calibrated range of flow variables. The value of 0.65 indicates that the effective yaw angle of the wire was approximately 40.5°. No attempt was made to measure the actual wire yaw angle, but it was intended to be nominally 45°.

The value of Δe_v for the yawed wire was also directly calibrated. The value of $\partial \ln E/\partial \phi$ is required for Δe_v. The value of ϕ was varied by

varying the angle of incidence of the probe holder, which was mounted on the sting. The lowest reliable overheat ratio for the yawed wire was found to be 0.2 (compared with Morkovin and Phinney's value of 0.15, ref. 26). The values of $\partial \ell n E/\partial\phi$ obtained from this calibration are shown in figure 38. There was no significant effect of overheat ratio on these values (above 0.2) and virtually no effect of Mach number.

The data-reduction procedures used for the mean and fluctuating flow are discussed below. The mean-flow data consisted of pitot pressure and surface and flow-field static pressures, and the wire resistances used in determining the total temperature. The data-reduction program described in reference 4 was used in the input static pressure mode and was modified to calculate the total temperature from the input wire resistance. Tabulated values of η versus Re_t obtained from the curves of figure 34 and the equation

$$T_w = \left(\frac{R_w}{R_\infty} - 1\right)\frac{1}{\alpha_1} + T_{t_\infty}$$

where R_∞ is the wire resistance at T_{t_∞}, were incorporated into the program to calculate the total temperature.

The fluctuating-flow data were reduced to usable form with computing programs that embody the analyses given for both the normal and yawed wires in appendix D. The programs are listed on the following pages - the first is for the normal wire and the second is for the yawed wire. The yawed wire program was used for both the r-x plane and x-θ plane data, and w' takes the role of v' when data for the x-θ plane are reduced.

For examination of the derivatives of the fluctuating-flow data, the data were smoothed by least-squares-fitting parabolas through five adjacent points, which allowed for a smooth curve to approximate the data locally rather than globally. The derivatives were then obtained directly from the smoothed data by the properties of each local parabola.

The normal hot wire was also used to locate the shock-wave positions. This was done by observing the qualitative behavior of the anemometer output voltage on an oscilloscope. In the region of a shock wave or compression wave, the slight unsteadiness of the waves gave rise to a large fluctuating voltage. These large fluctuations were quite distinct from the boundary-layer turbulence in the outer half of the boundary layer (and, of course, in the inviscid flow). The locations of the incident and reflected shock systems were mapped out by this technique and were used to aid in the interpretation of the pitot-pressure profiles.

```
C
C
C
C          PROGRAM FOR REDUCING NORMAL HOT-WIRE DATA
C
C
C
C
C                PROGRAM INPUT DESCRIPTION
C
C
C     CARD NO.      COL.NO.      NAME                DESCRIPTION
C
C       1            1-72        IDENT          ALPHANUMERIC IDENTIFICATION
C
C       2            1-10        TEST           TEST NUMBER
C                    11-20       RUN            RUN NUMBER
C                    21-30       WIRENO         WIRE NUMBER
C                    31-40       X              X LOCATION OF PROFILE SURVEY
C                    41-50       RB             ANEMOMETER FIXED BRIDGE RESISTANCE,OHMS
C                    51-60       RC             CABLE RESISTANCE,OHMS
C                    61-70       YNO            NUMBER OF Y LOCATIONS IN PROFILE. AT EACH
C                                               Y ONE SET OF CARDS 3,4,AND 5 ARE REQUIRED.
C       2A           1-50        AW             THE 5 OVERHEAT RATIOS AT THIS X (0.2,0.4,ETC.)
C       3            1-10        Y              Y LOCATION OF DATA POINT
C                    11-20       AM             LOCAL MACH NUMBER
C                    21-30       RET            LOCAL WIRE REYNOLDS NUMBER
C                    31-40       RR             RECOVERY RESISTANCE OF WIRE,OHMS
C                    41-50       UBAR           LOCAL MEAN VELOCITY,FT/SEC
C                    51-60       TBAR           LOCAL MEAN TEMPERATURE,DEG. R
C                    61-70       RHOBAR         LOCAL MEAN DENSITY,LB/FT**3
C                    71-80       ANGLE          LOCAL FLOW ANGLE,DEG.
C
C       4            1-10        EBAR(1)        MEAN BRIDGE VOLTAGE AT FIRST OVERHEAT RATIO,VOLTS
C                    11-20       EBAR(2)                  ''          SECOND          ''
C                                               ...
C                    41-50       EBAR(5)                  ''           FIFTH          ''
```

```
C
C       5           1-10      ERMS(1)       RMS FLUCT. BR. VOLTAGE AT FIRST OVRHT.,MILLIVOLTS
C                   11-20     ERMS(2)                    ''              SECOND       ''
C                                        ...
C                   41-50     ERMS(5)                    ''              FIFTH        ''
C
C
C
C
      DIMENSION  AIDENT(18), AW(10), EBAR(10),ERMS(10),RW(10),          -
     1ALNRW(50),ESQ(50),SLOPRU(10),SLOPRW(10),SLOPTT(10),AK(10),        -
     2DELERU(10),DELETT(10),R(50),S(10),B(20),W(6),W1(50),C(20),SSQ(50) -
     3,SCR(10,6),SCR1(10,6),SSQ2(3),R2(3),W2(3),D(20)
      DIMENSION AMAT(10,6),AMATT(10,6),DIAG(6),RESID(50),IPR(6),RHS(10),-
     1SOLN(6),SC (6)  ,A(20,3),APR(20,4)
      DIMENSION RECAL(6),SLOCAL(6)
C
C     NOOH IS THE NUMBER OF OVERHEAT RATIOS
C
      NOOH = 5
C
C
C     RECAL&SLOCAL ARE THE WIRE CALIBRATION DATA
C
C                 RECAL IS THE WIRE TOTAL REYNOLDS NUMBER
C
C                 SLOCAL IS DLN E/DLN RHO U  AT EACH RECAL
C
C
C
      DATA RECAL/1.,8.,20.,30.,40.,60./
      DATA SLOCAL/0.04,0.06,0.08,0.10,0.11,0.13/
      DMON = 0.
C
C
C     READ SEQUENCE
C
```

```
C
    1 READ(5,1000) (AIDENT(I),I=1,18)
    2 READ(5,1001) TEST,RUN,WIRENO,X,RB,RC,YNO
      IF(TEST.EQ.9999.) GO TO 999
      READ(5,1001) (AW(I),I=1,NOOH)
      NOY = YNO
      DO 99 LL=1,NOY
    3 READ(5,1001) Y,AM,RET,RR,UBAR,TBAR,RHOBAR,ANGLE
      READ(5,1001) (EBAR(I),I=1,NOOH)
      READ(5,1001) (ERMS(I),I=1,NOOH)
C
C        INITIALIZE
C
      EBARR = 0.0
      ANGLE = ANGLE/57.29578
      VBAR = UBAR*TAN(ANGLE)
      NWIRE = WIRENO
      NTEST = TEST
      NRUN = RUN
      RS = RB+RC
      DO 20 I=1,NOOH
      RW(I) = AW(I)*RR+RR
   20 W1(I) = 1.
C
C
C         CALCULATION OF WIRE SENSITIVITIES
C
C
C
C
C          RHO - U      SENSITIVITY
C
C
      DO 31 I=1,NOOH
C
C
```

```
C            TAINT IS A TABLE LOOKUP AND INTERPOLATION (USED AS 2ND ORDER) ROUTINE
C
C
      CALL TAINT(RECAL,SLOCAL,RET,SLOPRU(I),6,2,NER,DMON)
C
C
   31 DELERU(I) = EBAR(I)/100.*SLOPRU(I)
C
C
C
C
C      T-T   SENSITIVITY
C
C
C
      DO 41 I=1,NOOH
   41 AK(I) = 1.09+AW(I)*0.03
      JJ = NOOH+1
      ESQ(1) = EBARR  **2
      ALNRW(1) = ALOG(RR)
      W(1) = 1.
      DO 42 I=2,JJ
      K = I-1
      ESQ(I) = EBAR(K)**2
      W(I) = 1.
   42 ALNRW(I) = ALOG(RW(K))
      W1(6) = 1.
C
C
C           LSQPOL IS A LEAST SQUARES CURVE FIT
C
C
C
      CALL LSQPOL (ESQ,ALNRW,W1,RESID,6,SUM,1,APR,B,4)
      DO 43 I=1,NOOH
      SLOPRW(I) = 1./(2.*B(2) *EBAR(I)**2+4.*B(3)*EBAR(I)**4+6.*B(4)*    -
     1EBAR(I)**6)
      SLOPTT(I) = 0.942-AK(I)*(SLOPRW(I)+0.5-RW(I)/(RW(I)+RS))           -
```

```
     1-0.765*SLOPRU(I)
C
C
      DELETT(I) = EBAR(I)/100.*SLOPTT(I)
C
C
C
C
C    COMPUTE  THE  KOVASZNAY  VARIABLES
C
C
      R(I) = -DELERU(I)/DELETT(I)
   43 S(I) = -ERMS(I)/DELETT(I) *0.001
C
C
C
C      COMPUTE FLUCTUATING QUANTITIES BY CURVE FITTING  S**2 VS. R
C
C
C
      DO 51 I=1,NOOH
   51 SSQ(I) = S(I)**2
      CALL LSQPOL(R,SSQ,W1,RESID,5,SUM,1,A,C,3)
      IF(C(1).GE.0.0)  GO TO 52
      TTPOVR = 0.0
      RUPOVR = SQRT(C(3))
      RRUTT = 0.0
      GO TO 53
   52 TTPOVR = SQRT(C(1))
      RUPOVR = SQRT(C(3))
      RRUTT = -C(2)/(2.*TTPOVR*RUPOVR)
   53 DO 54 I=1,3
      R(I) = R(I+2)
   54 SSQ(I) = SSQ(I+2)
      CALL LSQPOL(R,SSQ,W1,RESID,4,SUM,1,A,D,3)
      IF(D(1).GE.0.0)  GO TO 55
```

```
      TTPOV3 = 0.0
      RUPOV3 = SQRT(D(3))
      RRUTT3 = 0.0
      GO TO 56
   55 TTPOV3 = SQRT(D(1))
      RUPOV3 = SQRT(D(3))
      RRUTT3 = -D(2)/(2.*TTPOV3*RUPOV3)
C
C
C     COMPUTE THE DERIVED TURBULENCE TERMS
C
C
   56 ALPHA = 1./(1.+0.2*AM**2)
      BETA = 0.4*AM**2*ALPHA
      RUTT = -C(2)/2.
      DENOM = 1./(ALPHA+BETA)**2
      USQOVR = DENOM*(TTPOVR**2+ALPHA**2*RUPOVR**2+2.*ALPHA* RUTT)
      IF (USQOVR.LT.0.0) USQOVR = 0.0
      UTOVR=DENOM*(TTPOVR**2+(ALPHA-BETA)* RUTT-ALPHA*BETA*RUPOVR**2)
       TSQOVR = DENOM*(BETA**2*RUPOVR**2+TTPOVR**2-2.*BETA* RUTT)
      UROVR = -UTOVR
      RTOVR = -TSQOVR
      PI = RUPOVR/(1.-1./AM**2)
      PPOVR = 1.4*PI
      TAU = SQRT(USQOVR)
      SIGMA = SQRT(TSQOVR)
      RUT = UTOVR/TAU/SIGMA
      UPSQ = USQOVR*UBAR**2
      TPSQ = TSQOVR*TBAR**2
      UPRP = UROVR*UBAR*RHOBAR*1.E-04
      UPTP = UTOVR*UBAR*TBAR*1.E-04
      RPTP = RTOVR*RHOBAR*TBAR*1.E-04
      TXX = (RHOBAR*UPSQ*1.E-04+2.*UBAR*UPRP)/32.174
       RUPSQ = RHOBAR*UPSQ/321740.
      TWOUUP = 2.*UBAR*UPRP/32.174
      RHOUT = RHOBAR*UPTP
```

```
      URPTP = UBAR*RPTP
      TRPUP = TBAR*UPRP
      VRPTP = VBAR*RPTP
      QX = RHOUT*URPTP*TRPUP
      QR = VRPTP
C
C                OUTPUT SEQUENCE
C
      WRITE(6,1100) (AIDENT(I),I=1,18)
      WRITE(6,1101)
      WRITE(6,1102) NTEST,NRUN,NWIRE,RB,RC
      WRITE(6,1103)
      WRITE(6,1104) X, Y, AM, RET,RR,UBAR,TBAR,RHOBAR
      WRITE(6,1105)
      WRITE(6,1106) (AW(I),RW(I),EBAR(I),ERMS(I),DELERU(I),DELETT(I),    -
     1R(I),S(I),I=1,NOOH)
      WRITE (6,1111)
      WRITE(6,1107)  TTPOVR,RUPOVR,RRUTT
      WRITE (6,1113)
      WRITE(6,1108) USQOVR,TSQOVR,UTOVR,UROVR,RTOVR,PPOVR
      WRITE(6,1109)
      WRITE(6,1110) PI,SIGMA,TAU,RUT
      WRITE (6,1114)
      WRITE(6,1112)  RUPSQ,TWOUUP,UPRP,RHOUT,URPTP,TRPUP
      WRITE(6,1115) TXX,QX,QR
C
C
   99 CONTINUE
      GO TO 2
  999 STOP
C
C
C   FORMAT STATEMENTS
C
C
1000  FORMAT(18A4)
```

```
1001  FORMAT(8F10.5)
1100  FORMAT(1H1 ,25X,18A4,//)
1101  FORMAT(1H ,10X,4HTEST,10X,3HRUN,10X,4HWIRE,5X,8HBRIDGE R,5X,      -
     17HCABLE R/)
1102  FORMAT(5X,I5,10X,I5,10X,I5, 5X,F10.1,5X,F10.2//)
 1103 FORMAT(10X,'X',10X,'Y',10X,'M ', 6X,'RET',5X,'RECOVERY R' ,5X,    -
     1'UBAR',5X,'TBAR',5X,'RHOBAR'/)
1104  FORMAT(5X,5F10.2,2F12.0,F10.5//)
1105  FORMAT(5X,8HOVERHEAT,5X,6HWIRE R,8X,4HEBAR,8X,4HERMS,4X,6HDELERU, -
     14X,6HDELETT,8X,1HR,8X,1HS/)
1106  FORMAT(5X,8F10.3 )
1107  FORMAT(25X,'TTPOVR = ',F6.2,10X,'RUPOVR = ',F6.2,10X,'RRUTT = ',   -
     1F6.2//)
1108  FORMAT( 2X,'USQOVR = ',F6.2,5X,'TSQOVR = ',F6.2,5X,                -
     1'UTOVR = ',F8.2,5X,'UROVR = ',F8.2,5X,'RTOVR = ',F8.2,             -
     25X,'PPOVR = ',F6.2//)
 1109 FORMAT(40X,'MORKOVIN MODE VARIABLES'/)
 1110 FORMAT(20X,'PI = ',F6.2,10X,'SIGMA = ',F6.2,10X,'TAU = ',F6.2     -
     1,10X,'RUT = ',F6.2//)
 1111 FORMAT(1X,/ ,40X,'KOVASZNAY VARIABLES'/)
 1112 FORMAT( 2X,'RHOUPSQ = ',F6.2,5X,'2U*UPRP = ',F6.2,5X,             -
     1'UPRP = ',F7.4,5X,'RHOUT =',F7.2,5X,'URPTP =',                    -
     2F7.2,5X,'TRPUP =',F6.2/)
 1113 FORMAT(40X,'DERIVED VARIABLES'/)
 1114 FORMAT(35X,'REYNOLDS STRESS AND OTHER TERMS IN EQUATIONS'/)
 1115 FORMAT(20X,'TXX = ',F6.2,3X,'LBF/SQFT',10X,'QX = ',F8.2,9X,-
     1'QR =',F7.4,3X,'LBM-DEG/SEC-SQFT')
      END
```

```
C
C
C
      PROGRAM FOR REDUCING YAWED HOT-WIRE DATA

C     THIS PROGRAM IS USED FOR BOTH V-PRIME RELATED AND
C     W-PRIME RELATED DATA. THE FORTRAN IS WRITTEN
C     IN TERMS OF V-PRIME FOR SIMPLICITY.

C               PROGRAM INPUT DESCRIPTION

C  CARD NO.     COL.NO.      NAME          DESCRIPTION
C
C    1          1-72         IDENT         ALPHANUMERIC IDENTIFICATION
C
C    2          1-10         TEST          TEST NUMBER
C               11-20        RUN           RUN NUMBER
C               21-30        WIRENO        WIRE NUMBER
C               31-40        X             X LOCATION OF PROFILE SURVEY
C               41-50        RB            ANEMOMETER FIXED BRIDGE RESISTANCE,OHMS
C               51-60        RC            CABLE RESISTANCE,OHMS
C               61-70        YNO           NUMBER OF Y LOCATIONS IN PROFILE. AT EACH
C                                          Y, ONE SET OF CARDS 3,4,5,6, AND 7  ARE REQUIRED.
C                                          DATA ON  4  AND 5 ARE FOR THE '+' WIRE ORIENTATION;
C                                          6 AND 7 ARE FOR THE '-'   (180 DEGREE ROLL FROM '+')
C    2A         1-50         AW            THE 5 OVERHEAT VALUES AT THIS X (0.2,0.4, ETC.)
C
C    3          1-10         Y             Y LOCATION OF DATA POINT
C               11-20        AM            LOCAL MACH NUMBER
C               21-30        RET           LOCAL WIRE REYNOLDS NUMBER
C               31-40        RR            RECOVERY RESISTANCE OF WIRE,OHMS
C               41-50        UBAR          LOCAL MEAN VELOCITY,FT/SEC
C               51-60        TBAR          LOCAL MEAN TEMPERATURE,DEG. R
C               61-70        RHOBAR        LOCAL MEAN DENSITY,LB/FT**3
C               71-80        ANGLE         LOCAL FLOW ANGLE,DEG.
C
```

```
C
C       4           1-10      EBAR(1)       MEAN BRIDGE VOLTAGE AT FIRST OVERHEAT RATIO,VOLTS
C                   11-20     EBAR(2)                  ''          SECOND          ''
C                                    ...
C                   41-50     EBAR(5)                  ''           FIFTH          ''
C
C       5           1-10      ERMS(1)       RMS FLUCT. BR. VOLTAGE AT FIRST OVRHT.,MILLIVOLTS
C                   11-20     ERMS(2)                  ''            SECOND        ''
C                                    ...
C                   41-50     ERMS(5)                  ''            FIFTH       ''
C
C     6 AND 7                 SAME INFORMATION AS 4 AND 5 ONLY THESE ARE FOR '-' ORIENTATION.
C
C       8           1-10      RUPOVR        (RHO U)' RHO U *10**4   FROM NORMAL WIRE
C                   11-20     TTPOVR        TT'/TT *10**4                  ''
C                   21-30     RRUTT         CORRELATION COEFFECIENT BETWEEN (RHO U)' AND TT'
C
C
C
C
      DIMENSION AIDENT(18),AW(10),EBAR(10),ERMS(10),RW(10),       -
     1ALNRW(50),ESQ(50),SLOPRU(10),SLOPRW(10),SLOPTT(10),AK(10),     -
     2DELERU(10),DELETT(10),R(50),S(10),B(20),W(6),W1(50),C(20),SSQ(50)  -
     3,SCR( 4,4),SCR1(10,6),SSQ2(4),R2(4),W2(4),D(2)
      DIMENSION AMAT( 4,4),AMATT(10,6),DIAG(6),RESID(50),IPR(6),RHS( 4),
     1SOLN(4),SC (6)    ,SPLOT(10)
      DIMENSION RPLOT(10),EBAR2(10),ERMS2(10),SSTAR(5),DIFFE(5),SLOPV(5)
      DIMENSION RECAL(6),SLOCAL(6)
      DIMENSION A(20,2),APR(20,4)
      DIMENSION SLOV(6),DELEV(10)
      DIMENSION SUME(5)
      DIMENSION ENORMS(5),V(5)
C       RECAL IS THE WIRE TOTAL REYNOLDS NUMBER
C       SLOCAL IS DLN E/DLN RHO U AT EACH RECAL
C       SLOV IS DLN E/D PHI AT EACH RECAL
C
```

```
C     RECAL,SLOCAL, AND SLOV ARE THE WIRE CALIBRATION DATA
C
      DATA RECAL/1.,8.,20.,30.,40.,60./
      DATA SLOCAL/0.04,0.06,0.08,0.10,0.11,0.13/
      DATA SLOV/ 0.06, 0.11, 0.15, 0.16, 0.17, 0.19/
      DMON = 0.
      EMON = 0.
C
C
C       NOOH IS THE NUMBER OF OVERHEAT RATIOS
C
C
      NOOH = 5
C
C
C     READ SEQUENCE
C
C
    1 READ(5,1000) (AIDENT(I),I=1,18)
    2 READ(5,1001) TEST,RUN,WIRENO,X,RB,RC,YNO
      IF(TEST.EQ.9999.) GO TO 999
    9 READ(5,1001) (AW(I),I=1,NOOH)
      NOY = YNO
      DO 99 LL=1,NOY
    3 READ(5,1001) Y,AM,RET,RR,UBAR,TBAR,RHOBAR,ANGLE
      READ(5,1001) (EBAR(I),I=1,NOOH)
      READ(5,1001) (ERMS (I),I=1,NOOH)
      READ(5,1001) (EBAR2(I),I=1,NOOH)
      READ(5,1001) (ERMS2(I),I=1,NOOH)
      READ(5,1001) RUPOVR, TTPOVR, RRUTT
C
C        INITIALIZE
C
      ANGLE = ANGLE/57.29578
      EBARR = 0.0
      NWIRE = WIRENO
```

```
      NTEST = TEST
      NRUN = RUN
      RS = RB+RC
      DO 20 I=1,NOOH
      RW(I) = AW(I)*RR+RR
   20 W1(I) = 1.
C
C
C          CALCULATION OF WIRE SENSITIVITIES
C
C
C
C
C
C          RHO - U      SENSITIVITY
C
C
      REFIT = RET*1.0
      DO 31 I=1,NOOH
C
C
C          TAINT IS A TABLE LOOKUP AND INTERPOLATION (USED AS A 2ND ORDER)ROUTINE
C
C
      CALL TAINT(RECAL,SLOCAL,REFIT,SLOPRU(I),6,2,NER,DMON)
C
C
C            THE VALUE 0.650 BELOW IS CALIBRATED AND MAY CHANGE FROM WIRE TO WIRE.
C
C
      SLOPRU(I) = SLOPRU(I)*0.650
C
C
   31 DELERU(I) = EBAR(I)/100.*SLOPRU(I)
C
C
C
```

```
C
C       T-T   SENSITIVITY
C
C
      DO 41 I=1,NOOH
   41 AK(I) = 1.09+AW(I)*0.03
      JJ = NOOH+1
      ESQ(1) = EBARR  **2
      ALNRW(1) = ALOG(RR)
      W(1) = 1.
      DO 42 I=2,JJ
      K = I-1
      ESQ(I) = EBAR(K)**2
      W(I) = 1.
   42 ALNRW(I) = ALOG(RW(K))
      W1(6) = 1.
C
C
C           LSQPOL IS A LEAST SQUARES CURVE FIT
C
C
      CALL LSQPOL(ESQ,ALNRW,W1,RESID,6,SUM,1,APR,B,4)
      DO 43 I=1,NOOH
      SLOPRW(I) = 1./(2.*B(2) *EBAR(I)**2+4.*B(3)*EBAR(I)**4+6.*B(4)*
     1EBAR(I)**6)
      SLOPTT(I) = 0.942-AK(I)*(SLOPRW(I)+0.5-RW(I)/(RW(I)+RS))
     1-0.765*SLOPRU(I)
C
C
      DELETT(I) = EBAR(I)/100.*SLOPTT(I)
C
C
C
C
C      V  SENSITIVITY
C
```

```
C
      CALL TAINT(RECAL,SLOV,RET,SLOPV(I),6,2,NER,EMON)
      DELEV(I) = EBAR(I)/100.*SLOPV(I)
C
C
C
C
C     COMPUTE  THE  KOVASZNAY  VARIABLES
C
C
   75 R(I) = -DELERU(I)/DELETT(I)
      DIFFE(I) = (ERMS(I)/EBAR(I))**2 - (ERMS2(I)/EBAR2(I))**2
      SUME(I) = ((ERMS(I)/EBAR(I))**2 + (ERMS2(I)/EBAR2(I))**2)*1.E-06
   43 SSTAR(I) = 0.01*DIFFE(I)/(4.*SLOPTT(I)*SLOPV(I))
C
C
C
C      COMPUTE FLUCTUATING QUANTITIES BY CURVE FITTING  SSTAR VS. R
C
C
C
      DO 51 I=1,NOOH
   51 SSQ(I) = SSTAR(I)
      CALL LSQPOL(R,SSQ,W1,RESID,5,SUM,1,A,C,2)
      C(2) = -C(2)
C
C
C          COMPUTE VPRIME**BAR
C
C
      ALPHA = 1./(1.+0.2*AM**2)
      BETA = 0.4*AM**2*ALPHA
      DO 71 I=1, 4
      L  = I+1
      RHS(I) = SUME(L )
      AMAT(I,1) = 2.*(SLOPRU(L)/100.)**2
```

```
      AMAT(I,2) = 4.*SLOPRU(L)/100.*SLOPTT(L)/100.
      AMAT(I,3) = 2.*(SLOPTT(L)/100.)**2
      AMAT(I,4) = 2.*(SLOPV(L)/100.)**2
      ENORMS(I) = AMAT(I,1)*RUPOVR**2+AMAT(I,2)*RRUTT*RUPOVR*TTPOVR+   -
     1AMAT(I,3)*TTPOVR**2
      V(I) = (RHS(I)-ENORMS(I))/AMAT(I,4)
   71 CONTINUE
C
C
C           COMPUTE THE DERIVED TURBULENCE TERMS
C
C
      VBAR = UBAR*TAN(ANGLE)
      RHOBAR = RHOBAR/32.174
      VPTPOV = (C(1)-BETA*C(2))/(ALPHA+BETA)
      VPRPOV = -VPTPOV
      UPVPOV = (C(1)+ALPHA*C(2))/(ALPHA+BETA)
      UPVP = UPVPOV*UBAR**2*1.E-04
      RHOUV = UPVP*RHOBAR
      URPVP = VPRPOV*RHOBAR*UBAR**2*1.E-04
      TRX = RHOUV+URPVP+VRPUP
      RPVP = VPRPOV*UBAR*RHOBAR*32.174*1.E-04
      VPSQ = V(3)    *UBAR**2*1.E-04
      RHOVSQ = VPSQ*RHOBAR
      TWOVRV = 2.*VBAR*RPVP/32.174
      TRPVP = TBAR*RPVP
      RHOVT = -TRPVP
      DENOM = 1./(ALPHA+BETA)**2
      TSQOVR = DENOM*(BETA**2*RUPOVR**2+TTPOVR**2-2.*BETA*SOLN(2))
      UTOVR = DENOM*(TTPOVR**2+(ALPHA-BETA)*SOLN(2)-ALPHA*BETA*RUPOVR**2)
      VRPUP =  -UTOVR*RHOBAR*UBAR*1.E-04
      VRPTP = -VBAR*TSQOVR*TBAR*RHOBAR*1.E-04*32.174
      TRR = RHOVSQ+TWOVRV
      QR = VRPTP
      RHOBAR = RHOBAR*32.174
      ANGLE = ANGLE*57.29578
```

```
C
C
C          OUTPUT SEQUENCE
C
C
   56 WRITE(6,1100) (AIDENT(I),I=1,18)
      WRITE(6,1101)
      WRITE(6,1102) NTEST,NRUN,NWIRE,RB,RC
      WRITE(6,1103)
      WRITE(6,1104) X,Y,AM,RET,RR,UBAR,TBAR,RHOBAR,ANGLE
      WRITE(6,1105)
      WRITE(6,1106) (AW(I),RW(I),EBAR(I),EBAR2(I),ERMS(I),ERMS2(I),
     1                                          DELERU(I),DELETT(I),
     2R(I),SSTAR(I),I=1,NOOH)
      WRITE(6,1108)
      WRITE(6,1107) RUPOVR,TTPOVR,RRUTT,C(1),C(2),V(3)
      WRITE (6,1109)
      WRITE (6,1110) RHOUV,URPVP,VRPUP, RHOVSQ,TWOVRV,RPVP
      WRITE (6,1111) RHOVT,VRPTP,TRPVP
      WRITE (6,1113) TRX,TRR,QR
C
C
   99 CONTINUE
      GO TO 2
  999 STOP
C
C
C    FORMAT STATEMENTS
C
C
1000  FORMAT(18A4)
1001  FORMAT(8F10.5)
1100  FORMAT(1H1/,10X,18A4,///)
 1101 FORMAT(1H ,10X,'TEST'10X,'RUN',10X,'WIRE',10X,'BRIDGE R',    -
     15X,'CABLE R')
1102  FORMAT(5X,I5,10X,I5,10X,I5,10X,F10.3,5X,F10.3///)
```

```
1103  FORMAT(10X,1HX,10X,1HY,10X,2HM , 6X,3HRET,5X,10HRECOVERY R/)
 1104 FORMAT(5X,5F10.2,2F10.1,F10.5,F10.2/)
1105  FORMAT(5X,8HOVERHEAT,5X,6HWIRE R,12X,4HEBAR,16X,4HERMS,8X,6HDELERU
     1,4X,6HDELETT,8X,1HR,8X,5HSSTAR/)
1106  FORMAT(5X,10F10.4 )
 1107 FORMAT(5X,'RUPOVR =',F6.2,5X,'TTPOVR =',F6.2,5X,'RRUTT =', F6.2,   -
     15X,'TTVOVR =',F6.2,5X,'RUVOVR =',F6.2,5X,'VPSOVR =',F6.2/)
1108  FORMAT(30X,'KOVASZNAY VARIABLES FOR YAWED WIRE'/)
 1109 FORMAT(20X,'REYNOLDS STRESS AND OTHER TERMS IN EQUATIONS'/)
 1110 FORMAT(10X,'RHOUV =',F6.2,5X,'URPVP =',F6.2,5X,'VRPUP =',F6.2,5X,   -
     1'RHOVSQ =',F6.2,5X,'2*VBAR*RPVP =',F8.4,5X,'RPVP =',F6.4          /)
 1111 FORMAT(30X,'RHOVT =',F8.2,5X,'VRPTP =',F8.2,5X,'TRPVP =',F8.2/)
 1113 FORMAT(30X,'TRX =',F6.2,5X,'TRR =',F6.2,5X,'QR =',F8.4/)
      END
```

APPENDIX D

MEASUREMENT OF TURBULENT TRANSPORT QUANTITIES IN A COMPRESSIBLE BOUNDARY LAYER

A brief review of the state of signal interpretation from hot-wire anemometers was given in the body of the thesis. This appendix summarizes the important features of the interpretation techniques and extends the techniques for wire calibration and shear-stress measurement. The procedures for signal interpretation followed in the present study were strongly based on the works of Morkovin and Phinney (ref. 26), Morkovin (ref. 27), and Kovasznay (refs. 28 and 30).

We begin by considering the heat loss from a heated wire held, possibly at a yawed angle, in a gas stream. We may write the energy balance for a correctly compensated wire (neglecting end losses) as:

$$W = \text{const } I_w^2 R_w = Nu_t(M, Re_t, \theta, \phi) \cdot \pi \ell k_t \cdot (T_w - \eta T_t) = H \tag{D1}$$

where $\theta = T_w/T_t$. Differentiating this expression logarithmically and using well-known relationships among Mach number, Reynolds number and velocity, density, and total temperature, and defining $n_t = \partial \ \ell n \ k_t / \partial \ \ell n \ T_t$ and $m_t = \partial \ \ell n \ \mu_t / \partial \ \ell n \ T_t$, we see that

$$d \ \ell n \ W = d \ \ell n \ H \tag{D2}$$

where

$$d \ \ell n \ W = 2d \ \ell n \ I_w + K d \ \ell n \ T_w = 2d \ \ell n \ E_w + d \ \ell n \left[\frac{R_w}{(R_w + R_s)^2} \right] \tag{D3}$$

and

$$
\begin{aligned}
d\ \ell n\ H = \Bigg[& n_t - m_t \frac{\partial\ \ell n\ Nu_t}{\partial\ \ell n\ Re_t} - \left\{ \frac{\partial\ \ell n\ Nu_t}{\partial\ \ell n\ \theta} + \frac{\theta}{\theta - \eta} \right\} + 1 \\
& - \frac{1}{\tau_{wr}} \left\{ \frac{1}{2\alpha} \frac{\partial\ \ell n\ \eta}{\partial\ \ell n\ M} - m_t \frac{\partial\ \ell n\ \eta}{\partial\ \ell n\ Re_t} \right\} - \frac{1}{2\alpha} \frac{\partial\ \ell n\ Nu_t}{\partial\ \ell n\ M} \Bigg] d\ \ell n\ T_t \\
& + \left[\frac{\partial\ \ell n\ Nu_t}{\partial\ \ell n\ Re_t} + \frac{1}{\alpha} \frac{\partial\ \ell n\ Nu_t}{\partial\ \ell n\ M} - \frac{1}{\tau_{wr}} \left\{ \frac{1}{\alpha} \frac{\partial\ \ell n\ \eta}{\partial\ \ell n\ M} + \frac{\partial\ \ell n\ \eta}{\partial\ \ell n\ Re_t} \right\} \right] d\ \ell n\ u \\
& + \left[\frac{\partial\ \ell n\ Nu_t}{\partial\ \ell n\ Re_t} - \frac{1}{\tau_{wr}} \frac{\partial\ \ell n\ \eta}{\partial\ \ell n\ Re_t} \right] d\ \ell n\ \rho + \left[\frac{\partial\ \ell n\ Nu_t}{\partial\ \ell n\ \theta} + \frac{\theta}{\theta - \eta} \right] d\ \ell n\ T_w \\
& \pm \left[\frac{1}{\tau_{wr}} \frac{\partial\ \ell n\ \eta}{\partial \phi} - \frac{\partial\ \ell n\ Nu_t}{\partial \phi} \right] d\phi
\end{aligned}
\tag{D4}
$$

where $d\phi \equiv v'/\bar{u}$. The + sign in the last term of equation (D4) is associated with a v' that increases the heat loss from the wire, as depicted in figure 39.

If we invoke the constant temperature operation assumptions ($d\ \ell n\ R_w = d\ \ell n\ T_w = 0$), we have

$$
2d\ \ell n\ E_w = [\quad]d\ \ell n\ T_t + [\quad]d\ \ell n\ u + [\quad]d\ \ell n\ \rho + [\quad]d\phi
$$

$$
= \frac{[\quad]}{100} \left(100\ \frac{T_t'}{\bar{T}_t} \right) + \frac{[\quad]}{100} \left(100\ \frac{u'}{\bar{u}} \right) + \frac{[\quad]}{100} \left(100\ \frac{\rho'}{\bar{\rho}} \right) \pm \frac{[\quad]}{100} \left(100\ \frac{v'}{\bar{u}} \right) \tag{D5}
$$

where the square brackets are those that appear in equation (D4). A substantial saving in time and effort during the data-acquisition phase can be made by noting that

$$
d\ \ell n\ E_w = d\ \ell n\ E
$$

where E is the bridge voltage. This is true since $E = E_w[(R_w+R_s)/R_w]$ and $d\ \ell n\ R_w$ is assumed to be zero. Thus, we may divide equation (D5) by 2 and write

$$d\ \ell n\ E = \frac{E'}{\bar{E}} = \frac{[\quad]}{200}\left(100\ \frac{T_t'}{\bar{T}_t}\right) + \frac{[\quad]}{200}\left(100\ \frac{u'}{\bar{u}}\right) + \frac{[\quad]}{200}\left(100\ \frac{\rho'}{\bar{\rho}}\right) \pm \frac{[\quad]}{200}\left(100\ \frac{v'}{\bar{u}}\right) \tag{D6}$$

The fluctuation of the physical variables then is related to the fluctuation of the bridge voltage by

$$E' = \Delta e_{T_t}\left(100\ \frac{T_t'}{\bar{T}_t}\right) + \Delta e_u\left(100\ \frac{u'}{\bar{u}}\right) + \Delta e_\rho\left(100\ \frac{\rho'}{\bar{\rho}}\right) \pm \Delta e_v\left(100\ \frac{v'}{\bar{u}}\right) \tag{D7}$$

The terms $\Delta e_{()}$ are the fluctuation sensitivities for the respective variables; and, from equations (D6) and (D7), they have the form

$$\Delta e_\rho = \frac{\bar{E}}{200}\left[\frac{\partial\ \ell n\ Nu_t}{\partial\ \ell n\ Re_t} - \frac{1}{\tau_{wr}}\frac{\partial\ \ell n\ \eta}{\partial\ \ell n\ Re_t}\right]$$

$$\Delta e_u = \frac{\bar{E}}{200}\left[\frac{\partial\ \ell n\ Nu_t}{\partial\ \ell n\ Re_t} + \frac{1}{\alpha}\frac{\partial\ \ell n\ Nu_t}{\partial\ \ell n\ M} - \frac{1}{\tau_{wr}}\left\{\frac{1}{\alpha}\frac{\partial\ \ell n\ \eta}{\partial\ \ell n\ M} + \frac{\partial\ \ell n\ \eta}{\partial\ \ell n\ Re_t}\right\}\right]$$

$$\Delta e_{T_t} = \frac{\bar{E}}{200}\left[n_t + 1 - m_t\frac{\partial\ \ell n\ Nu_t}{\partial\ \ell n\ Re_t} - \left\{\frac{\partial\ \ell n\ Nu_t}{\partial\ \ell n\ \theta} + \frac{\theta}{\theta-\eta}\right\}\right.$$

$$\left. + \frac{1}{\tau_{wr}}\left\{\frac{1}{2\alpha}\frac{\partial\ \ell n\ \eta}{\partial\ \ell n\ M} + m_t\frac{\partial\ \ell n\ \eta}{\partial\ \ell n\ Re_t}\right\} - \frac{1}{2\alpha}\frac{\partial\ \ell n\ Nu_t}{\partial\ \ell n\ M}\right]$$

$$\Delta e_v = \frac{\bar{E}}{200}\left[\frac{1}{\tau_{wr}}\frac{\partial\ \ell n\ \eta}{\partial\phi} - \frac{\partial\ \ell n\ Nu_t}{\partial\phi}\right]$$

These fluctuation sensitivities are completely general in that they apply in either subsonic or supersonic flow for arbitrary Reynolds numbers and for yawed or normal ($\Delta e_v = 0$) wires. For supersonic Mach numbers, the complexity of these sensitivities is reduced considerably. It has been found (e.g., ref. 26 or 54) that for $M \sin\phi > 1.2$, all derivatives with respect to Mach number can be considered small, and neglected. With this condition, the sensitivities can be written as

$$\Delta e_u = \Delta e_\rho \equiv \Delta e_{\rho u} = \frac{\bar{E}}{200}\left[\frac{\partial\ \ell n\ Nu_t}{\partial\ \ell n\ Re_t} - \frac{1}{\tau_{wr}}\frac{\partial\ \ell n\ \eta}{\partial\ \ell n\ Re_t}\right] \tag{D8a}$$

$$\Delta e_{T_t} = \frac{\bar{E}}{200}\left[n_t + 1 - m_t\left(\frac{\partial\ \ell n\ Nu_t}{\partial\ \ell n\ Re_t} - \frac{1}{\tau_{wr}}\frac{\partial\ \ell n\ \eta}{\partial\ \ell n\ Re_t}\right) - \left\{\frac{\partial\ \ell n\ Nu_t}{\partial\ \ell n\ \theta} + \frac{\theta}{\theta-\eta}\right\}\right]$$

$$= \frac{\bar{E}}{200}\left[n_t + 1 - \left\{\frac{\partial\ \ell n\ Nu_t}{\partial\ \ell n\ \theta} + \frac{\theta}{\theta-\eta}\right\}\right] - m_t(\Delta e_{\rho u}) \tag{D8b}$$

$$\Delta e_v = \frac{\bar{E}}{200}\left[\frac{1}{\tau_{wr}}\frac{\partial\ \ell n\ \eta}{\partial\phi} - \frac{\partial\ \ell n\ Nu_t}{\partial\phi}\right] \tag{D8c}$$

Thus, for $M \sin\phi > 1.2$, the relationship between the fluctuating voltage and fluctuations in the physical variables is just

$$E' = \Delta e_{T_t}\left(100\ \frac{T_t'}{\bar{T}_t}\right) + \Delta e_{\rho u}\left(100\ \frac{(\rho u)'}{\bar{\rho}\bar{u}}\right) \pm \Delta e_v\left(100\ \frac{v'}{\bar{u}}\right) \tag{D9}$$

We may evaluate the term $\{\partial\ \ell n\ Nu_t/\partial\ \ell n\ \theta + \theta/(\theta-\eta)\}$ in equation (D8b). Using Morkovin's $A_w = (1/2)(\partial\ \ell n\ R_w/\partial\ \ell n\ I_w)$ and $K = \partial\ \ell n\ R_w/\partial\ \ell n\ T_w$, it can be shown that $\{\partial\ \ell n\ Nu_t/\partial\ \ell n\ \theta + \theta/(\theta-\eta)\} = K[1 + (1/A_w)]$. Using the relation between I_w and E we see that

$$K\left(1 + \frac{1}{A_w}\right) = 2K\left[\frac{\partial\ \ell n\ E}{\partial\ \ell n\ R_w} + \left(\frac{1}{2} - \frac{R_w}{R_w + R_s}\right)\right]$$

Now K is simply the logarithmic slope of R_w versus T_w. For tungsten wire, the curve of R_w versus T_w was given by Grande (ref. 14). The logarithmic slope $\partial\ \ell n\ E/\partial\ \ell n\ R_w$ is obtained from the data taken at the time of the actual fluctuating measurements.

At this point we depart from the usual assumption (e.g., ref. 14) that $Re_t \sin\phi > 20$, which allows the variation of η with Re_t to be neglected so that, for example, the $\Delta e_{\rho u}$ sensitivity becomes

$$\Delta e_{\rho u} = \frac{\bar{E}}{200}\left[\frac{\partial \ \ell n \ Nu_t}{\partial \ \ell n \ Re_t}\right]$$

This simplification would be desirable since, for very long wires, $\partial \ \ell n \ Nu_t / \partial \ \ell n \ Re_t = 1/2$, and $\Delta e_{\rho u}$ thus becomes $\bar{E}/400$. For actual wires, however, the effects of end losses reduce this value, and approximations must be made to account for the influence of the losses.

During the present study, it became apparent that the assumption $Re_t \sin \phi > 20$ would not be suitable for the boundary-layer measurements. To avoid the use of this assumption, therefore, each wire was directly calibrated over the entire range of Mach and Reynolds numbers encountered in the boundary layer.

The direct calibration of the sensitivities is related to the above as follows. From equation (D9) we may write at once the mathematical form for the sensitivities

$$\left.\begin{aligned} \Delta e_{T_t} &= \frac{\bar{E}}{100}\frac{\partial \ \ell n \ E}{\partial \ \ell n \ T_t} \\ \Delta e_{\rho u} &= \frac{\bar{E}}{100}\frac{\partial \ \ell n \ E}{\partial \ \ell n \ \rho u} \\ \Delta e_{v} &= \frac{\bar{E}}{100}\frac{\partial \ \ell n \ E}{\partial \phi} \end{aligned}\right\} \qquad (D10)$$

The values of $\partial \ \ell n \ E / \partial \ \ell n \ \rho u$ and $\partial \ \ell n \ E / \partial \phi$ were obtained by the calibration method given in appendix C, where it also was noted that the value of $\partial \ \ell n \ E / \partial \ \ell n \ T_t$ could not be determined accurately. For Δe_{T_t}, equation (D8b) was used with the substitutions

$$\left\{\frac{\partial \ \ell n \ Nu_t}{\partial \ \ell n \ \theta} + \frac{\theta}{\theta - \eta}\right\} = 2K\left[\frac{\partial \ \ell n \ E}{\partial \ \ell n \ R_w} + \left(\frac{1}{2} - \frac{R_w}{R_w + R_s}\right)\right]$$

and, following Morkovin, $n_t = 0.885$ and $m_t = 0.765$.

The resulting set of sensitivities therefore is obtained from terms that are either calibrated in place, calibrated beforehand, or are known physical

properties of air and tungsten. The only restriction on these sensitivities is that $M \sin \phi > 1.2$, a condition satisfied in the present boundary-layer flow except for the first measuring station off the wall at two or three x locations. No end-loss corrections, peripheral calculations of Nusselt number, or similar calculations are required. We now discuss the use of these sensitivities in fluctuating flow measurements. We measure not E' but the rms of E'; therefore, we must separate the $(\rho u)'$, T_t', and v' contributions to the total rms E'.

For a single normal wire in supersonic flow, Grande (ref. 14) has shown that the Morkovin diagram approach (ref. 27) and the Kovasznay diagram approach (ref. 28) are equivalent. The Kovasznay technique will be used here since it uses the basic sensing variables of the wire discussed above. This technique examines the mean square of E'. Thus, for normal wire $\Delta e_v = 0$, we have

$$S^2 = \frac{\overline{E'^2}}{(\Delta e_{T_t})^2} = r^2 \frac{\overline{(\rho u)'^2}}{(\bar{\rho}\bar{u})^2} \cdot 10^4 - 2r \frac{\overline{(\rho u)'T_t'}}{\bar{\rho}\bar{u}\bar{T}_t} \cdot 10^4 + \frac{\overline{T_t'^2}}{\bar{T}_t^2} \cdot 10^4$$

where $r = -\Delta e_{\rho u}/\Delta e_{T_t}$. Now r changes with overheat ratio so that a plot of S versus r (the Kovasznay diagram) yields $\overline{(\rho u)'^2}/(\bar{\rho}\bar{u})^2$, $\overline{(\rho u)'T_t'}/\bar{\rho}\bar{u}\bar{T}_t$, and $\overline{T_t'^2}/\bar{T}_t^2$ as shown in reference 28. From these values and the definitions

$$\alpha = \frac{1}{1+[(\gamma-1)/2]M^2}, \qquad \beta = (\gamma-1)M^2\alpha$$

we can calculate

$$\overline{u'^2} = \bar{u}^2\left[\frac{1}{(\alpha+\beta)^2}\frac{\overline{T_t'^2}}{\bar{T}_t^2} + \frac{\alpha^2}{(\alpha+\beta)^2}\frac{\overline{(\rho u)'^2}}{(\bar{\rho}\bar{u})^2} + 2\frac{\alpha}{(\alpha+\beta)^2}\frac{\overline{(\rho u)'T_t'}}{\bar{\rho}\bar{u}\bar{T}_t}\right]$$

$$\overline{u'T'} = \bar{u}\bar{T}\left[\frac{1}{(\alpha+\beta)^2}\frac{\overline{T_t'^2}}{\bar{T}_t^2} + \frac{\alpha-\beta}{(\alpha+\beta)^2}\frac{\overline{(\rho u)'T_t'}}{\bar{\rho}\bar{u}\bar{T}_t} - \frac{\alpha\beta}{(\alpha+\beta)^2}\frac{\overline{(\rho u)'^2}}{(\bar{\rho}\bar{u})^2}\right]$$

and

$$\overline{\rho'u'} = -\frac{\bar{\rho}}{\bar{T}}\overline{u'T'}$$

For the output of a yawed wire, we examine the mean square of E' from the general equation for a yawed wire:

$$\overline{E'^2} = \overline{\left[\Delta e_{\rho u}\frac{100(\rho u)'}{\bar{\rho}\bar{u}} + \Delta e_{T_t}\frac{100T_t'}{\bar{T}_t} \pm \Delta e_v\frac{100v'}{\bar{u}}\right]^2}$$

$$= (\Delta e_{\rho u})^2\frac{\overline{(\rho u)'^2}}{(\bar{\rho}\bar{u})^2}\cdot 10^4 + (\Delta e_{T_t})^2\frac{\overline{T_t'^2}}{\bar{T}_t^2}\cdot 10^4 + (\Delta e_v)^2\frac{\overline{v'^2}}{\bar{u}^2}\cdot 10^4$$

$$+2\Delta e_{\rho u}\Delta e_{T_t}\frac{\overline{(\rho u)'T_t'}}{\bar{\rho}\bar{u}\bar{T}_t}\cdot 10^4 \pm 2\Delta e_{T_t}\Delta e_v\frac{\overline{T_t'v'}}{\bar{T}_t\bar{u}}\cdot 10^4$$

$$\pm 2\Delta e_{\rho u}\Delta e_v\frac{\overline{(\rho u)'v'}}{\bar{\rho}\bar{u}\bar{u}}\cdot 10^4 \qquad \text{(D11)}$$

Conceptually, all the physical quantities required can be obtained from a single yawed wire operated at at least six overheat ratios. Attempts to do this in the present study with up to ten overheat ratios were unsuccessful because the equations were not sufficiently linearly independent. The following procedure was used instead.

Mean square readings were taken before and after a 180° rotation about the probe axis. Then, taking the difference of these readings, we have:

$$\overline{E_{0°}'^2} - \overline{E_{180°}'^2} = 4\left[\Delta e_{T_t}\Delta e_v\frac{\overline{T_t'v'}}{\bar{T}_t\bar{u}} + \Delta e_{\rho u}\Delta e_v\frac{\overline{(\rho u)'v'}}{\bar{\rho}\bar{u}\bar{u}}\right]\cdot 10^4$$

We let

$$S^* = \frac{(\overline{E_{0°}'^2} - \overline{E_{180°}'^2})}{(4\Delta e_v\Delta e_{T_t}\cdot 10^4)} = \frac{\overline{T_t'v'}}{\bar{T}_t\bar{u}} - r\frac{\overline{(\rho u)'v'}}{\bar{\rho}\bar{u}\bar{u}}$$

Now a plot of S^* versus r will immediately yield $\overline{(\rho u)'v'}/\bar{\rho}\bar{u}^2$ and $\overline{T_t'v'}/\bar{u}\bar{T}_t$. We can substitute these expressions, plus those for $(\rho u)'/\bar{\rho}\bar{u}$, $T_t'/\bar{T}_t$, and

$\overline{(\rho u)'T_t'}/\bar{\rho}\bar{u}\bar{T}_t$ obtained from the normal wire, back into equation (D11) and obtain $v'^2/\bar{u}^2$. Further examination of the terms $\overline{T_t'v'}/\bar{T}_t\bar{u}$ and $\overline{(\rho u)'v'}/\bar{\rho}\bar{u}^2$ leads to

$$\frac{\overline{T_t'v'}}{\bar{T}_t\bar{u}} = \alpha \frac{\overline{v'T'}}{\bar{u}\bar{T}} + \beta \frac{\overline{u'v'}}{\bar{u}^2}$$

$$\frac{\overline{(\rho u)'v'}}{\bar{\rho}\bar{u}^2} = \frac{\overline{u'v'}}{\bar{u}^2} - \frac{\overline{v'T'}}{\bar{u}\bar{T}}$$

and finally

$$\overline{v'T'} = \bar{u}\bar{T}\left[\frac{1}{\alpha+\beta}\frac{\overline{T_t'v'}}{\bar{T}_t\bar{u}} - \frac{\beta}{\alpha+\beta}\frac{\overline{(\rho u)'v'}}{\bar{\rho}\bar{u}^2}\right]$$

$$\overline{u'v'} = \bar{u}^2\left[\frac{1}{\alpha+\beta}\frac{\overline{T_t'v'}}{\bar{T}_t\bar{u}} + \frac{\alpha}{\alpha+\beta}\frac{\overline{(\rho u)'v'}}{\bar{\rho}\bar{u}^2}\right]$$

We may also employ the yawed wire in the x-θ plane to obtain $\overline{w'^2}$. The equations leading to $\overline{w'^2}$ are identical to those leading to $\overline{v'^2}$, with the substitution $w' = v'$. Up to this point we have considered the mass-flux fluctuations and total-temperature fluctuations to be induced by vorticity and/or "temperature spottiness" and have neglected fluctuations in pressure (or sound).

When the hot wire is placed in a field in which only sound is present, the total-temperature and mass-flux fluctuation may be attributed to the sound field (ref. 28). The sensitivity of the wire to pressure fluctuations $\pi = 100(p'/\gamma\bar{p})$ is:

$$\Delta e_\pi = \alpha(\gamma-1)(1 + n_x M)\Delta e_{T_t} + [1 + (n_x/M)]\Delta e_{\rho u}$$

where n_x is the direction cosine of the wave. For example, if the sound wave is a Mach wave, then $n_x = -1/M$, in which case,

$$\Delta e_\pi = [1 - (1/M^2)]\Delta e_{\rho u}$$

Thus, for this case, π is related simply to $(\rho u)'/\bar{\rho}\bar{u}$ by

$$\pi = \frac{(\rho u)'/\bar{\rho}\bar{u}}{1 - (1/M^2)}$$

Based on the findings of Grande (ref. 14), we conclude that the primary source of sound (aerodynamic noise) in the interaction is Mach waves. The measurements reported in the main body of the thesis were obtained using the above procedures.

APPENDIX E

ACCURACY OF THE DATA

The estimated accuracy of the mean- and fluctuating-flow data is discussed in this appendix. The quoted accuracies are based on the past experience of others, the estimated uncertainty in the instrumentation of the present study, and, in some cases, the author's opinion. The opinions are more in the nature of honest estimates rather than attempts to present glowing impressions of 1 percent or 2 percent accuracy in one's own work. The quoted accuracies below are expressed as a percentage of the local value of each quantity.

The estimated accuracies of the mean-flow data are for pitot pressure p_{t_p}, ±1 percent; static pressure p, ±2 percent; and total temperature T_t, ±1/2 percent. These uncertainties introduce other uncertainties in the derived mean-flow quantities such as $\bar{u}$, $\bar{\rho}$, $\bar{T}$, etc, where the uncertainty is estimated to be less than 3 percent. The mean-flow measurements are quite "standard," and the 3 percent uncertainty in the individual terms should be considered extreme. Similarly, uncertainties exist in the products of these individual mean-flow terms - for example, $\overline{\rho}\overline{u}$ and $\overline{\rho}\overline{u}^2$ - that can be substantially larger than 3 percent, ±6 percent and ±9 percent, respectively. The last two uncertainties become significant if one attempts to check for a mass or momentum balance from the data. This is discussed further following a discussion of the uncertainty in the fluctuating-flow data.

The estimated accuracies for the fluctuating-flow data are: $\langle E' \rangle$, ±2 percent; and $\overline{E}$, ±1 percent. The errors in the reduced fluctuating data are, however, not simply reflections of these errors. The primary errors are introduced by the uncertainty in the sensitivity coefficients (appendix D) and the subsequent manipulations involving quantities of varying uncertainty.

The maximum errors in the ρu- and v-sensitivity coefficients are estimated from $\Delta e_{\rho u}$, ±5 percent from calibration; and Δe_{v}, ±5 percent from calibration.

For the total temperature sensitivity, the following quantities, in addition to the value of $\Delta e_{\rho u}$ are required: K, ±3 percent (Grande, ref. 14); R_w, ±1/2 percent; and A_w, ±2 percent (Grande, ref. 14). These lead to an expected accuracy for the total temperature sensitivity Δe_{T_t} of ±10 percent. This error is thought to be a maximum within the range of overheat ratios used in the present study, in spite of the fact that the errors at very low and very high overheat ratios can be much larger than 10 percent (Grande, ref. 14).

With these errors, we can state the maximum expected uncertainty in the values of basic sensing variables (see appendix D) determined from the hot-wire measurements as listed below. These values should definitely be considered the upper limits of the expected errors.

$\langle(\rho u)'\rangle$, ±8 percent

$\langle T_t'\rangle$, ±12 percent

$\overline{(\rho u)'T_t'}$, ±15 percent

$\overline{(\rho u)'v'}$, ±15 percent

$\overline{T_t'v'}$, ±15 percent

$\langle v'\rangle$, ±25 percent

$\overline{(\rho u)'w'}$, ±15 percent

$\overline{T_t'w'}$, ±15 percent

$\langle w'\rangle$, ±25 percent

Examples of the extent to which these uncertainties may affect the reported values of Reynolds stresses are given below. Again these should be considered extreme.

T_{xx} , ±15 percent

T_{rx} , ±20 percent

T_{rr} , ±30 percent

$T_{\theta\theta}$, ±30 percent

$T_{x\theta}$, ±20 percent

The derivatives of the Reynolds stresses reflect the uncertainties in the stresses themselves as modified by the smoothing and differencing algorithm used to obtain the derivatives (appendix C). To estimate the uncertainty in the reported values of the derivatives, the following procedure was used. A 10-percent variation was introduced in one value of T_{xx} and in one value of T_{rx}. The resulting variation of $(1/r)(\partial rT_{rx}/\partial r)$ and $\partial T_{xx}/\partial x$ was then examined. A 10-percent variation of T_{rx} introduced near a 10-percent variation in $(1/r)(\partial rT_{rx}/\partial r)$. A similar variation was found in $\partial T_{xx}/\partial x$, so that the reported radial and axial derivatives carry uncertainties near those for the Reynolds stresses themselves.

An attempt was made in the present study to verify the accuracy of the fluctuating flow measurements by comparing the left- and right-hand sides of the integrated x-momentum equation. The x-momentum equation was integrated from the wall to the boundary-layer edge at each streamwise station. The continuity equation was combined with the x-momentum equation to eliminate $\bar{v}$. Both mean-flow terms on the left-hand side of the momentum equation were integrated numerically (Simpson's rule) using the experimental data; terms on the right-hand side were treated in the same fashion. The streamwise derivatives that appear were determined by the smoothing and differentiating procedure (appendix C) before integrating. The radial derivatives were integrated directly from the data so that no smoothing or differentiating was required.

This attempt was only qualitatively successful. Both terms on the left-hand side are of the order of 100. Their sum, which should be the right-hand side, is the order of 10 to 20, so that a 9-percent error in $\overline{\rho}\overline{u}^2$ as discussed above could result in a value of this sum of as low as 0 and as high as 20 to 30. On the right-hand side, the pressure gradient term is of the order of 5 to 10, the normal stress term is of the order of 1 to 3, and the shear stress term is of the order of 2 to 4. Thus, the right-hand side is of the order of 8 to 17. The left-hand side, being a small difference of two large numbers, simply cannot be known accurately enough to permit use of the integrated momentum equation as a suitable check on the accuracy of the data.

The ratio of right- to left-hand sides, computed as discussed above, ranged randomly at the various streamwise stations from 0.7 to 2.5, indicating that the gradients of the experimental values of the Reynolds stresses are qualitatively correct; however, quantitative comparison cannot be realistically obtained.

REFERENCES

1. Lynes, L. L.; Nielsen, J. N.; and Kuhn, G. D.: Calculation of Compressible Turbulent Boundary Layers with Pressure Gradients and Heat Transfer. NASA CR-1303, 1969.

2. Watson, E. C.; Murphy, J. D.; and Rose, W. C.: Investigation of Laminar and Turbulent Boundary Layers Interacting with Externally Generated Shock Waves. NASA TN 5512, 1969.

3. Seebaugh, W. R.; Paynter, G. C.; and Childs, M. E.: Shock-Wave Reflection from a Turbulent Boundary Layer with Mass Bleed. J. Aircraft, Vol. 5, Sept.-Oct. 1968, pp. 461-467.

4. Mathews, D. C.: Shock-Wave Boundary Layer Interactions in Two-Dimensional and Axially-Symmetric Flows Including the Influence of Suction. Ph.D. Thesis, Univ. of Washington, 1969.

5. Rose, W. C.: A Method for Analyzing the Interaction of an Oblique Shock Wave with a Boundary Layer. NASA TN 6083, 1970.

6. Rose, W. C.; Nielsen, H. L.; and Watson, E. C.: Shock Wave - Turbulent Boundary Layer Interaction on a Blunted Compression Surface. J. Spacecraft Rockets, Vol. 9, April 1972, pp. 278-280.

7. Bogdonoff, S. M.; Kepler, C. E.; and Sanlorenzo, E.: A Study of Shock Wave Turbulent Boundary Layer Interaction at M = 3.0. Dept. of Aeronautical Engineering Rep. 222, Princeton Univ., July 1953.

8. Bogdonoff, S. M.: Some Experimental Studies of the Separation of Supersonic Turbulent Boundary Layers. 1955 Heat Transfer and Fluid Mechanics Institute, Univ. of Calif., Los Angeles, 1955.

9. Kuehn, Donald M.: Experimental Investigation of the Pressure Rise Required for the Incipient Separation of Turbulent Boundary Layers in Two-Dimensional Supersonic Flow. NASA Memo 1-21-59A, 1959.

10. Chapman, Dean R.; Kuehn, Donald M.; and Larson, Howard K.: Investigation of Separated Flows in Supersonic and Subsonic Streams with Emphasis on the Effect of Transition. NACA Rep. 1356, 1958.

11. Popinski, Z.: Shock-Wave Boundary-Layer Interaction. Rep. LR 18307, Lockheed-California Co., June 1965.

12. Pinckney, S. Z.: Data on Effects of Incident-Reflecting Shocks on the Turbulent Boundary Layer. NASA TM X-1221, 1966.

13. Watson, E. C.; Rose, W. C.; Morris, S. J., Jr.; and Gallo, W. F.: Studies of the Interaction of a Turbulent Boundary Layer and a Shock Wave at Mach Numbers Between about 2 and 10. NASA SP-216, 1969.

14. Grande, E.: An Investigation of the Unsteady Flow Properties of the Interaction Between a Shock Wave and a Turbulent Boundary Layer in Two-Dimensional Internal Flow. Ph.D. Thesis, Univ. of Washington, 1971.

15. Seebaugh, W. R.: An Investigation of the Interaction of a Shock Wave and a Turbulent Boundary Layer in Axially-Symmetric Internal Flow Including the Effects of Mass Bleed. Ph.D. Thesis, Univ. of Washington, 1968.

16. Teeter, G. C.: An Experimental Investigation of the Interaction of a Shock-Wave with a Decelerated Turbulent Boundary Layer. M.S. Thesis, Univ. of Washington, 1971.

17. Renton, G. W.: An Experimental Investigation of Shock-Wave Turbulent Boundary Layer Interactions in Axisymmetric Flow at Mach 3.80 Including Suction Effects. M.S. Thesis, Univ. of Washington, 1971.

18. Alzner, E.; and Zakkay, V.: Turbulent Boundary Layer - Shock Interaction with and without Injection. AIAA J., Vol. 9, No. 9, Sept. 1971, pp. 1769-1776.

19. Lewis, John E.: Experimental Investigation of Supersonic Laminar, Two-Dimensional Boundary Layer Separation in a Compression Corner with and without Cooling. Ph.D. Thesis, Calif. Inst. Technol., 1967.

20. Green, J. E.: Interactions Between Shock Waves and Turbulent Boundary Layers. Progr. Aero. Sci., Vol. 11, 1970, pp. 235-340.

21. Reda, D. C.; and Murphy, J. D.: Shock Wave - Turbulent Boundary Layer Interactions in Rectangular Channels. AIAA Paper 72-715, 1972.

22. Reda, D. C.; and Page, R. H.: Supersonic Turbulent Flow Reattachment Downstream of a Two-Dimensional Backstep. AFOSR 69-1592 TR, 1969.

23. Back, L. H.; and Cuffel, R. F.: Static Pressure Measurements Near an Oblique Shock Wave. AIAA J., Vol. 9, No. 2, Feb. 1971, pp. 345-346.

24. Winkler, E. M.: Stagnation Temperature Probes for Use at High Supersonic Speeds and Elevated Temperatures. NAVORD Rep. 3834, U. S. Naval Ordnance Lab., White Oak, Md., Oct. 1952.

25. Meier, H. U.: A Combined Temperature and Pressure Probe for Compressible Flow. AIAA J., Vol. 7, No. 3, March 1969, pp. 529-530.

26. Morkovin, M. V.; and Phinney, R. E.: Extended Applications of Hot-Wire Anemometry to High-Speed Turbulent Boundary Layers. AFOSR TN-58-469, Johns Hopkins Univ., Dept. of Aeronautics, June 1958.

27. Morkovin, M. V.: Fluctuations and Hot-Wire Anemometry in Compressible Fluids. AGARDograph No. 24, Nov. 1956.

28. Kovasznay, L. S. G.: The Hot Wire Anemometer in Supersonic Flow. J. Aero. Sci., Vol. 17, 1950, pp. 565-572.

29. Kistler, Alan L.: Fluctuation Measurements in a Supersonic Turbulent Boundary Layer. Phys. Fluids, Vol. 2, No. 3, May-June 1959, pp. 290-296.

30. Kovasznay, L. S. G.: Turbulence in Supersonic Flow. J. Aero. Sci., Vol. 20, No. 10, Oct. 1953, p. 657.

31. Way, J.; and Libby, P. A.: Application of Hot Wire Anemometry and Digital Techniques to Measurements in a Turbulent Helium Jet. AIAA J., Vol. 9, No. 8, Aug. 1971, pp. 1567-1573.

32. Wallace, J. E.: Hypersonic Turbulent Boundary-Layer Measurements Using an Electron Beam. NASA SP-216, 1969.

33. Morkovin, M. V.: Effects of High Acceleration on a Turbulent Supersonic Shear Layer. 1955 Heat Transfer and Fluid Mechanics Institute (published by Stanford Univ. Press).

34. Kistler, A. L.; and Chen, W. S.: The Fluctuating Pressure Field in a Supersonic Turbulent Boundary Layer. J. Fluid Mech., Vol. 16, Pt. 1, May 1963, pp. 41-64.

35. Vrebalovich, T.: Application of Hot-Wire Techniques in Unsteady Compressible Flows. Symposium on Measurement in Unsteady Flow, Worcester, Amer. Soc. Mech. Eng. Publ., May 1962.

36. Laufer, J.: Aerodynamic Noise in Supersonic Wind Tunnels. J. Aero. Sci., Vol. 28, 1961.

37. Kovasznay, L. S. G.: Development of Turbulence-Measuring Equipment. NACA Tech. Rep. 1209, 1954.

38. Kovasznay, L. S. G.: Should We Still Use Hot Wires? In Advances in Hot-Wire Anemometry, Proc. Intern. Symposium on Hot-Wire Anemometry, Univ. of Maryland, March 20-21, 1967.

39. Morkovin, M. V.: Signal Interpretation in High Speed Anemometry. In Advances in Hot-Wire Anemometry, Proc. Intern. Symposium on Hot-Wire Anemometry, Univ. of Maryland, March 20-21, 1967.

40. Ribner, H. S.: Shock-Turbulence Interaction and the Generation of Noise. NACA Rep. 1233, 1955.

41. Kovasznay, L. S. G.: Interaction of a Shock Wave and Turbulence. 1955 Heat Transfer and Fluid Mechanics Institute, Univ. of Calif., Los Angeles, 1955.

42. Laufer, J.: Sound Radiation from a Turbulent Boundary Layer. In The Mechanics of Turbulence. Gordon and Breach, 1961.

43. Laufer, J.; Ffowcs-Williams, J. E.; and Childress, S.: Mechanism of Noise Generation in the Turbulent Boundary Layer. AGARDograph 90, 1964.

44. Ribner, H. A.: Acoustic Energy Flux from Shock-Turbulence Interaction. J. Fluid Mech., Vol. 35, Pt. 2, 1969, pp. 299-310.

45. Hoagland, L. C.: Fully Developed Turbulent Flow in Straight Rectangular Ducts. D. Sc. Thesis, Mass. Inst. Tech., Sept. 1960.

46. Laufer, J.: Thoughts on Compressible Turbulent Boundary Layers. NASA SP-216, 1969.

47. Favre, A.: Equations des Gaz Turbulents Compressibles. J. Mecan., Vol. 4, No. 3, Sept. 1965, pp. 361-390.

48. Bertram, M. H.; and Neal, L., Jr.: Recent Experiments in Hypersonic Turbulent Boundary Layers. NASA TM X-56335, May 1965.

49. Meier, H. U.; and Rotta, J. C.: Temperature Distributions in Supersonic Turbulent Boundary Layers. AIAA J., Vol. 9, No. 11, Nov. 1971, pp. 2149, 2156.

50. Sandborn, V. A.; and Slogar, R. J.: Study of the Momentum Distribution of Turbulent Boundary Layers in Adverse Pressure Gradients. NACA TN 3264, 1955.

51. Bradshaw, P.: The Turbulence Structure of Equilibrium Boundary Layers. NPL Aero. Rep. 1184, Jan. 1966.

52. Clauser, F. H.: The Turbulent Boundary Layer. Advances Appl. Mech., Vol. 4, 1956, pp. 1-51.

53. Bradshaw, P.; and Ferris, D. H.: Calculation of Boundary-Layer Development Using the Turbulent Energy Equation: Compressible Flow on Adiabatic Walls. J. Fluid Mech., Vol. 46, Pt. 1, 1971, pp. 83-110.

54. Laurence, J. C.; and Sandborn, V. A.: Heat Transfer from Cylinders. Symposium on Measurements in Unsteady Flow, Worcester, Amer. Soc. Mech. Eng. Publ., May 1962.

TABLE 1

MEAN FLOW DATA

KEY FOR TABLE 1

X = x, cm

Y = y, cm

PTINF = p_{t_∞} = 3.7×10^5 N/m^2

TTINF = T_{t_∞} = 300° K

PWALL = p_{wall}

PTP = p_{tp}

TT = T_t

P = p

U = u, m/s

RHO = ρ, kg/m^3

T = T, °K

M = M

TABLE 1

MEAN FLOW DATA

X = 6.10 CM ,PWALL = 2920. N/SQ M

Y	PTP/PTINF	TT/TTINF	P/PWALL	M	U	RHO	T
0.000	0.008	0.925	1.000	0.00	0.	0.0369	276.
0.025	0.024	0.962	1.000	1.42	407.	0.0498	204.
0.051	0.037	0.970	1.000	1.82	481.	0.0585	174.
0.076	0.044	0.967	1.000	2.01	509.	0.0639	159.
0.102	0.050	0.968	1.000	2.15	528.	0.0680	150.
0.127	0.056	0.972	1.000	2.29	546.	0.0720	141.
0.152	0.064	0.978	1.000	2.45	565.	0.0769	133.
0.178	0.072	0.986	1.000	2.61	583.	0.0817	125.
0.203	0.081	0.992	1.000	2.77	600.	0.0874	117.
0.229	0.089	0.998	1.000	2.92	614.	0.0927	110.
0.254	0.100	1.005	1.000	3.09	628.	0.0991	103.
0.279	0.109	1.010	1.000	3.24	640.	0.1049	97.
0.305	0.119	1.015	1.000	3.38	650.	0.1107	92.
0.330	0.129	1.018	1.000	3.53	659.	0.1170	87.
0.356	0.136	1.017	1.000	3.63	664.	0.1222	83.
0.381	0.143	1.014	1.000	3.73	668.	0.1275	80.
0.406	0.149	1.010	1.000	3.81	670.	0.1320	77.
0.432	0.153	1.008	1.000	3.86	672.	0.1348	76.
0.457	0.156	1.005	1.000	3.89	672.	0.1368	74.
0.483	0.156	1.002	1.000	3.90	672.	0.1378	74.
0.508	0.157	1.000	1.000	3.91	671.	0.1384	74.
0.533	0.157	1.000	1.000	3.91	671.	0.1384	74.
0.559	0.157	1.000	1.000	3.91	671.	0.1384	74.
0.584	0.157	1.000	1.000	3.91	671.	0.1384	74.

TABLE 1 - continued

MEAN FLOW DATA

X = 6.60 CM ,PWALL = 2920. N/SQ M

Y	PTP/PTINF	TT/TTINF	P/PWALL	M	U	RHO	T
0.000	0.008	0.925	1.000	0.00	0.	0.0369	276.
0.025	0.024	0.963	1.000	1.40	404.	0.0495	206.
0.051	0.036	0.970	1.000	1.78	475.	0.0575	177.
0.076	0.043	0.967	1.000	1.98	504.	0.0629	162.
0.102	0.049	0.968	1.000	2.12	524.	0.0671	152.
0.127	0.055	0.973	1.000	2.26	542.	0.0710	143.
0.152	0.062	0.978	1.000	2.41	561.	0.0755	135.
0.178	0.070	0.985	1.000	2.57	579.	0.0805	126.
0.203	0.079	0.991	1.000	2.73	596.	0.0859	119.
0.229	0.087	0.997	1.000	2.88	610.	0.0912	112.
0.254	0.097	1.003	1.000	3.04	624.	0.0970	105.
0.279	0.106	1.010	1.000	3.19	637.	0.1027	99.
0.305	0.115	1.014	1.000	3.33	647.	0.1083	94.
0.330	0.124	1.018	1.000	3.47	656.	0.1143	89.
0.356	0.135	1.017	1.000	3.62	664.	0.1216	84.
0.381	0.143	1.013	1.000	3.72	667.	0.1273	80.
0.406	0.149	1.010	1.000	3.80	670.	0.1317	77.
0.432	0.153	1.008	1.000	3.86	672.	0.1348	76.
0.457	0.156	1.004	1.000	3.89	672.	0.1369	74.
0.483	0.156	1.001	1.000	3.90	671.	0.1379	74.
0.508	0.157	1.000	1.000	3.91	671.	0.1384	74.
0.533	0.157	1.000	1.000	3.91	671.	0.1384	74.
0.559	0.157	1.000	1.000	3.91	671.	0.1384	74.
0.584	0.157	1.000	1.000	3.91	671.	0.1384	74.

TABLE 1 - continued

MEAN FLOW DATA

X = 7.11 CM ,PWALL = 2913. N/SQ M

Y	PTP/PTINF	TT/TTINF	P/PWALL	M	U	RHO	T
0.000	0.008	0.926	1.000	0.00	0.	0.0366	278.
0.025	0.021	0.950	1.000	1.28	375.	0.0473	215.
0.051	0.034	0.959	1.000	1.71	462.	0.0561	181.
0.076	0.042	0.960	1.000	1.94	498.	0.0619	164.
0.102	0.048	0.964	1.000	2.09	520.	0.0659	154.
0.127	0.054	0.968	1.000	2.23	539.	0.0698	145.
0.152	0.061	0.974	1.000	2.37	557.	0.0740	137.
0.178	0.069	0.980	1.000	2.54	576.	0.0791	128.
0.203	0.078	0.987	1.000	2.71	594.	0.0847	120.
0.229	0.087	0.994	1.000	2.87	610.	0.0902	113.
0.254	0.096	1.001	1.000	3.02	624.	0.0957	106.
0.279	0.106	1.004	1.000	3.17	635.	0.1017	100.
0.305	0.116	1.010	1.000	3.32	647.	0.1077	94.
0.330	0.125	1.015	1.000	3.46	657.	0.1135	89.
0.356	0.133	1.014	1.000	3.58	662.	0.1190	85.
0.381	0.141	1.012	1.000	3.68	667.	0.1241	82.
0.406	0.148	1.008	1.000	3.78	670.	0.1296	78.
0.432	0.190	1.006	1.390	3.63	662.	0.1701	83.
0.457	0.195	1.004	1.410	3.65	663.	0.1744	82.
0.483	0.198	1.000	1.440	3.64	661.	0.1780	82.
0.508	0.200	1.000	1.450	3.64	661.	0.1793	82.
0.533	0.202	1.000	1.470	3.64	661.	0.1815	82.
0.559	0.203	1.000	1.480	3.63	660.	0.1821	83.
0.584	0.204	1.000	1.500	3.62	660.	0.1837	83.
0.610	0.205	1.000	1.510	3.61	660.	0.1846	83.

TABLE 1 - continued

MEAN FLOW DATA

X = 7.62 CM ,PWALL = 2978. N/SQ M

Y	PTP/PTINF	TT/TTINF	P/PWALL	M	U	RHO	T
0.000	0.008	0.926	1.000	0.00	0.	0.0374	278.
0.025	0.019	0.950	1.000	1.20	358.	0.0470	221.
0.051	0.033	0.961	0.990	1.68	456.	0.0557	184.
0.076	0.041	0.963	0.990	1.89	492.	0.0611	168.
0.102	0.046	0.965	0.990	2.03	512.	0.0649	158.
0.127	0.053	0.970	0.990	2.18	534.	0.0691	149.
0.152	0.060	0.976	0.990	2.35	555.	0.0739	139.
0.178	0.068	0.983	0.990	2.50	573.	0.0786	131.
0.203	0.077	0.990	0.990	2.67	592.	0.0842	122.
0.229	0.097	1.003	1.310	2.60	589.	0.1063	128.
0.254	0.116	1.015	1.330	2.85	614.	0.1189	116.
0.279	0.132	1.018	1.350	3.01	628.	0.1293	108.
0.305	0.147	1.018	1.370	3.16	639.	0.1400	102.
0.330	0.164	1.017	1.390	3.32	649.	0.1516	95.
0.356	0.179	1.013	1.400	3.46	656.	0.1624	90.
0.381	0.189	1.009	1.410	3.55	659.	0.1705	86.
0.406	0.197	1.006	1.430	3.60	661.	0.1767	84.
0.432	0.200	1.003	1.450	3.60	660.	0.1800	84.
0.457	0.202	1.001	1.470	3.59	659.	0.1820	84.
0.483	0.203	1.001	1.480	3.59	659.	0.1829	84.
0.508	0.204	1.000	1.500	3.57	658.	0.1847	84.
0.533	0.205	1.000	1.520	3.56	657.	0.1863	85.
0.559	0.206	1.000	1.530	3.56	657.	0.1873	85.
0.584	0.207	1.000	1.540	3.55	656.	0.1879	85.
0.610	0.208	1.000	1.550	3.55	656.	0.1889	85.

TABLE 1 - continued

MEAN FLOW DATA

X = 8.13 CM ,PWALL = 4888. N/SQ M

Y	PTP/PTINF	TT/TTINF	P/PWALL	M	U	RHO	T
0.000	0.013	0.926	1.000	0.00	0.	0.0614	278.
0.025	0.022	0.955	1.000	0.90	282.	0.0691	247.
0.051	0.034	0.965	1.000	1.26	374.	0.0777	219.
0.076	0.048	0.971	1.000	1.57	439.	0.0873	195.
0.102	0.060	0.977	0.990	1.79	479.	0.0945	179.
0.127	0.071	0.988	0.970	1.98	511.	0.0996	166.
0.152	0.087	0.996	0.930	2.26	550.	0.1073	148.
0.178	0.103	1.006	0.890	2.54	584.	0.1152	132.
0.203	0.119	1.014	0.850	2.80	611.	0.1226	118.
0.229	0.131	1.018	0.810	3.02	629.	0.1278	108.
0.254	0.143	1.018	0.800	3.19	641.	0.1357	100.
0.279	0.159	1.016	0.810	3.35	650.	0.1470	94.
0.305	0.174	1.014	0.820	3.48	657.	0.1575	89.
0.330	0.187	1.009	0.830	3.60	662.	0.1678	84.
0.356	0.195	1.006	0.840	3.65	663.	0.1738	82.
0.381	0.198	1.003	0.850	3.66	663.	0.1770	82.
0.406	0.200	1.001	0.870	3.63	661.	0.1797	83.
0.432	0.202	1.001	0.890	3.61	659.	0.1821	83.
0.457	0.204	1.000	0.910	3.58	658.	0.1845	84.
0.483	0.205	1.000	0.920	3.57	657.	0.1857	84.
0.508	0.206	1.000	0.930	3.56	657.	0.1869	85.
0.533	0.207	1.000	0.940	3.55	656.	0.1880	85.

TABLE 1 - continued

MEAN FLOW DATA

X = 8.64 CM ,PWALL = 5969. N/SQ M

Y	PTP/PTINF	TT/TTINF	P/PWALL	M	U	RHO	T
0.000	0.016	0.926	1.000	0.00	0.	0.0750	278.
0.025	0.031	0.958	1.000	1.03	317.	0.0877	237.
0.051	0.042	0.966	1.000	1.26	374.	0.0946	220.
0.076	0.056	0.976	1.000	1.52	430.	0.1039	200.
0.102	0.075	0.988	1.000	1.80	483.	0.1158	180.
0.127	0.091	1.000	1.000	2.01	518.	0.1253	166.
0.152	0.112	1.012	0.990	2.26	554.	0.1371	150.
0.178	0.133	1.018	0.990	2.47	581.	0.1502	137.
0.203	0.156	1.020	0.990	2.68	602.	0.1646	125.
0.229	0.178	1.019	0.980	2.90	620.	0.1789	114.
0.254	0.194	1.018	0.960	3.06	632.	0.1883	106.
0.279	0.205	1.012	0.930	3.21	640.	0.1950	99.
0.305	0.214	1.006	0.880	3.37	648.	0.1990	92.
0.330	0.212	1.002	0.820	3.47	653.	0.1941	88.
0.356	0.200	1.000	0.730	3.59	658.	0.1810	84.
0.381	0.198	1.000	0.730	3.57	657.	0.1797	85.
0.406	0.199	1.000	0.740	3.55	656.	0.1810	85.
0.432	0.200	1.000	0.740	3.56	657.	0.1813	85.
0.457	0.202	1.000	0.750	3.55	657.	0.1836	85.
0.483	0.204	1.000	0.760	3.55	656.	0.1858	85.
0.508	0.206	1.000	0.770	3.54	656.	0.1877	85.
0.533	0.207	1.000	0.780	3.53	655.	0.1890	86.

TABLE 1 - continued

MEAN FLOW DATA

X = 9.14 CM ,PWALL = 6817. N/SQ M

Y	PTP/PTINF	TT/TTINF	P/PWALL	M	U	RHO	T
0.000	0.018	0.926	1.000	0.00	0.	0.0856	278.
0.025	0.037	0.960	1.000	1.06	326.	0.1011	235.
0.051	0.049	0.968	1.000	1.28	380.	0.1088	218.
0.076	0.064	0.978	1.000	1.52	431.	0.1185	201.
0.102	0.083	0.991	1.000	1.77	479.	0.1300	183.
0.127	0.104	1.006	1.000	2.00	519.	0.1422	167.
0.152	0.129	1.013	1.000	2.25	554.	0.1575	151.
0.178	0.152	1.018	1.000	2.46	579.	0.1723	138.
0.203	0.182	1.021	0.990	2.72	606.	0.1908	123.
0.229	0.212	1.021	0.980	2.96	625.	0.2095	111.
0.254	0.235	1.016	0.960	3.16	638.	0.2241	102.
0.279	0.248	1.007	0.950	3.26	642.	0.2342	96.
0.305	0.251	1.003	0.930	3.32	645.	0.2359	94.
0.330	0.249	1.000	0.920	3.33	644.	0.2343	93.
0.356	0.242	1.000	0.880	3.35	645.	0.2266	92.
0.381	0.230	1.000	0.810	3.41	649.	0.2135	90.
0.406	0.222	1.000	0.780	3.42	649.	0.2063	90.
0.432	0.214	1.000	0.720	3.49	653.	0.1965	87.
0.457	0.202	1.000	0.660	3.54	656.	0.1838	85.
0.483	0.202	1.000	0.650	3.57	657.	0.1828	85.
0.508	0.203	1.000	0.660	3.56	657.	0.1848	85.
0.533	0.206	1.000	0.670	3.55	656.	0.1871	85.
0.559	0.208	1.000	0.680	3.54	656.	0.1891	85.
0.584	0.209	1.000	0.690	3.52	655.	0.1905	86.
0.610	0.211	1.000	0.700	3.51	654.	0.1925	86.
0.635	0.212	1.000	0.700	3.52	655.	0.1934	86.
0.660	0.213	1.000	0.710	3.51	654.	0.1948	87.

TABLE 1 - continued

MEAN FLOW DATA

X = 9.65 CM ,PWALL = 7449. N/SQ M

Y	PTP/PTINF	TT/TTINF	P/PWALL	M	U	RHO	T
0.000	0.020	0.926	1.000	0.00	0.	0.0936	278.
0.025	0.043	0.964	1.000	1.11	338.	0.1120	232.
0.051	0.057	0.972	1.000	1.34	392.	0.1210	215.
0.076	0.073	0.982	1.000	1.56	440.	0.1311	198.
0.102	0.093	0.996	1.000	1.79	483.	0.1425	182.
0.127	0.113	1.005	1.000	2.00	518.	0.1551	167.
0.152	0.141	1.012	1.000	2.25	553.	0.1722	151.
0.178	0.168	1.018	0.990	2.49	582.	0.1883	137.
0.203	0.203	1.021	0.990	2.75	608.	0.2106	122.
0.229	0.234	1.019	0.990	2.96	625.	0.2319	111.
0.254	0.256	1.012	0.990	3.10	633.	0.2479	104.
0.279	0.266	1.006	0.970	3.20	638.	0.2545	99.
0.305	0.268	1.002	0.960	3.23	638.	0.2558	97.
0.330	0.267	1.000	0.950	3.24	638.	0.2550	97.
0.356	0.265	1.000	0.940	3.24	639.	0.2526	97.
0.381	0.263	1.000	0.920	3.27	640.	0.2497	96.
0.406	0.261	1.000	0.910	3.27	640.	0.2477	95.
0.432	0.258	1.000	0.890	3.29	642.	0.2445	95.
0.457	0.256	1.000	0.880	3.29	642.	0.2418	95.
0.483	0.242	1.000	0.800	3.36	646.	0.2262	92.
0.508	0.227	1.000	0.720	3.44	650.	0.2096	89.
0.533	0.212	1.000	0.640	3.52	655.	0.1930	86.
0.559	0.206	1.000	0.610	3.56	657.	0.1868	85.
0.584	0.208	1.000	0.630	3.52	655.	0.1900	86.
0.610	0.210	1.000	0.640	3.51	654.	0.1921	87.
0.635	0.211	1.000	0.650	3.49	653.	0.1932	87.
0.660	0.212	1.000	0.650	3.49	653.	0.1938	87.

TABLE 1 - continued

MEAN FLOW DATA

X =10.16 CM ,PWALL = 7880. N/SQ M

Y	PTP/PTINF	TT/TTINF	P/PWALL	M	U	RHO	T
0.000	0.021	0.926	1.000	0.00	0.	0.0990	278.
0.025	0.049	0.967	1.000	1.17	354.	0.1208	227.
0.051	0.066	0.976	1.000	1.41	409.	0.1312	209.
0.076	0.082	0.986	1.000	1.61	450.	0.1411	195.
0.102	0.101	0.999	1.000	1.82	489.	0.1526	180.
0.127	0.124	1.005	1.000	2.03	523.	0.1667	165.
0.152	0.149	1.012	1.000	2.25	554.	0.1824	151.
0.178	0.181	1.018	1.000	2.50	583.	0.2026	136.
0.203	0.218	1.020	1.000	2.76	609.	0.2263	121.
0.229	0.249	1.019	1.000	2.96	625.	0.2472	111.
0.254	0.270	1.012	0.990	3.10	633.	0.2619	104.
0.279	0.280	1.006	0.990	3.16	635.	0.2700	101.
0.305	0.281	1.003	0.990	3.16	634.	0.2715	100.
0.330	0.281	1.000	0.980	3.18	634.	0.2711	99.
0.356	0.280	1.000	0.970	3.19	635.	0.2696	99.
0.381	0.281	1.000	0.970	3.19	635.	0.2703	99.
0.406	0.279	1.000	0.960	3.20	636.	0.2682	98.
0.432	0.277	1.000	0.960	3.19	635.	0.2669	99.
0.457	0.275	1.000	0.950	3.19	635.	0.2648	99.
0.483	0.274	1.000	0.940	3.21	636.	0.2633	98.
0.508	0.272	1.000	0.930	3.21	636.	0.2609	98.
0.533	0.268	1.000	0.910	3.23	637.	0.2570	97.
0.559	0.265	1.000	0.890	3.25	639.	0.2534	97.
0.584	0.259	1.000	0.860	3.26	640.	0.2464	96.
0.610	0.230	1.000	0.710	3.39	648.	0.2146	91.
0.635	0.208	1.000	0.600	3.51	654.	0.1904	87.
0.660	0.207	1.000	0.590	3.53	655.	0.1886	86.

TABLE 1 - continued

MEAN FLOW DATA

X =10.67 CM ,PWALL = 8314. N/SQ M

Y	PTP/PTINF	TT/TTINF	P/PWALL	M	U	RHO	T
0.000	0.022	0.927	1.000	0.00	0.	0.1045	278.
0.025	0.055	0.970	1.000	1.22	365.	0.1294	224.
0.051	0.073	0.980	1.000	1.46	419.	0.1409	206.
0.076	0.091	0.993	1.000	1.66	460.	0.1513	192.
0.102	0.109	1.000	1.000	1.84	493.	0.1627	178.
0.127	0.131	1.006	1.000	2.03	523.	0.1759	165.
0.152	0.159	1.014	1.000	2.27	556.	0.1938	150.
0.178	0.192	1.018	1.000	2.51	583.	0.2147	135.
0.203	0.231	1.021	1.000	2.76	609.	0.2395	121.
0.229	0.262	1.021	1.000	2.95	624.	0.2600	112.
0.254	0.282	1.014	1.000	3.06	630.	0.2748	105.
0.279	0.290	1.006	1.000	3.11	631.	0.2824	103.
0.305	0.292	1.003	1.000	3.12	631.	0.2850	102.
0.330	0.293	1.002	1.000	3.13	631.	0.2856	101.
0.356	0.293	1.002	1.000	3.13	631.	0.2856	101.
0.381	0.293	1.002	1.000	3.13	631.	0.2856	101.
0.406	0.291	1.002	0.990	3.13	631.	0.2838	101.
0.432	0.290	1.002	0.980	3.15	632.	0.2823	101.
0.457	0.289	1.002	0.970	3.15	633.	0.2804	100.
0.483	0.288	1.002	0.960	3.16	633.	0.2786	100.
0.508	0.286	1.002	0.960	3.16	633.	0.2777	100.
0.533	0.284	1.002	0.950	3.16	633.	0.2755	100.
0.559	0.282	1.002	0.940	3.17	634.	0.2730	100.
0.584	0.280	1.002	0.930	3.17	634.	0.2709	100.
0.610	0.278	1.002	0.910	3.19	635.	0.2675	99.
0.635	0.275	1.002	0.890	3.22	637.	0.2642	98.
0.660	0.271	1.002	0.870	3.23	638.	0.2592	97.

TABLE 1 - continued

MEAN FLOW DATA

X =11.18 CM ,PWALL = 8813. N/SQ M

Y	PTP/PTINF	TT/TTINF	P/PWALL	M	U	RHO	T
0.000	0.024	0.926	1.000	0.00	0.	0.1107	278.
0.025	0.060	0.973	1.000	1.24	372.	0.1380	223.
0.051	0.081	0.983	1.000	1.50	429.	0.1512	203.
0.076	0.100	0.994	1.000	1.69	467.	0.1623	189.
0.102	0.120	0.997	1.000	1.88	498.	0.1753	175.
0.127	0.142	1.004	1.000	2.06	527.	0.1887	163.
0.152	0.171	1.010	1.000	2.28	557.	0.2072	148.
0.178	0.203	1.016	1.000	2.50	583.	0.2268	135.
0.203	0.241	1.021	1.000	2.74	607.	0.2510	122.
0.229	0.272	1.018	1.000	2.92	621.	0.2723	113.
0.254	0.290	1.012	1.000	3.02	627.	0.2857	108.
0.279	0.300	1.006	1.000	3.07	629.	0.2940	105.
0.305	0.302	1.003	1.000	3.08	629.	0.2964	104.
0.330	0.303	1.000	1.000	3.08	628.	0.2976	103.
0.356	0.302	1.000	0.990	3.10	629.	0.2960	103.
0.381	0.302	1.000	0.990	3.10	629.	0.2960	103.
0.406	0.301	1.000	0.990	3.09	629.	0.2957	103.
0.432	0.300	1.000	0.980	3.10	629.	0.2938	102.
0.457	0.299	1.000	0.970	3.11	630.	0.2923	102.

TABLE 1 - concluded

MEAN FLOW DATA

X =11.68 CM ,PWALL = 9280. N/SQ M

Y	PTP/PTINF	TT/TTINF	P/PWALL	M	U	RHO	T
0.000	0.025	0.926	1.000	0.00	0.	0.1166	278.
0.025	0.066	0.976	1.000	1.27	378.	0.1463	221.
0.051	0.088	0.987	1.000	1.53	435.	0.1607	201.
0.076	0.107	0.994	1.000	1.71	470.	0.1722	188.
0.102	0.127	0.997	1.000	1.89	500.	0.1855	174.
0.127	0.150	1.003	1.000	2.07	528.	0.1999	162.
0.152	0.180	1.011	1.000	2.28	557.	0.2183	148.
0.178	0.212	1.018	1.000	2.49	582.	0.2376	136.
0.203	0.250	1.020	1.000	2.72	605.	0.2621	123.
0.229	0.281	1.018	1.000	2.89	619.	0.2828	114.
0.254	0.299	1.012	1.000	2.99	625.	0.2969	109.
0.279	0.307	1.006	1.000	3.02	626.	0.3036	107.
0.305	0.309	1.002	1.000	3.04	625.	0.3065	106.
0.330	0.309	1.000	1.000	3.04	625.	0.3070	105.
0.356	0.308	1.000	0.990	3.05	625.	0.3054	105.
0.381	0.307	1.000	0.980	3.06	626.	0.3038	104.
0.406	0.306	1.000	0.970	3.07	627.	0.3022	104.
0.432	0.301	1.000	0.950	3.07	627.	0.2964	104.
0.457	0.293	1.000	0.890	3.14	632.	0.2851	101.
0.483	0.282	1.000	0.840	3.17	634.	0.2731	100.
0.508	0.272	1.000	0.780	3.23	638.	0.2602	97.
0.533	0.260	1.000	0.720	3.29	642.	0.2463	95.
0.559	0.249	1.000	0.670	3.34	645.	0.2340	93.
0.584	0.237	1.000	0.620	3.39	648.	0.2208	91.
0.610	0.224	1.000	0.570	3.44	650.	0.2072	89.
0.635	0.213	1.000	0.570	3.35	645.	0.1999	92.
0.660	0.204	1.000	0.450	3.70	664.	0.1819	80.

TABLE 2

FLUCTUATING FLOW DATA

KEY FOR TABLE 2

X = x, cm

Y = y, cm

RHO'U' = $\overline{\rho' u'}$, kg/m^2-s

RHO'V' = $\overline{\rho' v'}$, kg/m^2-s

RHO'W' = $\overline{\rho' w'}$, kg/m^2-s

RHOU'T' = $\overline{\rho u' T'}$, kg °K/m^2-s

RHOV'T' = $\overline{\rho v' T'}$, kg °K/m^2-s

RHOU'U' = $\overline{\rho u'^2}$, N/m^2

RHOV'V' = $\overline{\rho v'^2}$, N/m^2

RHOW'W' = $\overline{\rho w'^2}$, N/m^2

RHOU'V' = $\overline{\rho u' v'}$, N/m^2

RHOU'W' = $\overline{\rho u' w'}$, N/m^2

TABLE 2

FLUCTUATING FLOW DATA

X = 6.10 CM

Y	RHO'U'	RHO'V'	RHO'W'	RHOU'T'	RHOV'T'
0.000	0.00	0.00	0.00	0.00	0.00
0.051	0.29	0.04	0.00	-50.21	-7.97
0.102	0.20	0.07	0.00	-29.59	-10.90
0.152	0.26	0.11	0.00	-34.20	-13.78
0.203	0.35	0.16	0.00	-40.47	-17.63
0.254	0.33	0.18	0.00	-34.07	-17.79
0.305	0.32	0.17	0.00	-29.95	-15.33
0.356	0.29	0.15	0.05	-19.94	-12.29
0.406	0.13	0.07	0.00	-9.87	-5.29
0.457	0.04	0.01	0.00	-3.09	-0.65
0.508	0.01	0.00	0.00	-0.52	0.19
0.559	0.00	0.00	0.00	-0.30	0.16

Y	RHOU'U'	RHOV'V'	RHOW'W'	RHOU'V'	RHOU'W'
0.000	0.0	0.0	0.0	0.0	0.0
0.051	114.9	6.2	16.3	18.2	3.8
0.102	64.2	43.6	60.3	24.4	-1.0
0.152	69.4	65.6	85.7	31.6	-4.3
0.203	80.0	93.8	112.5	37.3	-1.9
0.254	64.6	131.7	141.2	35.4	1.0
0.305	56.5	147.5	154.7	28.7	0.5
0.356	36.9	131.2	117.3	25.4	-2.4
0.406	17.7	69.9	50.3	10.1	6.7
0.457	5.7	20.1	19.6	1.4	1.0
0.508	1.0	12.4	14.8	-0.5	0.0
0.559	0.5	12.0	12.9	-0.5	0.0

TABLE 2 - continued

FLUCTUATING FLOW DATA

X = 6.60 CM

Y	RHO'U'	RHO'V'	RHO'W'	RHOU'T'	RHOV'T'
0.000	0.00	0.00	0.00	0.00	0.00
0.051	0.28	0.05	0.00	-49.94	-8.60
0.102	0.21	0.07	0.00	-31.19	-10.71
0.152	0.27	0.12	0.00	-37.24	-15.65
0.203	0.32	0.16	0.00	-37.70	-18.28
0.254	0.29	0.19	0.00	-31.11	-19.91
0.305	0.31	0.19	0.05	-28.89	-17.85
0.356	0.27	0.17	0.05	-22.65	-13.97
0.406	0.16	0.10	0.05	-12.15	-7.46
0.457	0.04	0.01	0.00	-3.12	-0.98
0.508	0.00	0.00	0.00	-0.76	0.11
0.559	0.00	0.00	0.00	-0.30	0.41

Y	RHOU'U'	RHOV'V'	RHOW'W'	RHOU'V'	RHOU'W'
0.000	0.0	0.0	0.0	0.0	0.0
0.051	114.9	6.7	8.1	21.1	5.3
0.102	67.0	44.5	45.0	24.9	-1.9
0.152	77.6	65.6	79.0	34.0	-1.0
0.203	74.7	108.2	108.2	36.4	0.5
0.254	56.5	149.4	184.3	38.8	4.8
0.305	53.1	142.7	142.2	38.8	9.1
0.356	42.6	151.8	129.8	27.3	9.1
0.406	22.0	80.4	61.8	13.9	6.7
0.457	5.3	27.8	35.4	1.4	0.0
0.508	1.4	14.8	13.4	0.0	0.5
0.559	0.5	13.4	13.4	-1.0	0.0

TABLE 2 - continued

FLUCTUATING FLOW DATA

X = 7.11 CM

Y	RHO'U'	RHO'V'	RHO'W'	RHOU'T'	RHOV'T'
0.000	0.00	0.00	0.00	0.00	0.00
0.051	0.28	0.06	0.00	-49.59	-11.28
0.102	0.19	0.09	0.00	-28.40	-13.29
0.152	0.24	0.13	0.00	-32.58	-17.55
0.203	0.28	0.21	0.00	-33.77	-24.41
0.254	0.32	0.24	0.00	-33.96	-25.34
0.305	0.30	0.28	0.00	-27.67	-26.58
0.356	0.28	0.25	0.00	-24.06	-21.70
0.406	0.16	0.17	0.00	-12.07	-13.24
0.457	0.05	0.00	0.00	-4.23	-3.61
0.508	0.01	0.00	0.00	-0.68	-0.27
0.559	0.01	0.00	0.00	-0.49	0.27

Y	RHOU'U'	RHOV'V'	RHOW'W'	RHOU'V'	RHOU'W'
0.000	0.0	0.0	0.0	0.0	0.0
0.051	115.4	17.2	16.8	28.2	1.4
0.102	59.9	52.7	54.1	30.2	-1.0
0.152	67.0	78.0	90.0	38.3	-2.9
0.203	64.6	126.4	120.2	51.7	-2.4
0.254	64.6	170.0	150.8	51.7	6.2
0.305	49.3	198.2	165.2	57.9	-0.5
0.356	45.0	189.1	136.0	46.0	-1.0
0.406	21.5	128.8	95.8	35.4	2.9
0.457	7.2	55.5	43.1	8.6	0.5
0.508	1.0	18.2	21.1	1.0	-0.5
0.559	1.0	15.3	16.3	-1.0	-0.5

TABLE 2 - continued

FLUCTUATING FLOW DATA

X = 7.62 CM

Y	RHO'U'	RHO'V'	RHO'W'	RHOU'T'	RHOV'T'
0.000	0.00	0.00	0.00	0.00	0.00
0.051	0.28	0.05	0.00	-52.00	-8.79
0.102	0.18	0.10	0.00	-28.56	-15.30
0.152	0.24	0.16	0.00	-33.69	-21.56
0.203	0.30	0.20	0.00	-36.59	-24.41
0.254	0.49	0.39	0.00	-57.48	-45.22
0.305	0.42	0.38	0.00	-42.53	-38.49
0.356	0.32	0.28	0.05	-28.32	-24.98
0.406	0.08	0.04	0.00	-7.05	-3.91
0.457	0.01	0.00	0.00	-1.25	0.05
0.508	0.00	-0.00	0.00	-0.57	0.65
0.559	0.00	0.00	0.00	-0.33	0.19

Y	RHOU'U'	RHOV'V'	RHOW'W'	RHOU'V'	RHOU'W'
0.000	0.0	0.0	0.0	0.0	0.0
0.051	126.9	16.3	22.0	22.5	0.5
0.102	62.2	57.0	63.7	37.8	1.4
0.152	68.9	102.0	85.7	46.0	0.5
0.203	72.3	121.6	109.2	57.5	28.7
0.254	111.1	216.4	235.1	95.3	-2.9
0.305	78.5	275.8	274.4	80.4	-4.3
0.356	54.6	240.8	217.4	49.3	9.1
0.406	12.0	62.7	65.6	9.6	0.5
0.457	2.4	17.2	12.4	0.0	0.5
0.508	1.0	16.8	15.3	-1.0	-0.5
0.559	0.5	16.8	13.4	-0.5	-0.5

TABLE 2 - continued

FLUCTUATING FLOW DATA

X = 8.13 CM

Y	RHO'U'	RHO'V'	RHO'W'	RHOU'T'	RHOV'T'
0.000	0.00	0.00	0.00	0.00	0.00
0.051	0.23	0.06	0.00	-49.99	-12.83
0.102	0.31	0.17	0.00	-63.77	-29.89
0.152	0.42	0.25	0.00	-62.90	-37.49
0.203	0.51	0.46	0.00	-60.90	-54.74
0.254	0.38	0.43	0.00	-38.44	-43.78
0.305	0.27	0.30	0.00	-24.44	-27.07
0.356	0.10	0.11	0.05	-8.08	-8.79
0.406	0.02	0.00	0.00	-1.25	-0.60
0.457	0.00	0.00	0.00	-0.54	0.05
0.508	0.00	-0.00	0.00	-0.38	0.46
0.559	0.00	-0.00	0.00	-0.22	0.49

Y	RHOU'U'	RHOV'V'	RHOW'W'	RHOU'V'	RHOU'W'
0.000	0.0	0.0	0.0	0.0	0.0
0.051	149.9	37.8	44.0	48.8	-1.0
0.102	150.8	72.3	53.1	77.1	2.4
0.152	131.7	190.1	169.0	84.7	-3.4
0.203	113.5	218.3	232.7	136.5	-2.9
0.254	72.8	257.6	234.6	100.1	2.9
0.305	45.0	234.6	216.9	65.6	0.0
0.356	14.8	80.9	57.0	23.5	6.2
0.406	1.9	20.1	15.3	1.4	1.0
0.457	1.0	20.1	13.4	-0.5	0.0
0.508	0.5	17.7	14.4	-1.0	0.5
0.559	0.0	18.7	15.8	-1.0	-0.5

TABLE 2 - continued

FLUCTUATING FLOW DATA

X = 8.64 CM

Y	RHO'U'	RHO'V'	RHU'W'	RHOU'T'	RHOV'T'
0.000	0.00	0.00	0.00	0.00	0.00
0.051	0.26	0.04	0.00	-56.88	-10.12
0.102	0.62	0.27	0.00	-112.98	-48.93
0.152	0.64	0.49	0.00	-97.35	-74.70
0.203	0.60	0.79	0.00	-74.21	-99.06
0.254	0.45	0.54	0.05	-47.50	-57.23
0.305	0.16	0.09	0.05	-14.48	-8.30
0.356	0.12	-0.01	0.00	-5.80	1.38
0.406	0.01	0.00	0.00	-0.38	-0.08
0.457	0.01	0.00	0.00	-0.38	-0.16
0.508	0.01	0.00	0.00	-0.60	0.08
0.559	0.01	0.00	0.00	-0.35	0.05

Y	RHOU'U'	RHOV'V'	RHOW'W'	RHOU'V'	RHOU'W'
0.000	0.0	0.0	0.0	0.0	0.0
0.051	174.3	32.6	39.7	44.5	-2.4
0.102	265.7	141.2	91.0	115.9	-0.5
0.152	200.1	254.2	247.5	196.8	-2.9
0.203	141.2	460.6	412.7	273.9	-1.0
0.254	87.6	377.3	351.4	140.3	26.3
0.305	26.8	129.3	122.1	23.5	12.4
0.356	11.0	30.2	25.4	-0.5	1.9
0.406	0.5	17.2	14.4	0.0	-0.5
0.457	0.5	14.8	14.4	1.0	0.0
0.508	1.0	13.9	14.4	0.0	0.0
0.559	0.5	16.8	15.3	-0.5	0.5

TABLE 2 - continued

FLUCTUATING FLOW DATA

X = 9.14 CM

Y	RHO'U'	RHO'V'	RHO'W'	RHOU'T'	RHOV'T'
0.000	0.00	0.00	0.00	0.00	0.00
0.051	0.34	0.08	0.00	-73.43	-17.52
0.102	0.65	0.34	0.00	-119.41	-61.98
0.152	0.80	0.74	0.00	-120.90	-111.70
0.203	0.72	1.22	0.00	-89.08	-149.32
0.254	0.61	0.75	0.15	-51.51	-76.41
0.305	0.08	0.13	0.05	-7.16	-11.72
0.356	0.02	-0.01	0.00	-2.17	0.87
0.406	0.07	-0.03	0.00	-6.86	2.60
0.457	0.05	-0.01	0.00	-4.94	1.27
0.508	0.00	0.00	0.00	-0.22	-0.05
0.559	0.00	0.00	0.00	-0.35	0.00

Y	RHOU'U'	RHOV'V'	RHOW'W'	RHOU'V'	RHOU'W'
0.000	0.0	0.0	0.0	0.0	0.0
0.051	222.2	35.4	31.6	68.0	1.9
0.102	283.5	140.3	116.8	172.4	2.4
0.152	249.5	423.7	357.2	297.8	5.7
0.203	172.8	731.6	510.4	388.8	13.9
0.254	97.7	464.9	404.6	195.8	16.3
0.305	12.9	86.7	58.9	30.2	6.2
0.356	3.8	41.2	38.8	0.5	-1.9
0.406	13.4	25.9	22.5	-3.8	0.0
0.457	9.1	14.8	30.6	-1.9	-1.4
0.508	0.0	17.2	15.8	0.0	0.5
0.559	0.5	18.2	17.7	0.5	0.0

TABLE 2 - continued

FLUCTUATING FLOW DATA

X = 9.65 CM

Y	RHO'U'	RHO'V'	RHO'W'	RHOU'T'	RHOV'T'
0.000	0.00	0.00	0.00	0.00	0.00
0.051	0.42	0.08	0.00	-90.54	-17.25
0.102	0.63	0.32	0.00	-114.28	-57.56
0.152	0.87	0.70	0.05	-131.04	-105.03
0.203	0.94	1.05	0.10	-114.71	-128.09
0.254	0.70	0.56	0.20	-52.51	-57.70
0.305	0.07	0.05	0.05	-6.35	-4.53
0.356	0.00	-0.01	0.00	-1.44	0.84
0.406	0.01	-0.00	0.00	-1.41	-0.16
0.457	0.01	-0.01	0.00	-1.44	1.57
0.508	0.08	-0.05	0.00	-6.75	4.34
0.559	0.05	-0.00	0.00	-4.48	-0.84

Y	RHOU'U'	RHOV'V'	RHOW'W'	RHOU'V'	RHOU'W'
0.000	0.0	0.0	0.0	0.0	0.0
0.051	260.5	32.6	36.9	57.5	-1.9
0.102	265.7	162.3	163.3	146.0	-1.9
0.152	275.8	491.3	452.0	259.0	9.6
0.203	220.7	803.4	665.1	306.0	21.1
0.254	92.9	446.2	447.7	142.2	35.4
0.305	12.0	46.9	61.3	9.6	6.2
0.356	2.4	30.6	23.5	-1.4	-1.4
0.406	2.4	40.2	23.5	-1.0	-0.5
0.457	2.4	37.3	23.5	-2.4	-1.9
0.508	12.9	44.5	48.4	-7.7	-3.8
0.559	8.1	7.7	32.1	1.4	1.0

TABLE 2 - continued

FLUCTUATING FLOW DATA

X = 10.16 CM

Y	RHO'U'	RHO'V'	RHO'W'	RHOU'T'	RHOV'T'
0.000	0.00	0.00	0.00	0.00	0.00
0.051	0.49	0.09	0.00	-103.70	-19.56
0.102	0.64	0.36	0.00	-114.96	-55.17
0.152	0.95	0.75	0.00	-142.98	-112.03
0.203	1.17	1.23	0.10	-141.78	-149.54
0.254	0.62	0.55	0.10	-64.23	-57.51
0.305	0.06	0.06	0.00	-6.10	-6.27
0.356	0.02	0.00	0.00	-1.84	-0.14
0.406	0.01	-0.00	0.00	-1.06	0.54
0.457	0.01	-0.00	0.00	-1.09	0.33
0.508	0.01	0.00	0.00	-1.36	0.16
0.559	0.01	-0.01	0.00	-1.25	1.27

Y	RHOU'U'	RHOV'V'	RHOW'W'	RHOU'V'	RHOU'W'
0.000	0.0	0.0	0.0	0.0	0.0
0.051	284.4	24.9	49.8	57.9	7.7
0.102	264.8	168.5	220.7	143.2	1.9
0.152	305.0	491.7	551.6	297.3	3.4
0.203	279.1	883.9	765.1	379.7	49.3
0.254	120.2	443.4	527.6	144.6	16.8
0.305	10.1	59.9	72.3	14.8	-2.4
0.356	3.4	22.5	23.0	1.0	-0.5
0.406	1.4	25.9	23.0	-1.0	-1.4
0.457	1.9	25.4	22.5	-0.5	-1.0
0.508	2.4	27.8	23.5	0.5	-1.0
0.559	1.9	31.6	24.4	-1.9	-1.9

TABLE 2 - continued

FLUCTUATING FLOW DATA

X = 10.67 CM

Y	RHO'U'	RHO'V'	RHO'W'	RHOU'T'	RHOV'T'
0.000	0.00	0.00	0.00	0.00	0.00
0.051	0.59	0.11	0.00	-122.01	-21.75
0.102	0.64	0.29	0.00	-113.90	-51.65
0.152	1.01	0.76	0.00	-150.76	-113.63
0.203	1.32	1.26	0.05	-159.71	-153.10
0.254	0.69	0.61	0.15	-73.29	-64.37
0.305	0.07	0.05	0.00	-6.56	-5.53
0.356	0.01	0.00	0.00	-0.87	0.03
0.406	0.01	0.00	0.00	-0.79	0.22
0.457	0.01	0.00	0.00	-1.19	0.24
0.508	0.01	0.00	0.00	-1.09	0.71

Y	RHOU'U'	RHOV'V'	RHOW'W'	RHOU'V'	RHOU'W'
0.000	0.0	0.0	0.0	0.0	0.0
0.051	331.3	20.6	40.7	61.8	1.4
0.102	261.9	169.5	236.5	126.4	-16.3
0.152	328.0	580.3	585.1	279.1	11.0
0.203	319.8	973.4	999.7	384.0	23.0
0.254	141.2	490.3	553.0	161.4	21.5
0.305	11.0	57.5	84.7	11.5	-2.4
0.356	1.0	28.2	25.9	0.0	-1.0
0.406	1.0	25.4	26.3	-0.5	-1.0
0.457	1.9	24.4	22.5	-0.5	-1.4
0.508	1.9	22.5	23.0	-1.0	-1.0

TABLE 2 - continued

FLUCTUATING FLOW DATA

X = 11.18 CM

Y	RHO'U'	RHO'V'	RHO'W'	RHOU'T'	RHOV'T'
0.000	0.00	0.00	0.00	0.00	0.00
0.051	0.64	0.12	0.00	-130.04	-23.54
0.102	0.65	0.35	0.00	-114.03	-60.22
0.152	1.06	0.74	0.00	-157.90	-109.72
0.203	1.43	1.27	0.20	-174.04	-155.10
0.254	0.77	0.54	0.15	-77.47	-57.64
0.305	0.08	0.06	0.05	-8.41	-6.59
0.356	0.01	0.00	0.00	-1.00	0.24
0.406	0.01	0.00	0.00	-0.81	0.00

Y	RHOU'U'	RHOV'V'	RHOW'W'	RHOU'V'	RHOU'W'
0.000	0.0	0.0	0.0	0.0	0.0
0.051	340.4	10.1	50.3	73.3	-6.7
0.102	257.6	192.5	268.6	163.3	-4.8
0.152	345.7	569.3	657.4	298.8	13.4
0.203	353.4	1020.8	927.9	379.2	38.8
0.254	147.0	512.3	562.6	138.4	15.8
0.305	14.4	67.0	98.2	13.4	8.1
0.356	1.4	23.9	23.0	-1.0	-0.5
0.406	1.0	26.8	23.0	-0.5	-1.0

TABLE 2 - concluded

FLUCTUATING FLOW DATA

X = 11.68 CM

Y	RHO'U'	RHO'V'	RHO'W'	RHOU'T'	RHOV'T'
0.000	0.00	0.00	0.00	0.00	0.00
0.051	0.64	0.13	0.00	-129.31	-26.56
0.102	0.63	0.35	0.00	-110.75	-61.17
0.152	1.15	0.76	0.05	-169.80	-112.19
0.203	1.53	1.18	0.15	-188.55	-144.98
0.254	0.81	0.60	0.15	-87.72	-65.53
0.305	0.10	0.07	0.05	-10.61	-7.54
0.356	0.01	0.00	0.00	-1.33	-0.14
0.406	0.01	0.00	0.00	-1.19	0.08

Y	RHOU'U'	RHOV'V'	RHOW'W'	RHOU'V'	RHOU'W'
0.000	0.0	0.0	0.0	0.0	0.0
0.051	327.5	22.5	57.5	75.2	1.4
0.102	241.3	191.5	294.0	158.0	2.4
0.152	373.0	581.3	638.2	279.6	28.2
0.203	385.4	997.3	949.0	337.1	45.5
0.254	167.6	637.3	558.8	126.9	20.1
0.305	19.2	71.3	91.0	16.8	5.3
0.356	1.9	23.0	21.1	0.5	0.5
0.406	1.9	19.2	17.7	0.0	0.0

TABLE 3

NOZZLE COORDINATES

X(RELATIVE TO NOZZLE THROAT) AND R ARE IN CM. FROM X=15.24 TO 31.75 , R IS 2.642.

X	R	X	R	X	R	X	R	X	R
-3.175	3.051	0.508	0.848	4.191	1.831	7.874	2.365	11.557	2.588
-3.048	2.903	0.635	0.871	4.318	1.857	8.001	2.377	11.684	2.593
-2.921	2.746	0.762	0.899	4.445	1.882	8.128	2.388	11.811	2.596
-2.794	2.591	0.889	0.932	4.572	1.908	8.255	2.398	11.938	2.601
-2.667	2.438	1.016	0.970	4.699	1.930	8.382	2.410	12.065	2.603
-2.540	2.286	1.143	1.008	4.826	1.956	8.509	2.421	12.192	2.606
-2.413	2.134	1.270	1.049	4.953	1.976	8.636	2.431	12.319	2.609
-2.286	1.981	1.397	1.090	5.080	1.999	8.763	2.441	12.446	2.614
-2.159	1.824	1.524	1.130	5.207	2.022	8.890	2.451	12.573	2.616
-2.032	1.671	1.651	1.168	5.334	2.042	9.017	2.459	12.700	2.619
-1.905	1.519	1.778	1.209	5.461	2.062	9.144	2.466	12.827	2.621
-1.778	1.384	1.905	1.247	5.588	2.083	9.271	2.476	12.954	2.624
-1.651	1.265	2.032	1.285	5.715	2.103	9.398	2.487	13.081	2.626
-1.524	1.176	2.159	1.326	5.842	2.121	9.525	2.494	13.208	2.629
-1.397	1.110	2.286	1.361	5.969	2.141	9.652	2.502	13.335	2.631
-1.270	1.052	2.413	1.400	6.096	2.156	9.779	2.510	13.462	2.631
-1.143	1.006	2.540	1.435	6.223	2.177	9.906	2.515	13.589	2.631
-1.016	0.965	2.667	1.471	6.350	2.192	10.033	2.522	13.716	2.634
-0.889	0.930	2.794	1.504	6.477	2.207	10.160	2.530	13.843	2.634
-0.762	0.897	2.921	1.537	6.604	2.225	10.287	2.537	13.970	2.637
-0.635	0.869	3.048	1.570	6.731	2.240	10.414	2.543	14.097	2.637
-0.508	0.846	3.175	1.603	6.858	2.258	10.541	2.548	14.224	2.639
-0.381	0.828	3.302	1.633	6.985	2.271	10.668	2.555	14.351	2.639
-0.254	0.815	3.429	1.664	7.112	2.286	10.795	2.560	14.478	2.639
-0.127	0.810	3.556	1.694	7.239	2.301	10.922	2.565	14.605	2.642
0.000	0.808	3.683	1.722	7.366	2.311	11.049	2.570	14.732	2.642
0.127	0.810	3.810	1.750	7.493	2.327	11.176	2.576	14.859	2.642
0.254	0.818	3.937	1.778	7.620	2.339	11.303	2.581	14.986	2.642
0.381	0.831	4.064	1.806	7.747	2.352	11.430	2.586	15.113	2.642

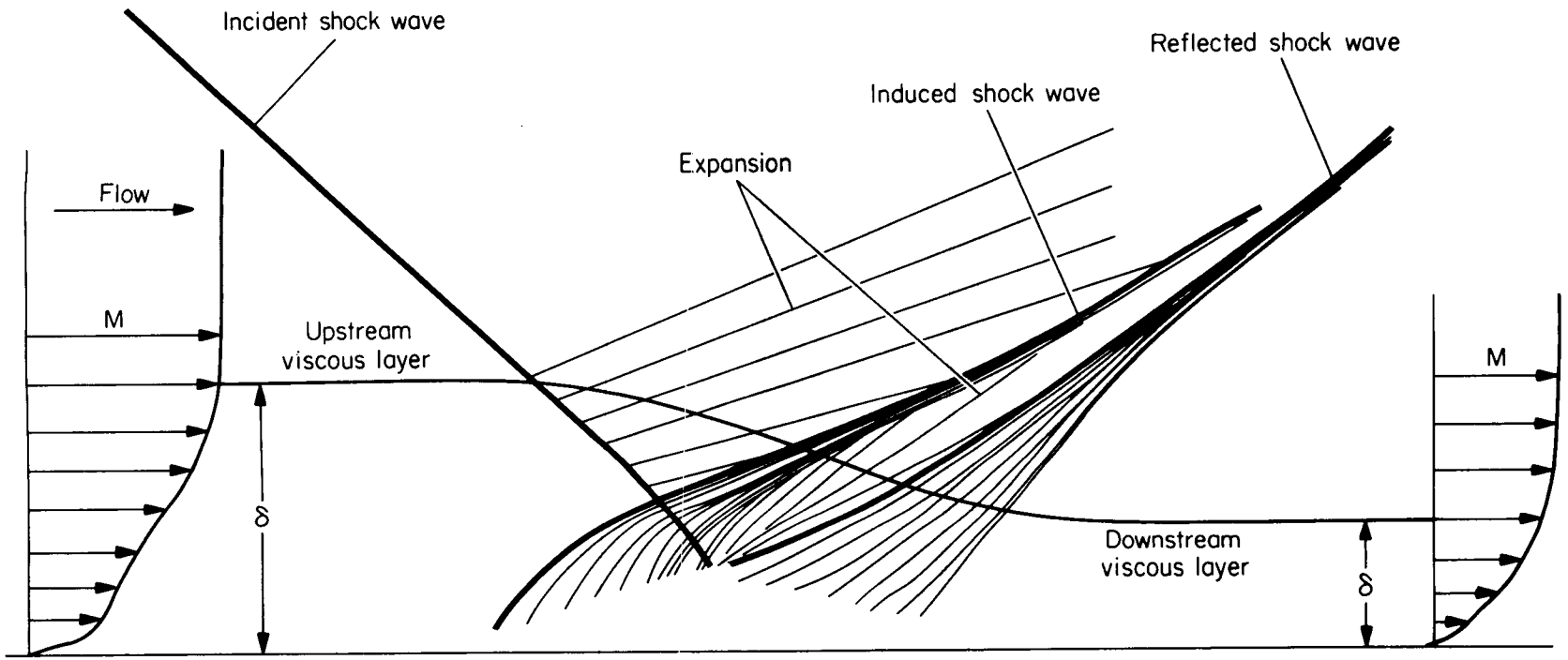

Figure 1.- Schematic of shock-wave - boundary-layer interaction region.

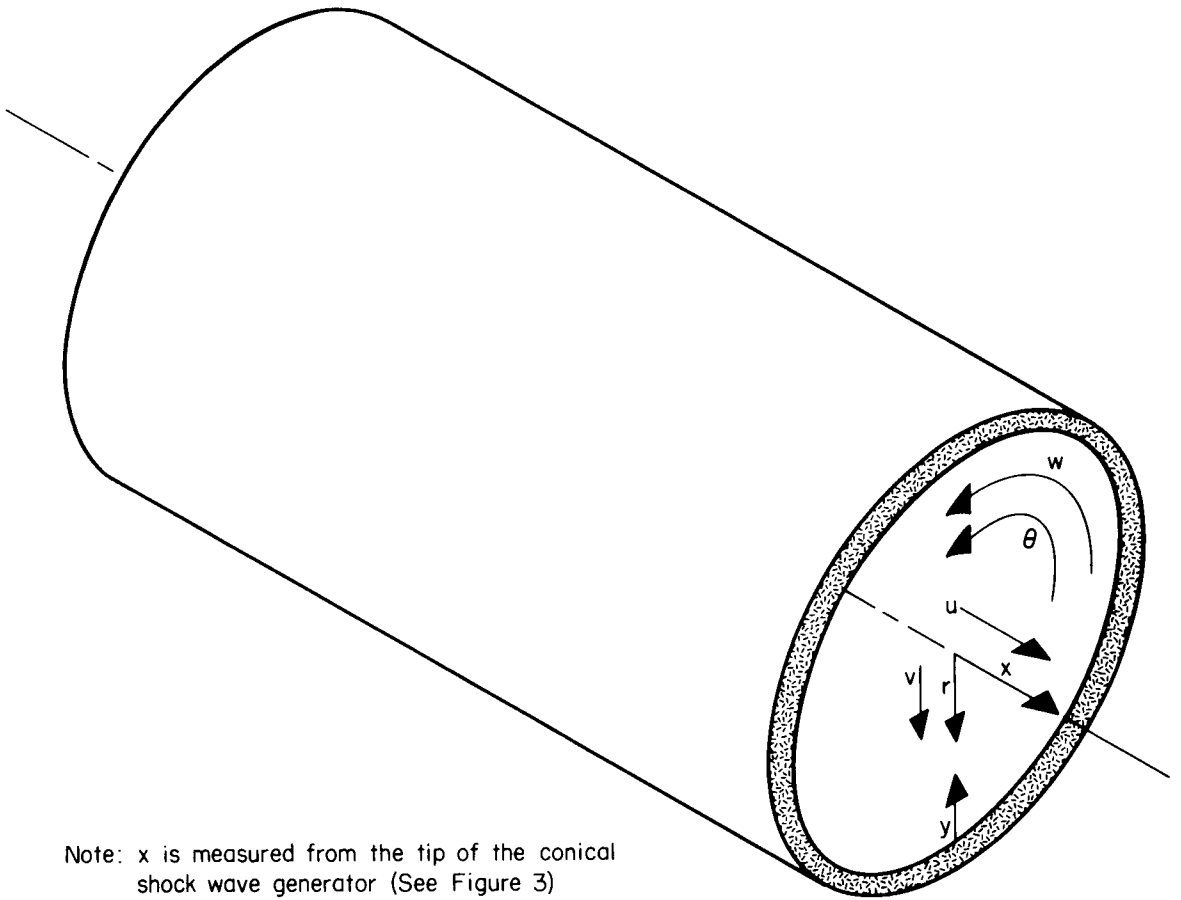

Note: x is measured from the tip of the conical shock wave generator (See Figure 3)

Figure 2.- Nomenclature for coordinates and velocity components.

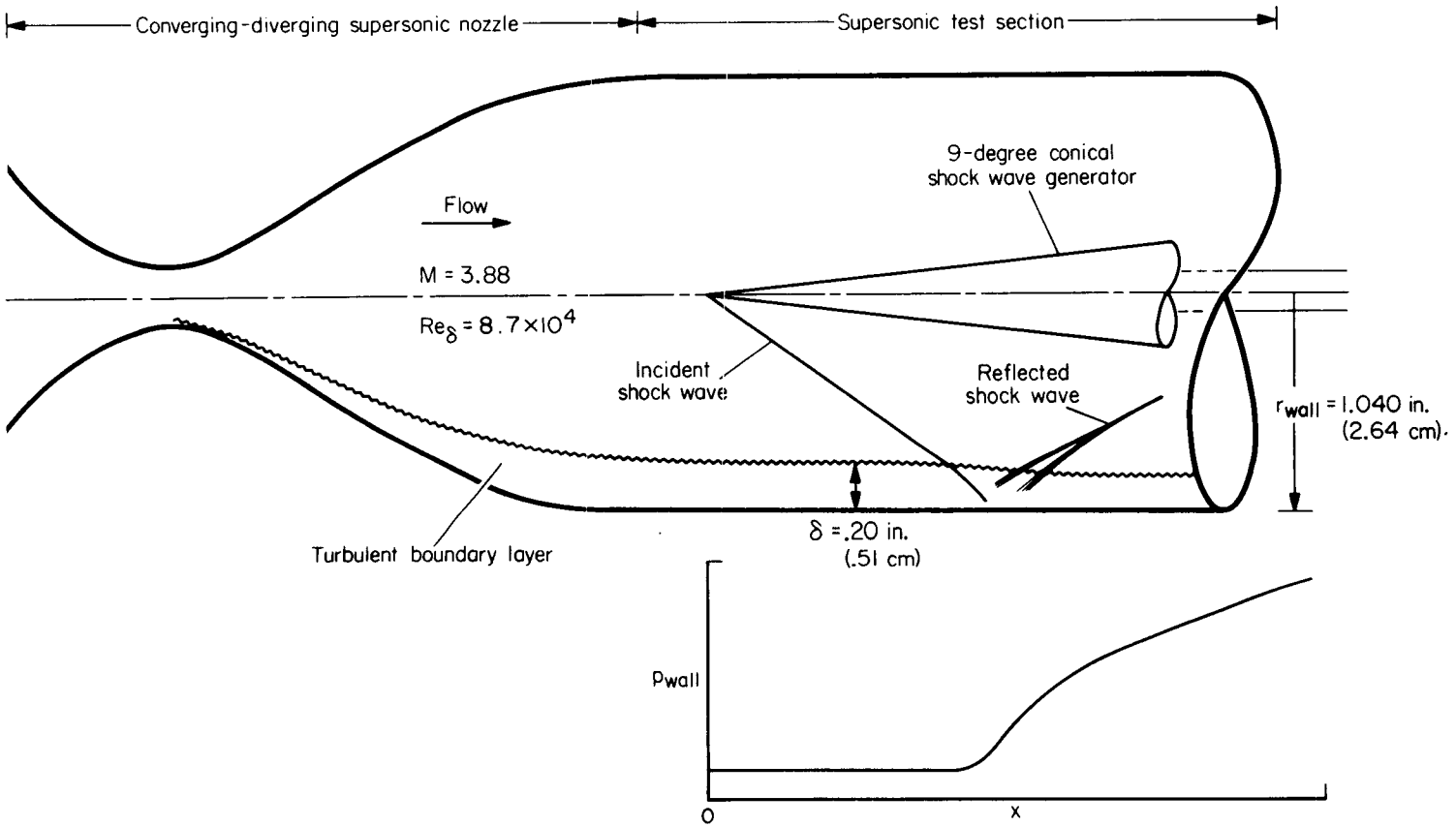

Figure 3.- Schematic of experimental facility.

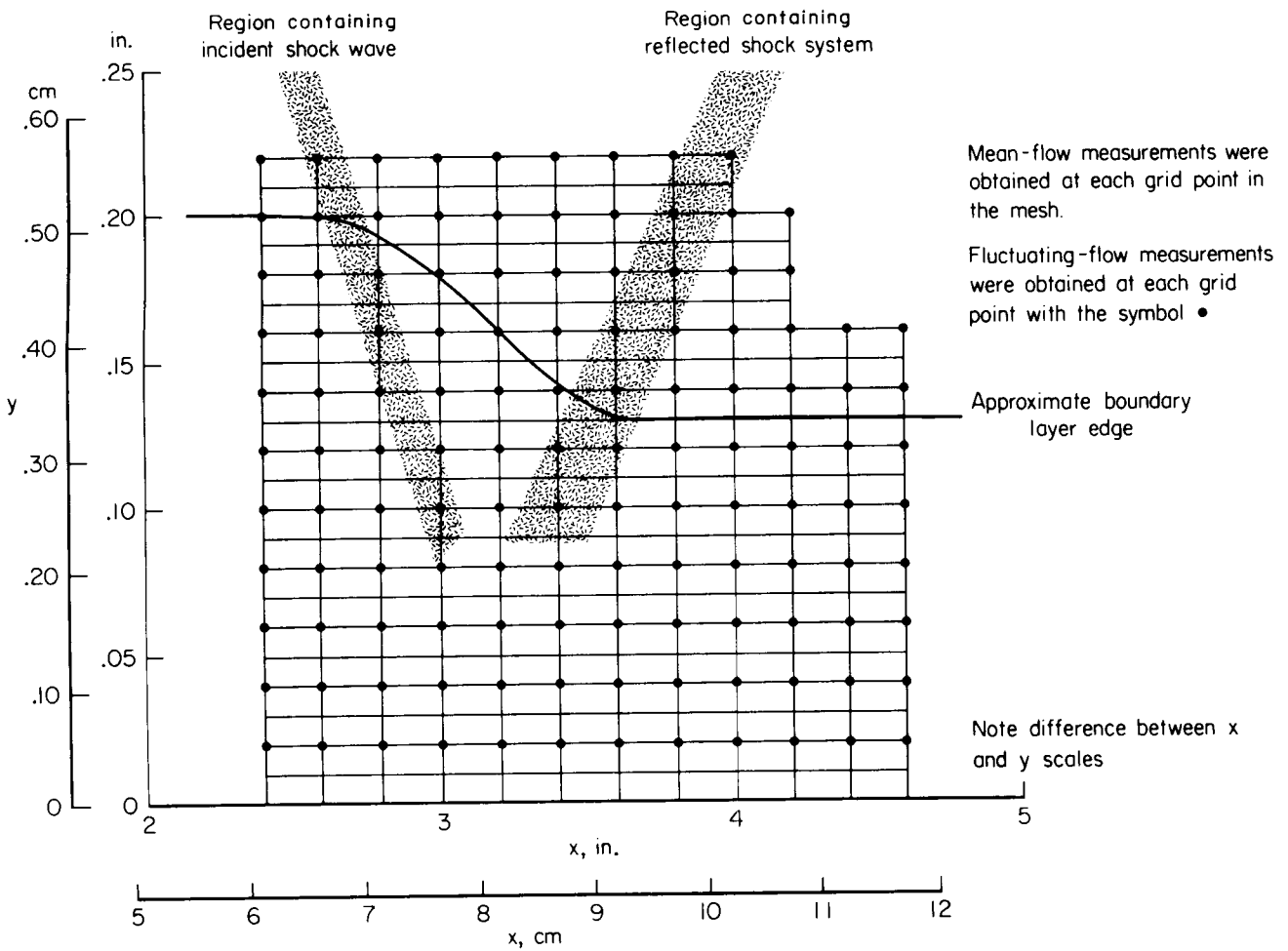

Figure 4.- Location of measuring positions.

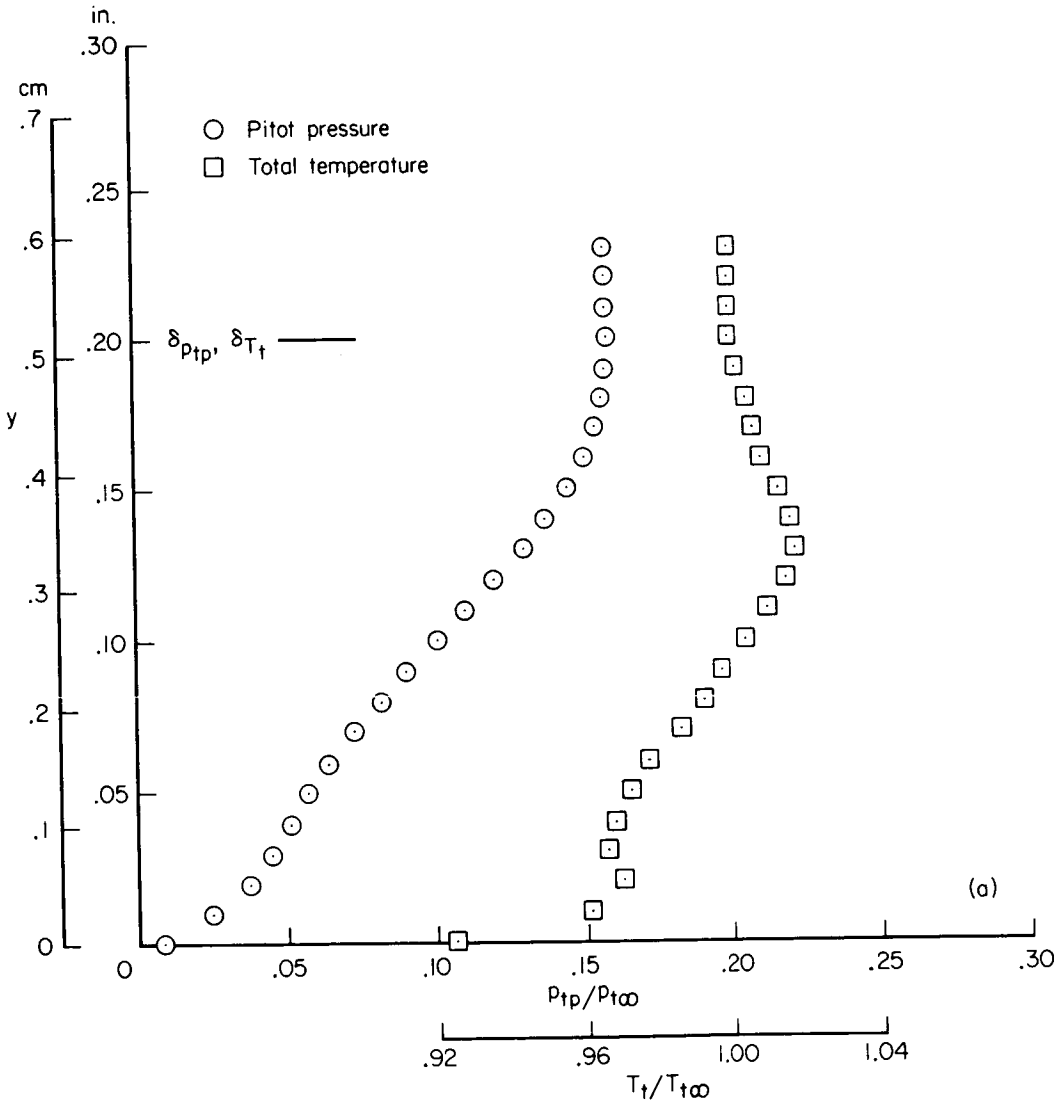

(a) x = 2.40 in. (6.10 cm)

Figure 5.- Pitot pressures and total temperatures; p_{t_∞} = 53.7 psia (3.7×10^5 N/m^2), T_{t_∞} = 540° R (300° K).

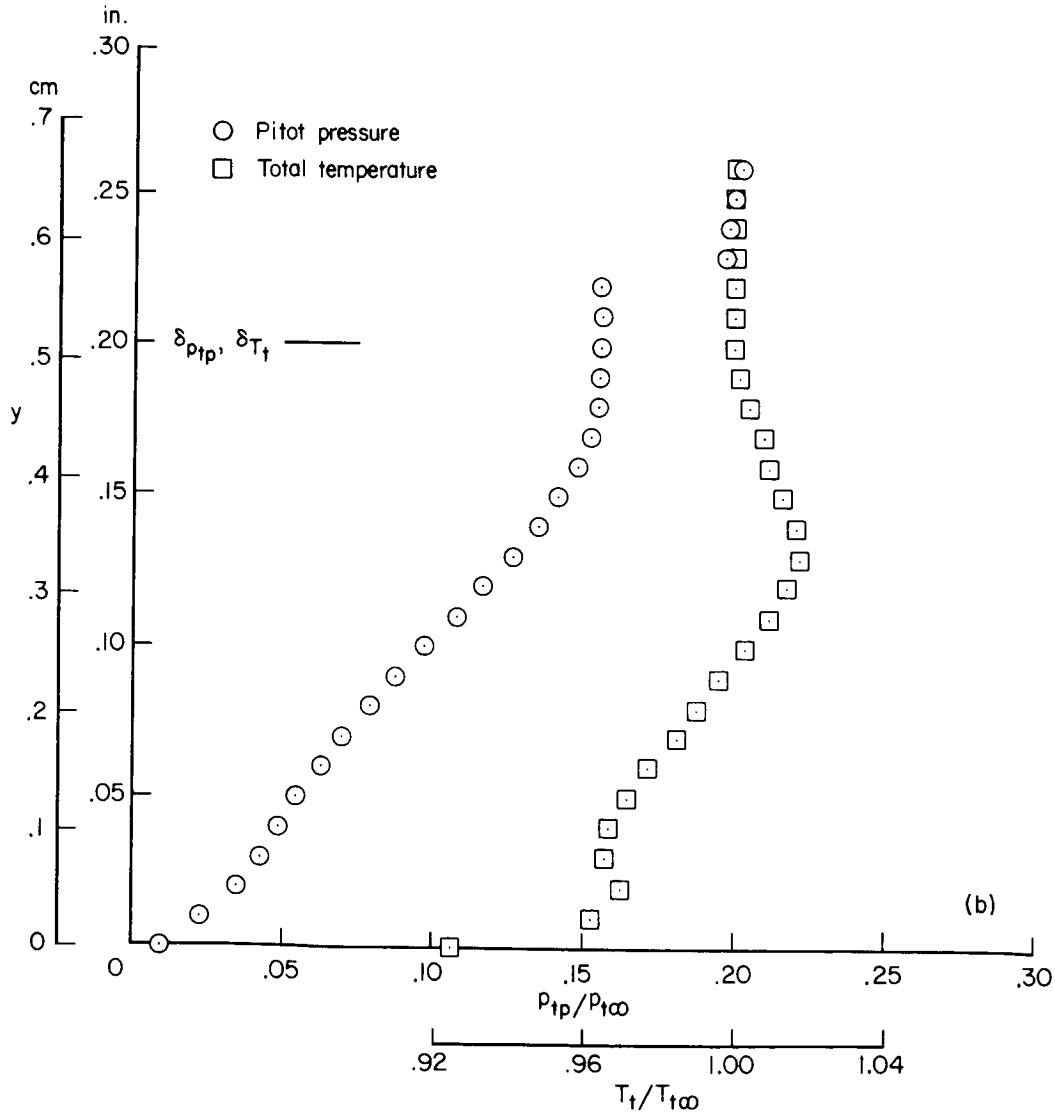

(b) x = 2.60 in. (6.60 cm)

Figure 5.- Continued.

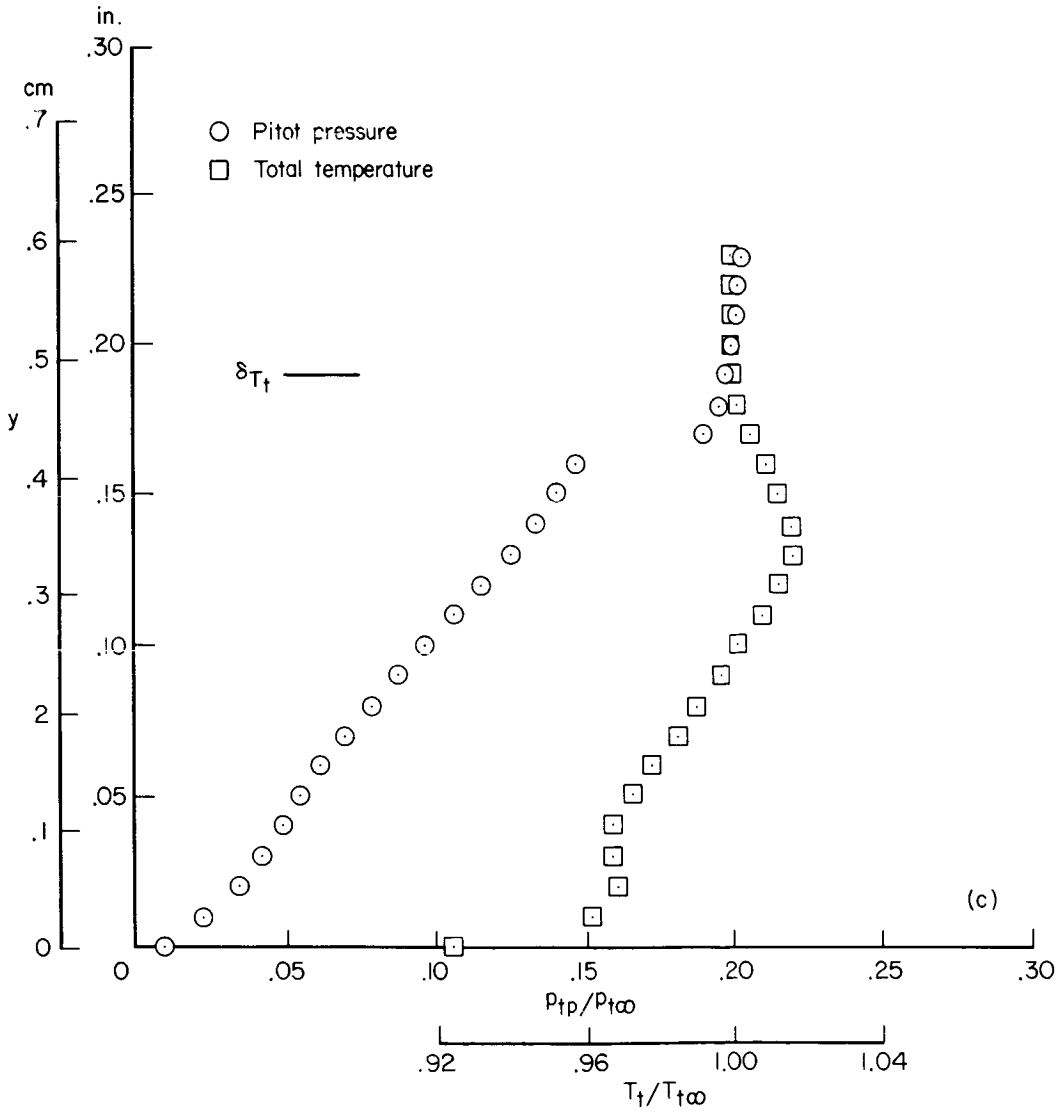

(c) x = 2.80 in. (7.11 cm)

Figure 5.- Continued.

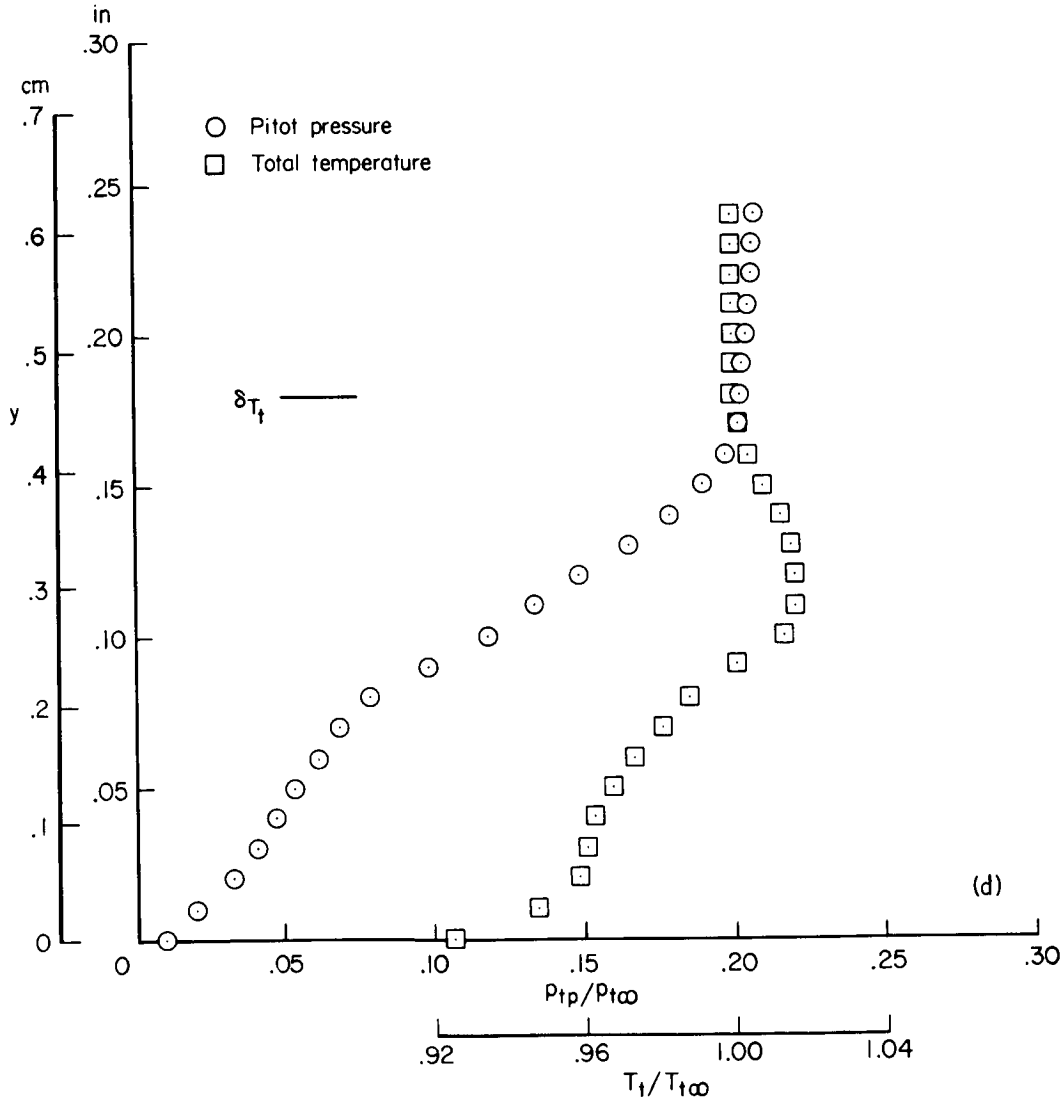

(d) x = 3.00 in. (7.62 cm)

Figure 5.- Continued.

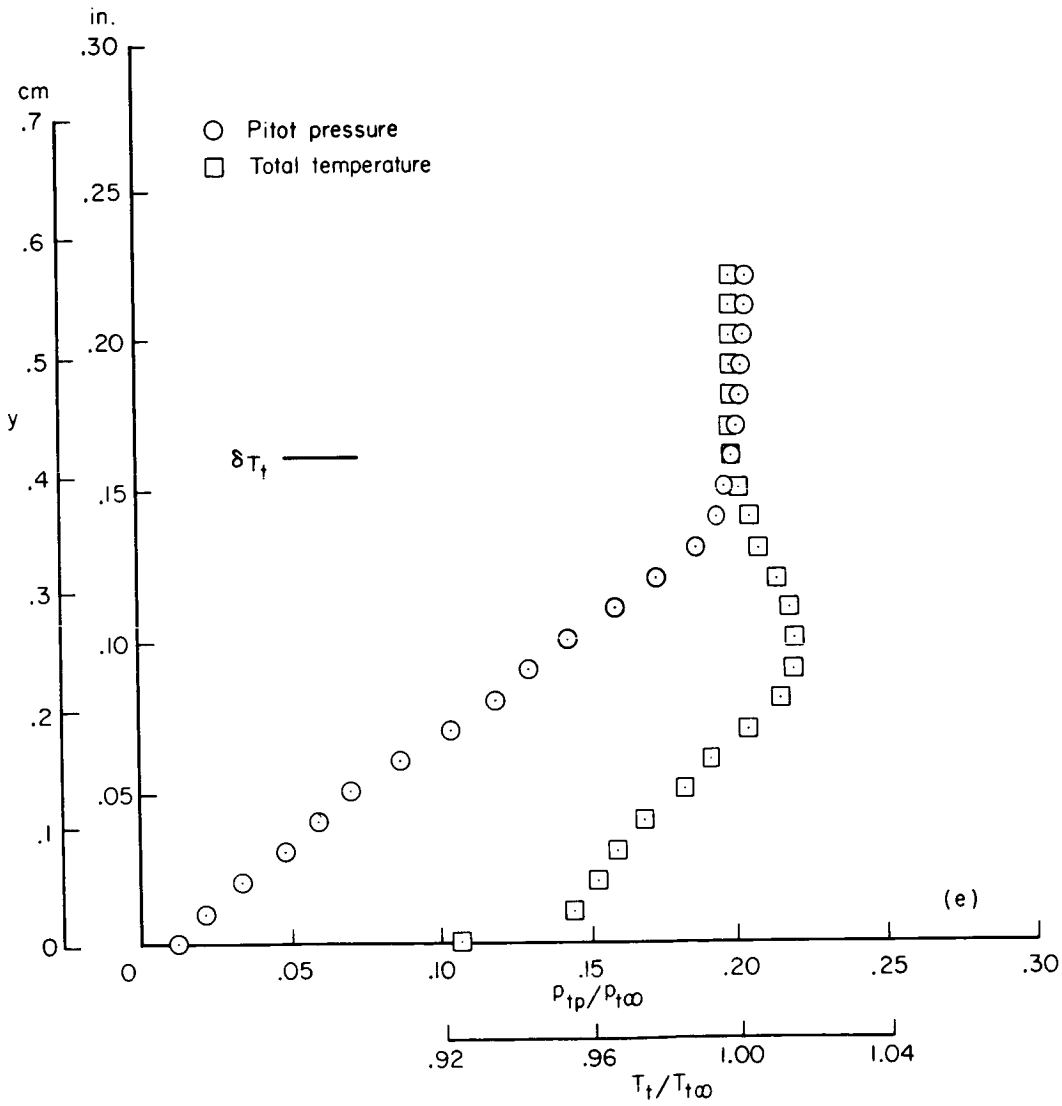

(e) x = 3.20 in. (8.13 cm)

Figure 5.- Continued.

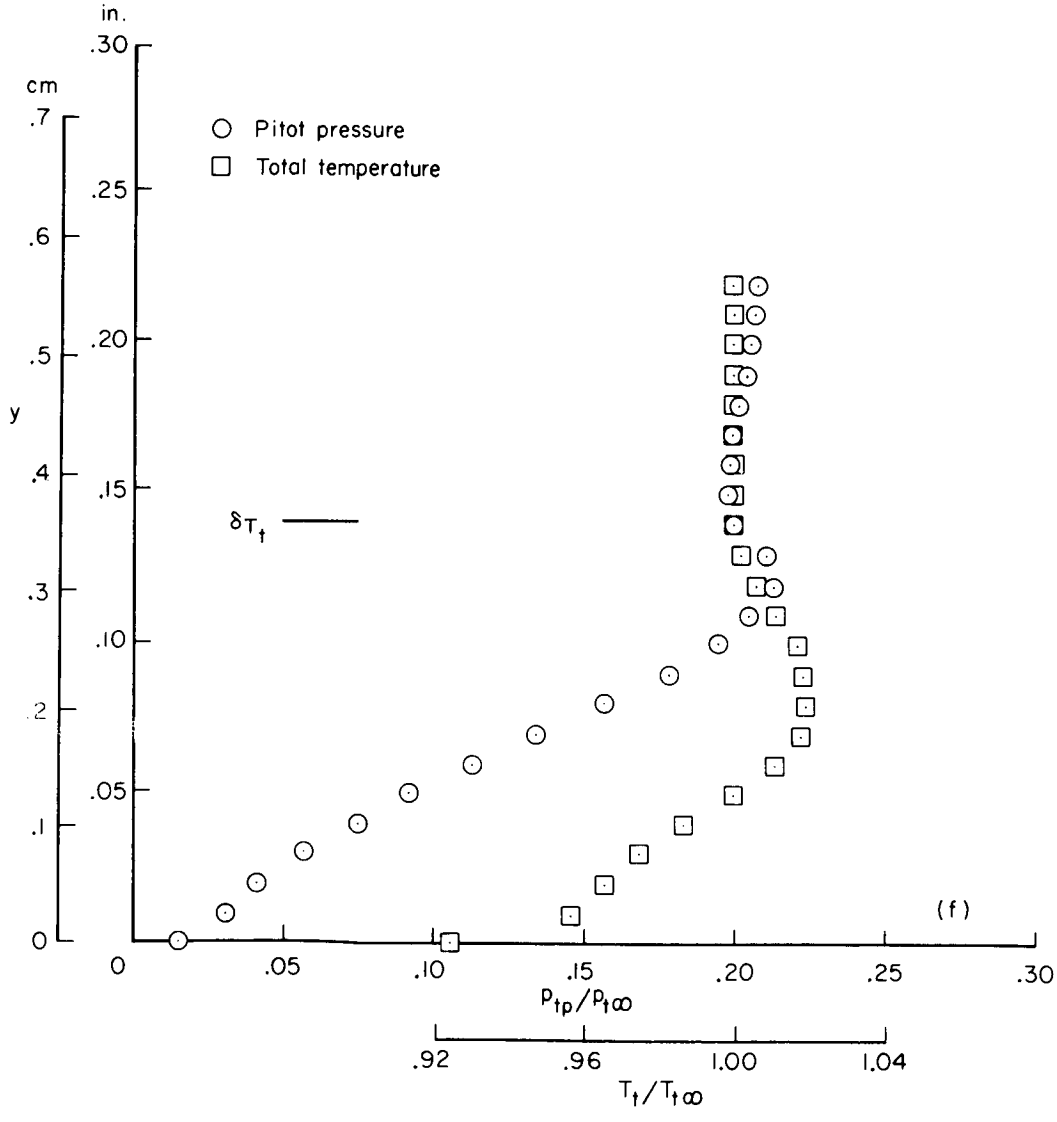

(f) x = 3.40 in. (8.64 cm)

Figure 5.- Continued.

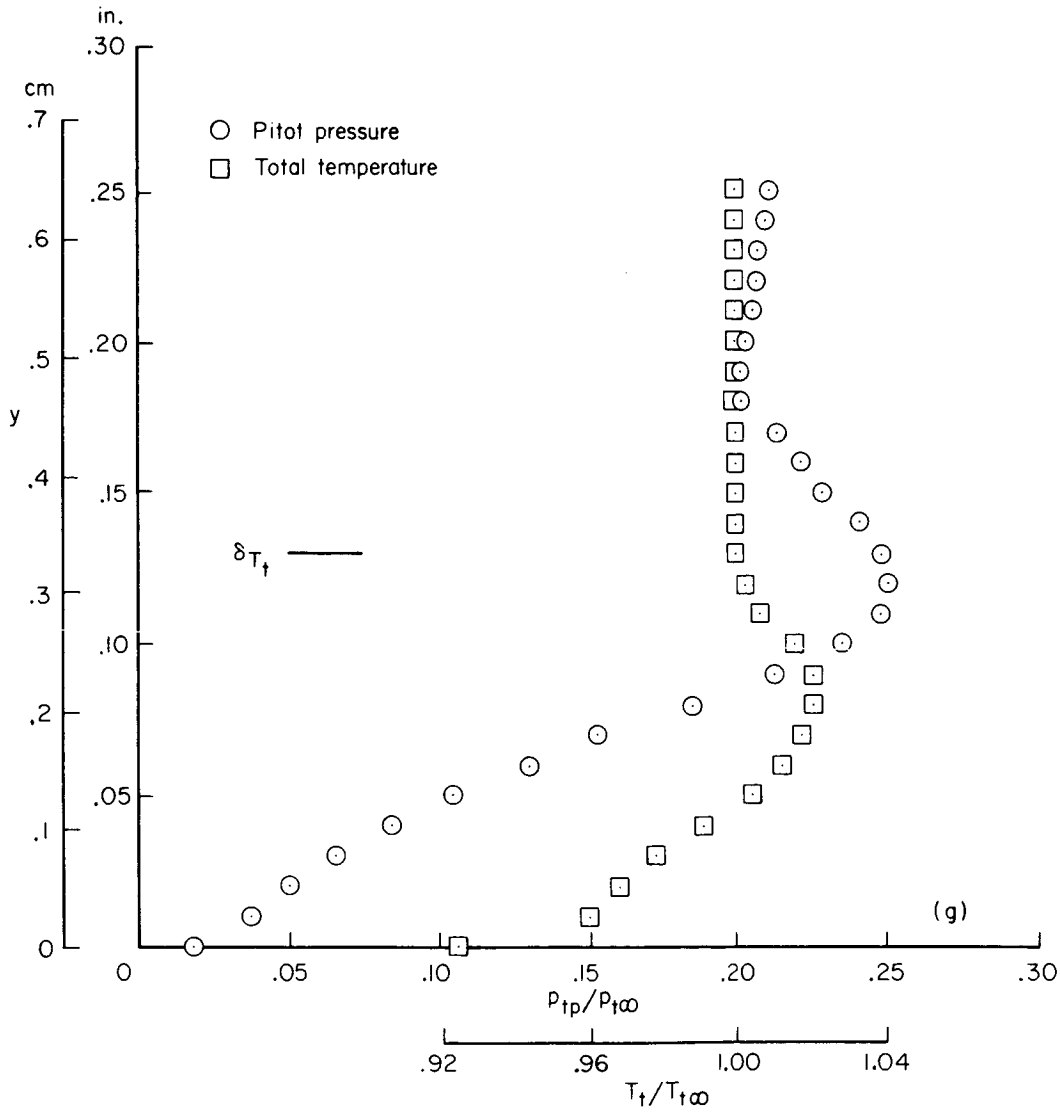

(g) x = 3.60 in. (9.15 cm)

Figure 5.- Continued.

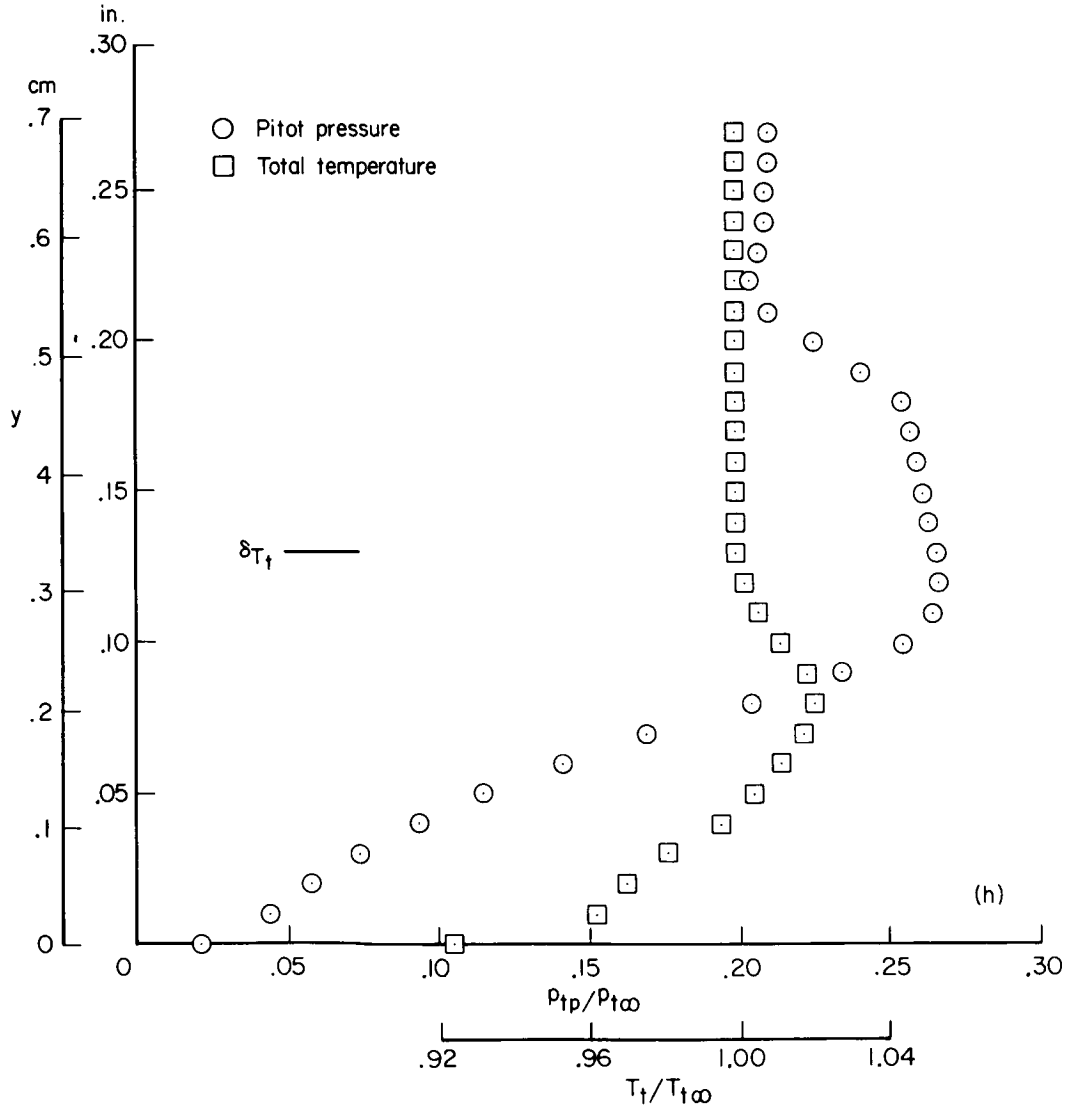

(h) x = 3.80 in. (9.66 cm)

Figure 5.- Continued.

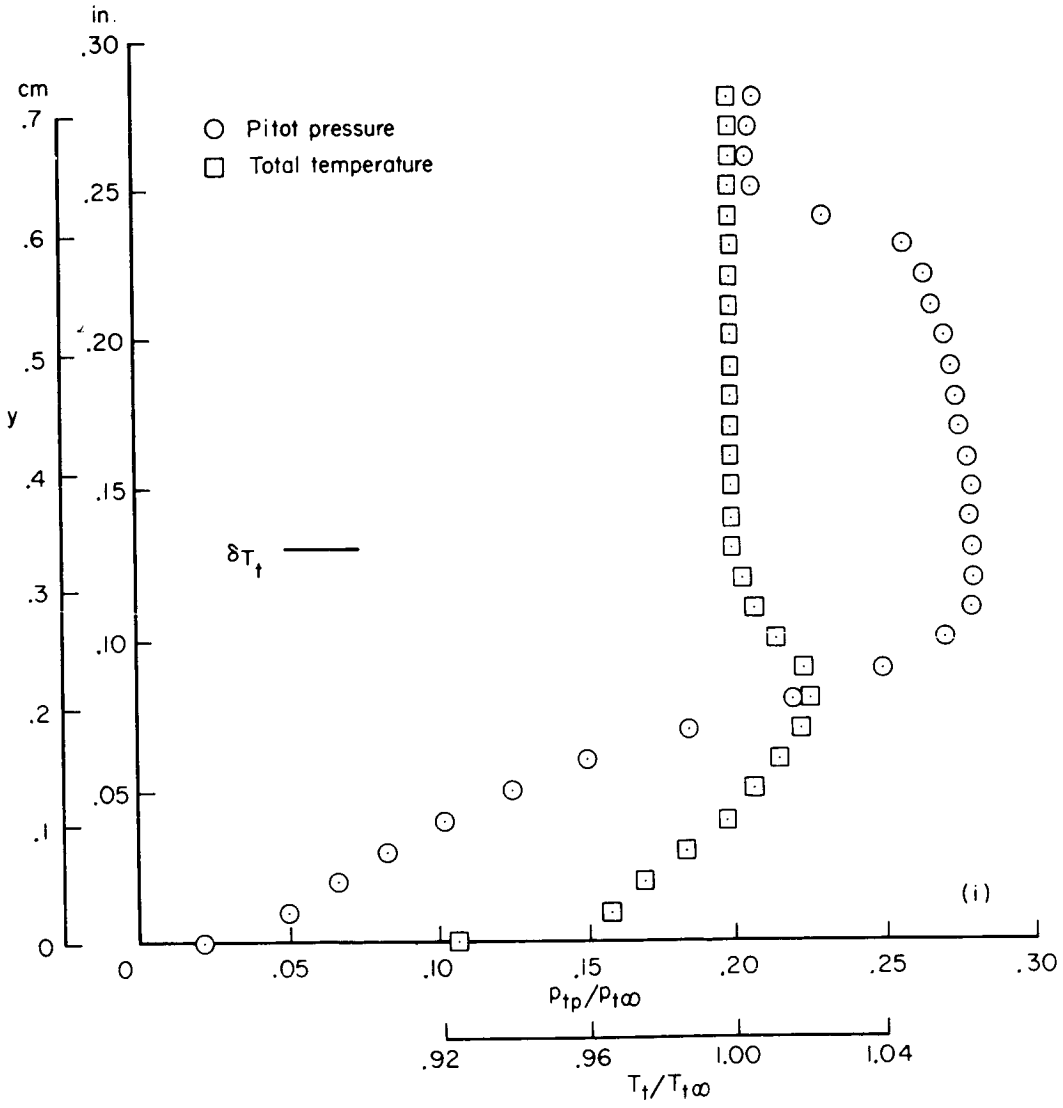

(i) x = 4.00 in. (10.16 cm)

Figure 5.- Continued.

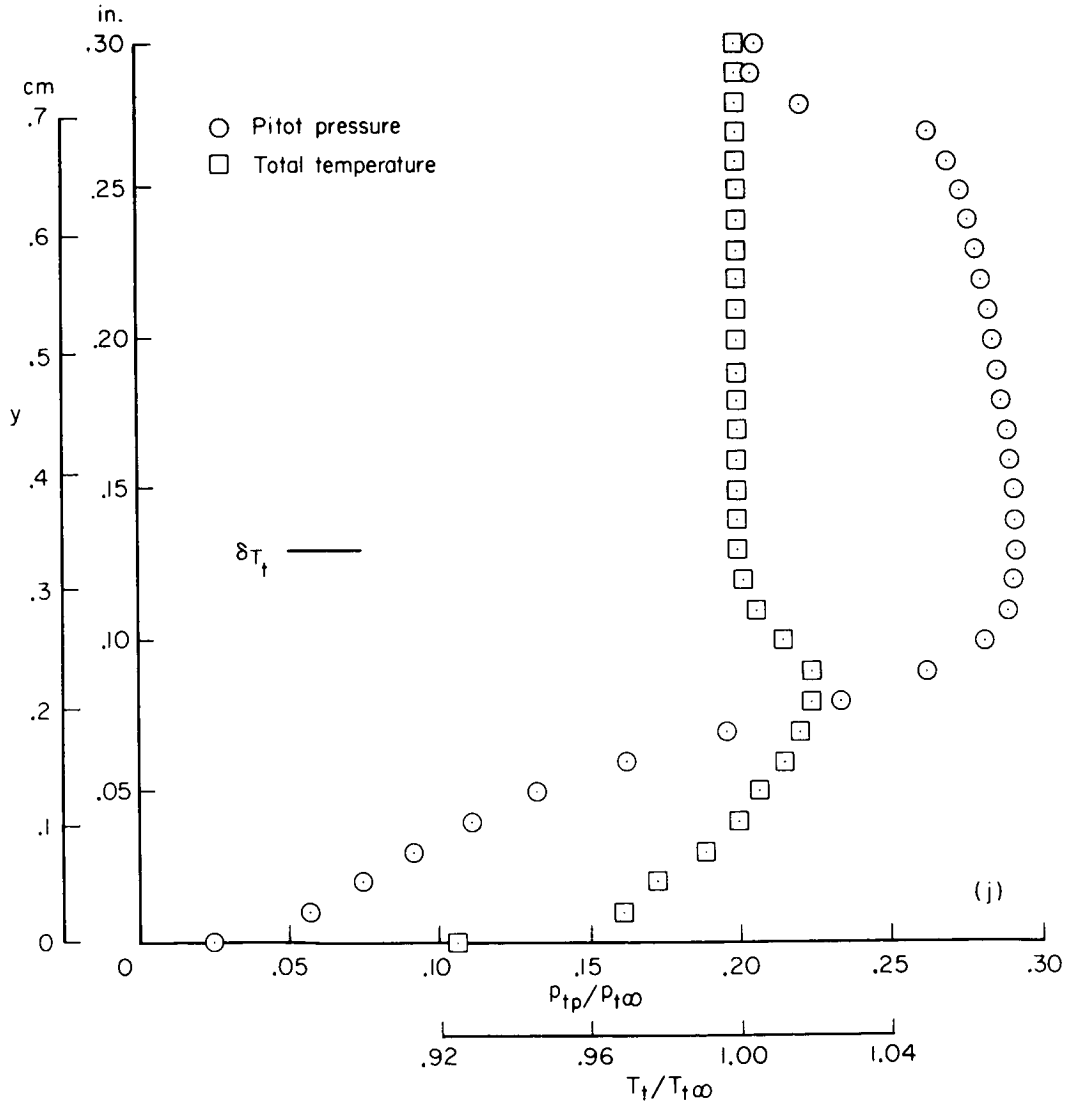

(j) x = 4.20 in. (10.67 cm)

Figure 5.- Continued.

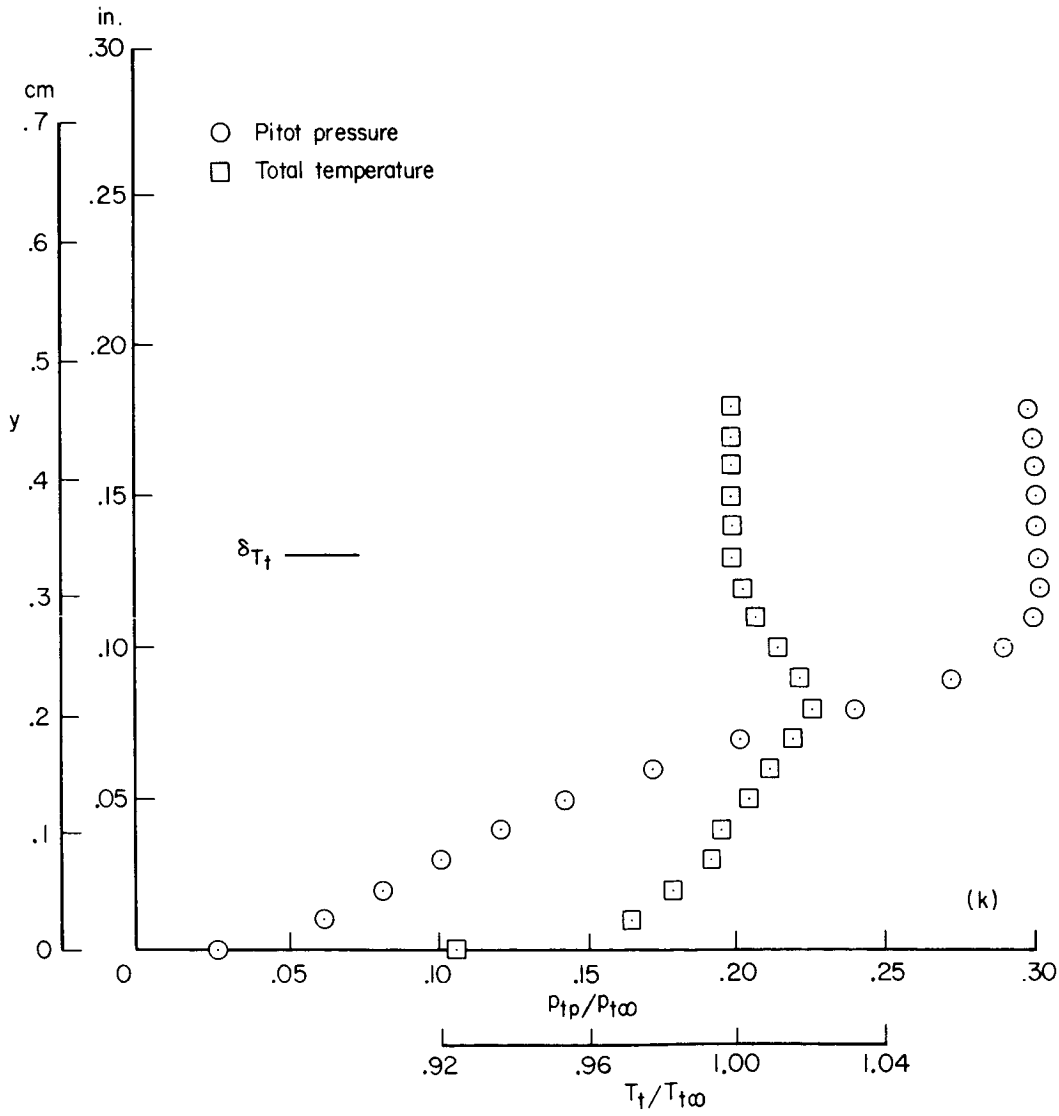

(k) x = 4.40 in. (11.18 cm)

Figure 5.- Continued.

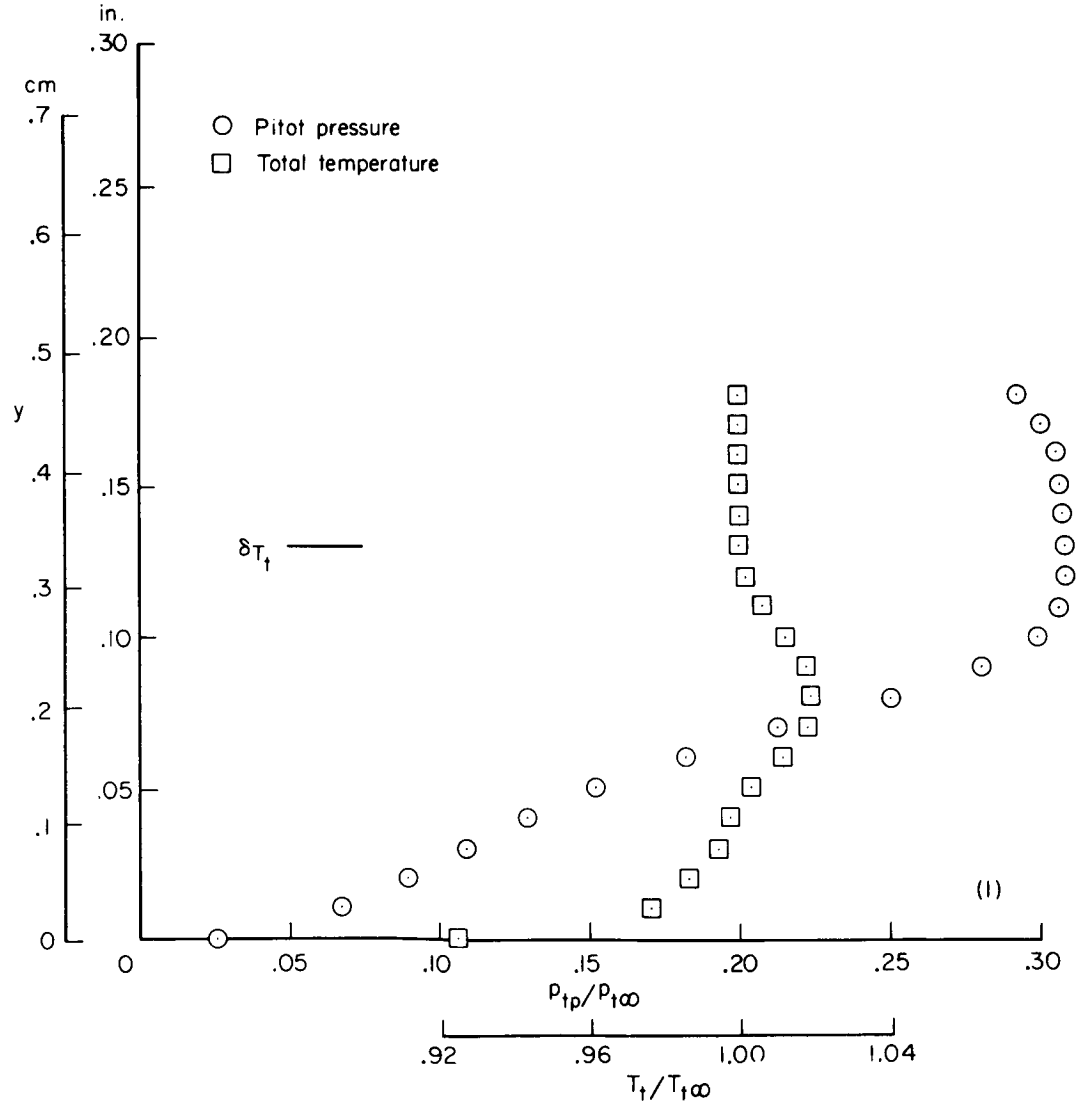

(ℓ) x = 4.60 in. (11.68 cm)

Figure 5.- Concluded.

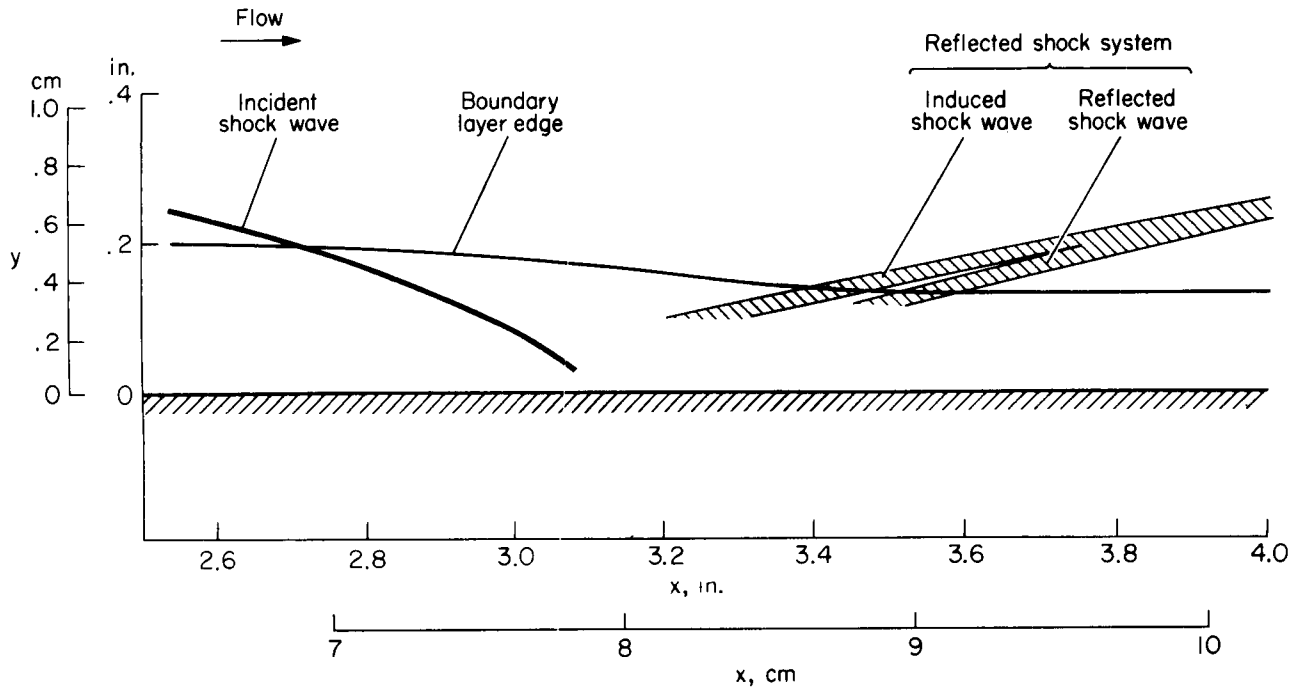

Figure 6.- Experimentally deduced flow field.

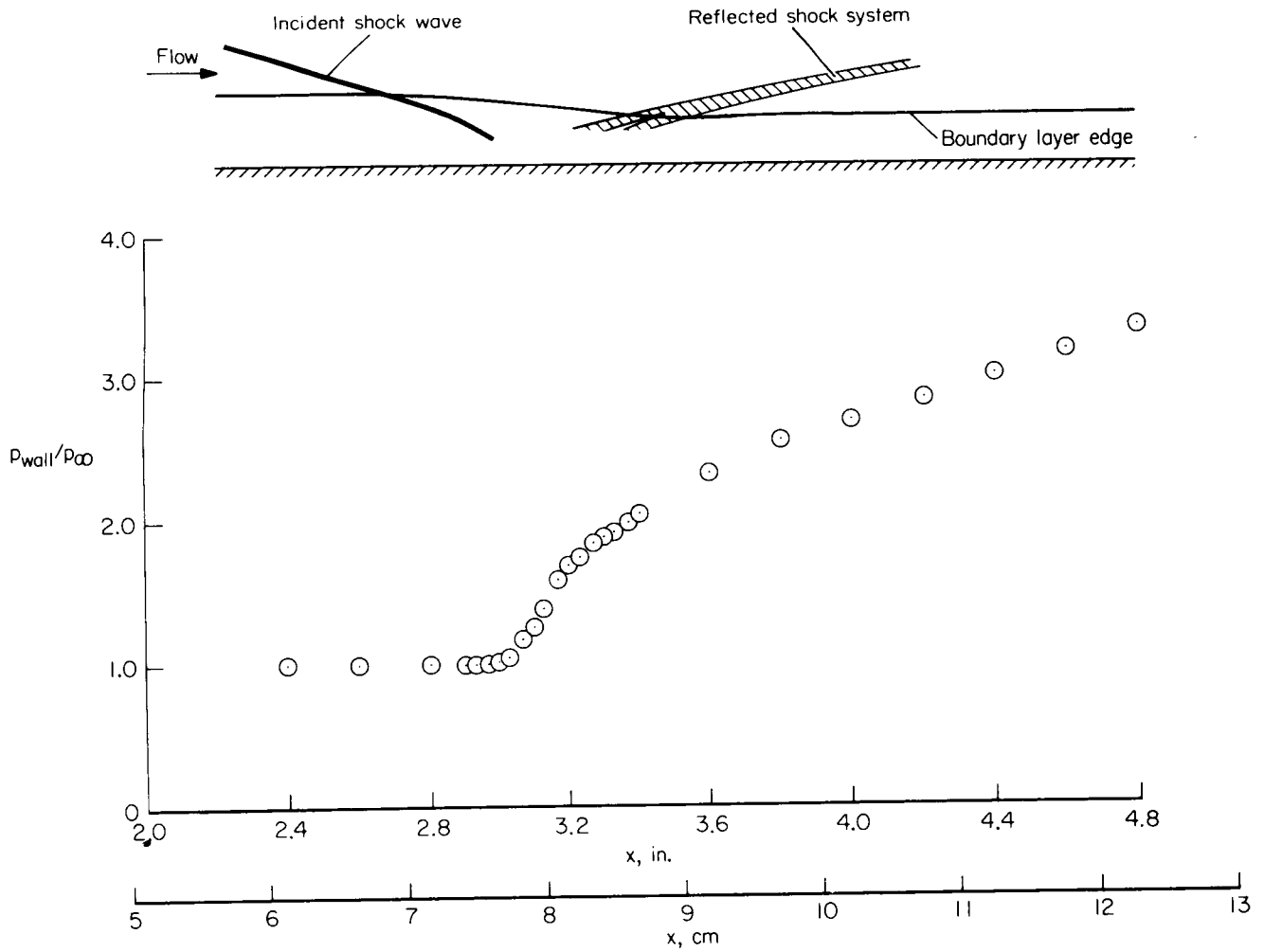

Figure 7.- Surface static pressures.

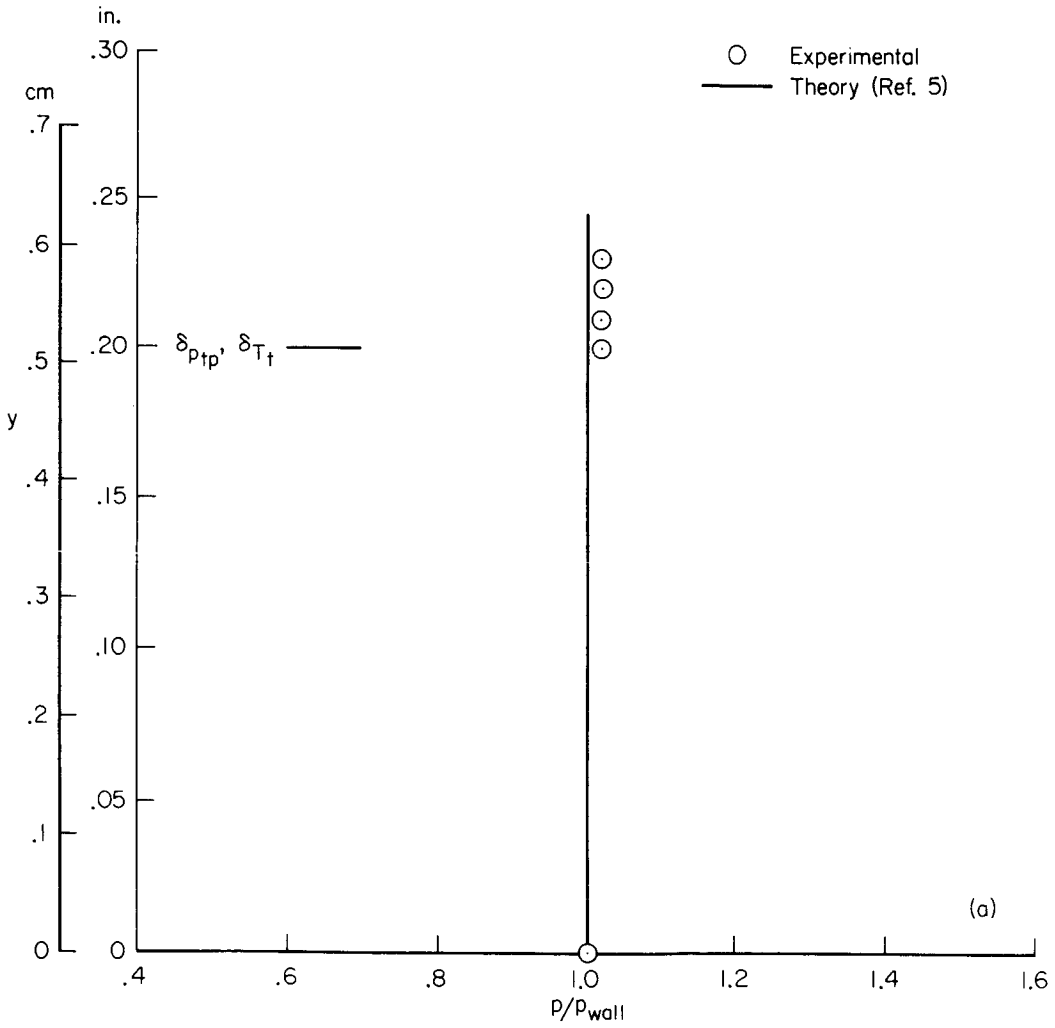

(a) x = 2.40 in. (6.10 cm), p_{wall}/p_∞ = 1.00

Figure 8.- Experimental and theoretical static pressures; p_∞ = 0.42 psia (2.9×10^3 N/m^2).

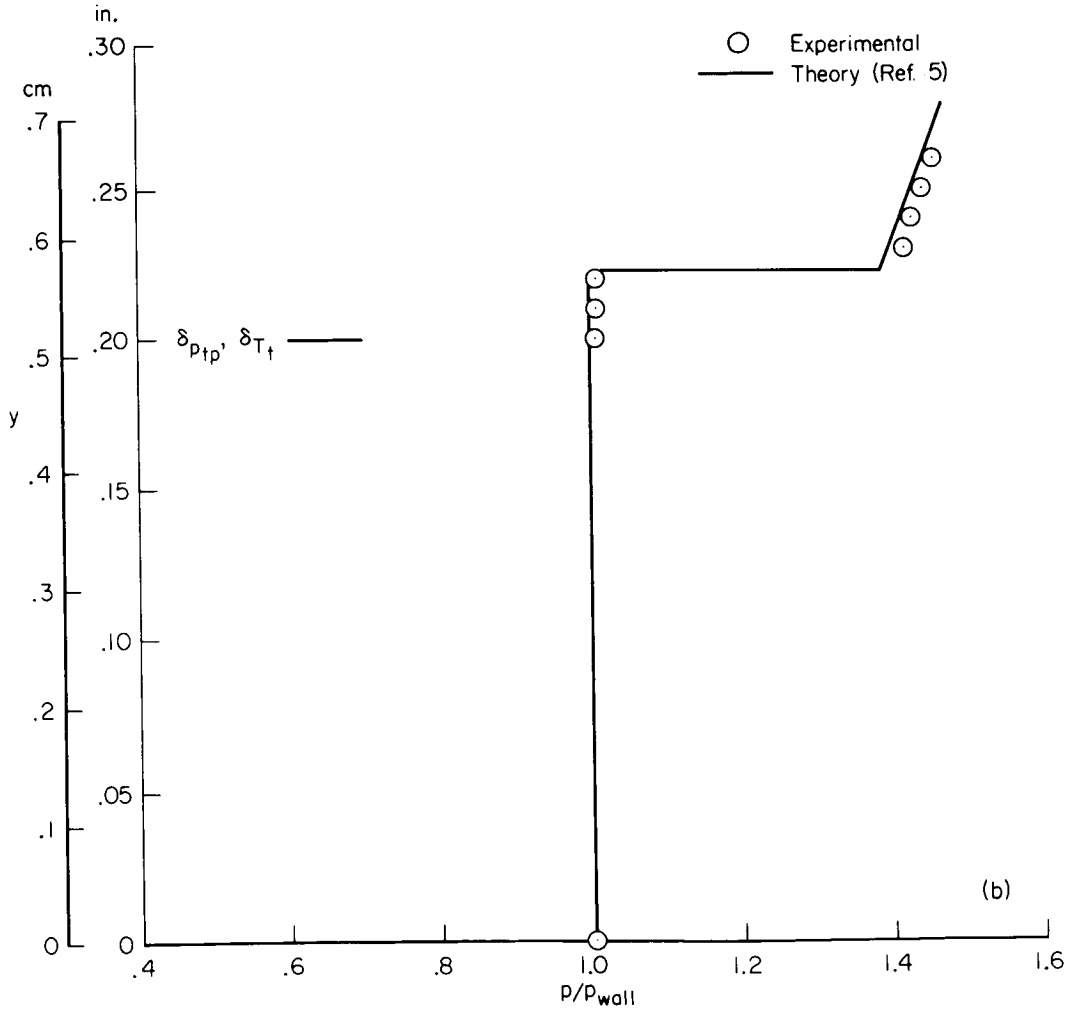

(b) x = 2.60 in. (6.60 cm), p_{wall}/p_{∞} = 1.00

Figure 8.- Continued.

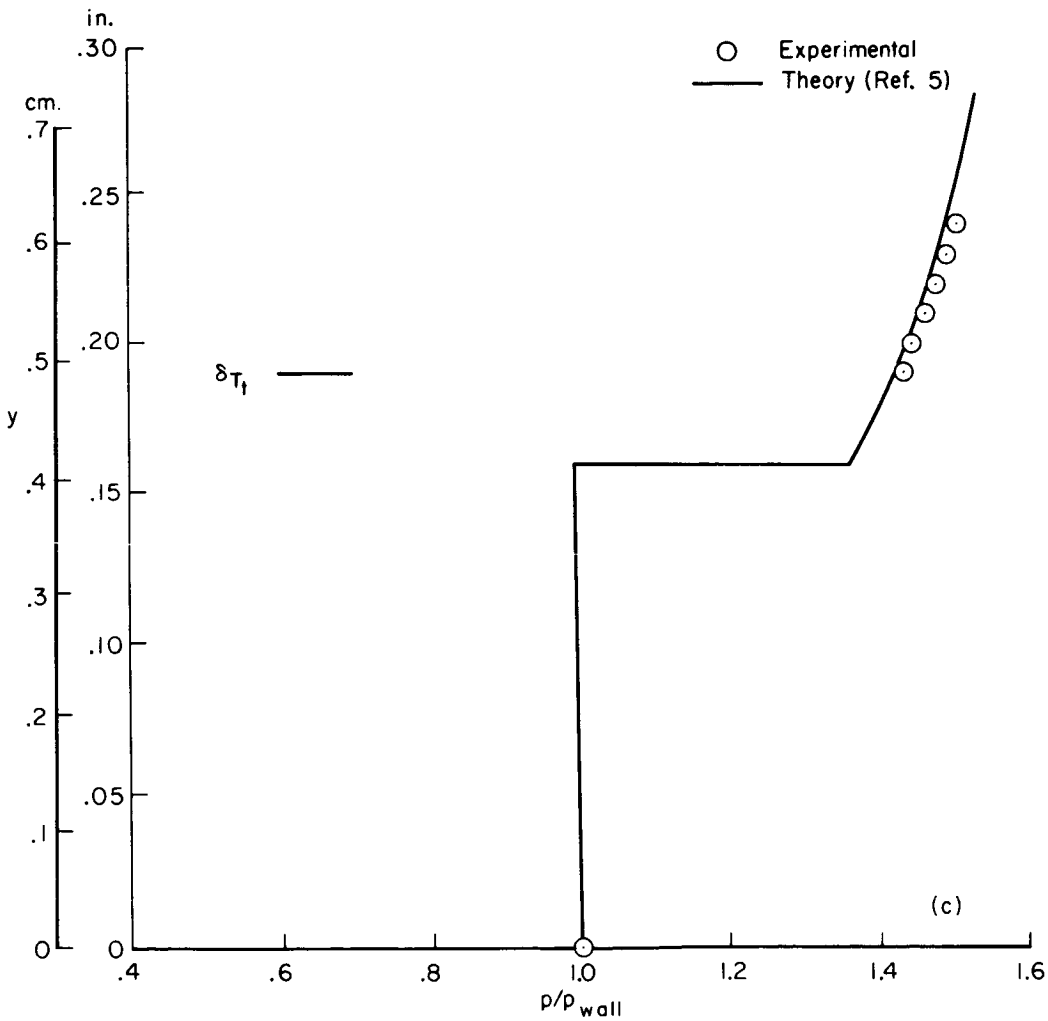

(c) x = 2.80 in. (7.11 cm), p_{wall}/p_{∞} = 1.00

Figure 8.- Continued.

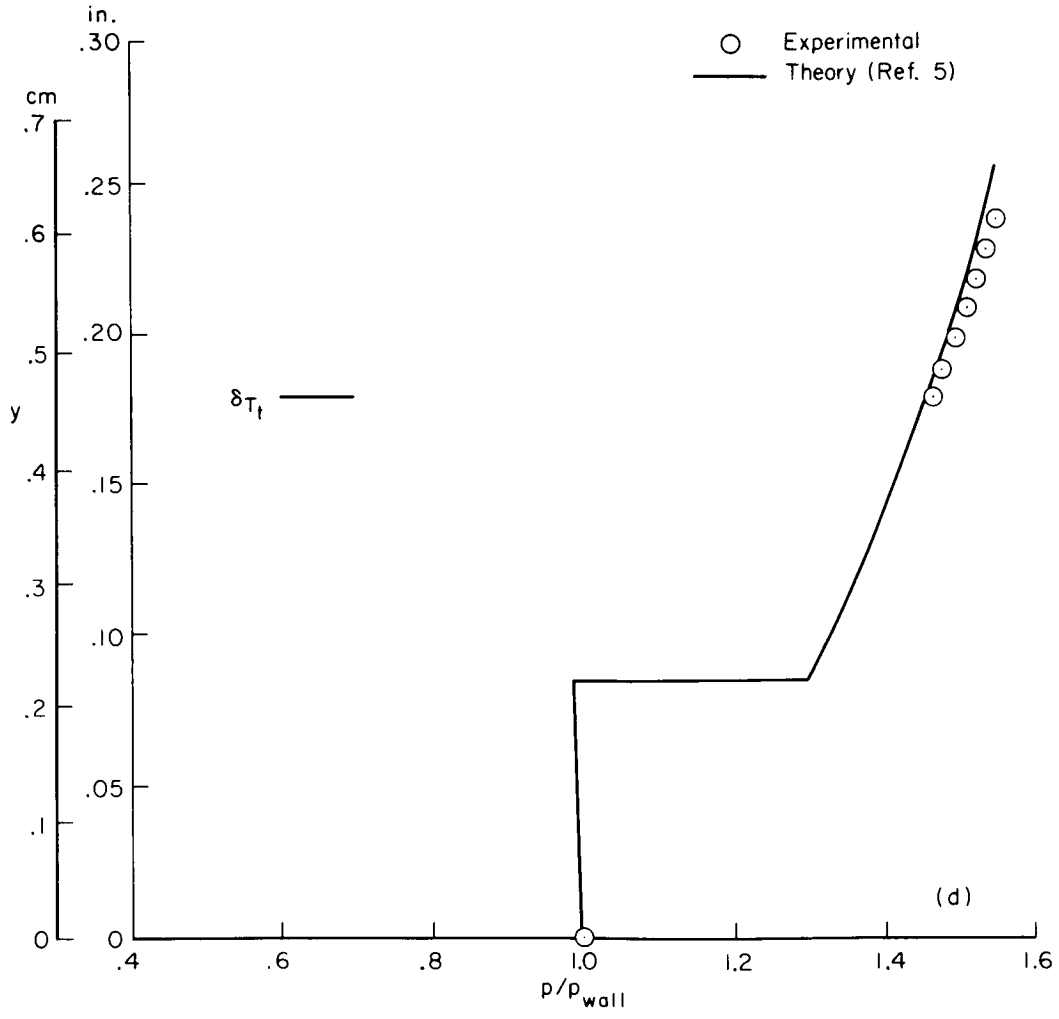

(d) x = 3.00 in. (7.62 cm), $p_{wall}/p_\infty = 1.02$

Figure 8.- Continued.

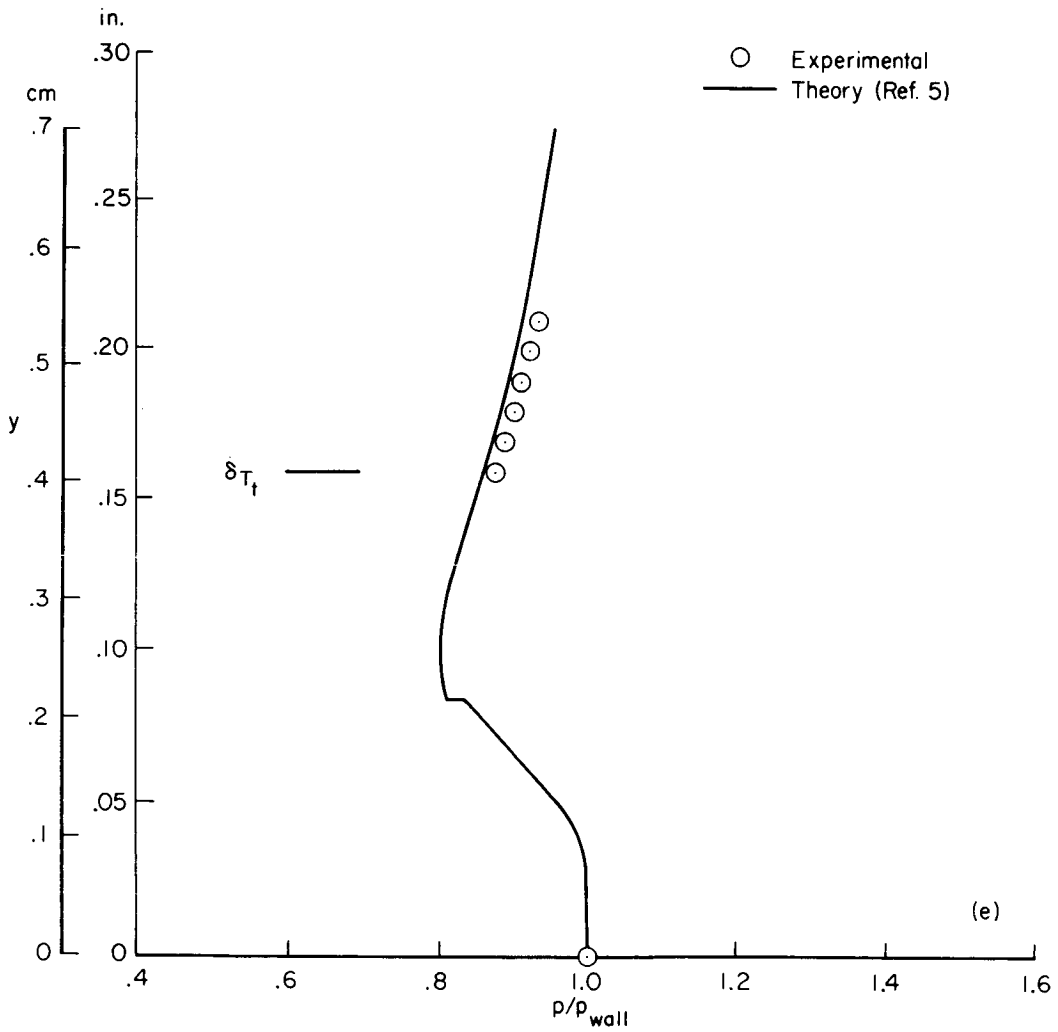

(e) x = 3.20 in. (8.13 cm), p_{wall}/p_{∞} = 1.68

Figure 8.- Continued.

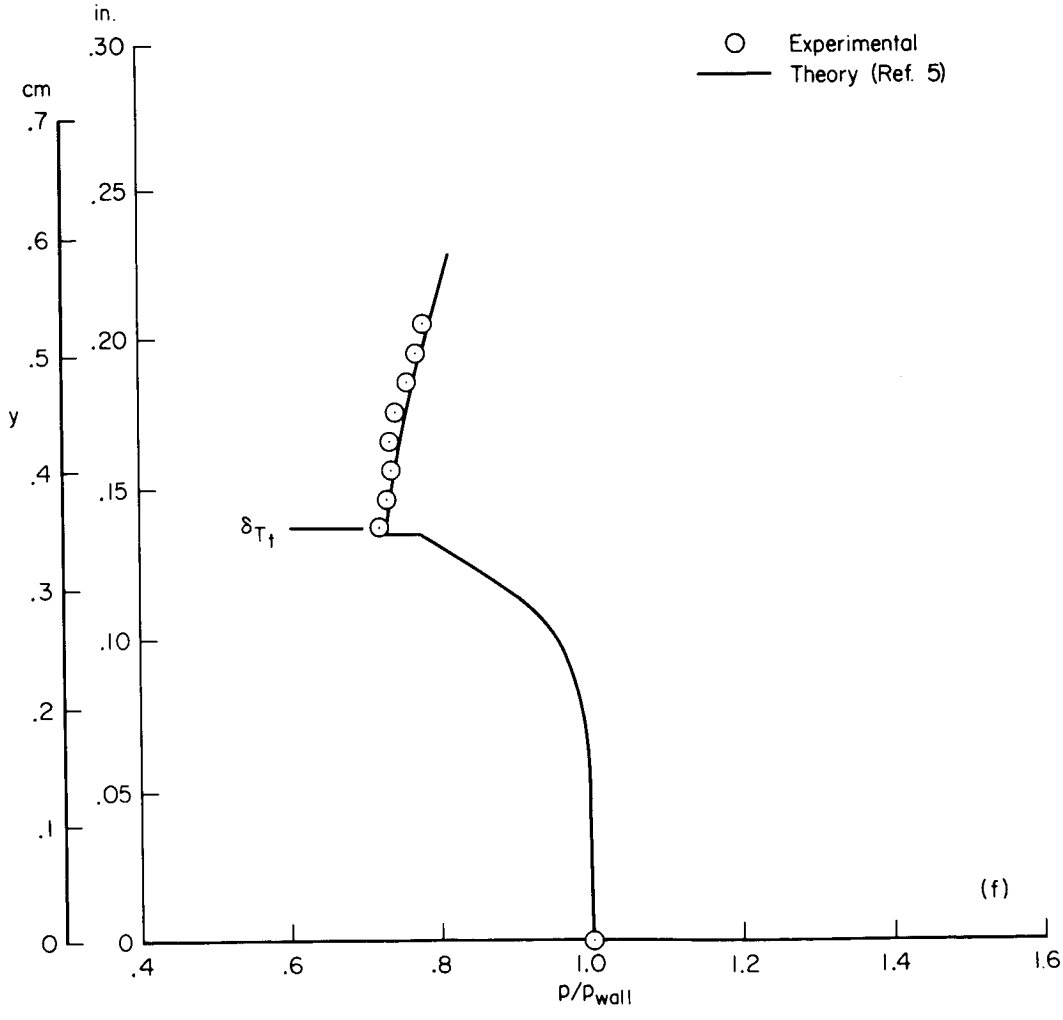

(f) x = 3.40 in. (8.64 cm), p_{wall}/p_{∞} = 2.05

Figure 8.- Continued.

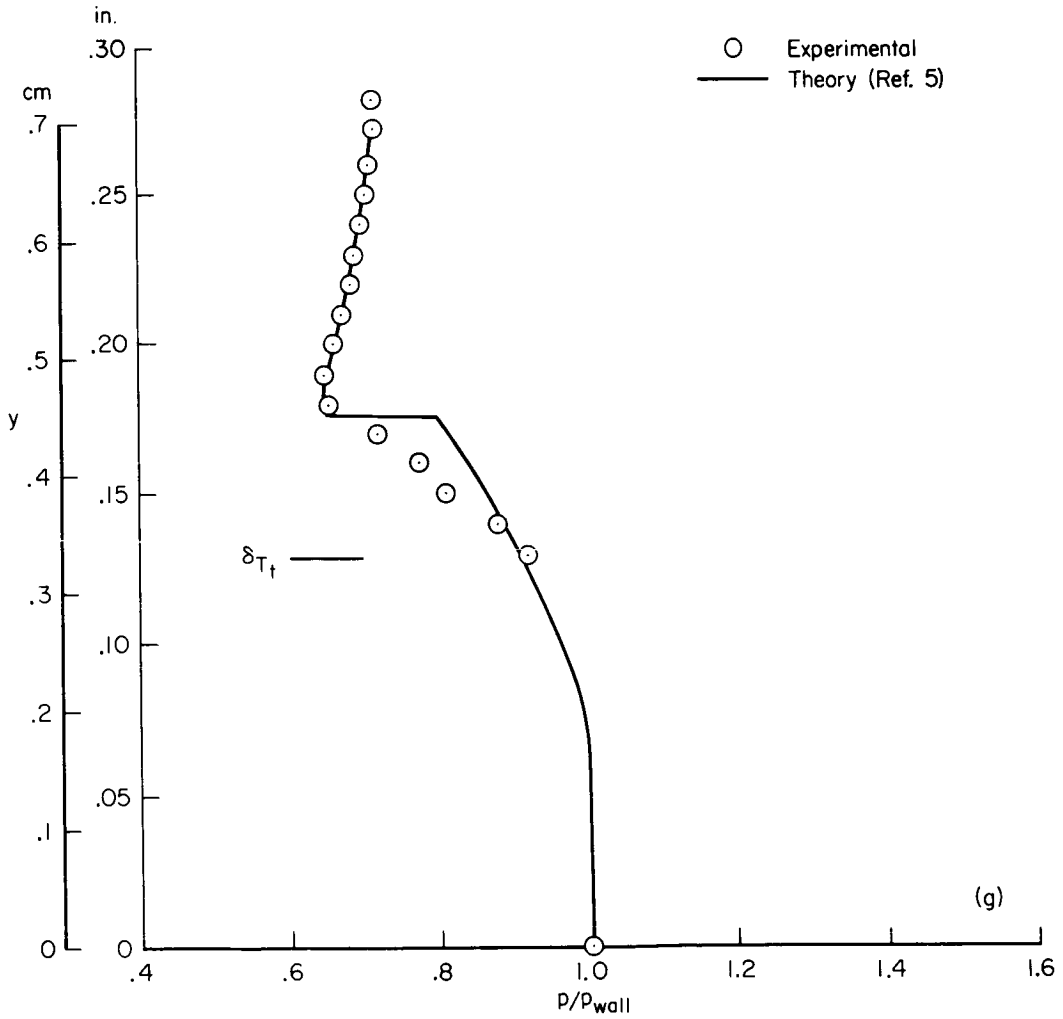

(g) x = 3.60 in. (9.15 cm), p_{wall}/p_{∞} = 2.34

Figure 8.- Continued.

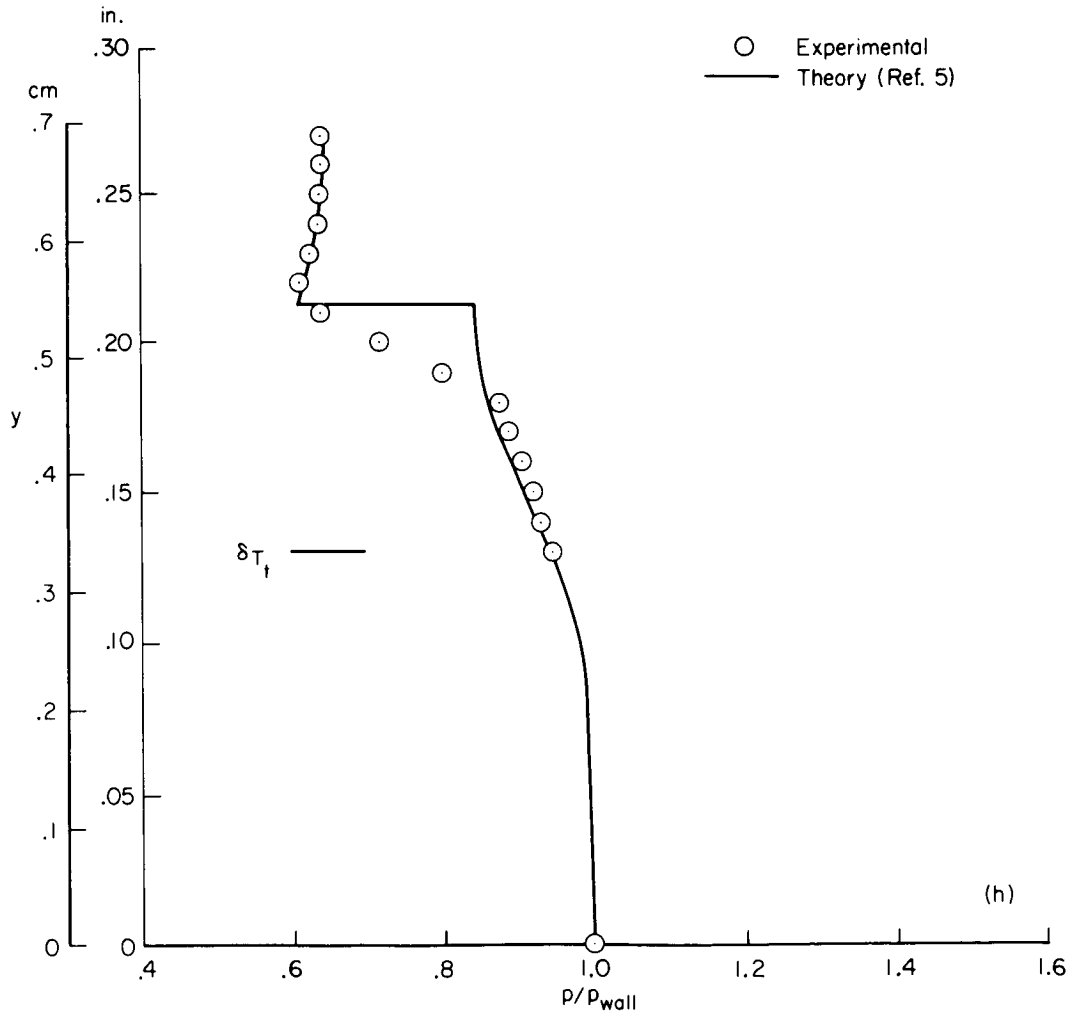

(h) x = 3.80 in. (9.66 cm), p_{wall}/p_{∞} = 2.56

Figure 8.- Continued.

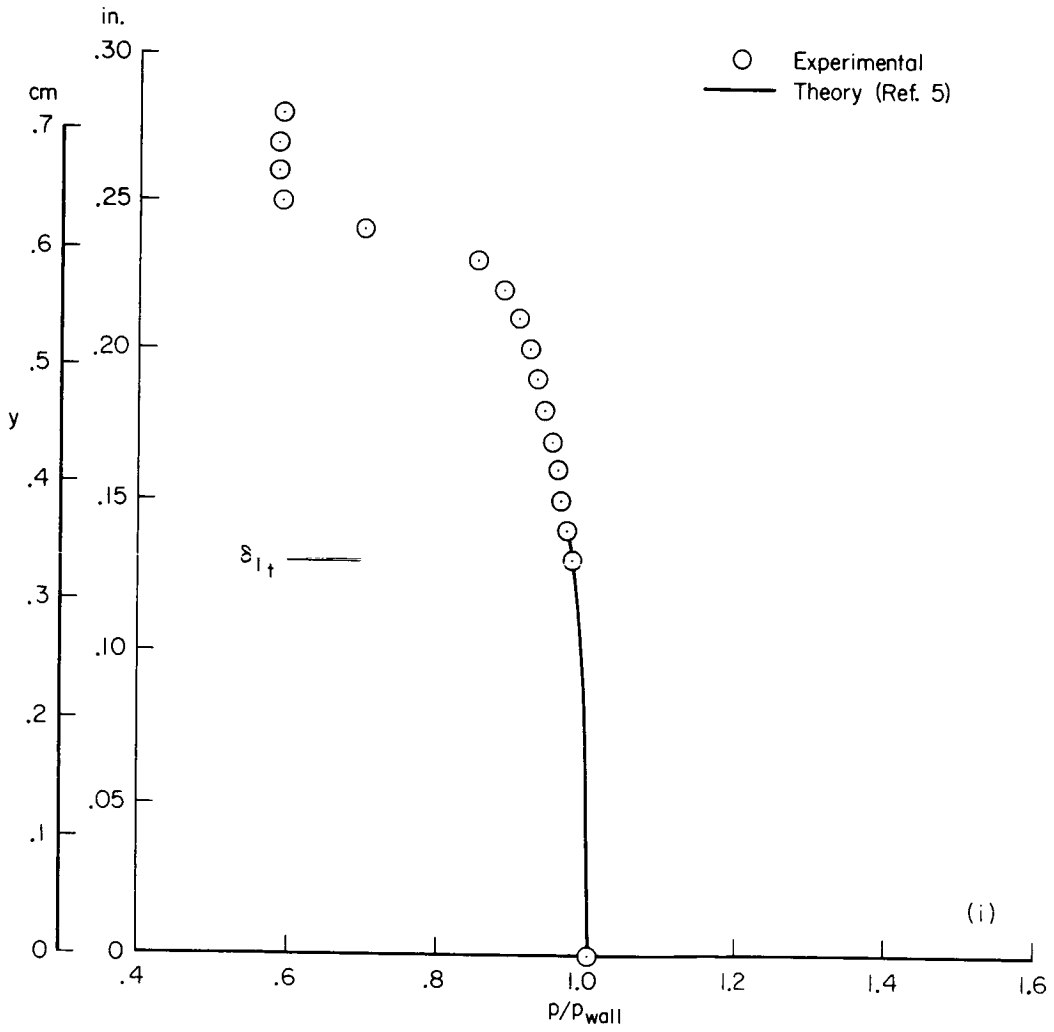

(i) x = 4.00 in. (10.16 cm), p_{wall}/p_∞ = 2.70

Figure 8.- Continued.

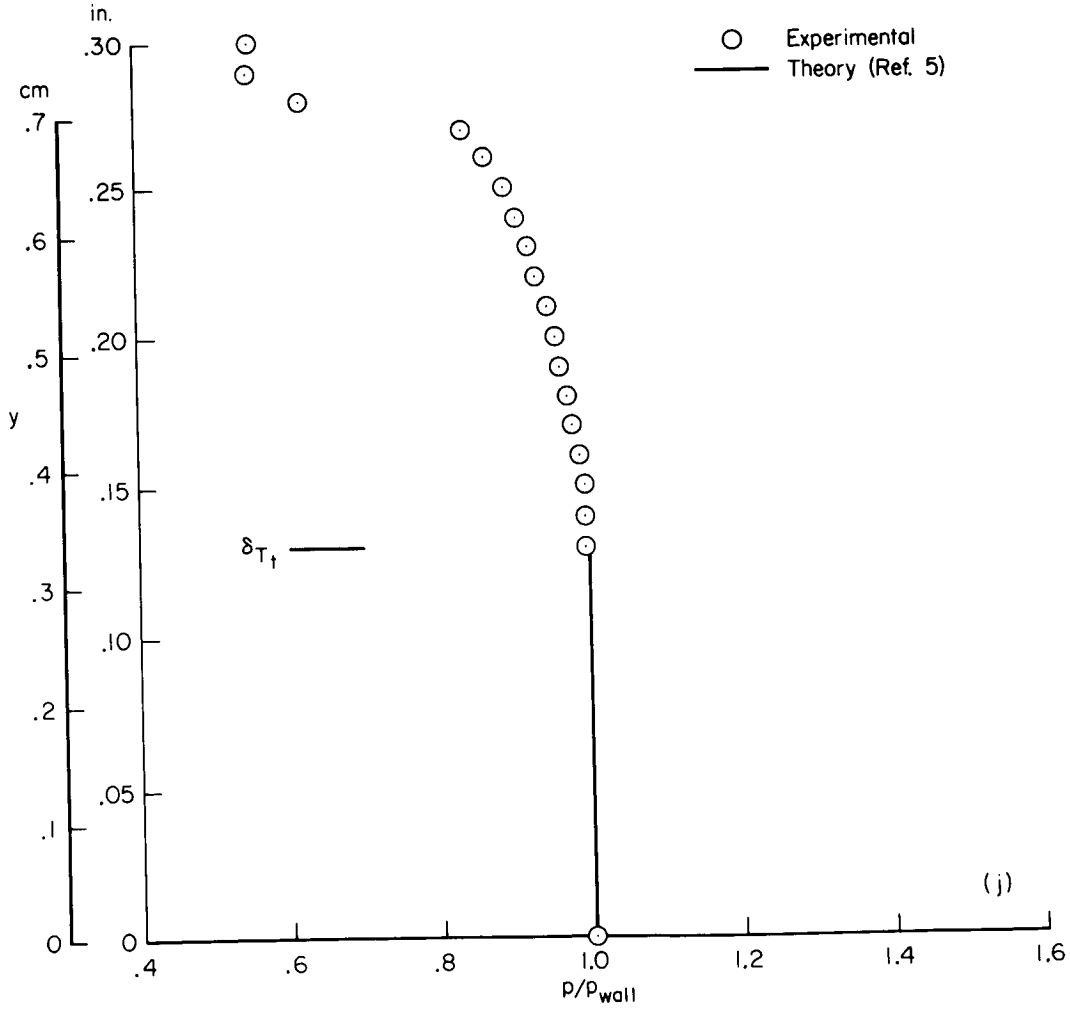

(j) x = 4.20 in. (10.67 cm), p_{wall}/p_{∞} = 2.85

Figure 8.- Continued.

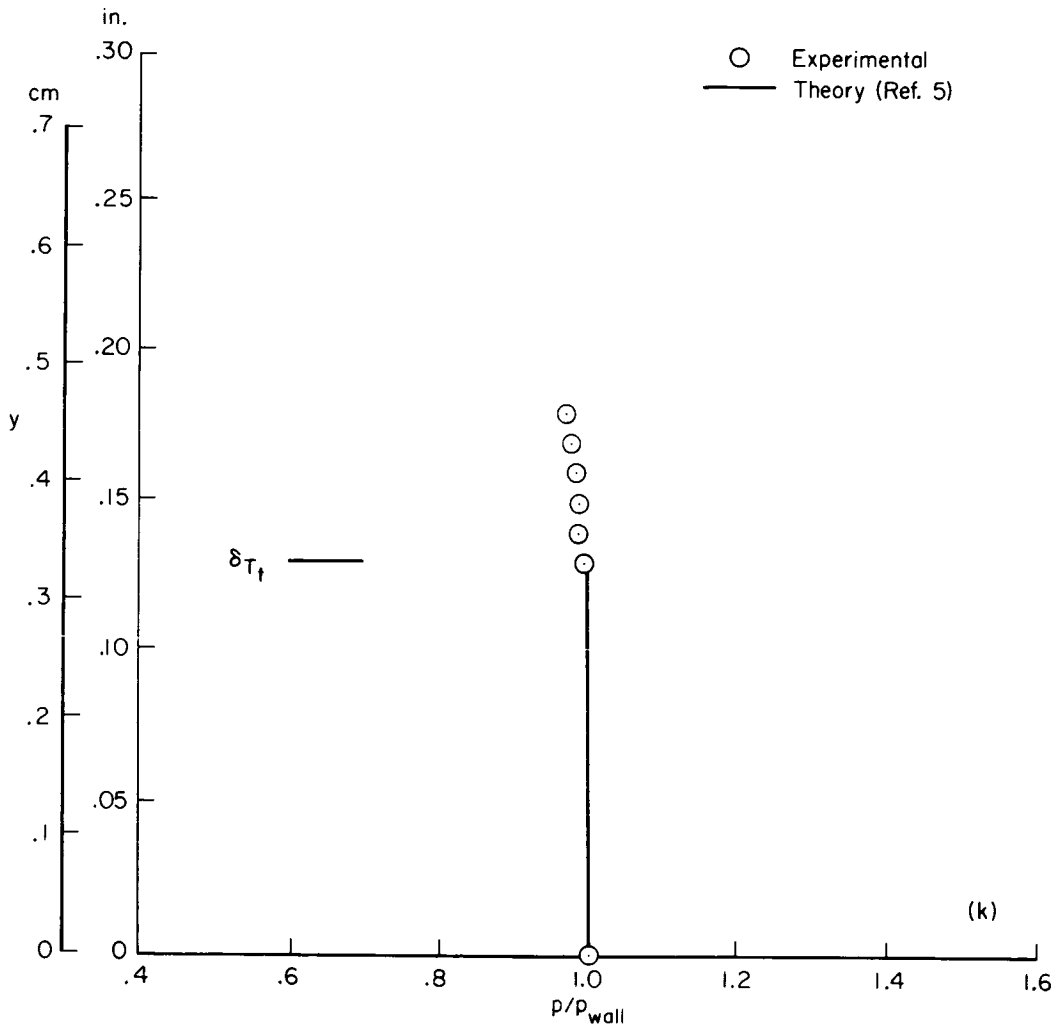

(k) x = 4.40 in. (11.18 cm), p_{wall}/p_{∞} = 3.03

Figure 8.- Continued.

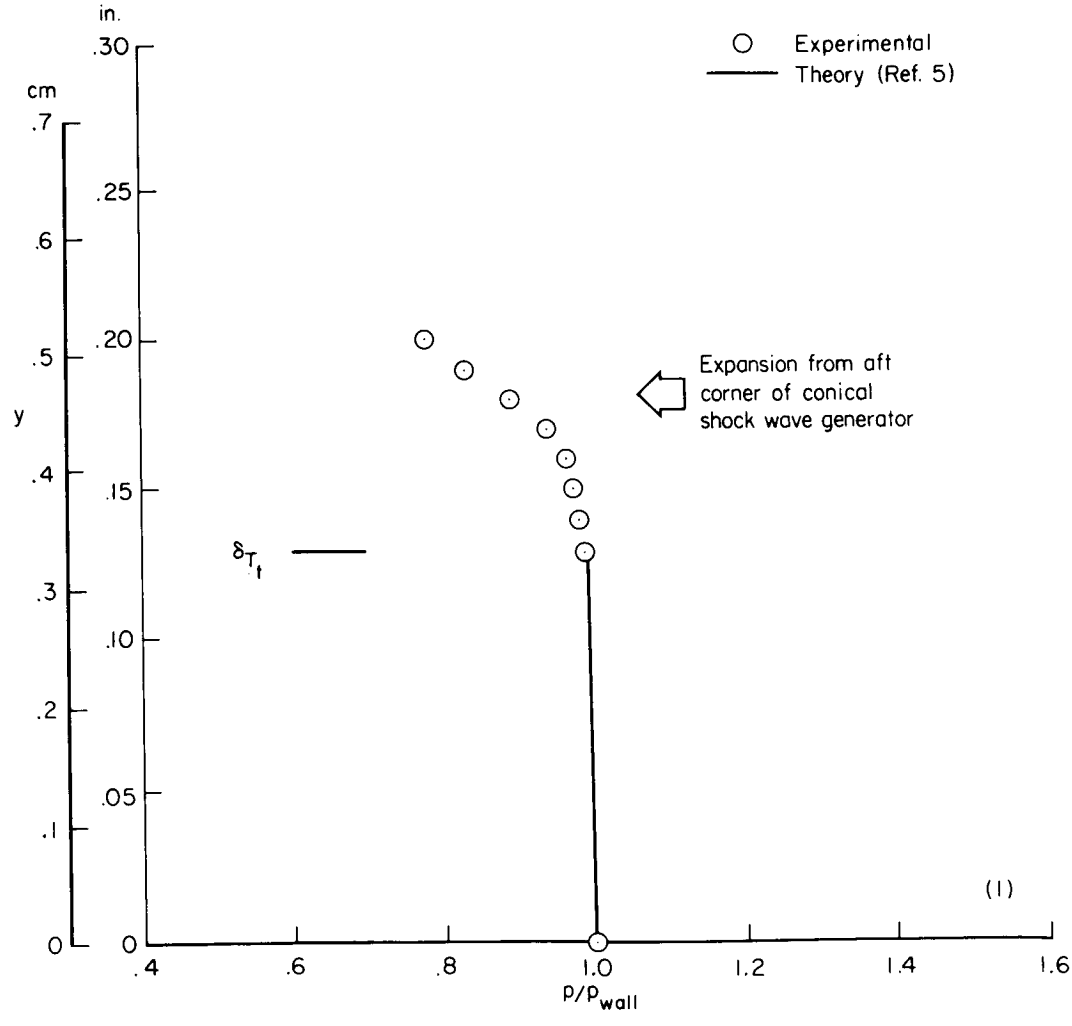

(ℓ) x = 4.60 in. (11.68 cm), p_{wall}/p_{∞} = 3.18

Figure 8.- Concluded.

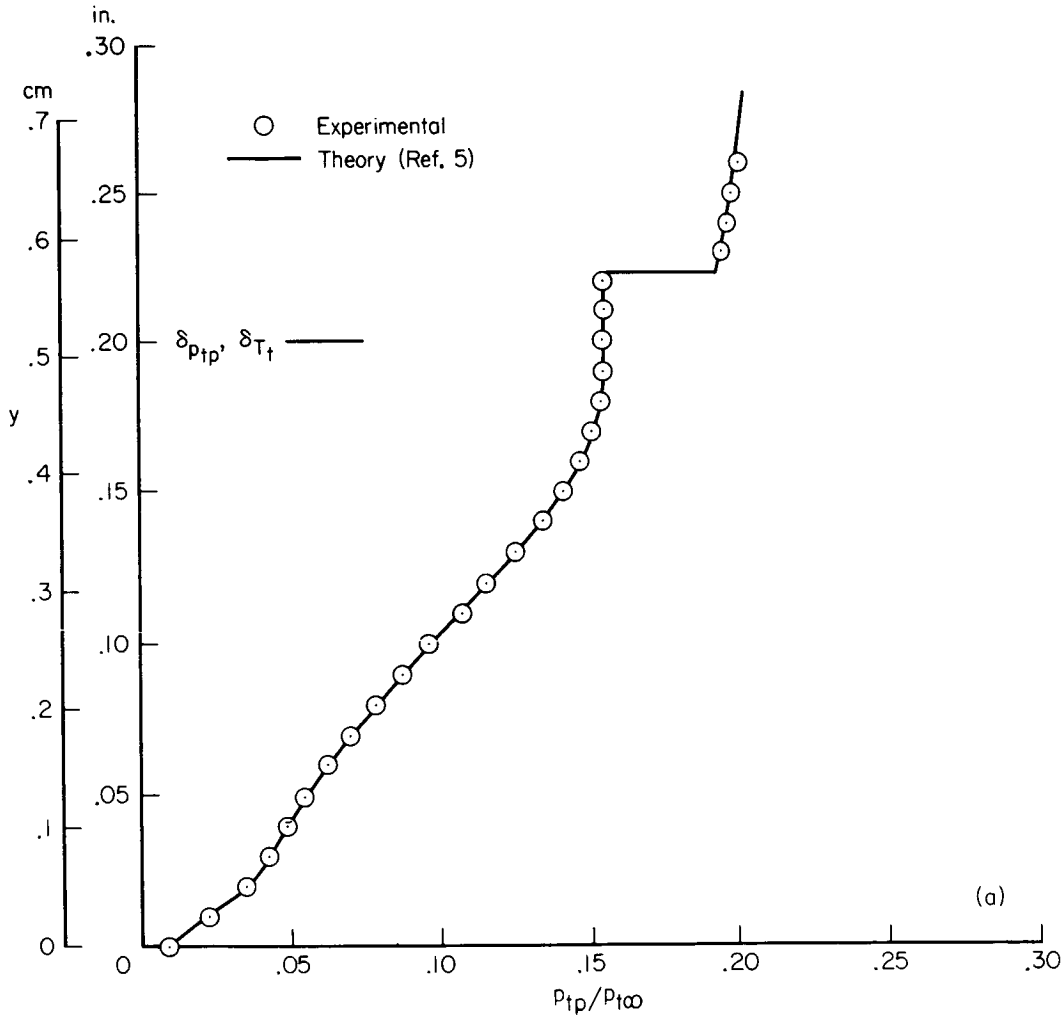

(a) x = 2.60 in. (6.60 cm)

Figure 9.- Experimental and theoretical pitot pressures.

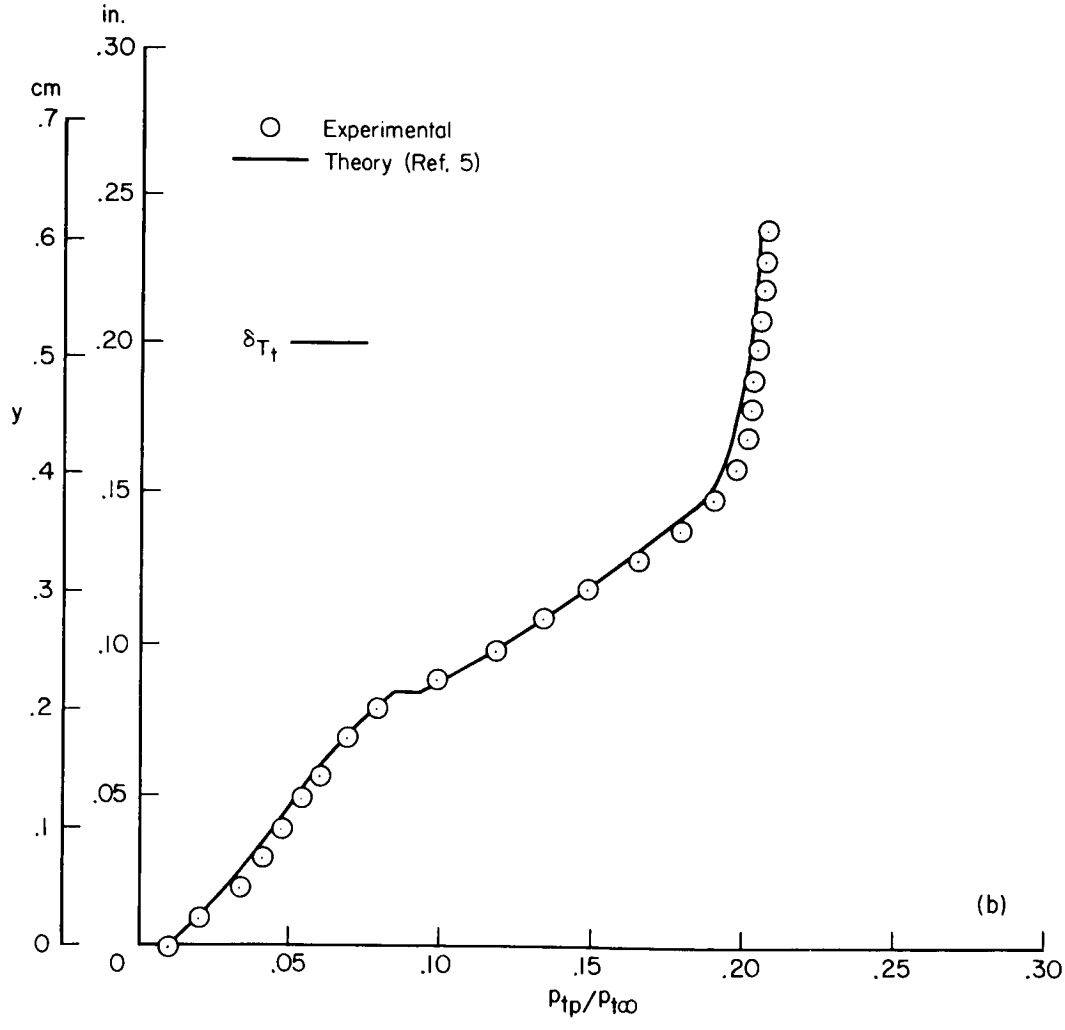

(b) x = 3.00 in. (7.62 cm)

Figure 9.- Continued.

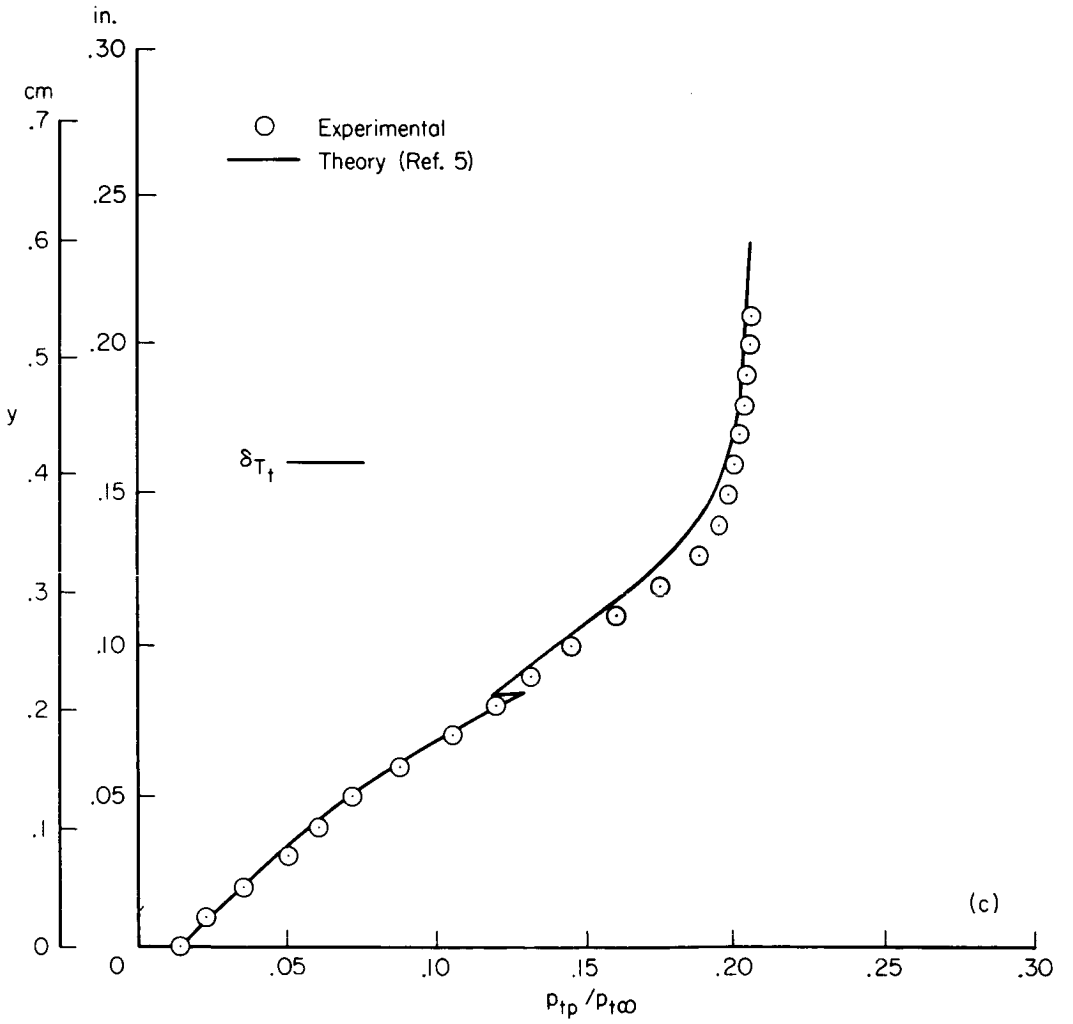

(c) x = 3.20 in. (8.13 cm)

Figure 9.- Continued.

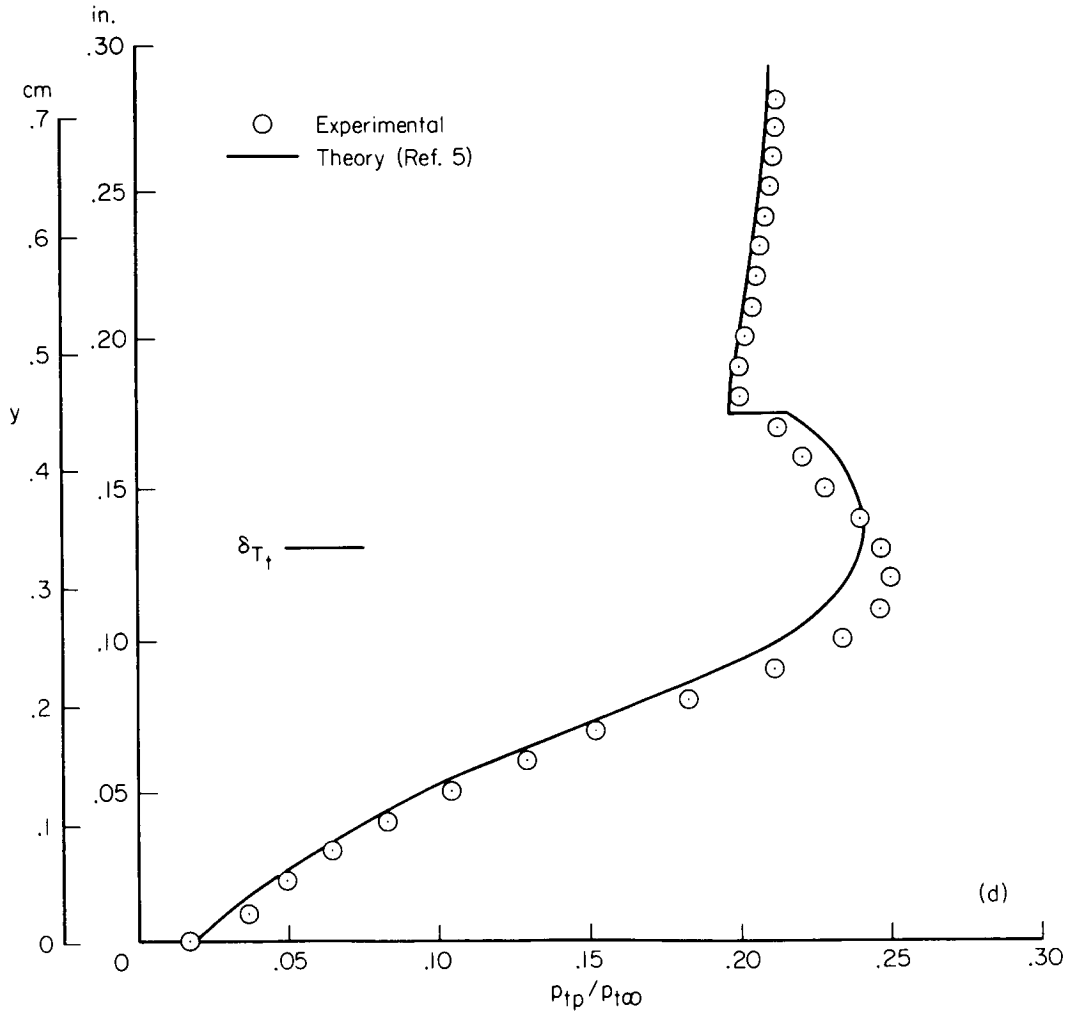

(d) x = 3.60 in. (9.15 cm)

Figure 9.- Concluded.

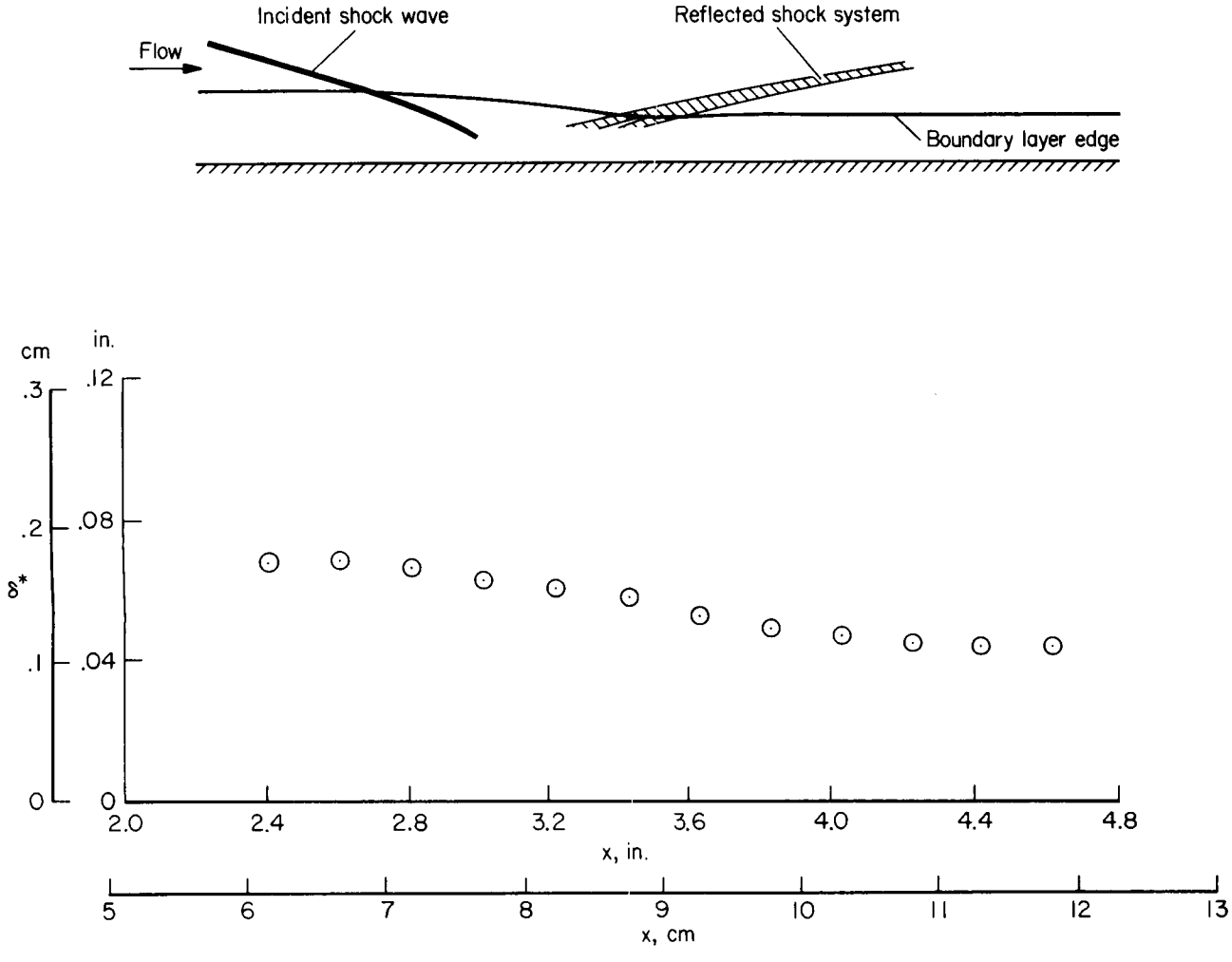

Figure 10.- Variation of δ^* through interaction.

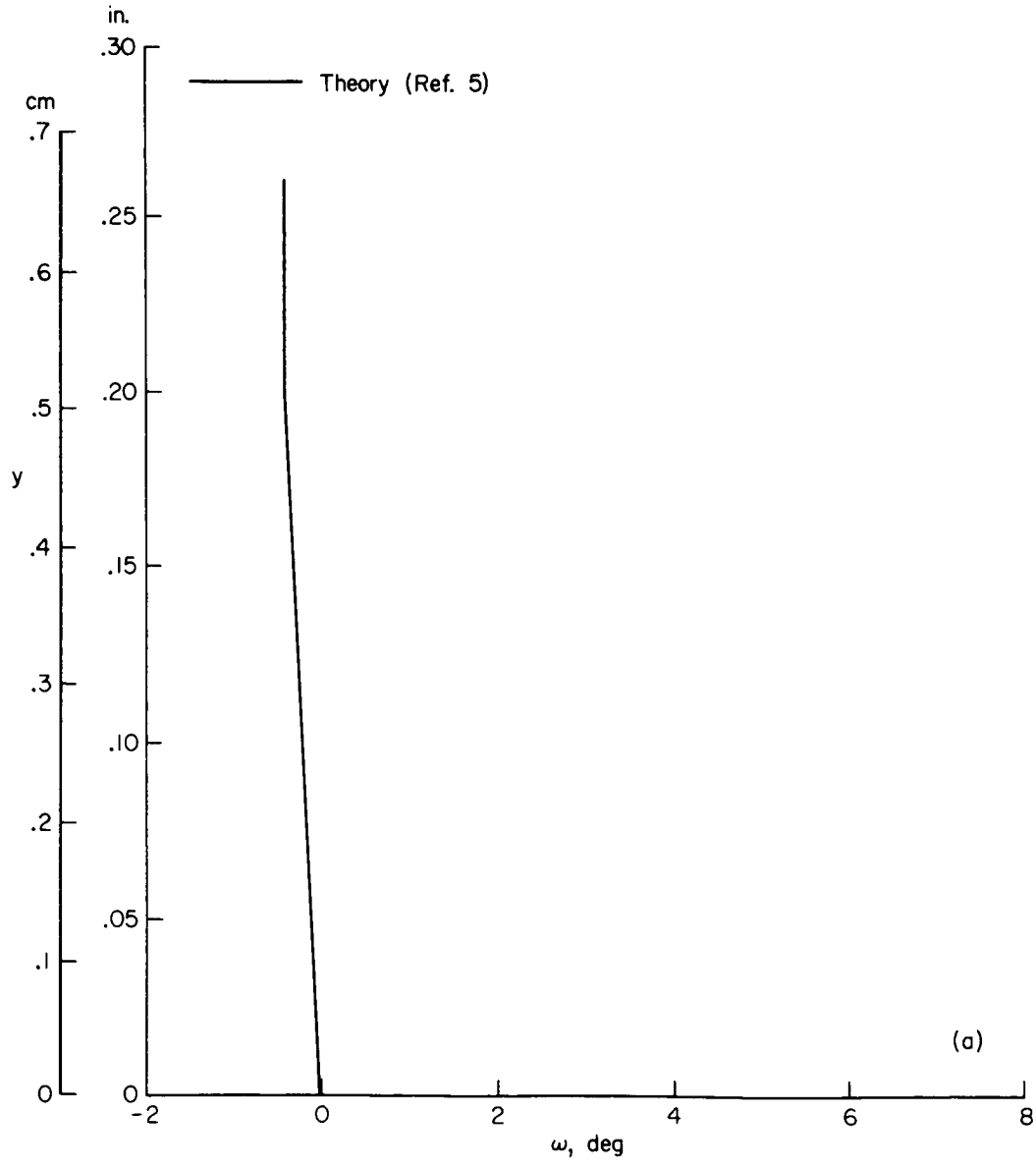

(a) x = 2.40 in. (6.10 cm)

Figure 11.- Flow angles.

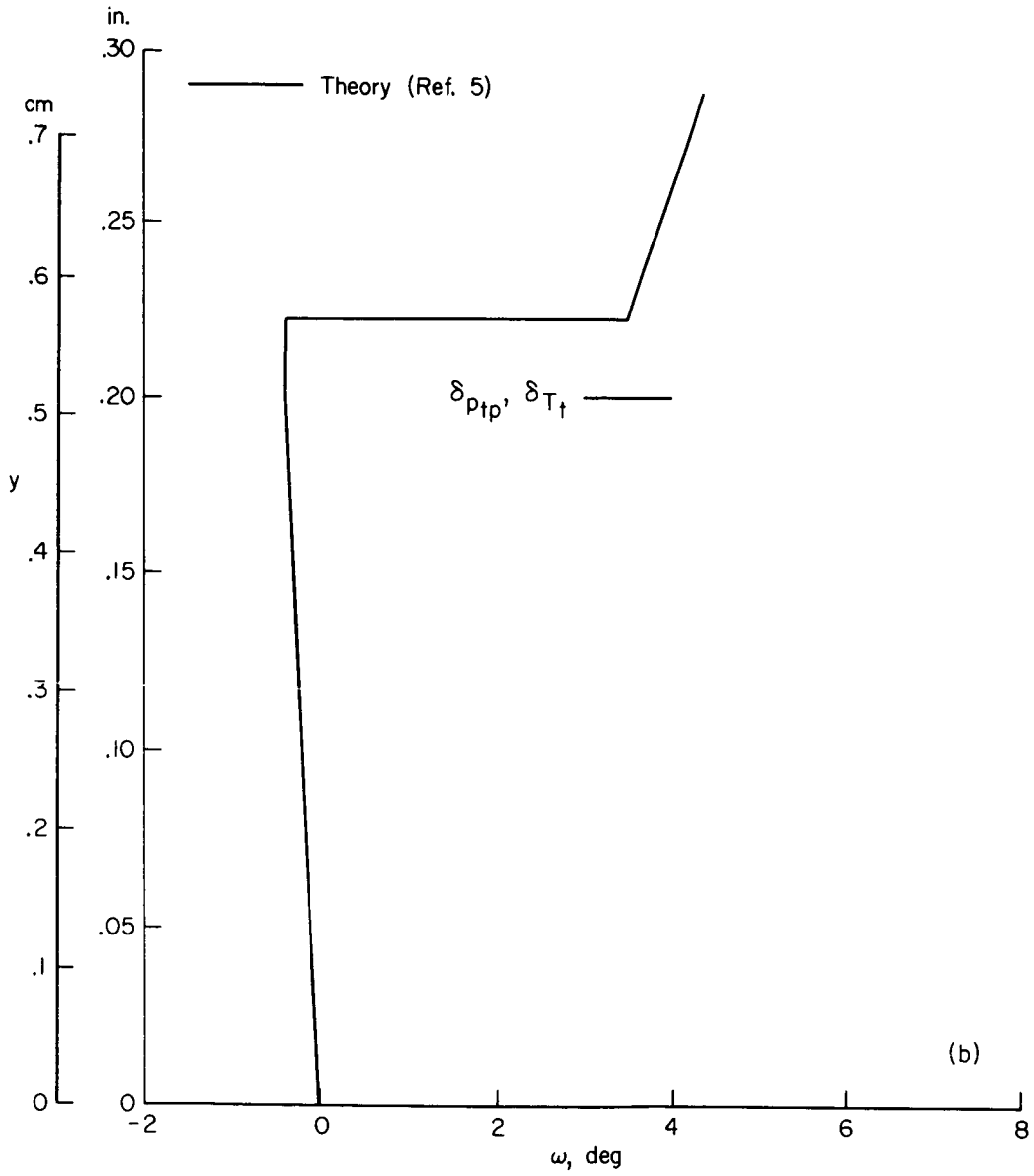

(b) x = 2.60 in. (6.60 cm)

Figure 11.- Continued.

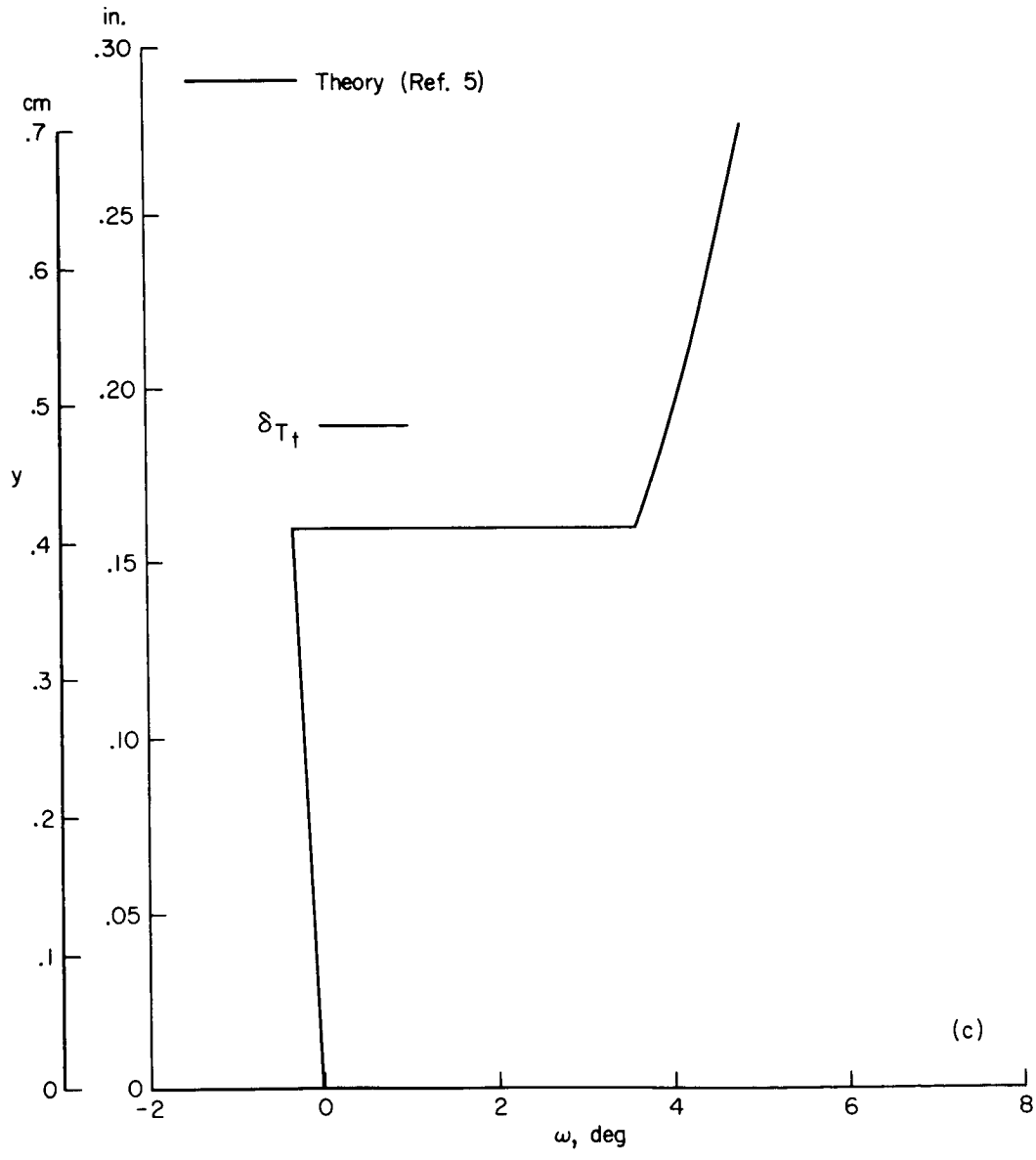

(c) x = 2.80 in. (7.11 cm)

Figure 11.- Continued.

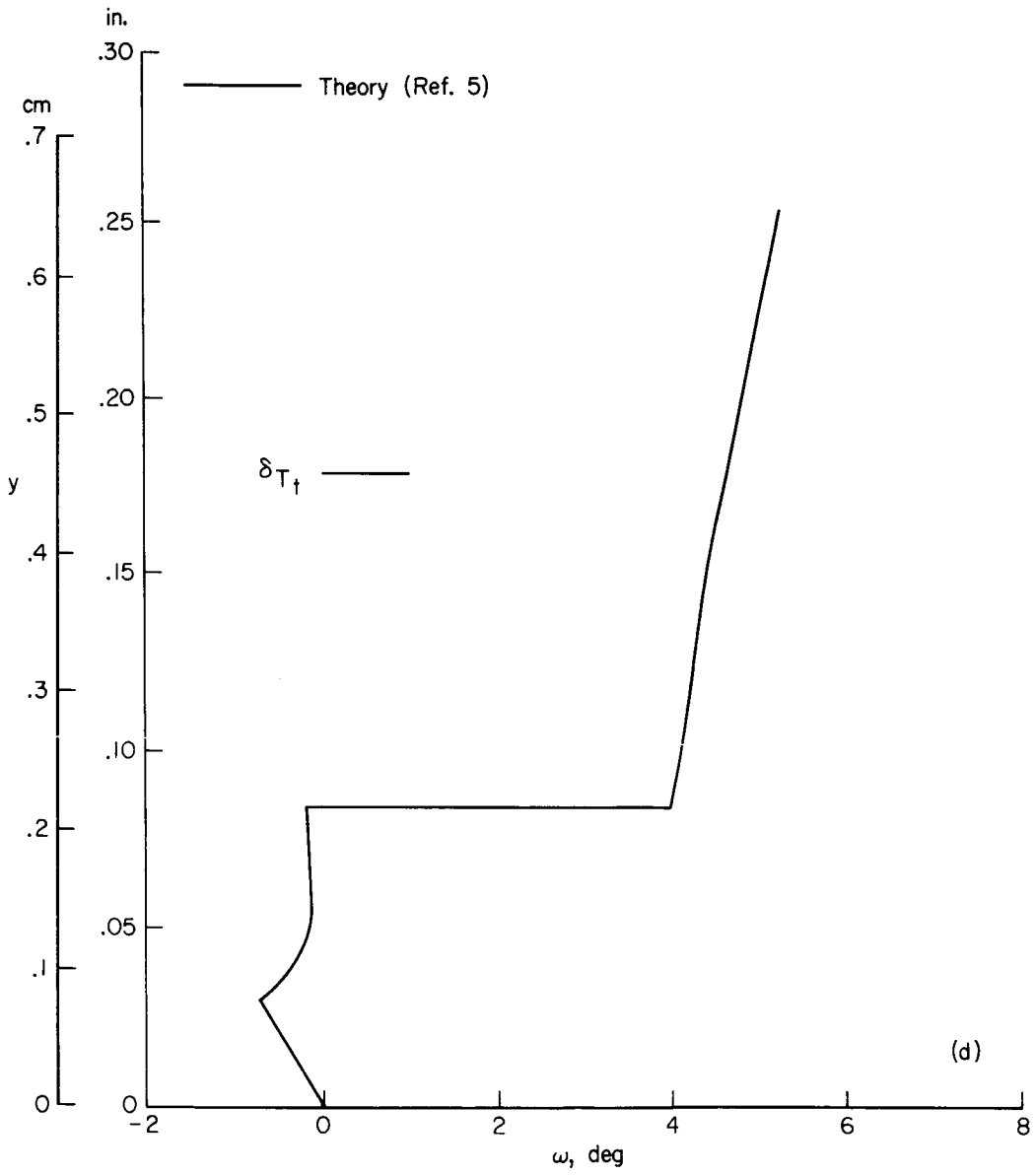

(d) x = 3.00 in. (7.62 cm)

Figure 11.- Continued.

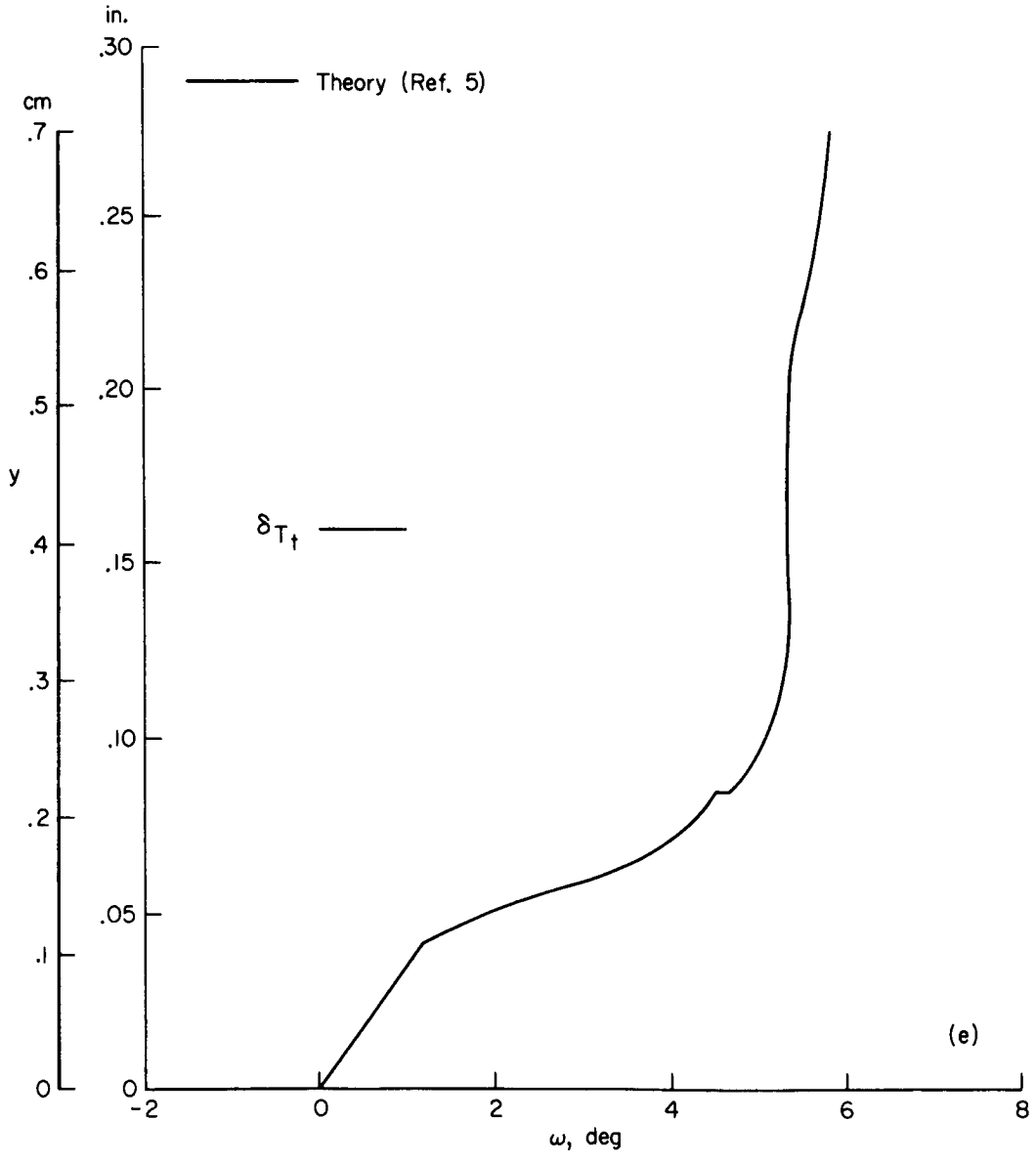

(e) x = 3.20 in. (8.13 cm)

Figure 11.- Continued.

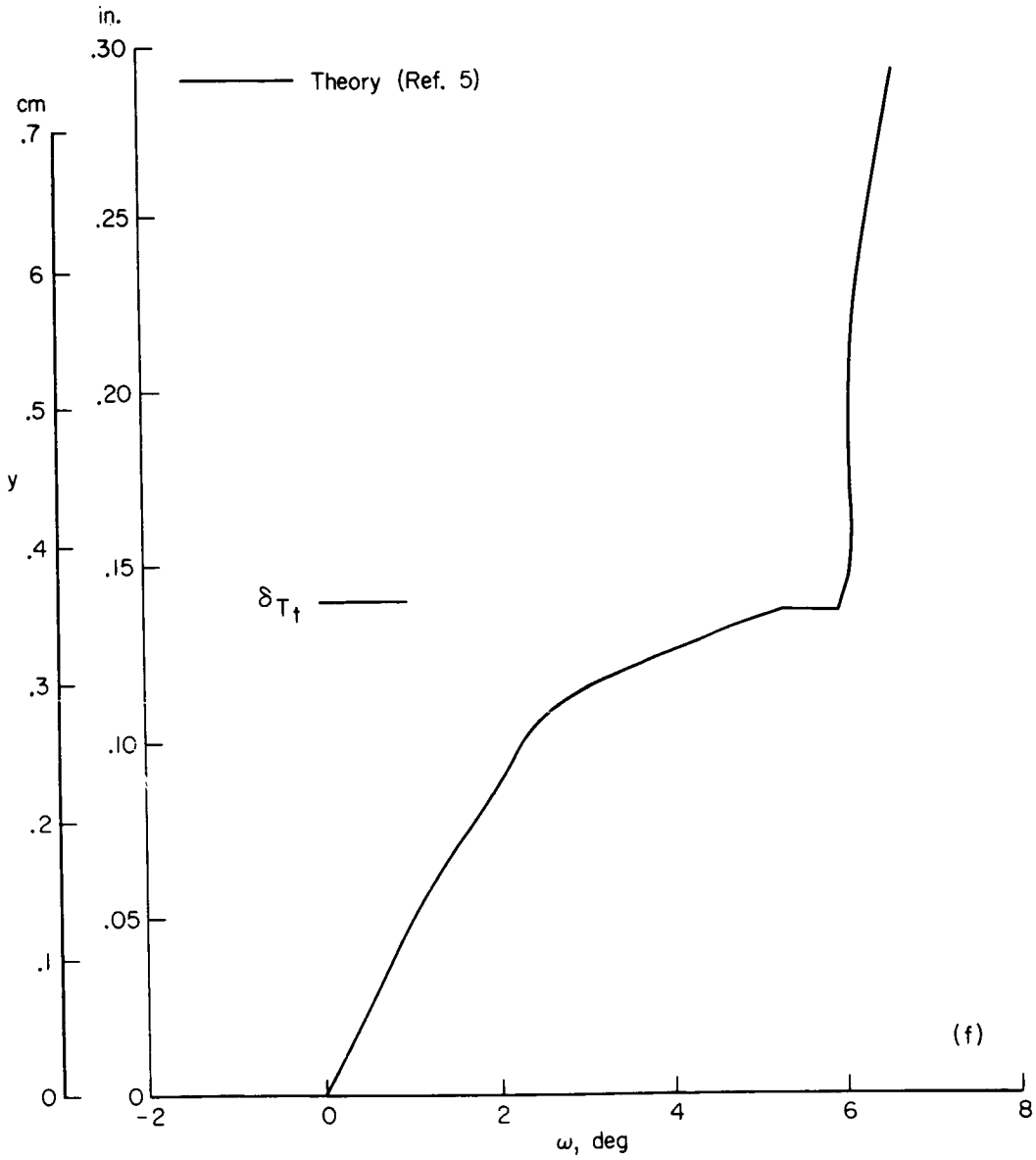

(f) x = 3.40 in. (8.64 cm)

Figure 11.- Continued.

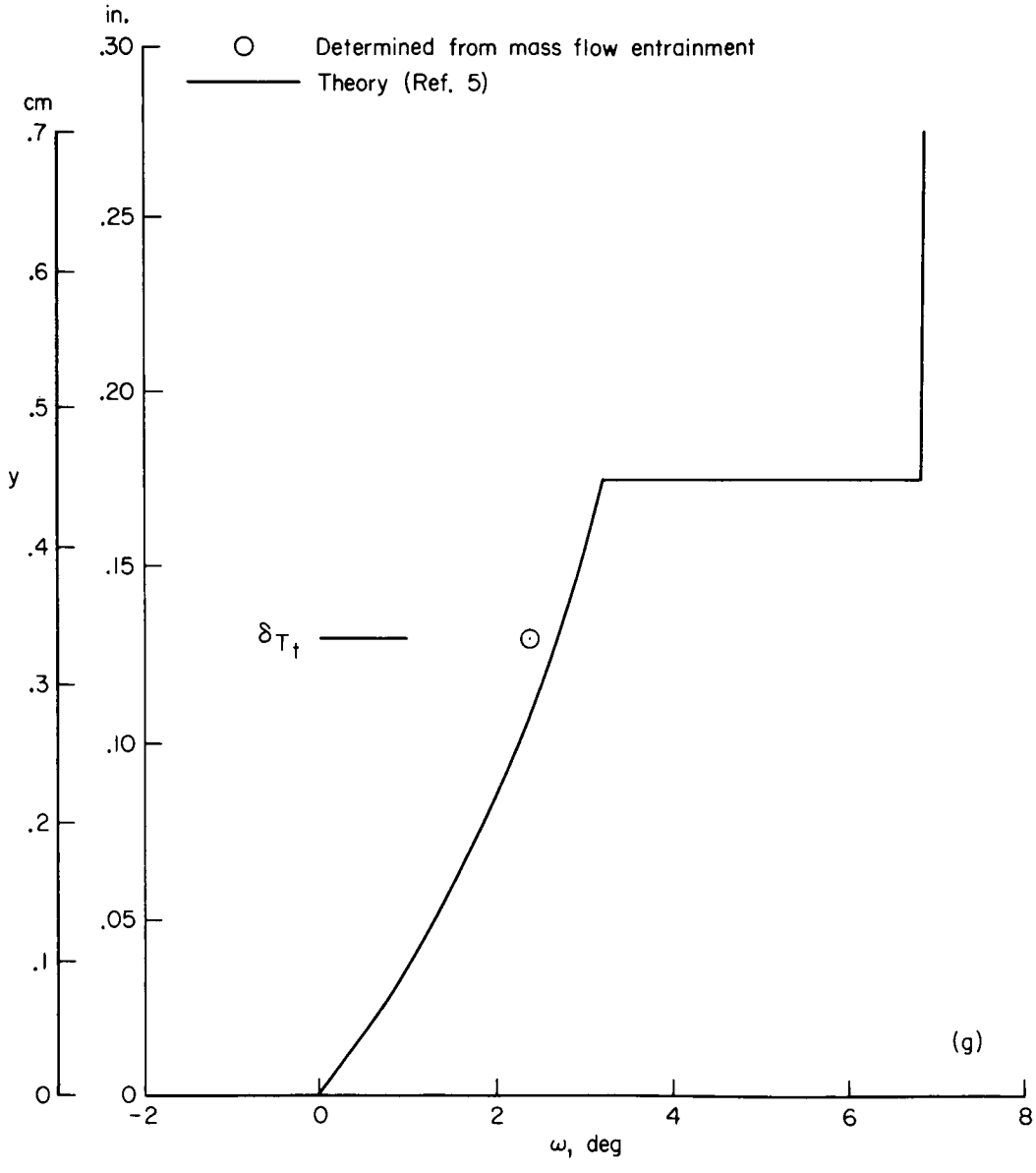

(g) x = 3.60 in. (9.15 cm)

Figure 11.- Continued.

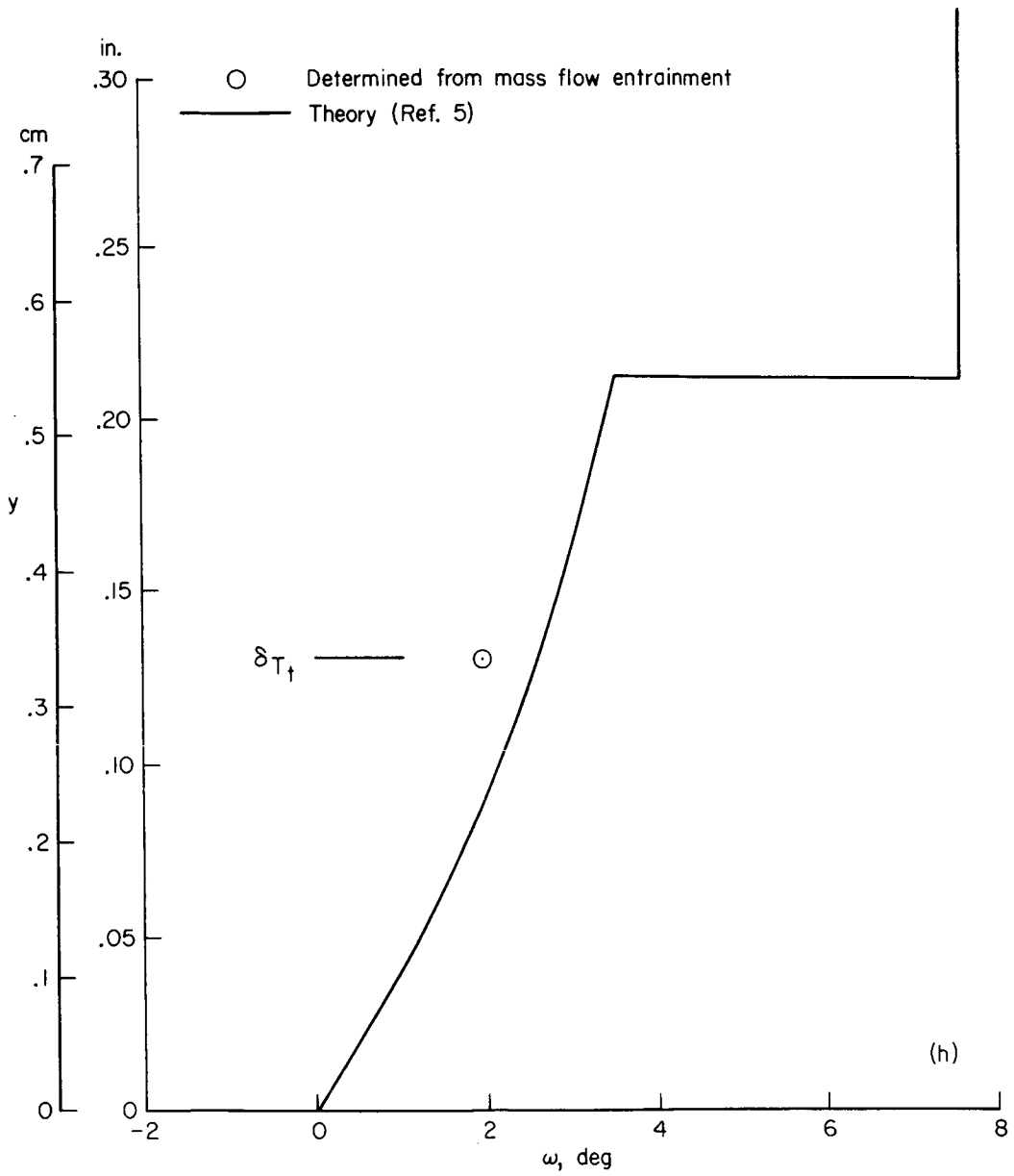

(h) x = 3.80 in. (9.66 cm)

Figure 11.- Continued.

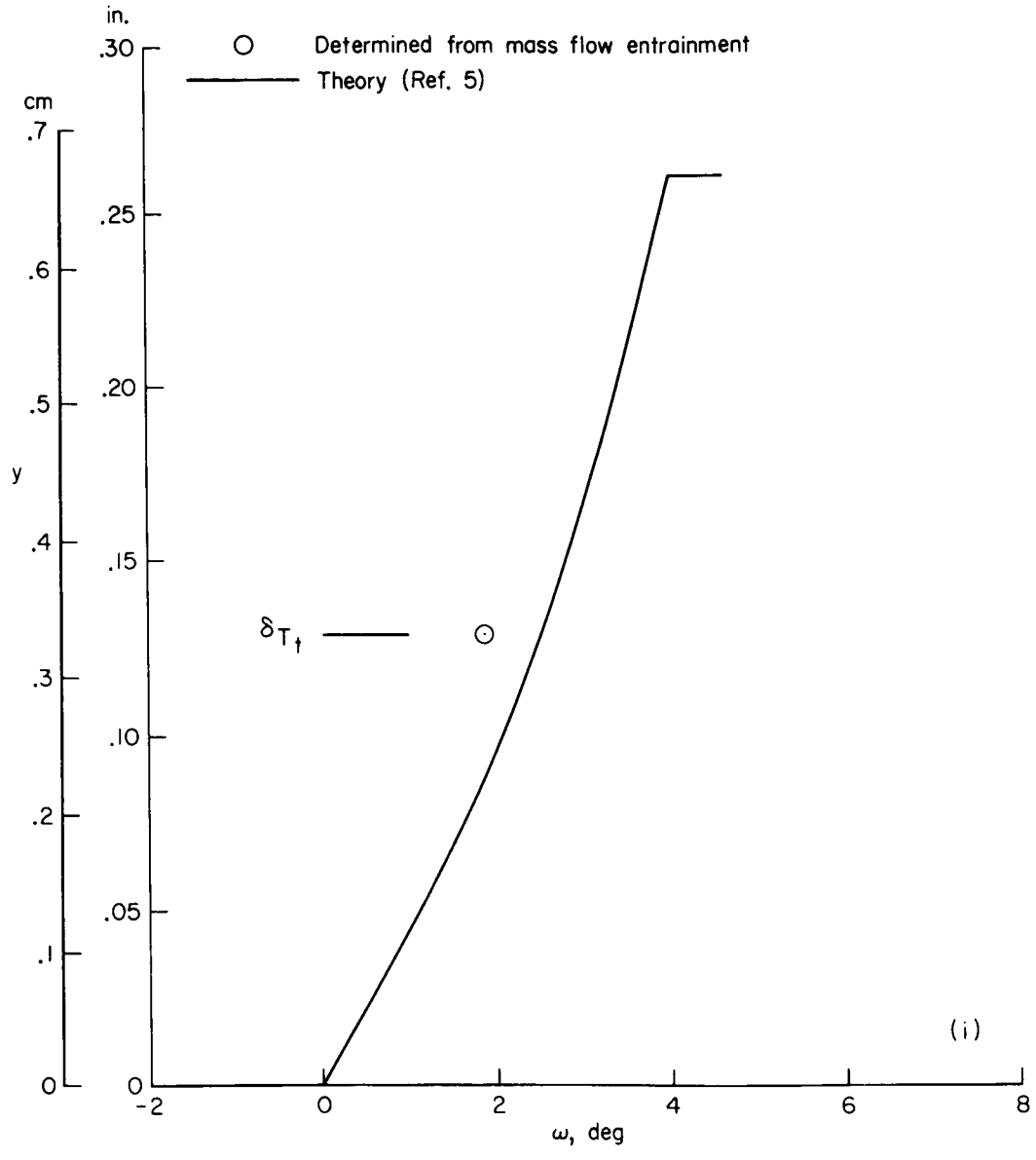

(i) x = 4.00 in. (10.16 cm)

Figure 11.- Continued.

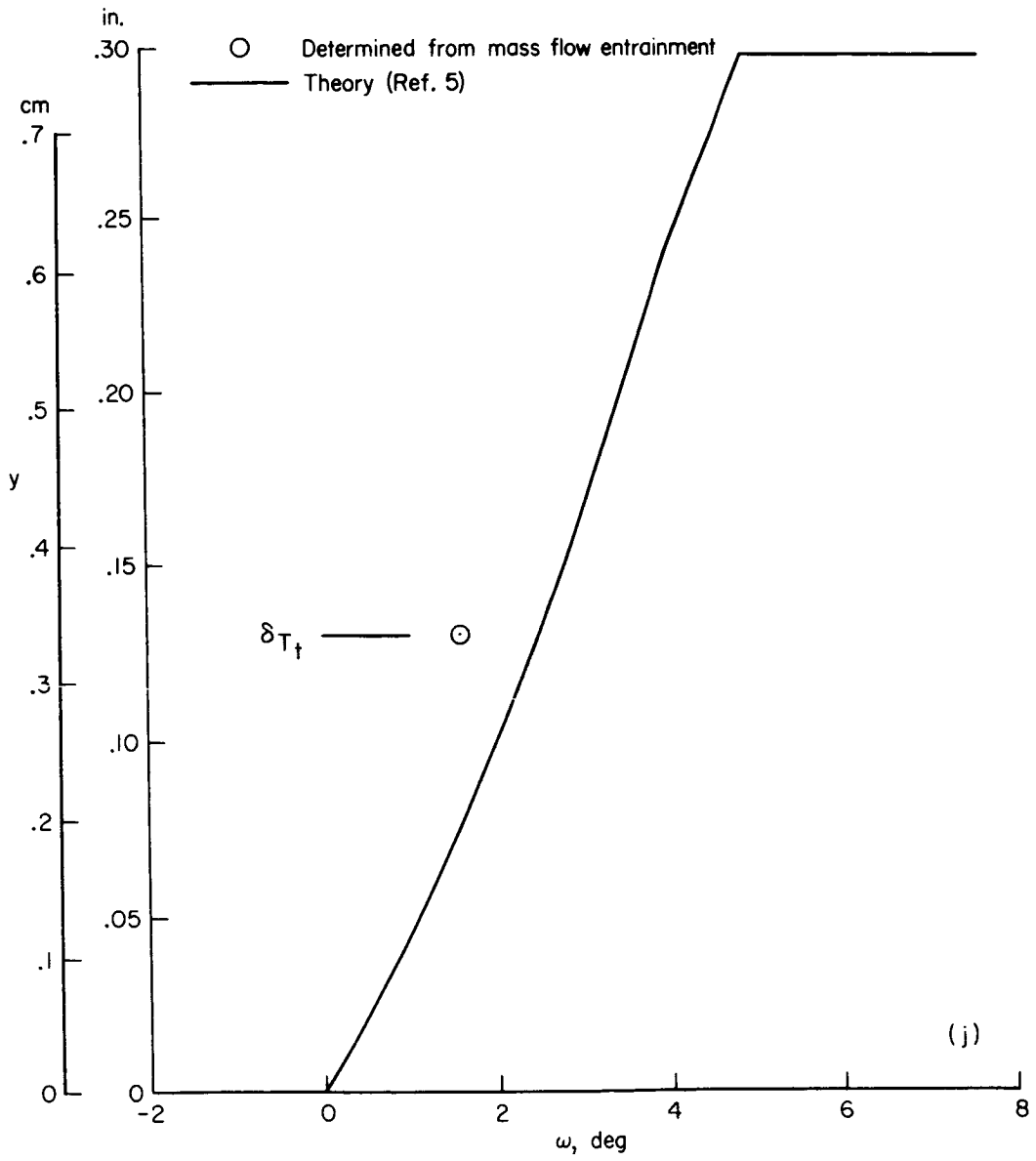

(j) x = 4.20 in. (10.67 cm)

Figure 11.- Continued.

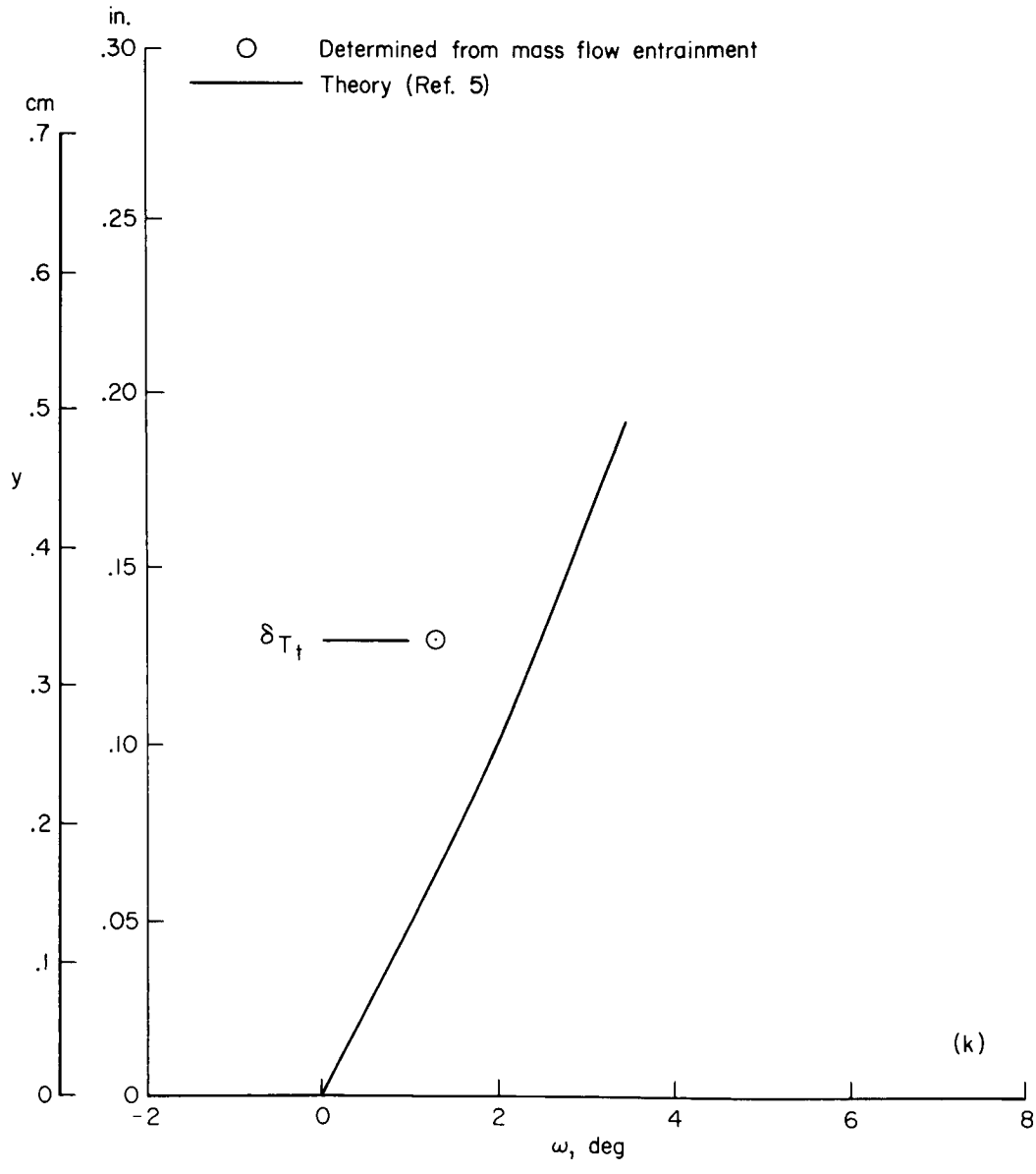

(k) x = 4.40 in. (11.18 cm)

Figure 11.- Continued.

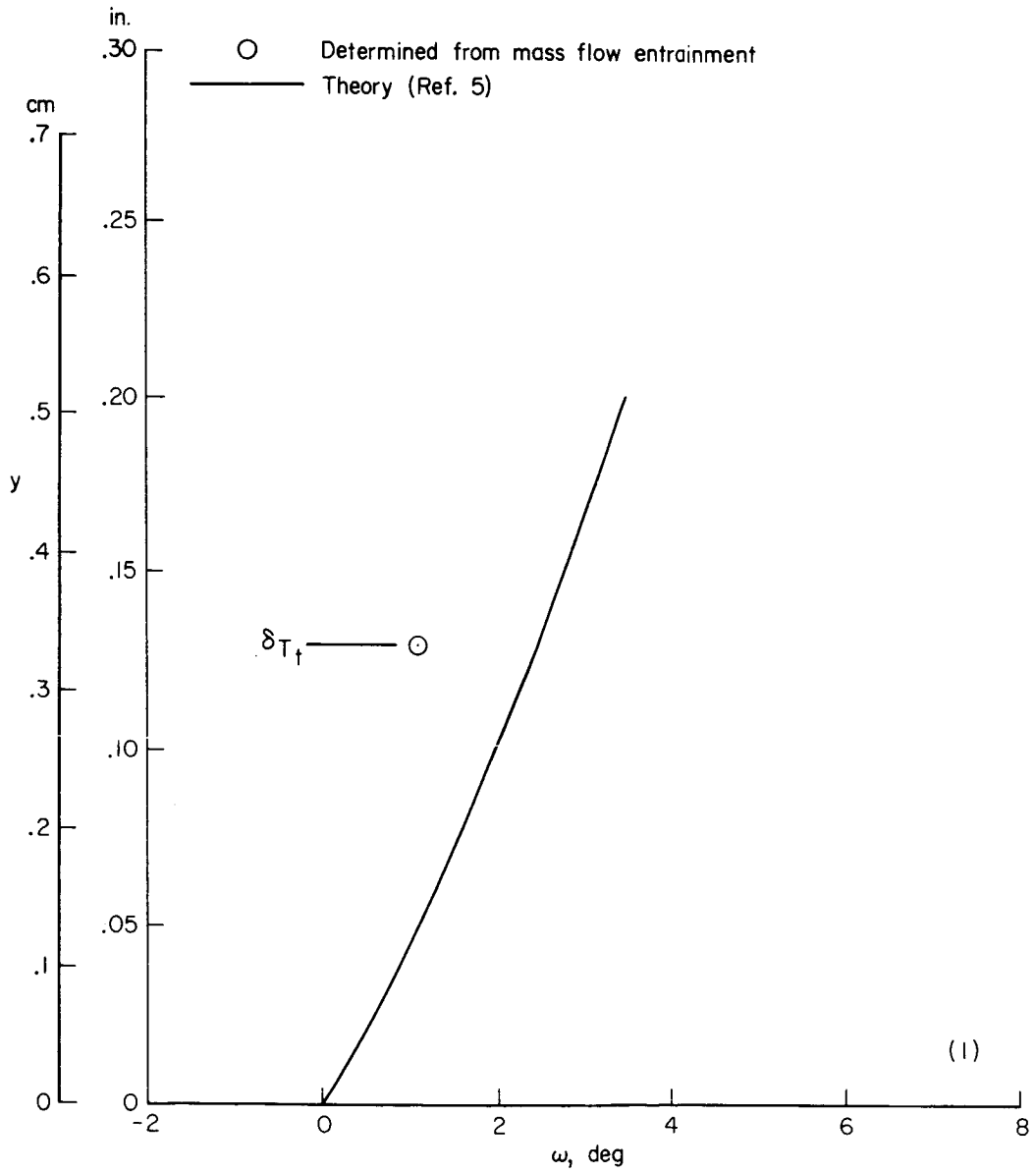

(ℓ) x = 4.60 in. (11.68 cm)

Figure 11.- Concluded.

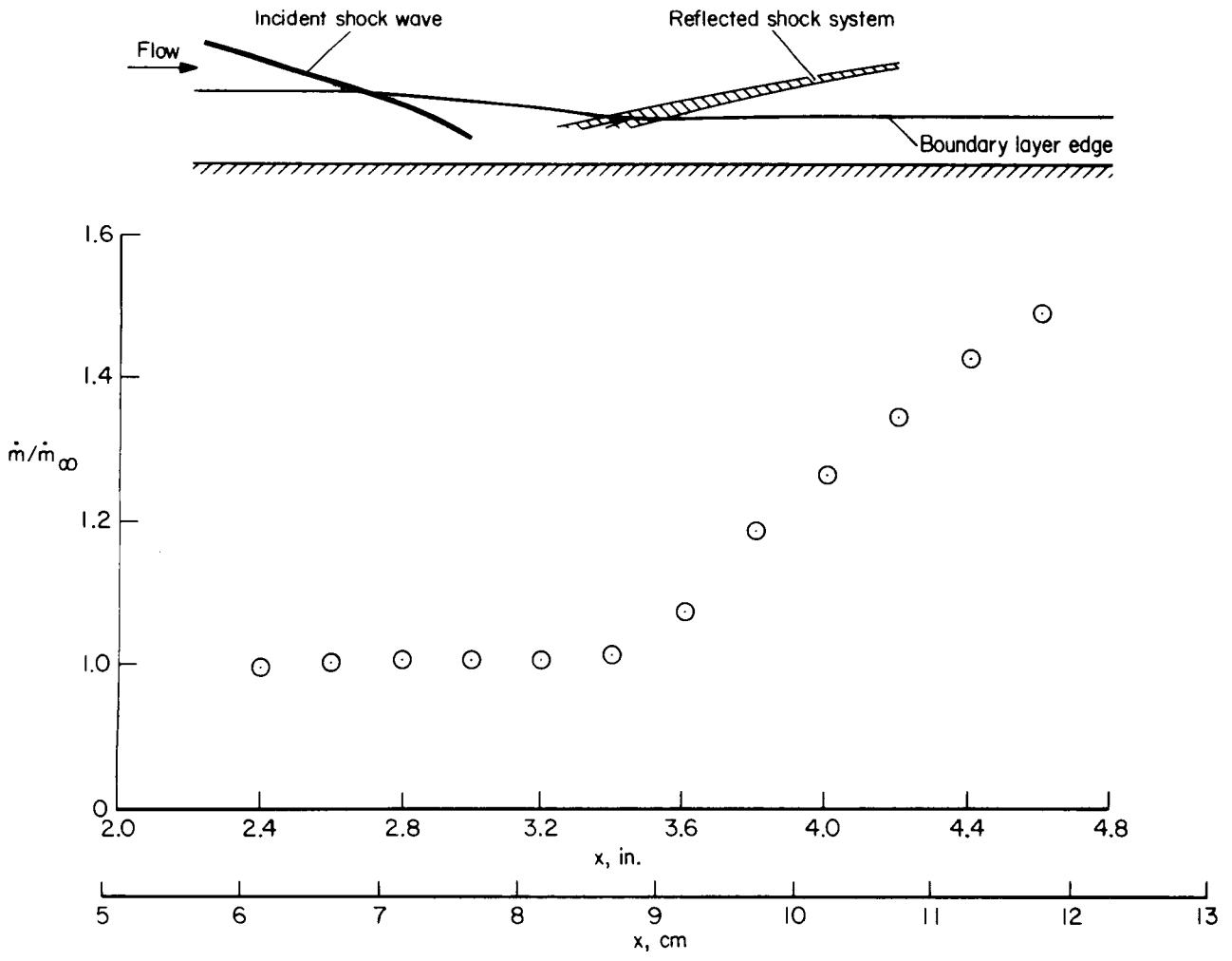

Figure 12.- Boundary-layer mass flow.

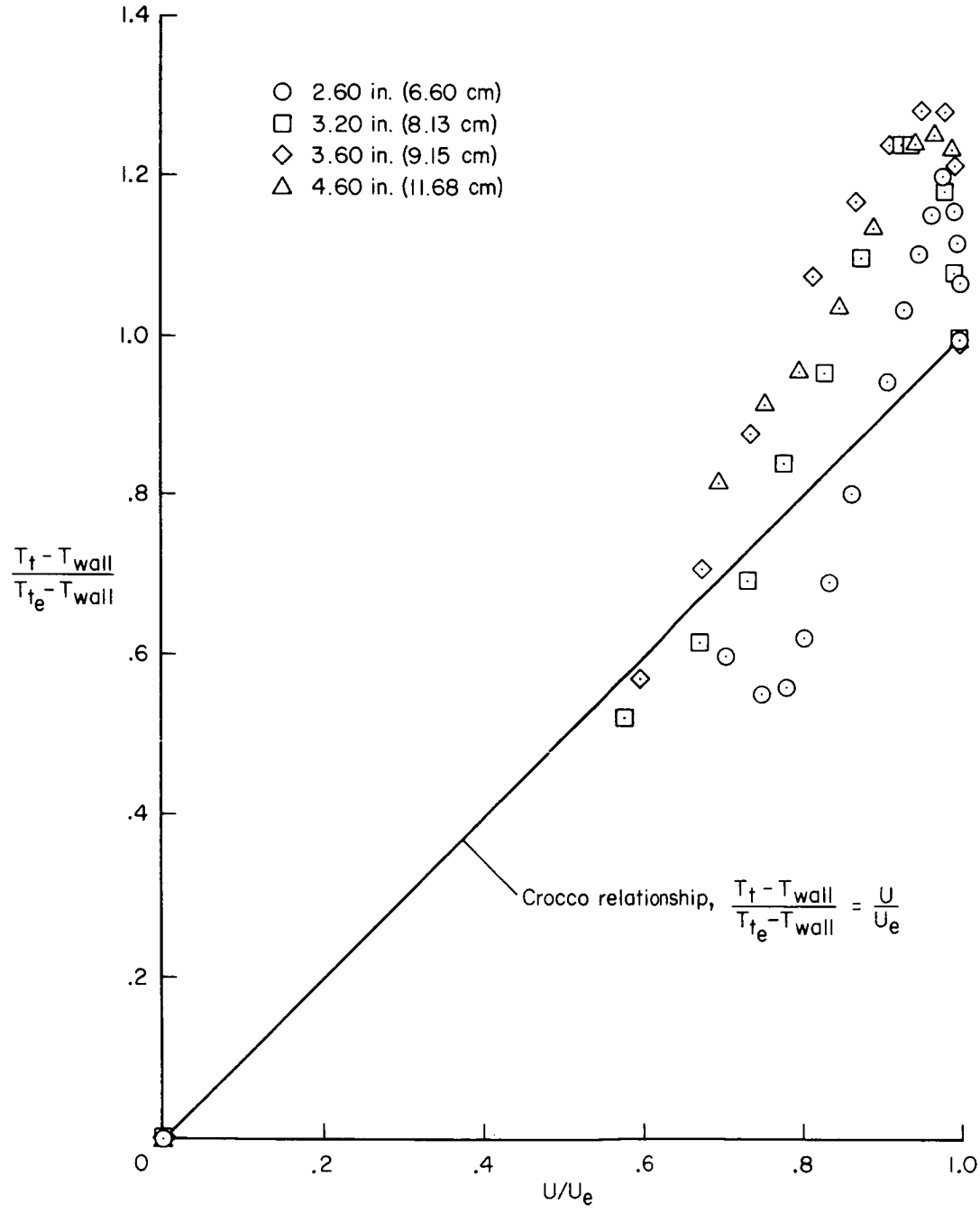

Figure 13.- Effect of adverse pressure gradient on total temperature distribution.

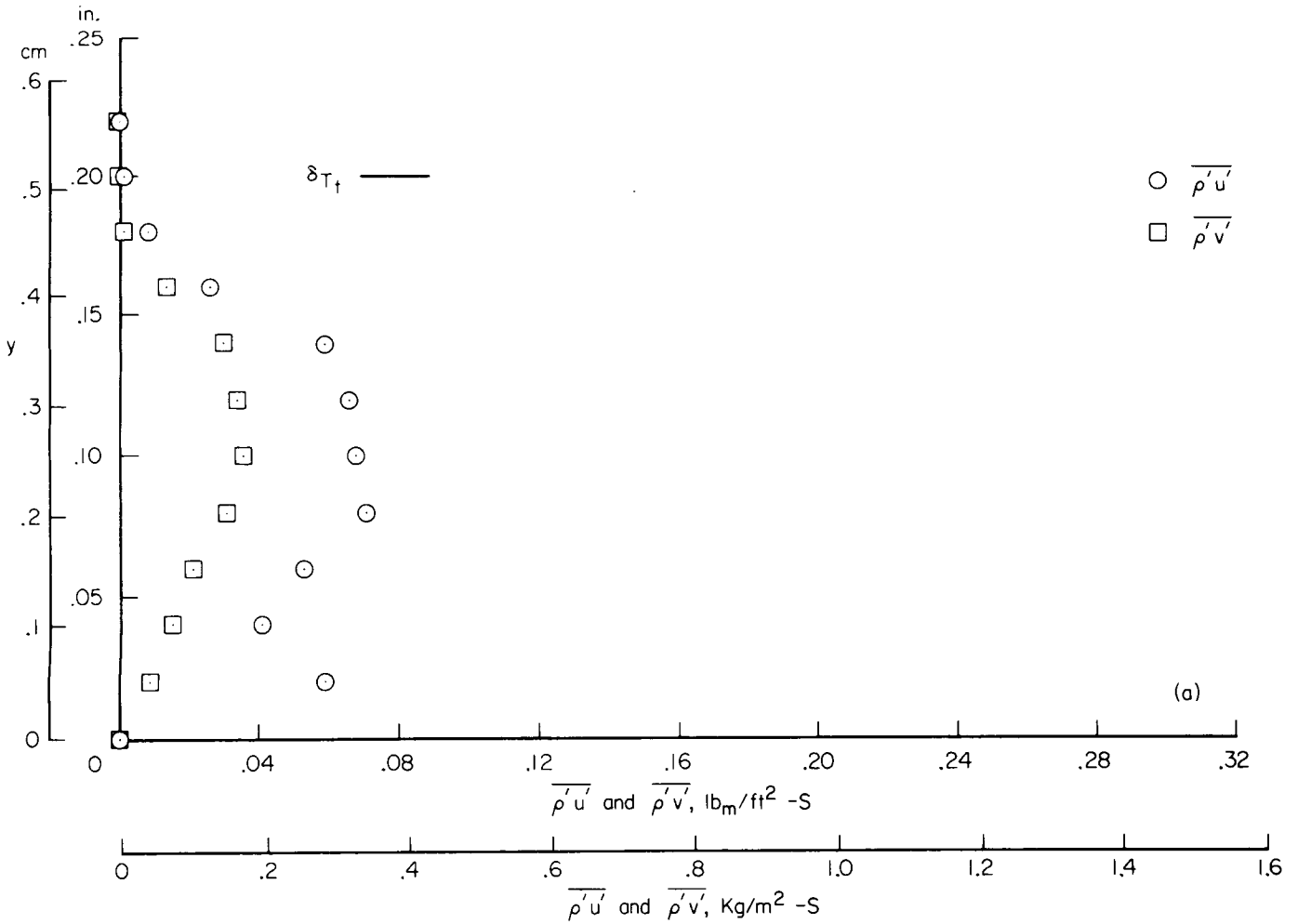

(a) x = 2.40 in. (6.10 cm)

Figure 14.- Turbulent mass transfer terms.

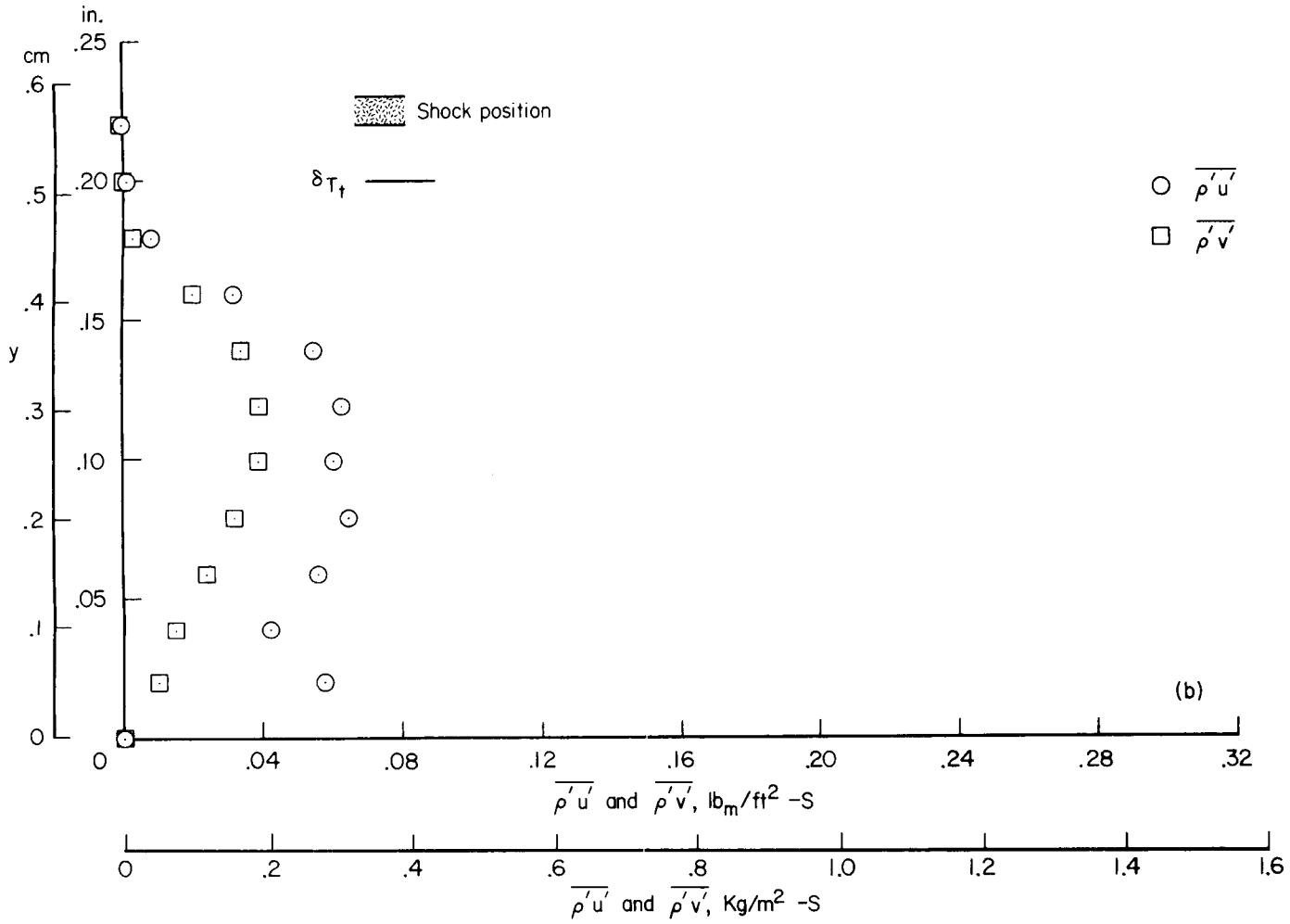

(b) x = 2.60 in. (6.60 cm)

Figure 14.- Continued.

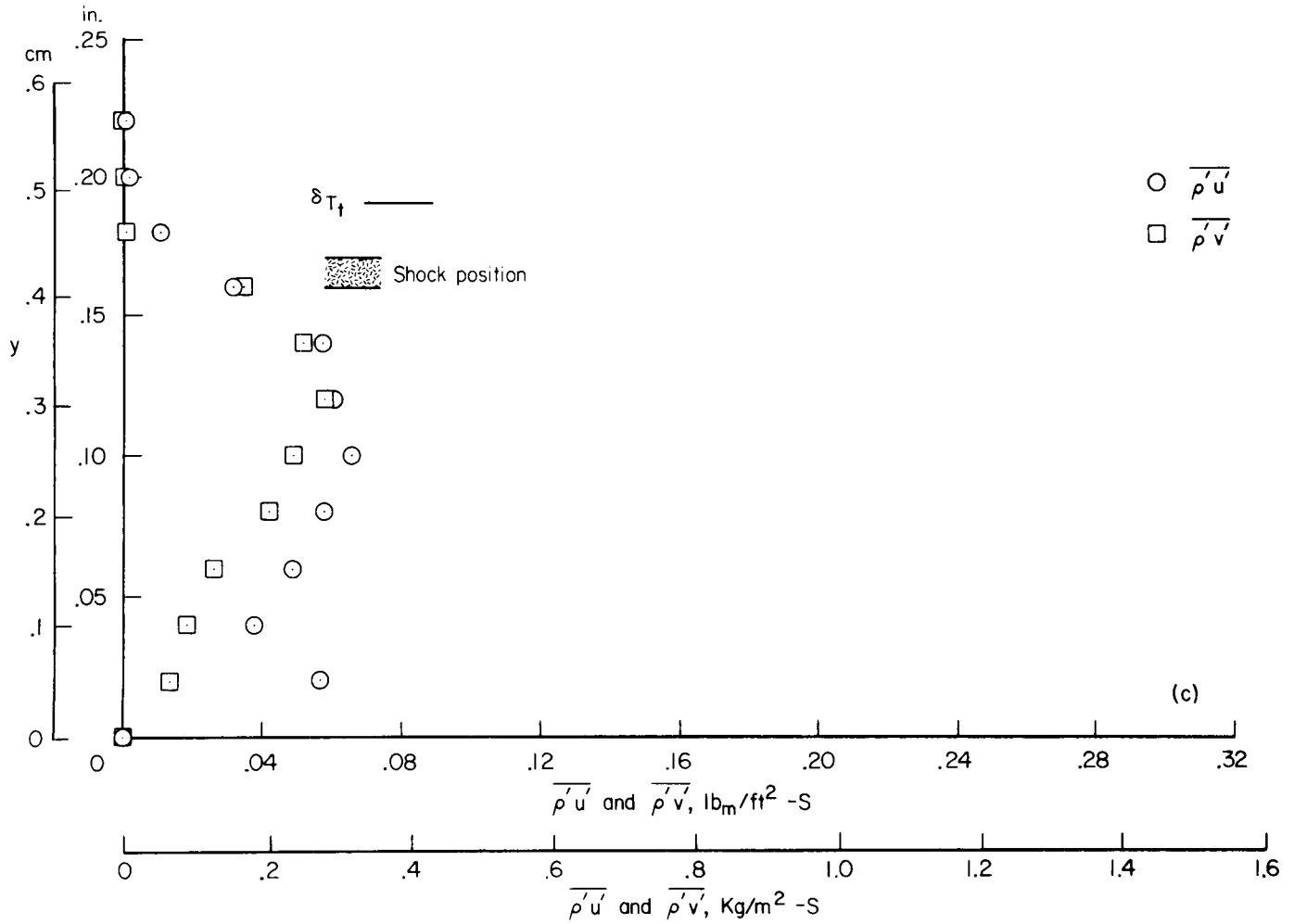

(c) x = 2.80 in. (7.11 cm)

Figure 14.- Continued.

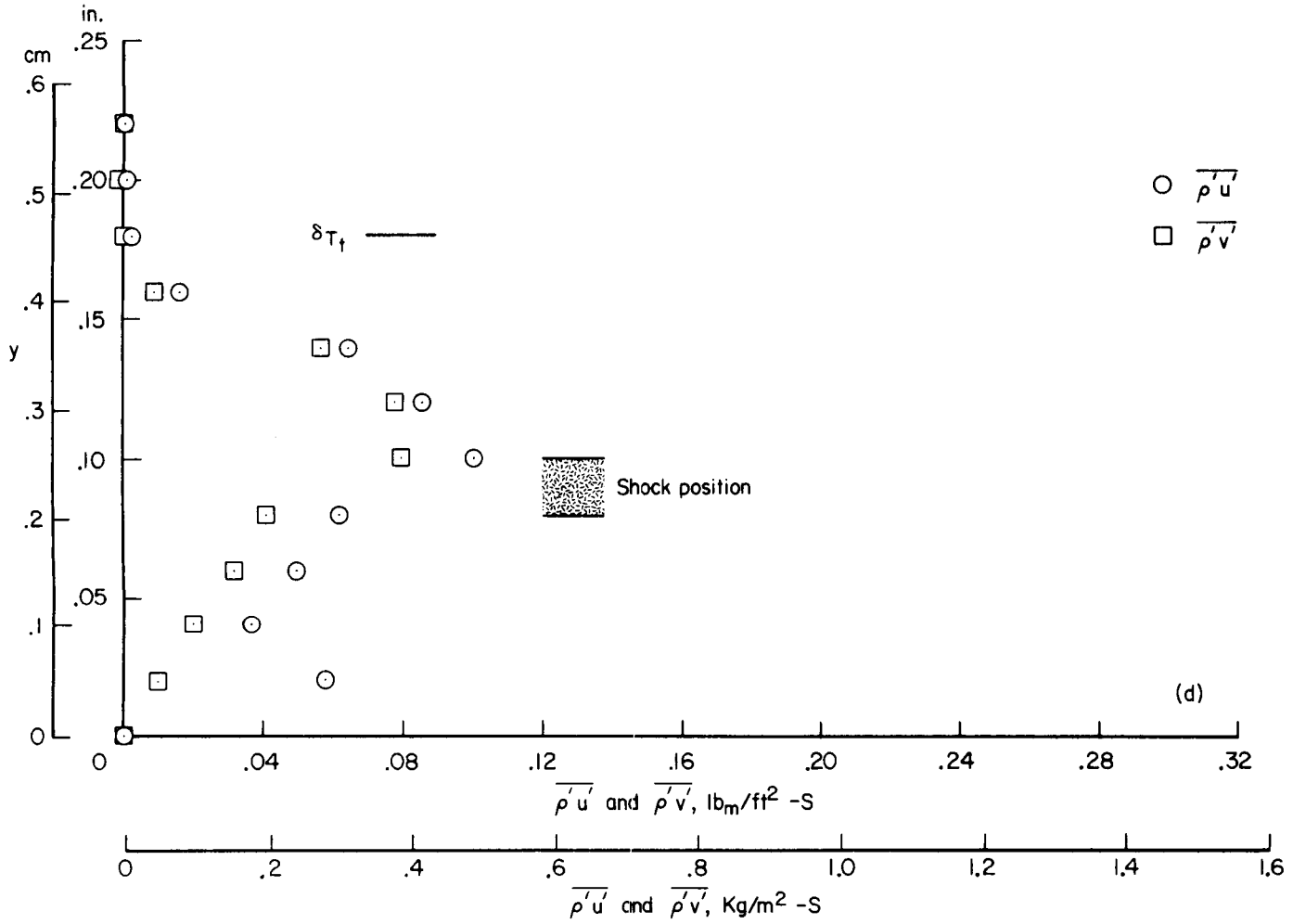

(d) x = 3.00 in. (7.62 cm)

Figure 14.- Continued.

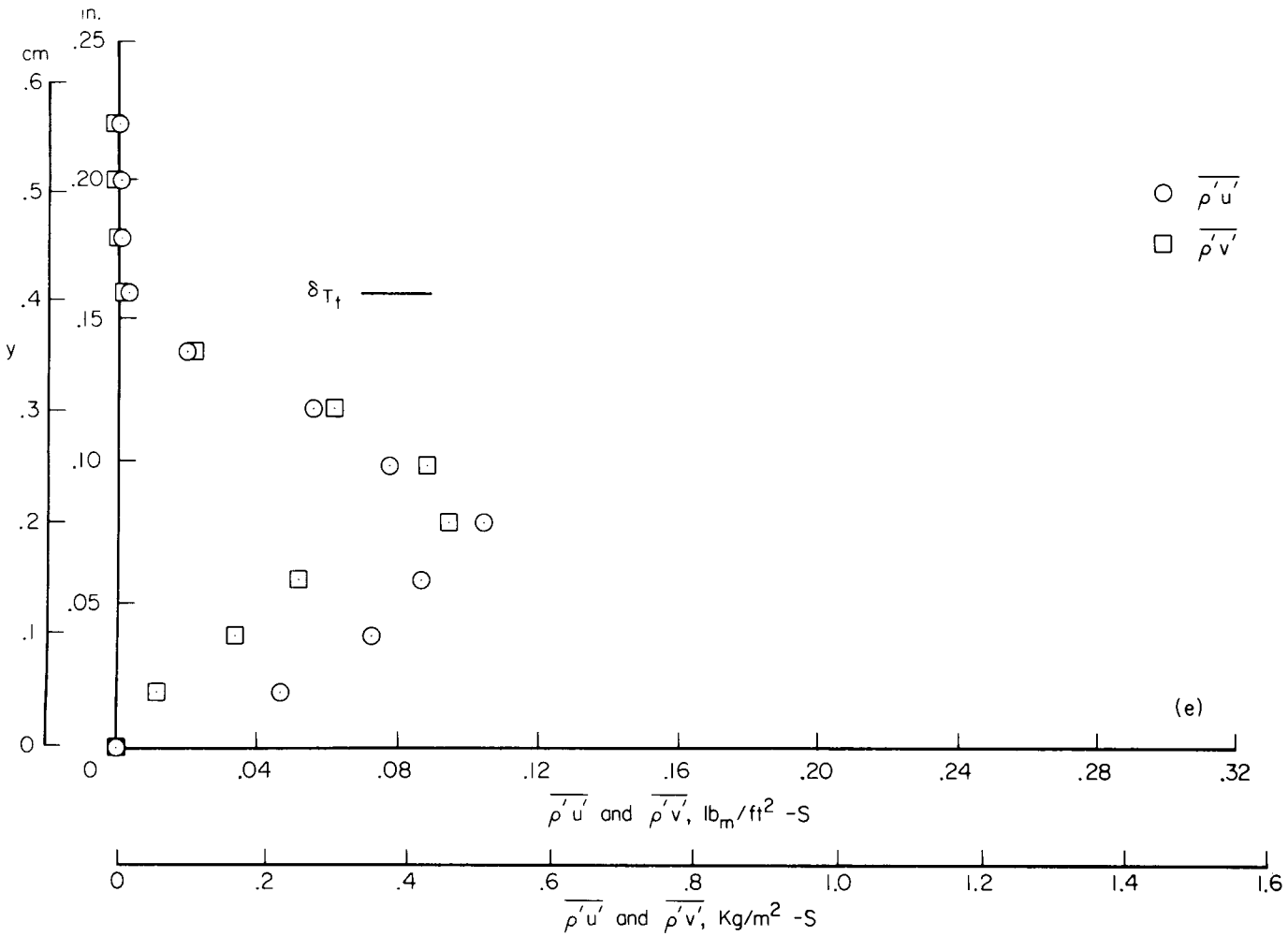

(e) x = 3.20 in. (8.13 cm)

Figure 14.- Continued.

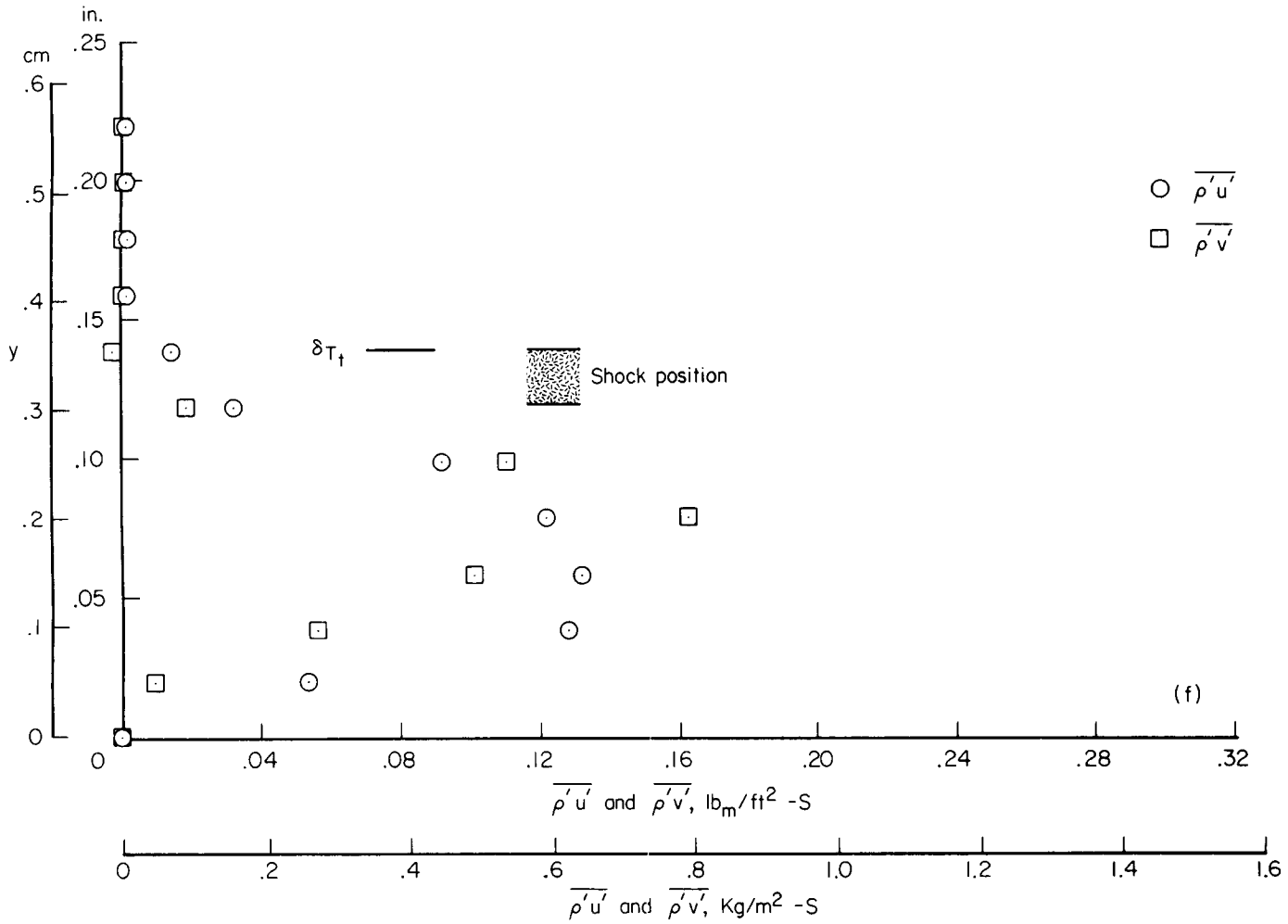

(f) x = 3.40 in. (8.64 cm)

Figure 14.- Continued.

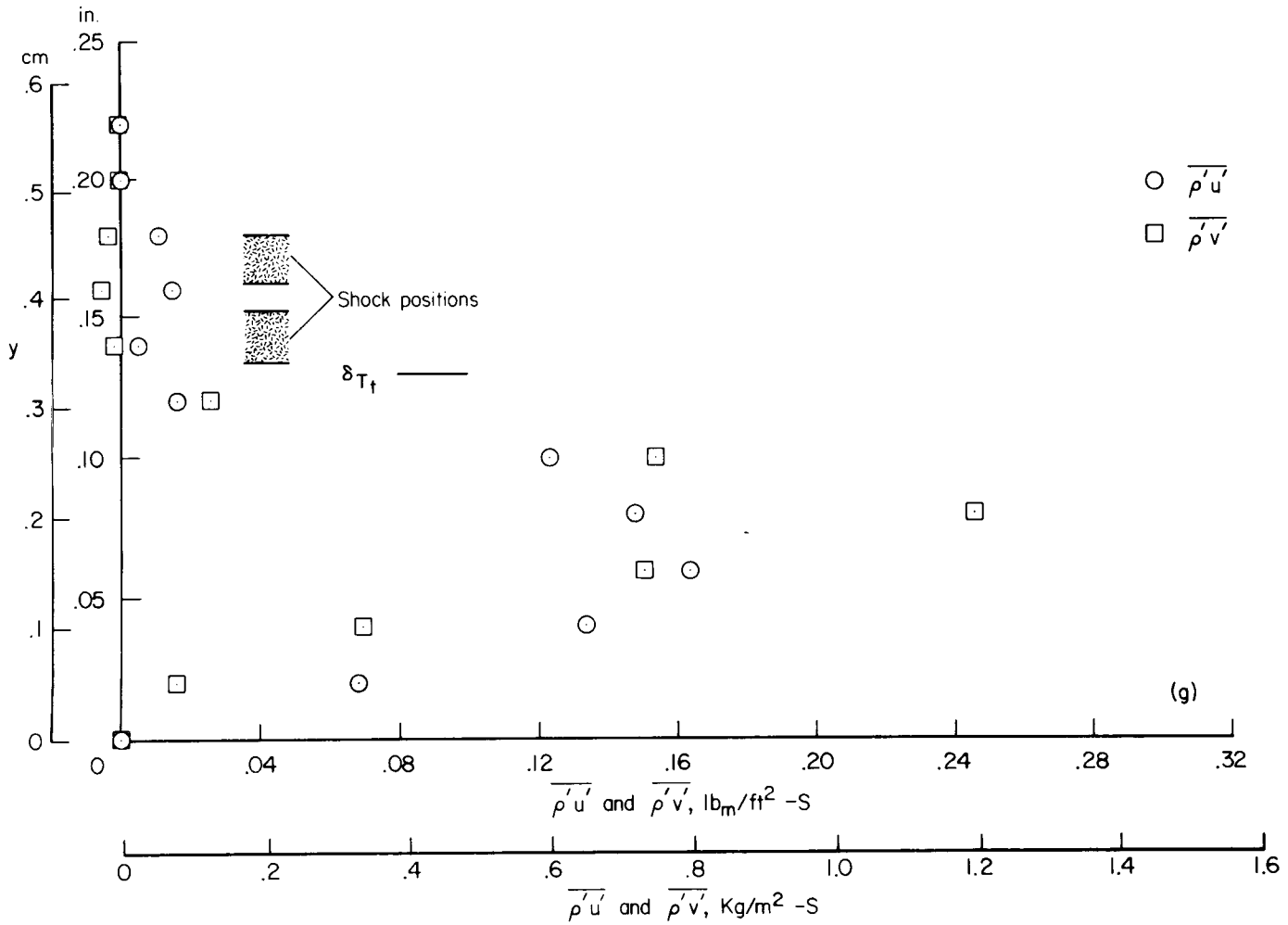

(g) x = 3.60 in. (9.15 cm)

Figure 14.- Continued.

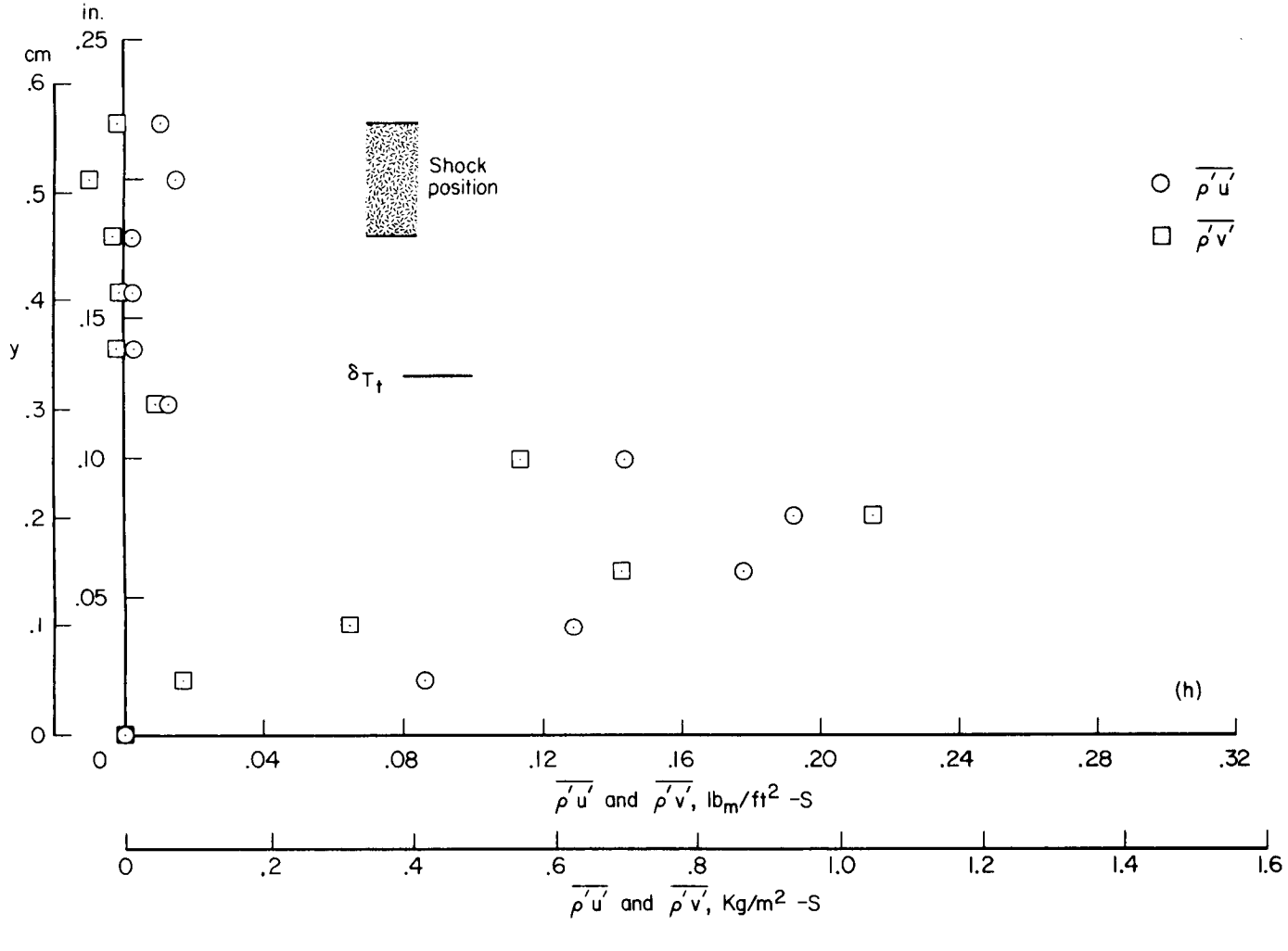

(h) x = 3.80 in. (9.66 cm)

Figure 14.- Continued.

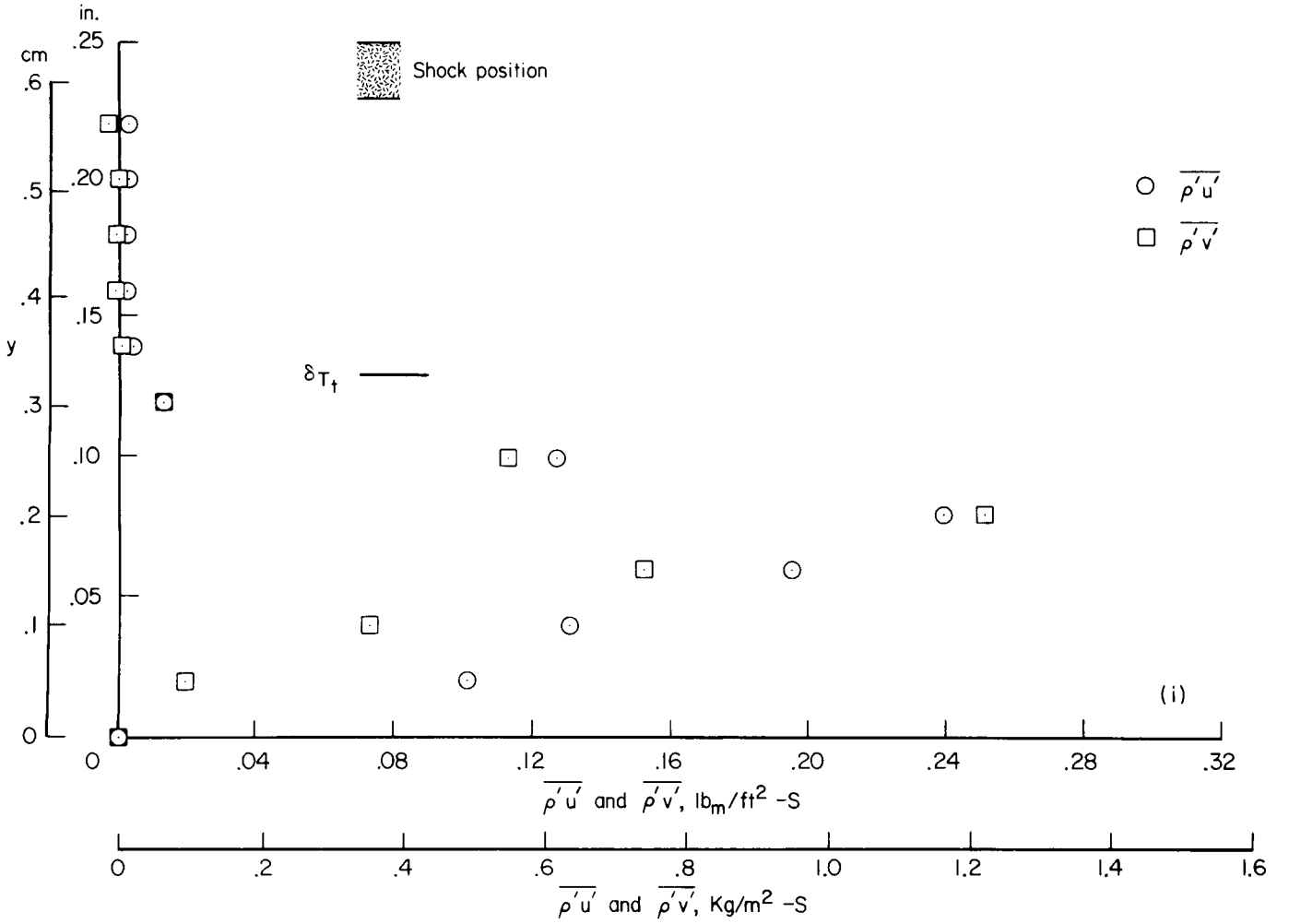

(i) x = 4.00 in. (10.16 cm)

Figure 14.- Continued.

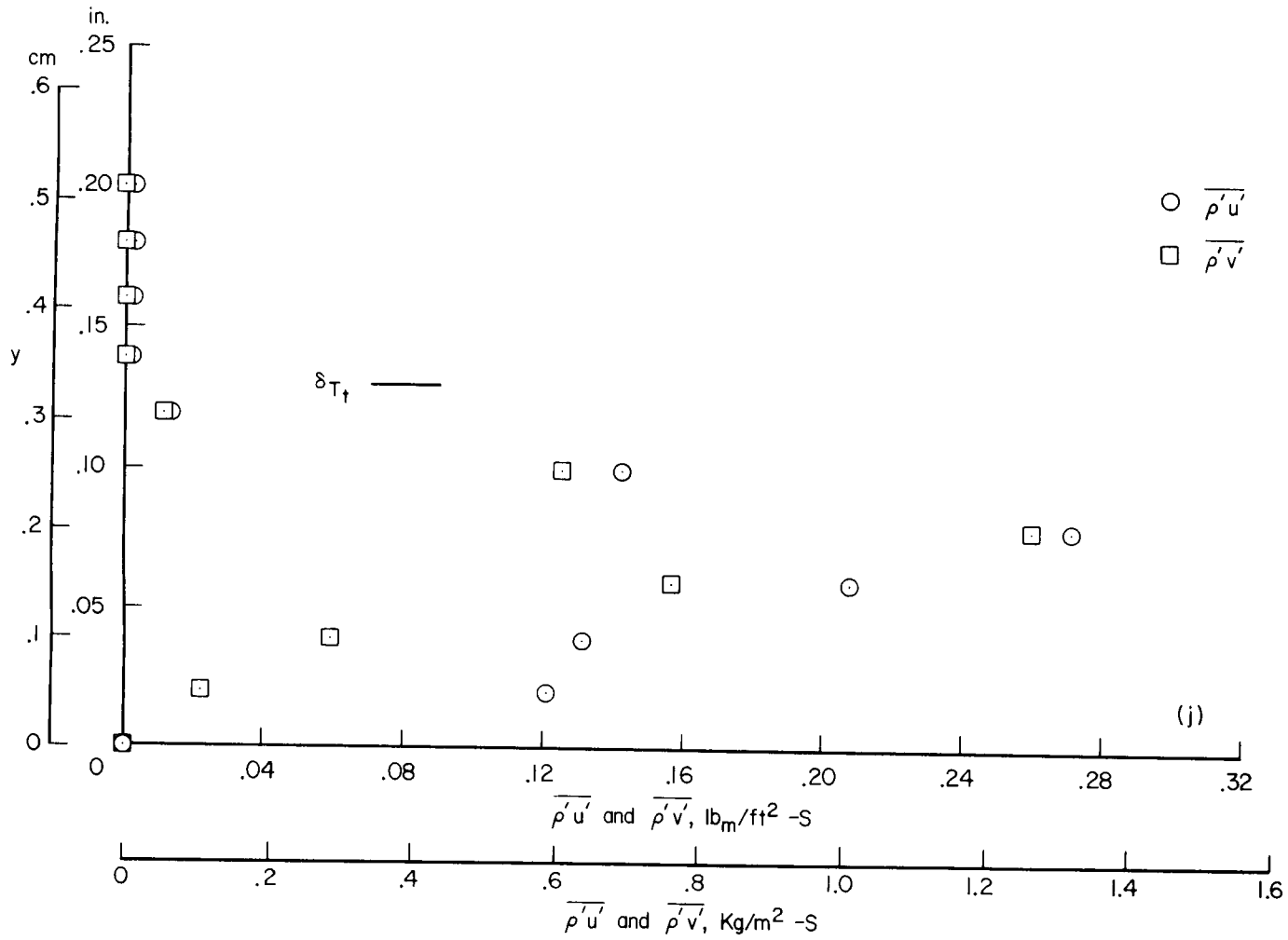

(j) x = 4.20 in. (10.67 cm)

Figure 14.- Continued.

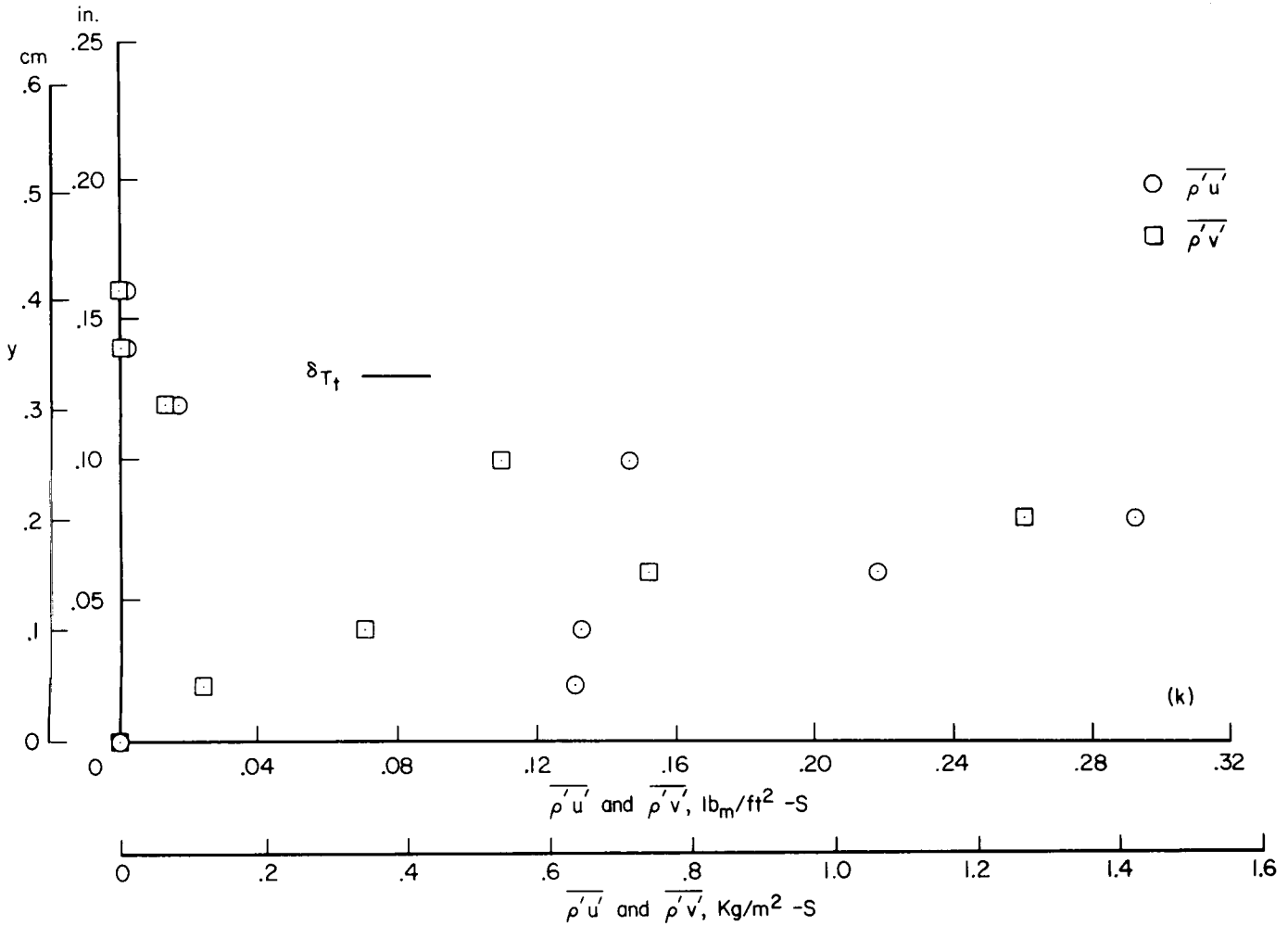

(k) x = 4.40 in. (11.18 cm)

Figure 14.- Continued.

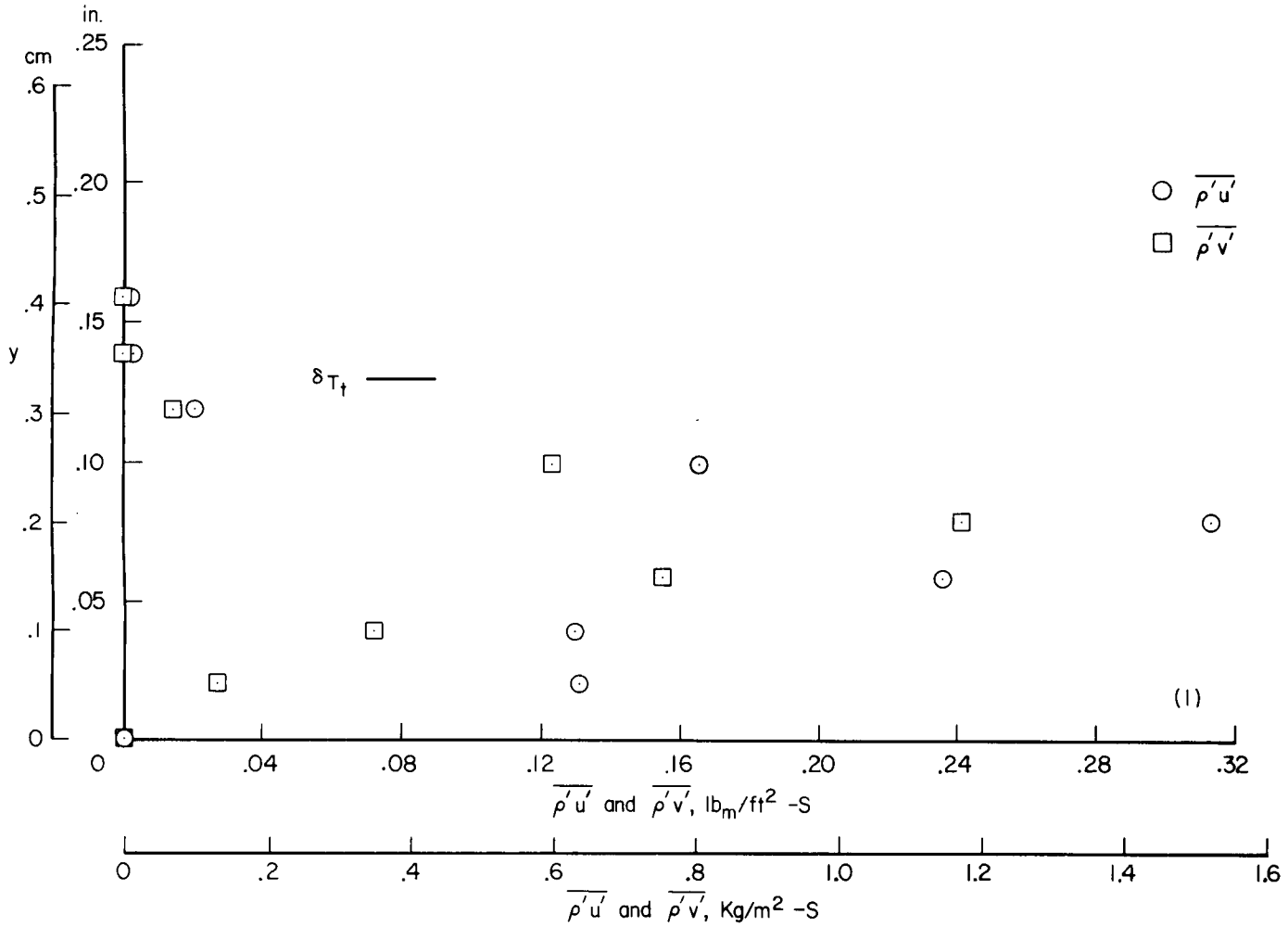

(ℓ) x = 4.60 in. (11.68 cm)

Figure 14.- Concluded.

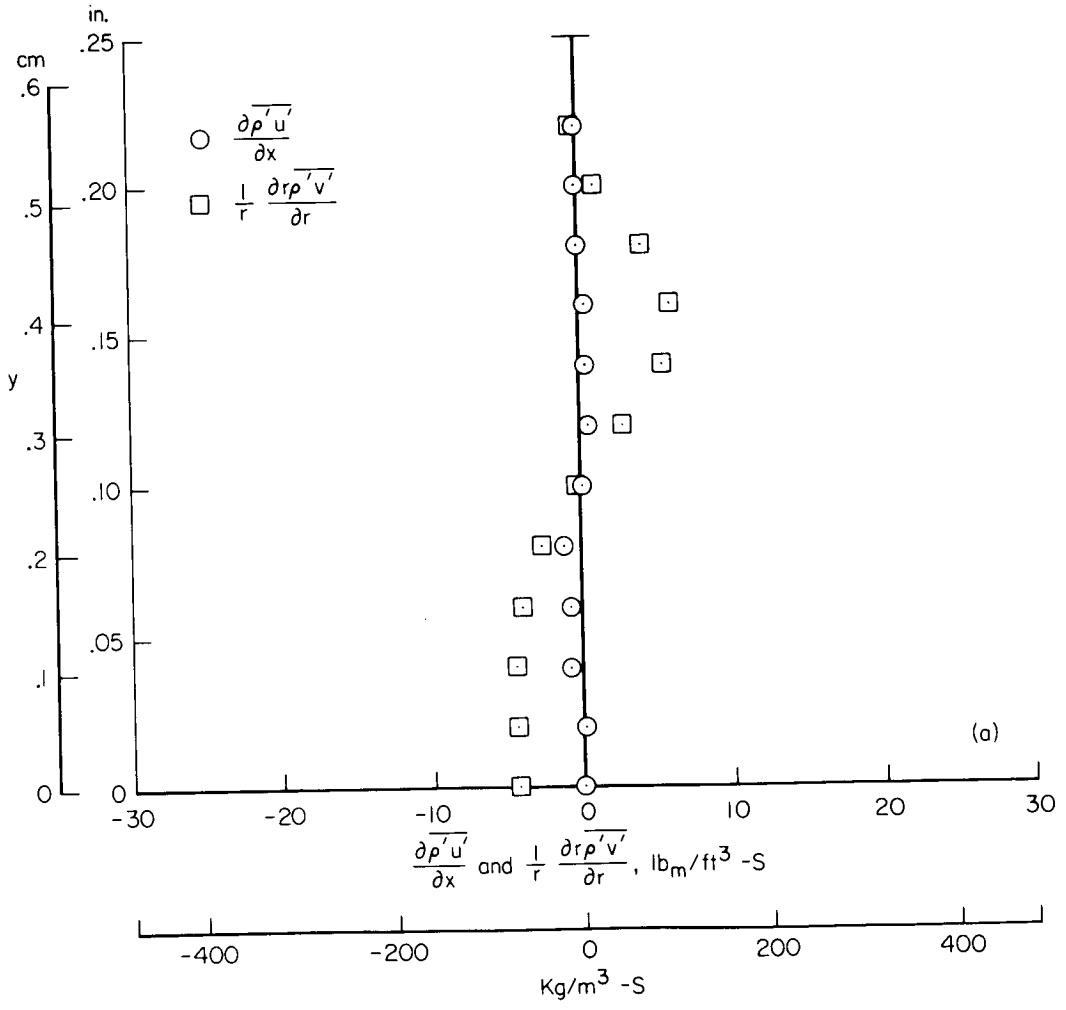

(a) x = 2.40 in. (6.10 cm)

Figure 15.- Gradients of fluctuating terms from continuity equation (eq. (10)).

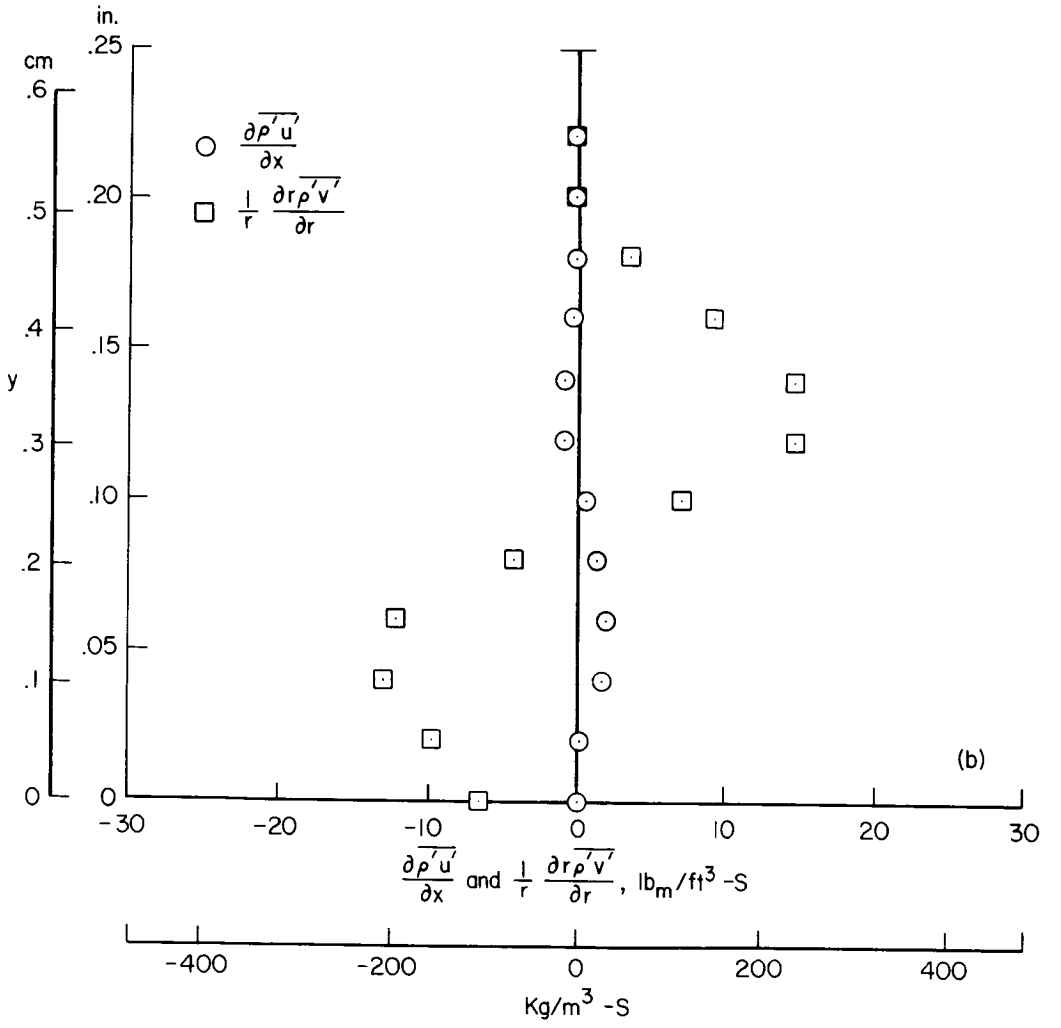

(b) x = 3.20 in. (8.13 cm)

Figure 15.- Continued.

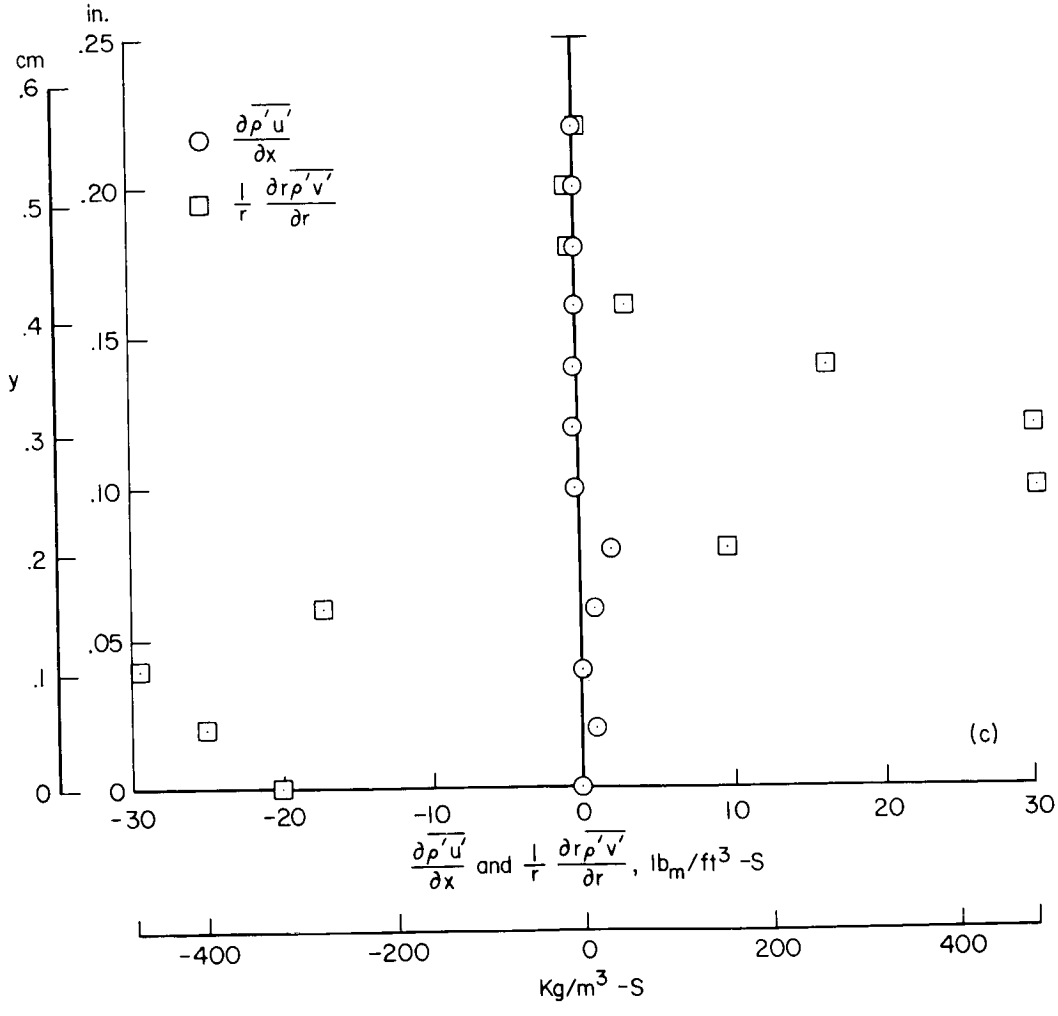

(c) x = 3.80 in. (9.66 cm)

Figure 15.- Continued.

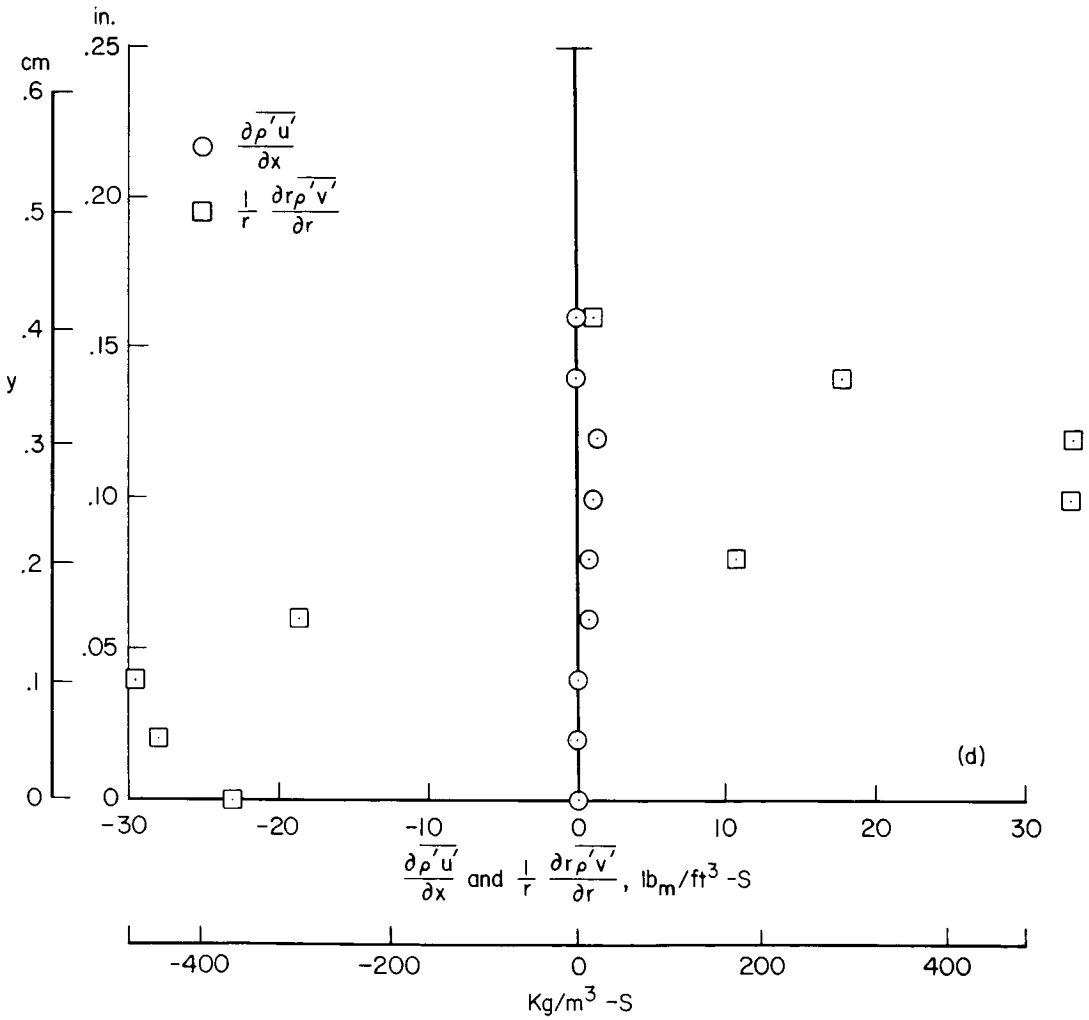

(d) x = 4.60 in. (11.68 cm)

Figure 15.- Concluded.

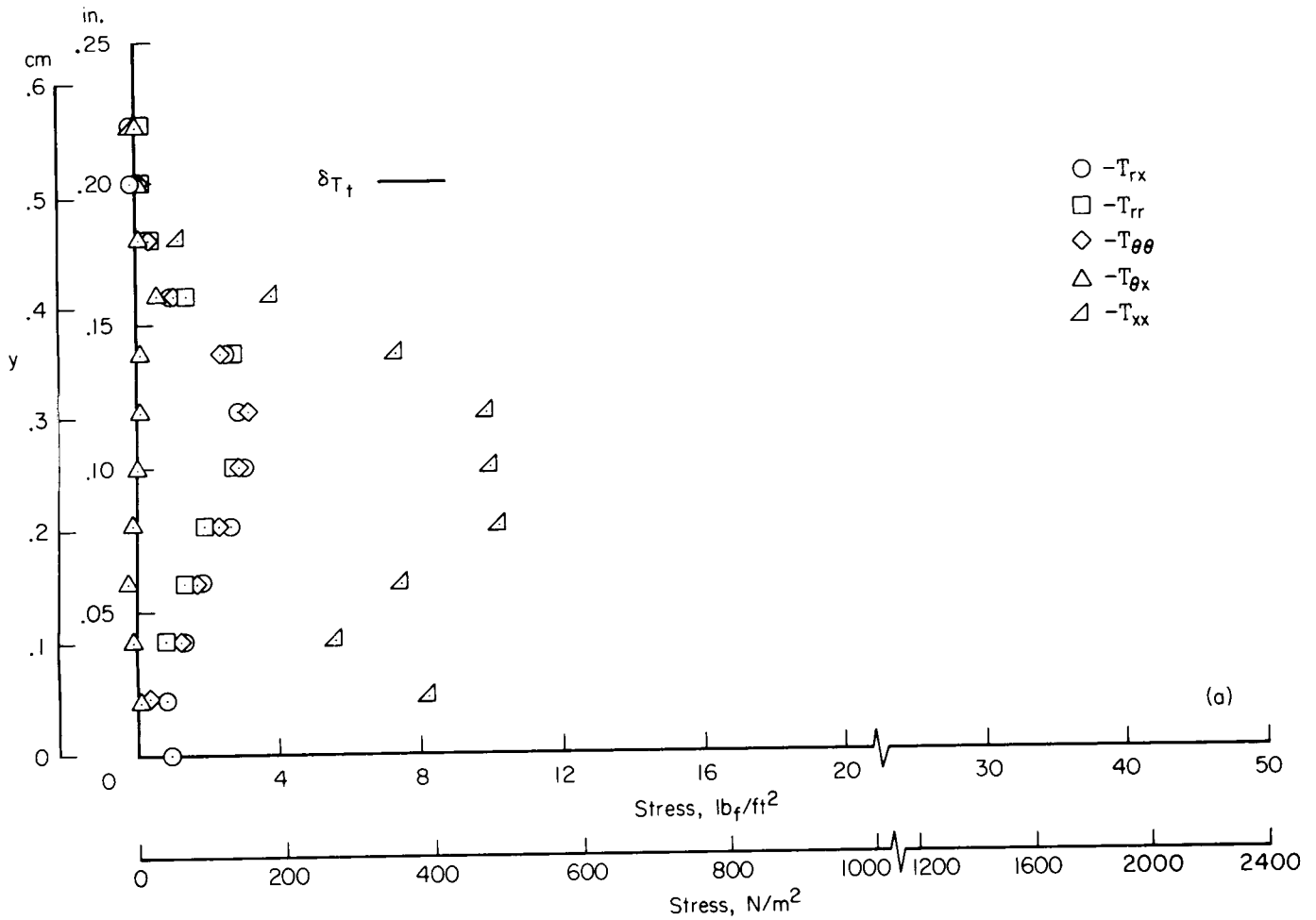

(a) x = 2.40 in. (6.10 cm)

Figure 16.- Reynolds stress terms.

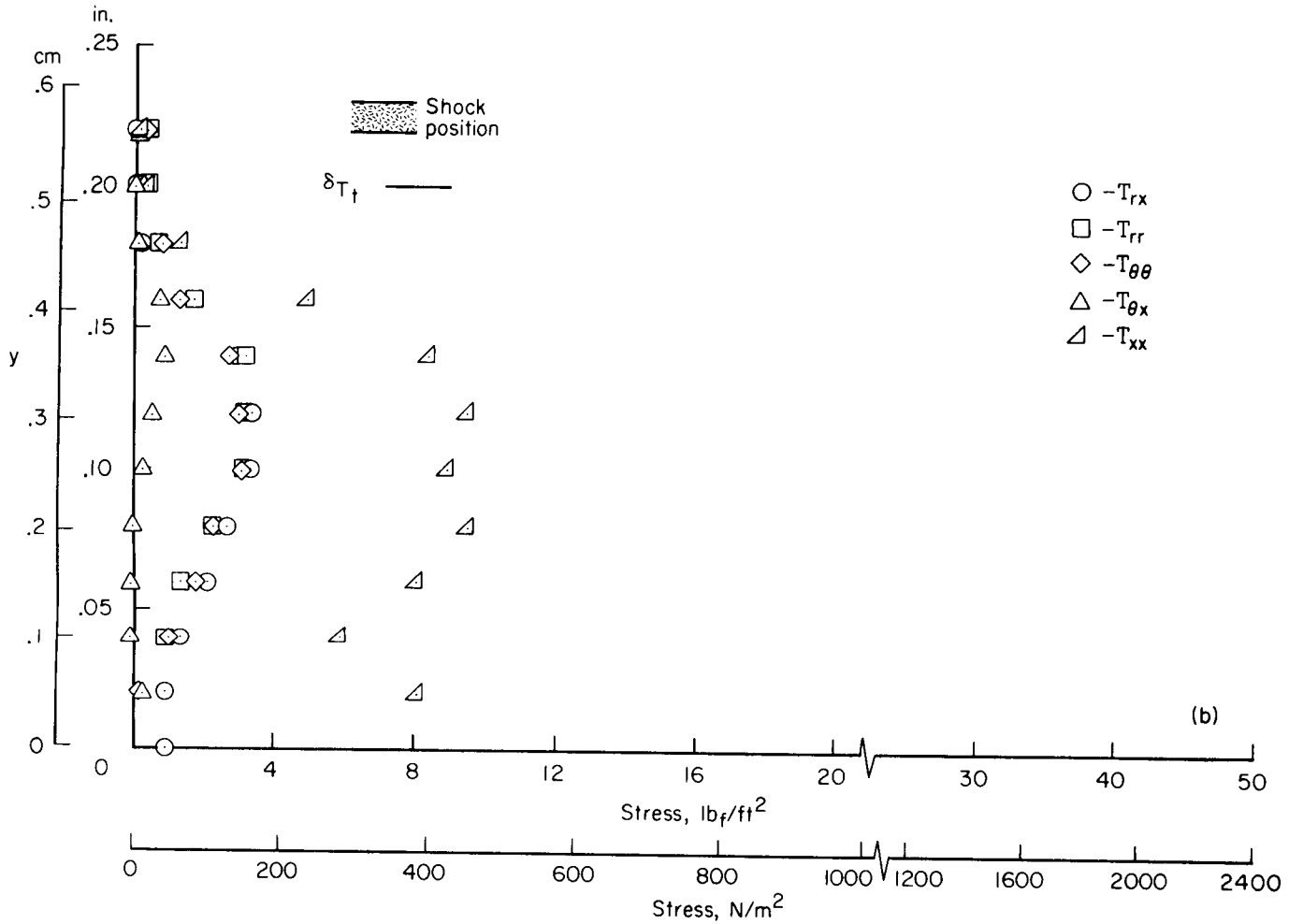

(b) x = 2.60 in. (6.60 cm)

Figure 16.- Continued.

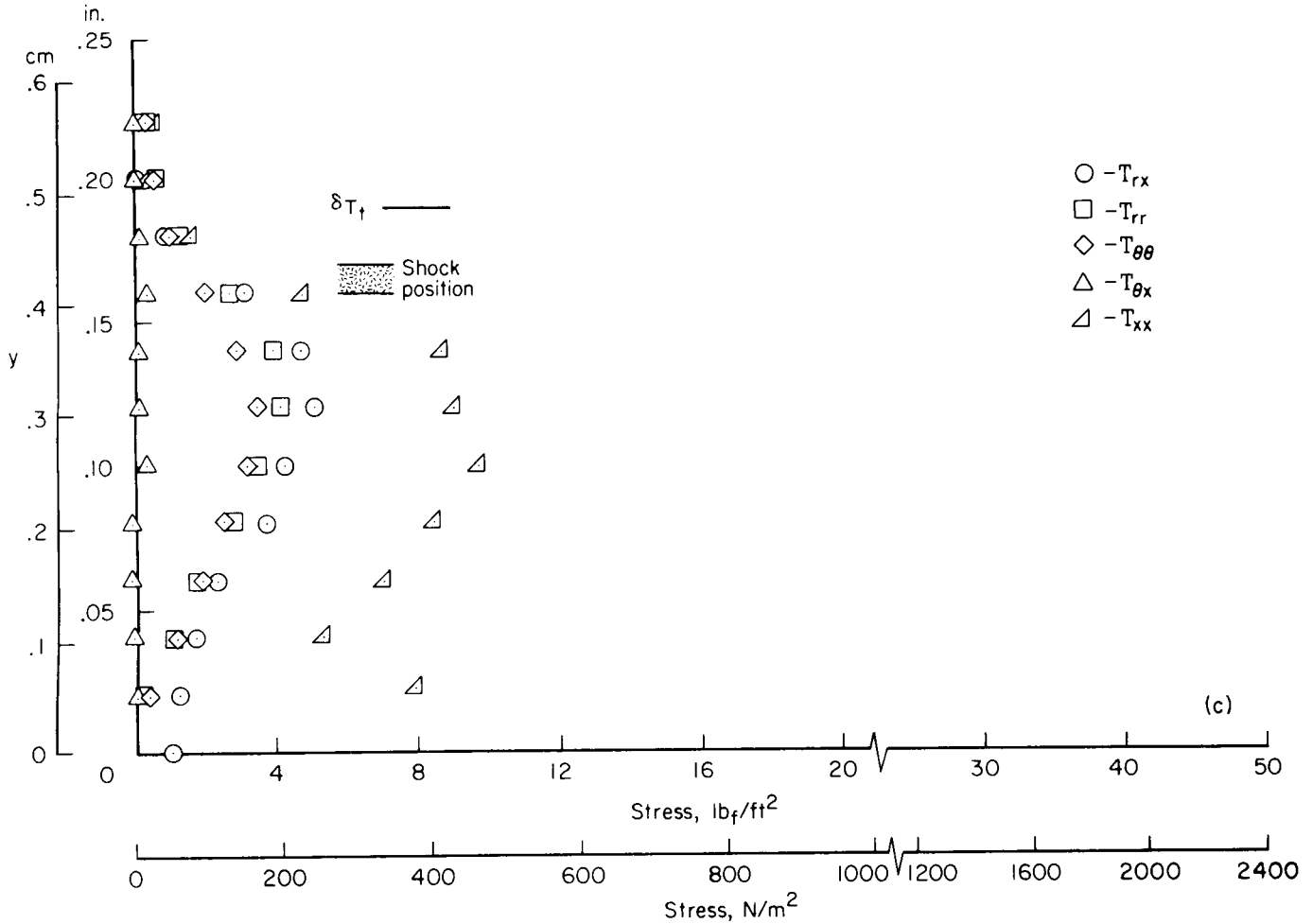

(c) x = 2.80 in. (7.11 cm)

Figure 16.- Continued.

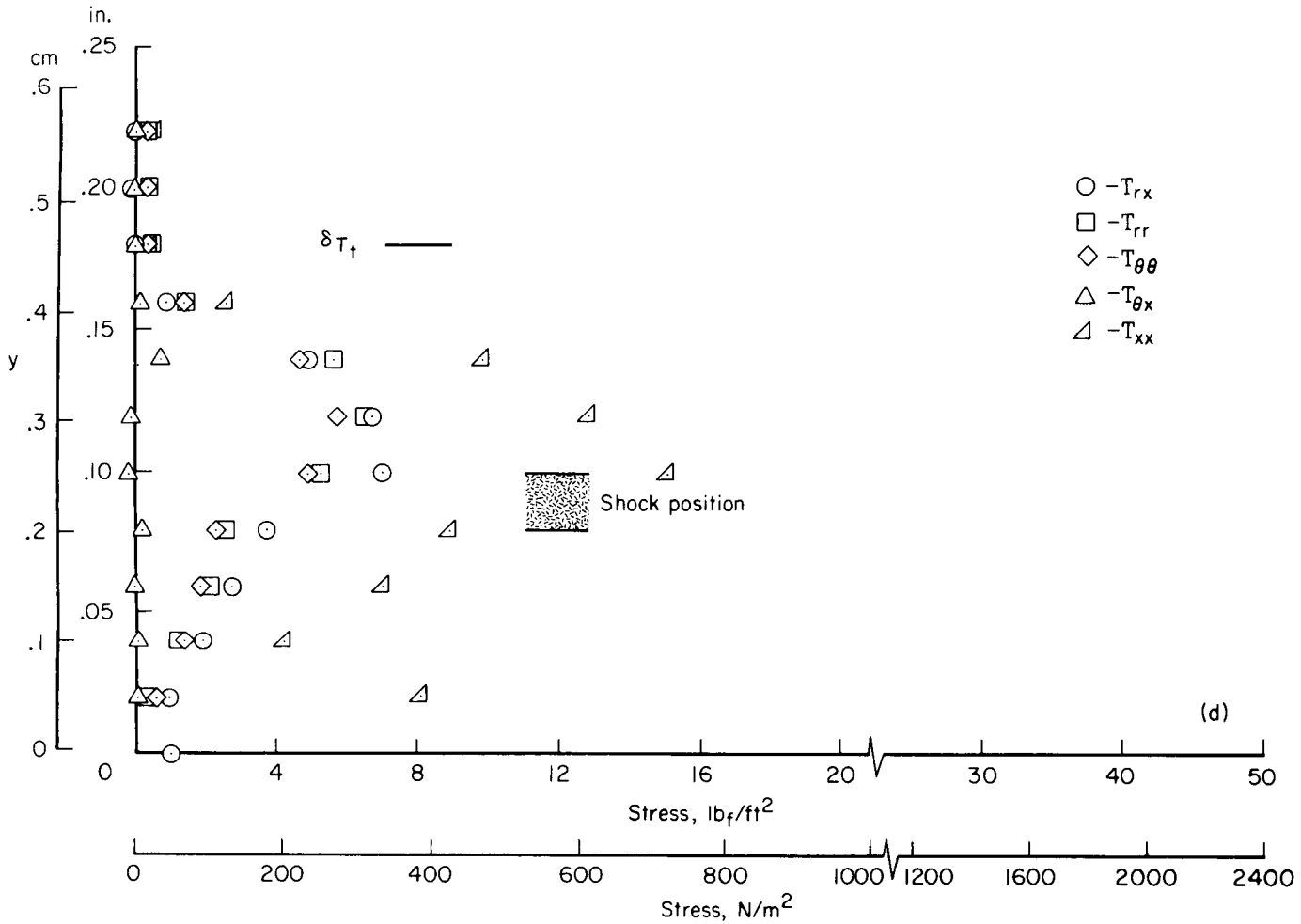

(d) x = 3.00 in. (7.62 cm)

Figure 16.- Continued.

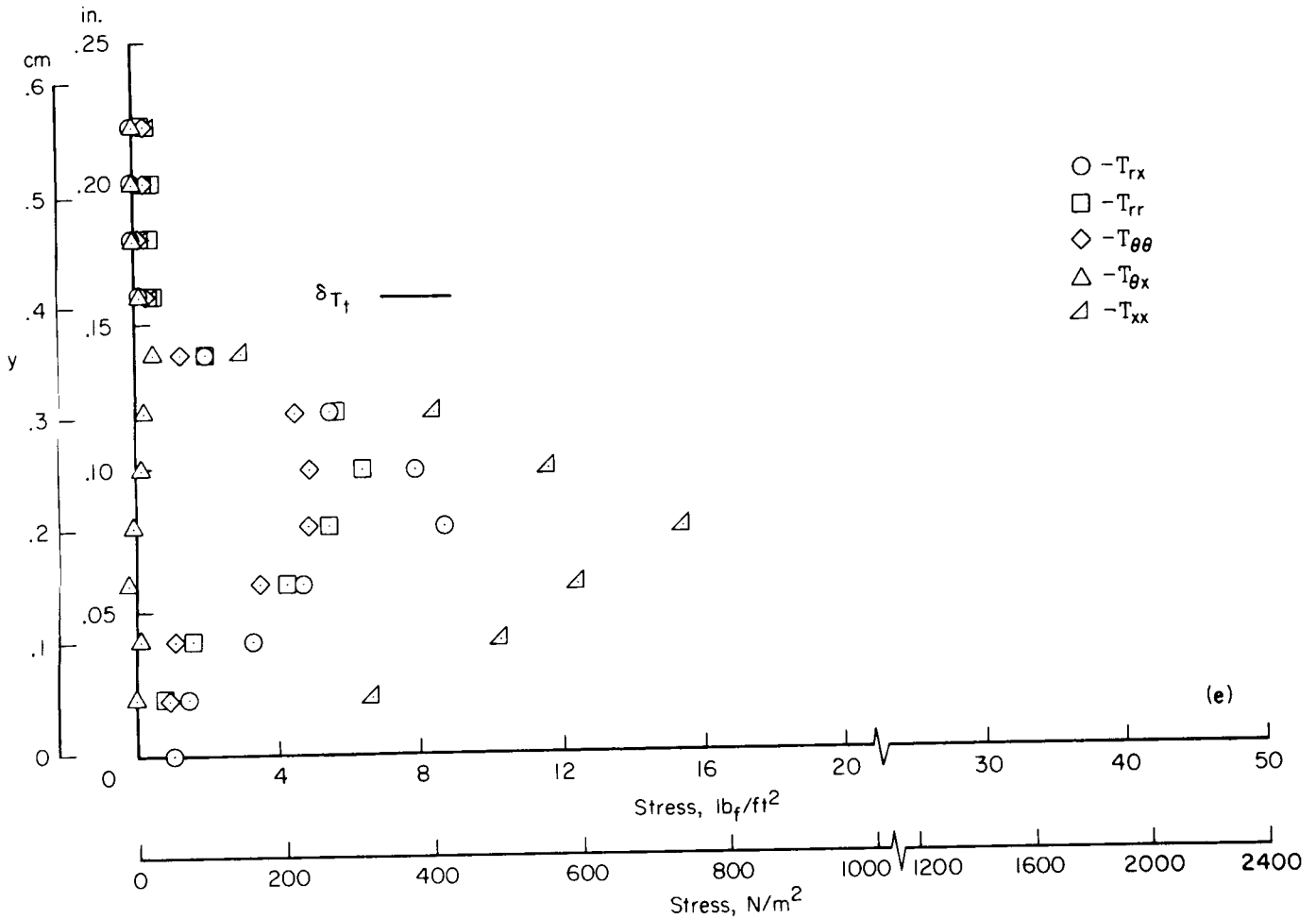

(e) x = 3.20 in. (8.13 cm)

Figure 16.- Continued.

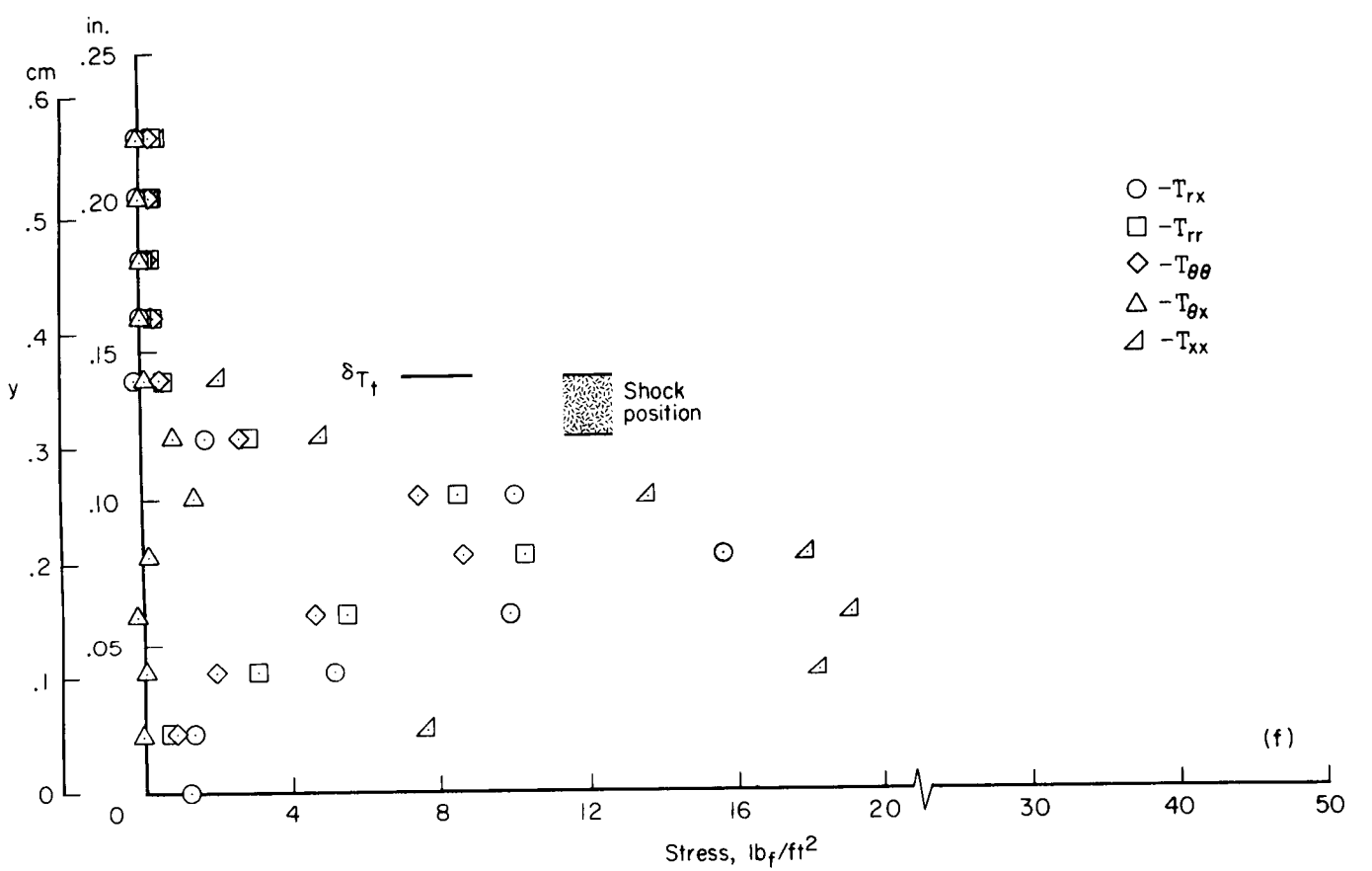

(f) x = 3.40 in. (8.64 cm)

Figure 16.- Continued.

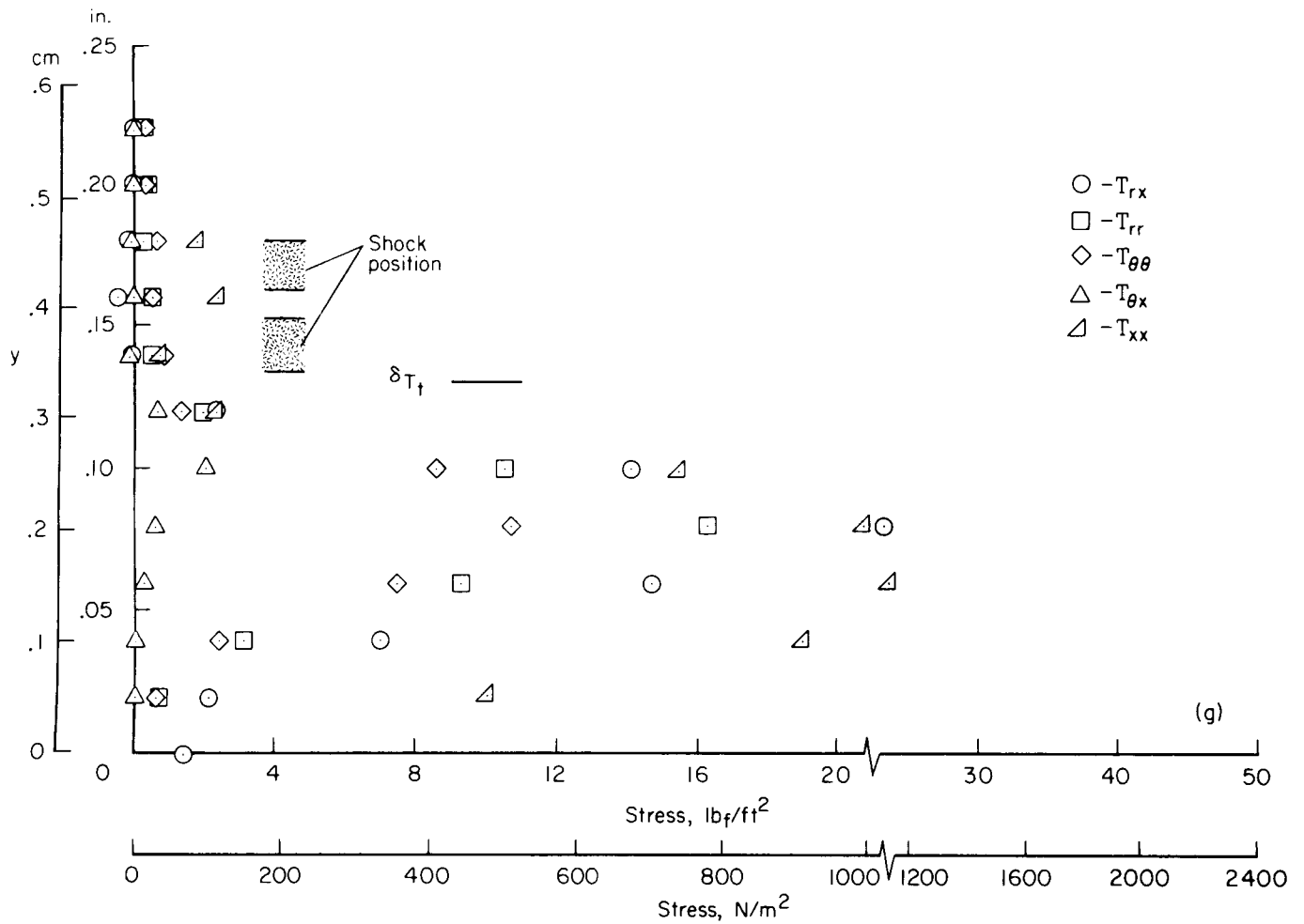

(g) x = 3.60 in. (9.15 cm)

Figure 16.- Continued.

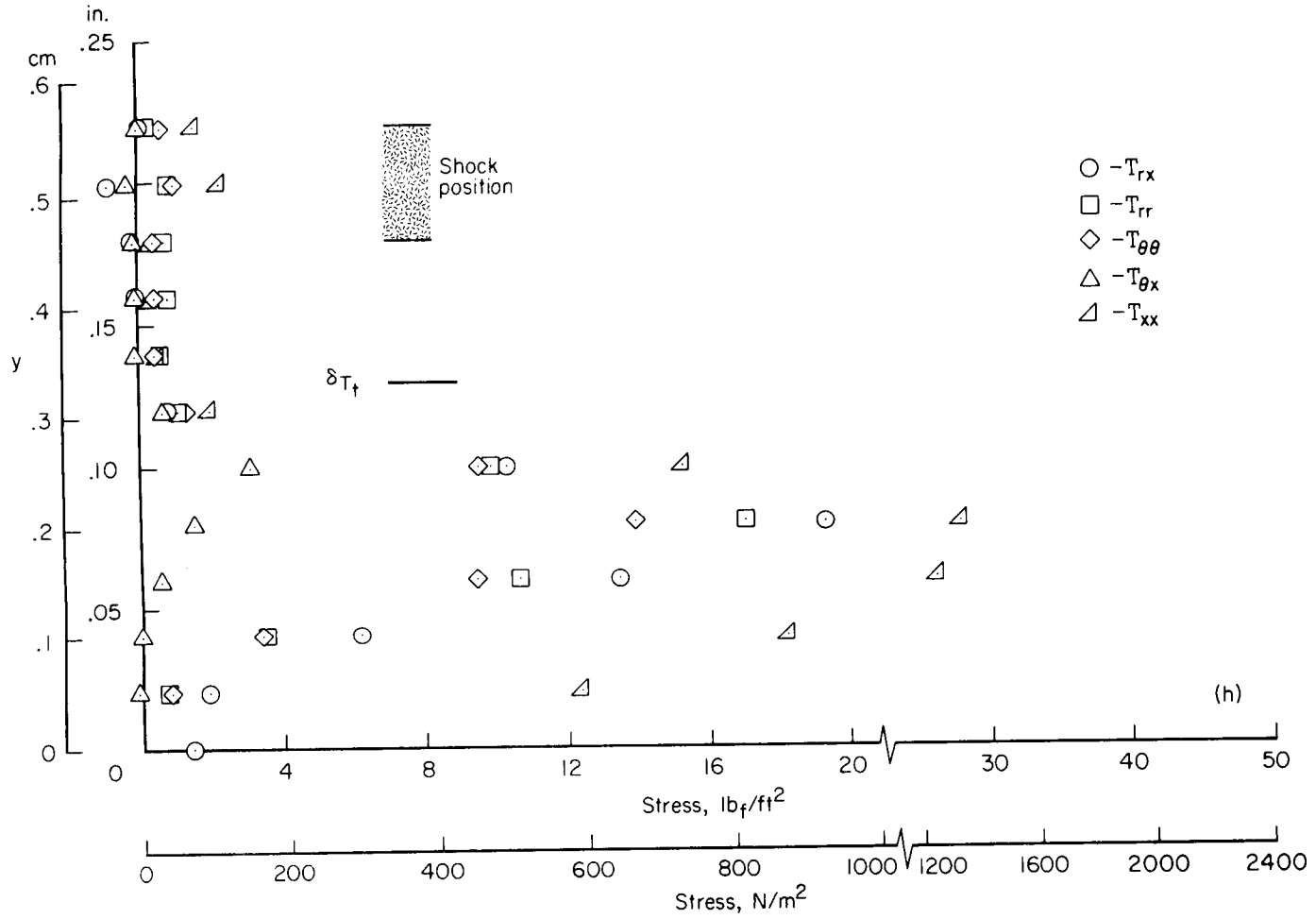

(h) x = 3.80 in. (9.66 cm)

Figure 16.- Continued.

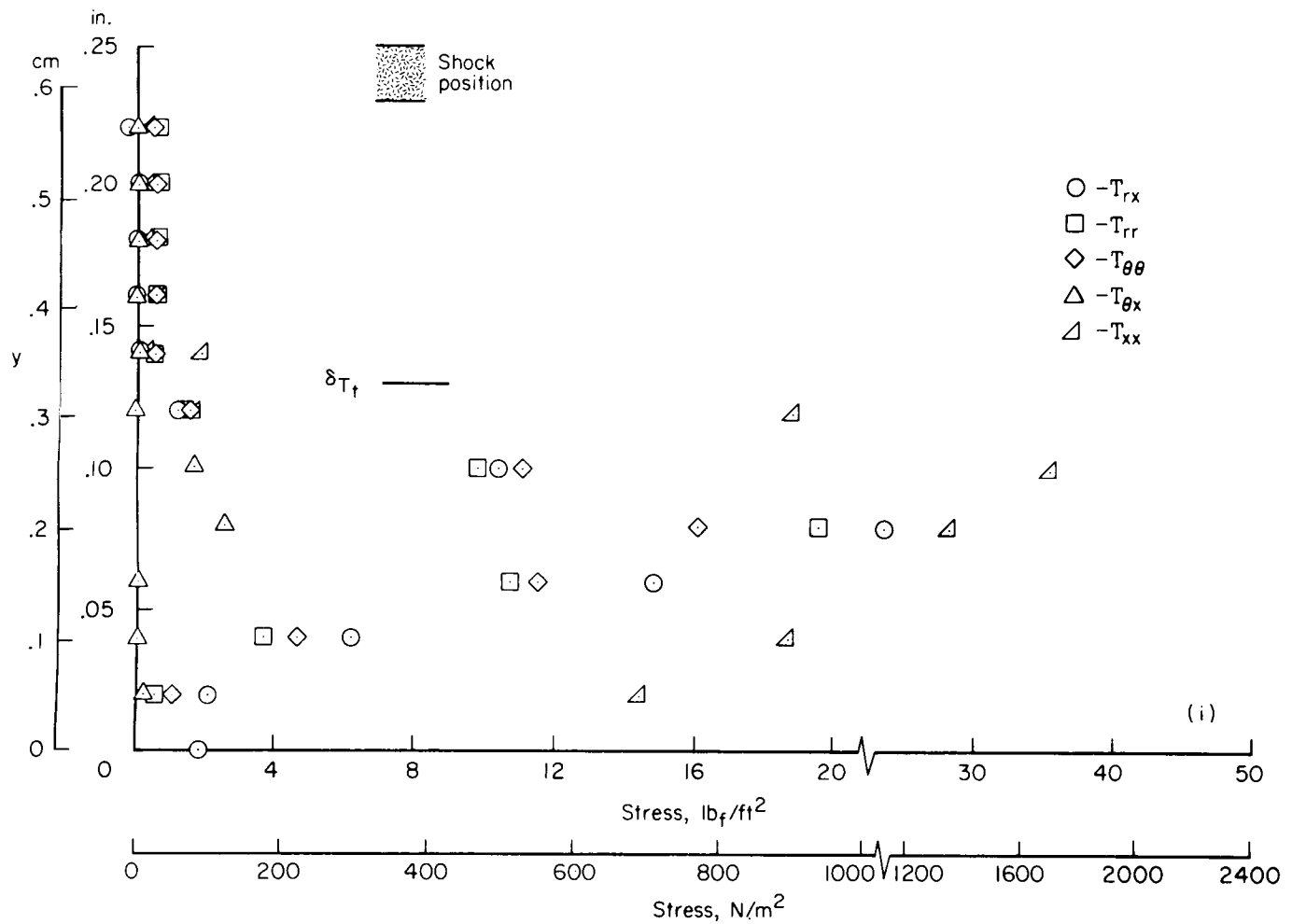

(i) x = 4.00 in. (10.16 cm)

Figure 16.- Continued.

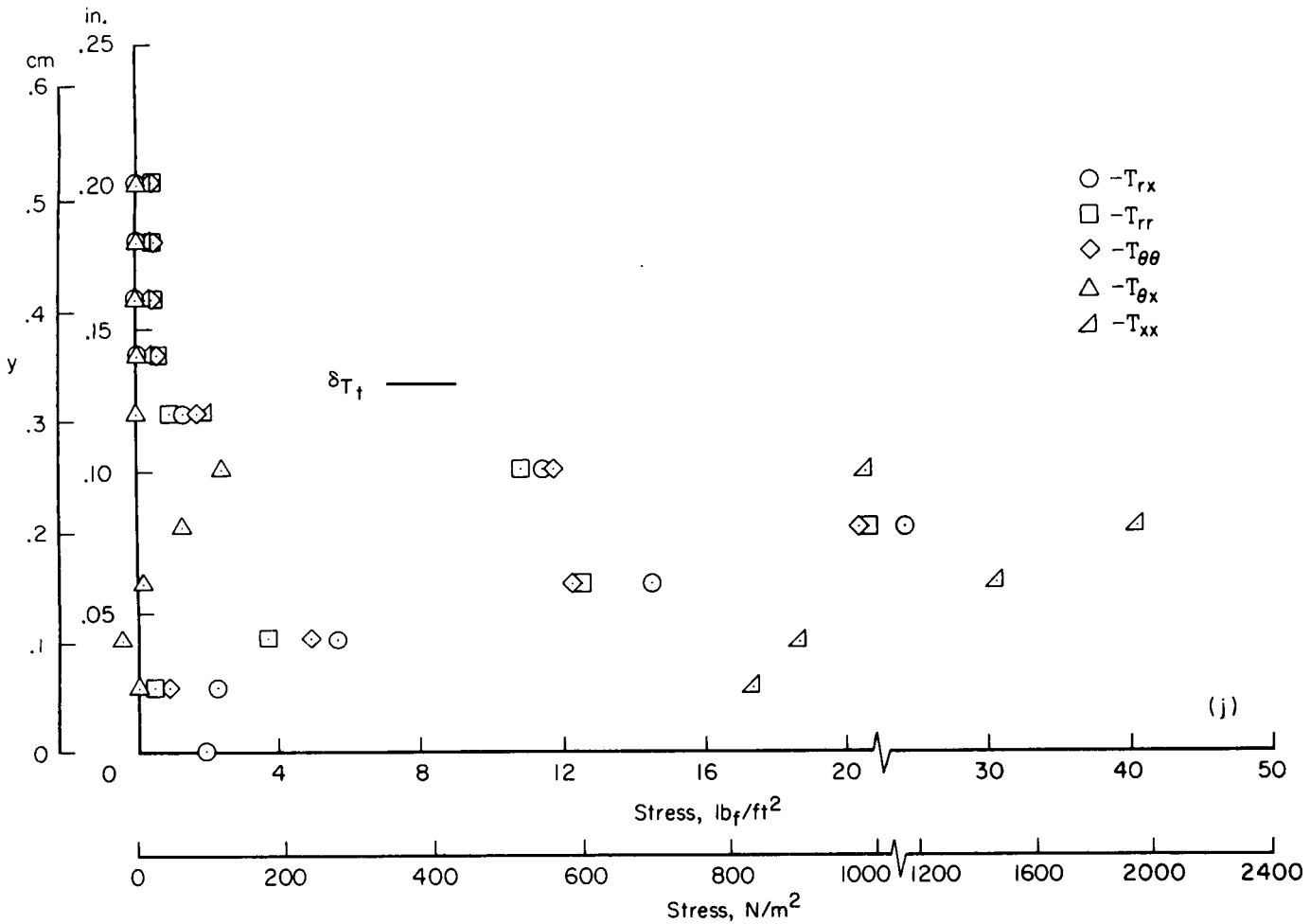

(j) x = 4.20 in. (10.67 cm)

Figure 16.- Continued.

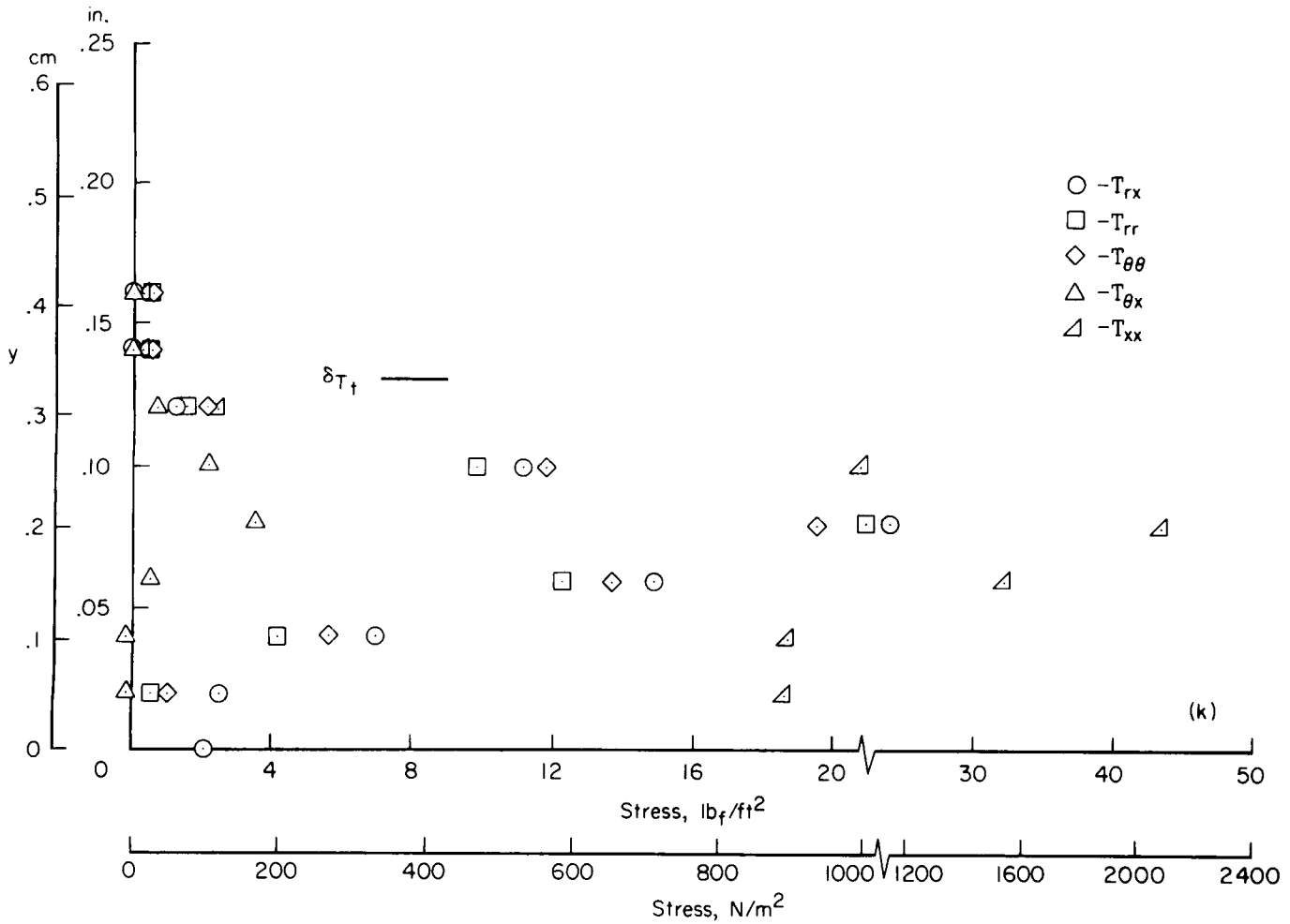

(k) x = 4.40 in. (11.18 cm)

Figure 16.- Continued.

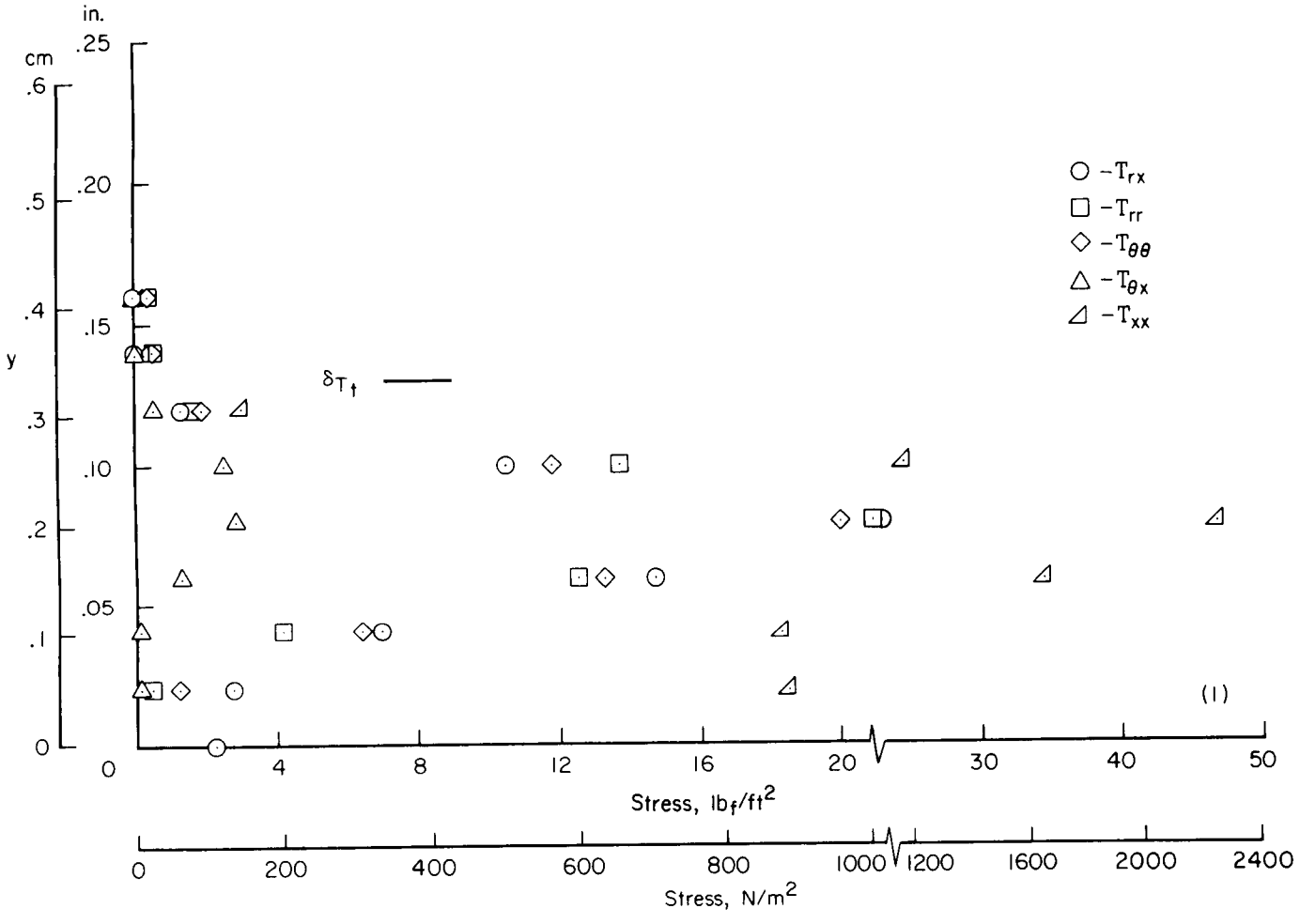

(ℓ) x = 4.60 in. (11.68 cm)

Figure 16.- Concluded.

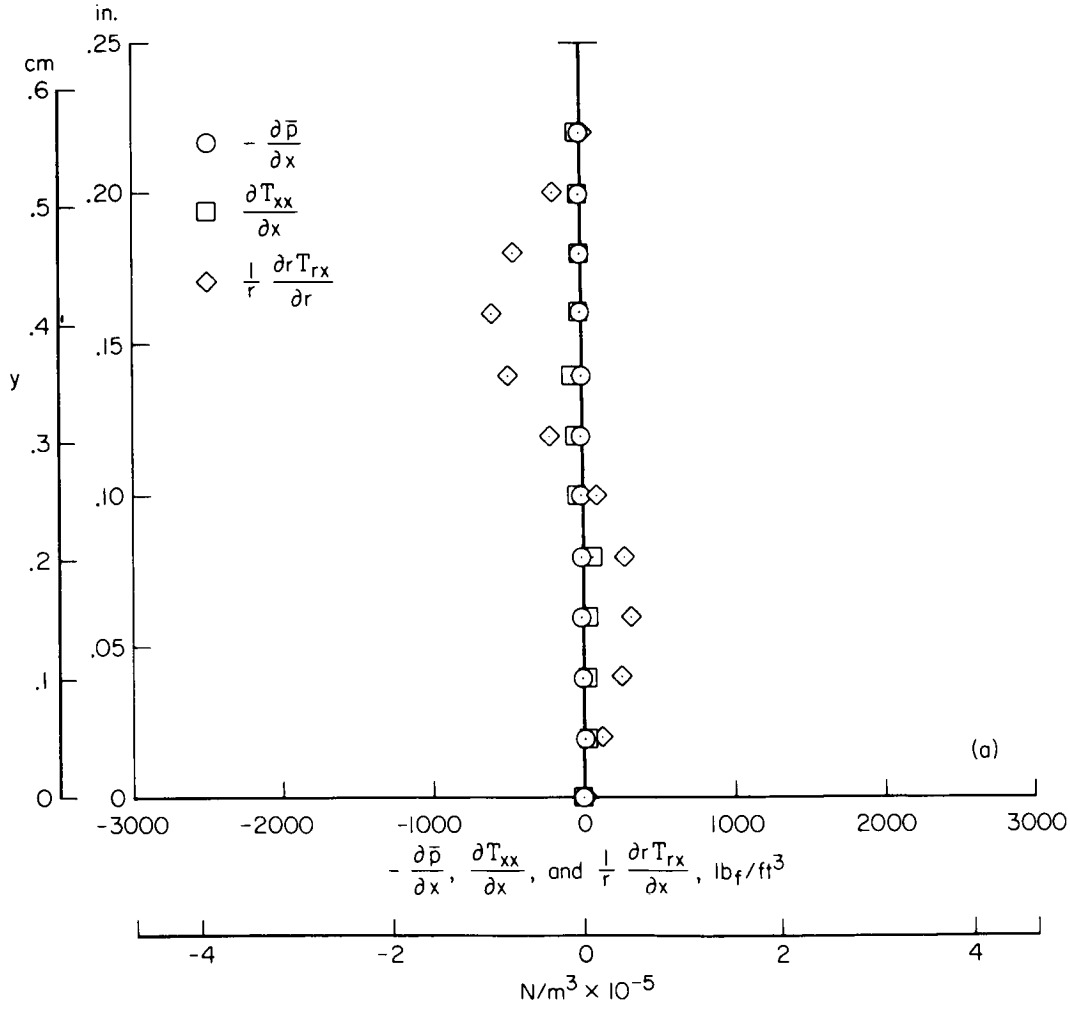

(a) x = 2.40 in. (6.10 cm)

Figure 17.- Gradients of terms from right-hand side of x-momentum equation (eq. 11(a)).

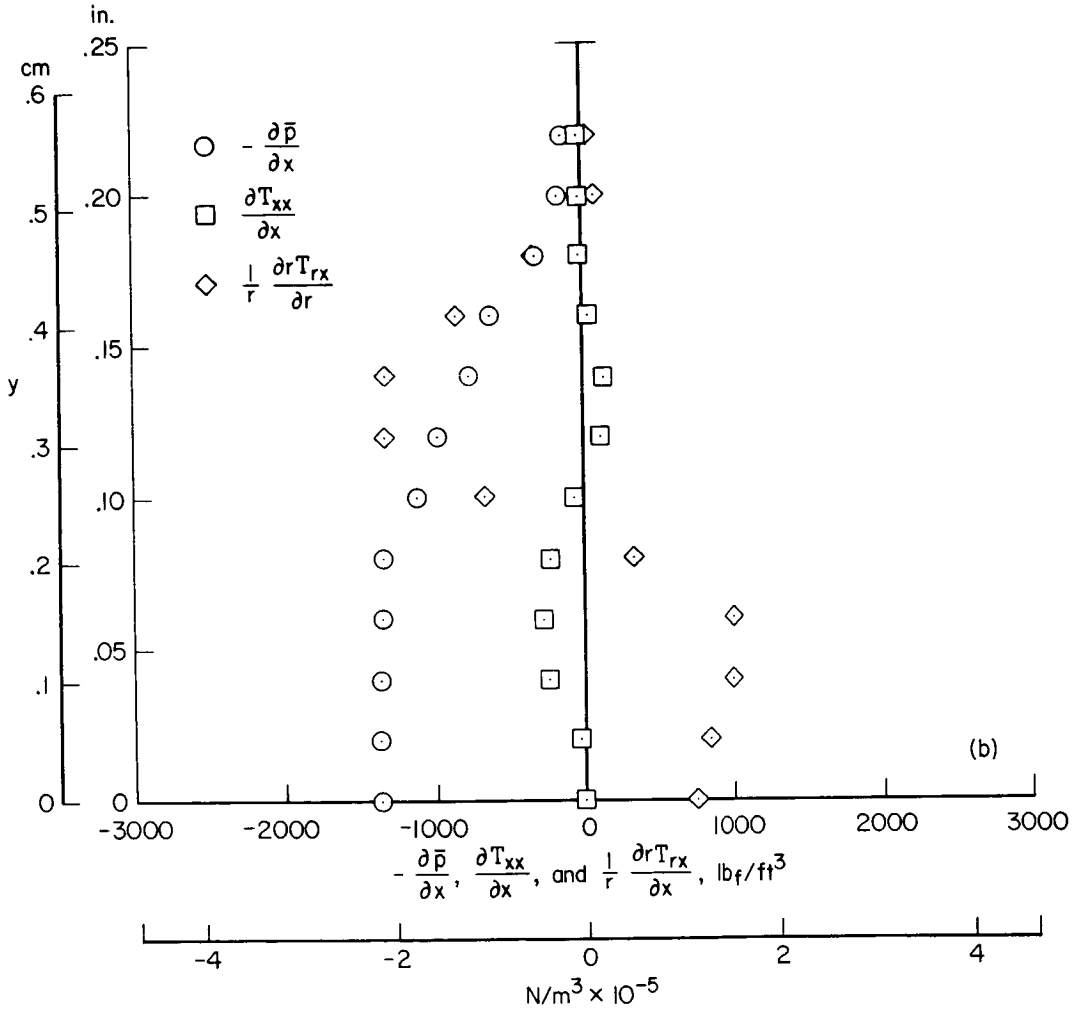

(b) x = 3.20 in. (8.13 cm)

Figure 17.- Continued.

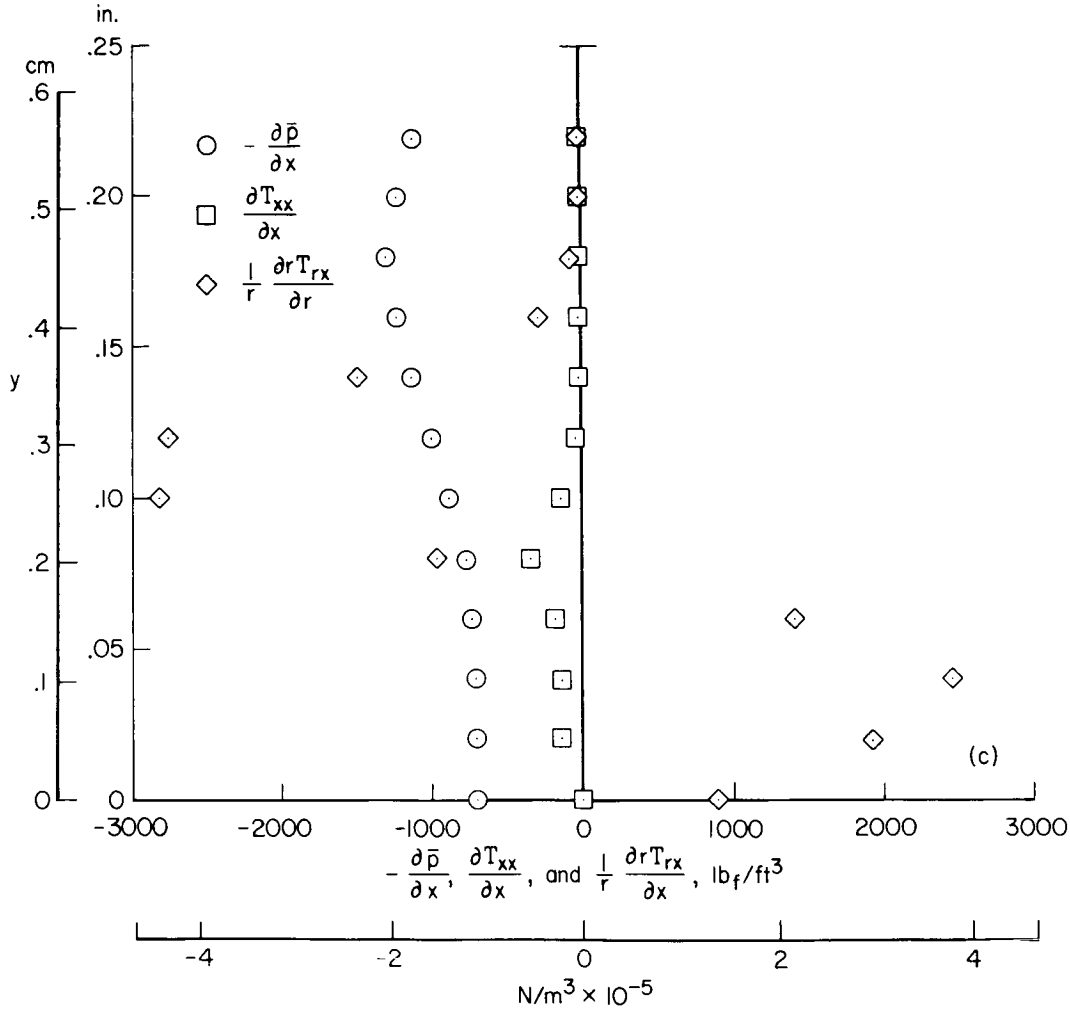

(c) x = 3.80 in. (9.66 cm)

Figure 17.- Continued.

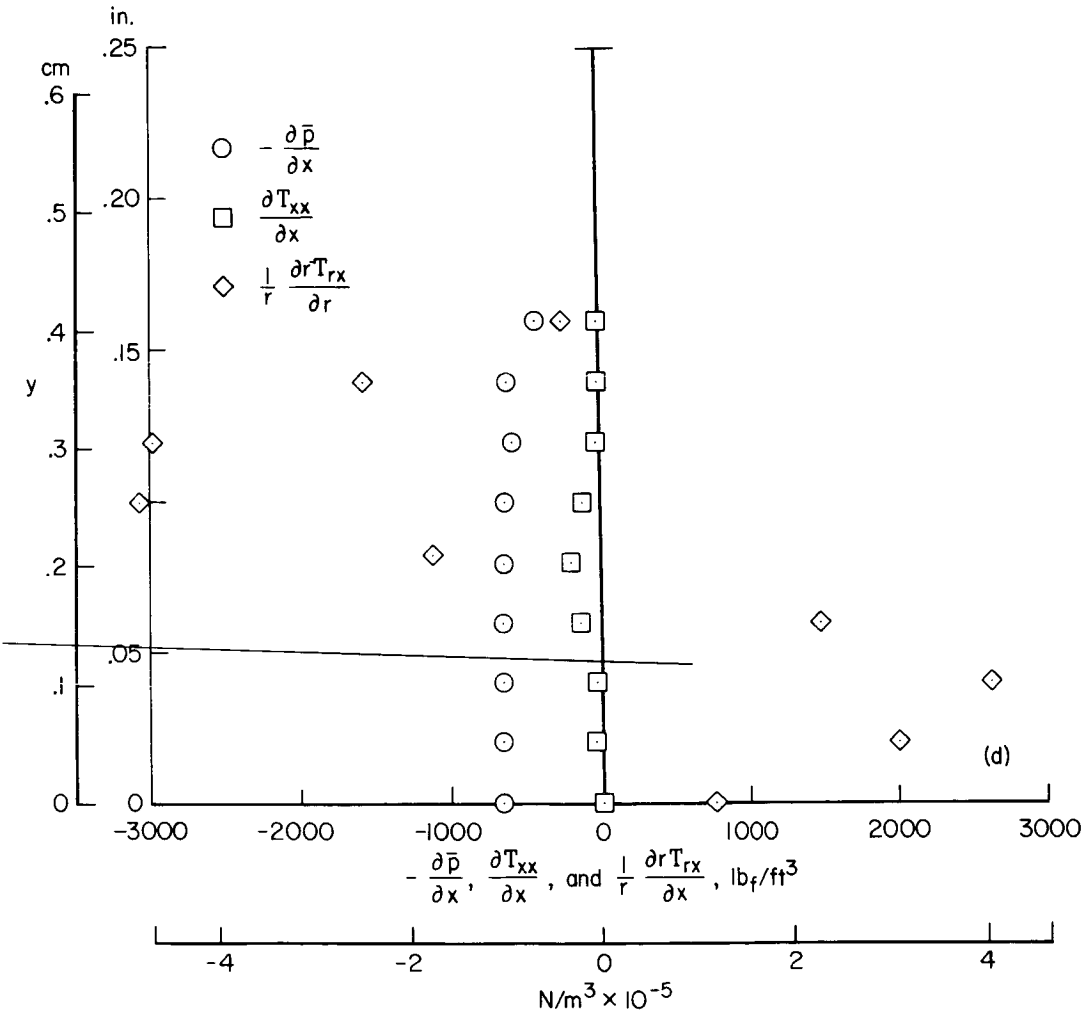

(d) x = 4.60 in. (11.68 cm)

Figure 17.- Concluded.

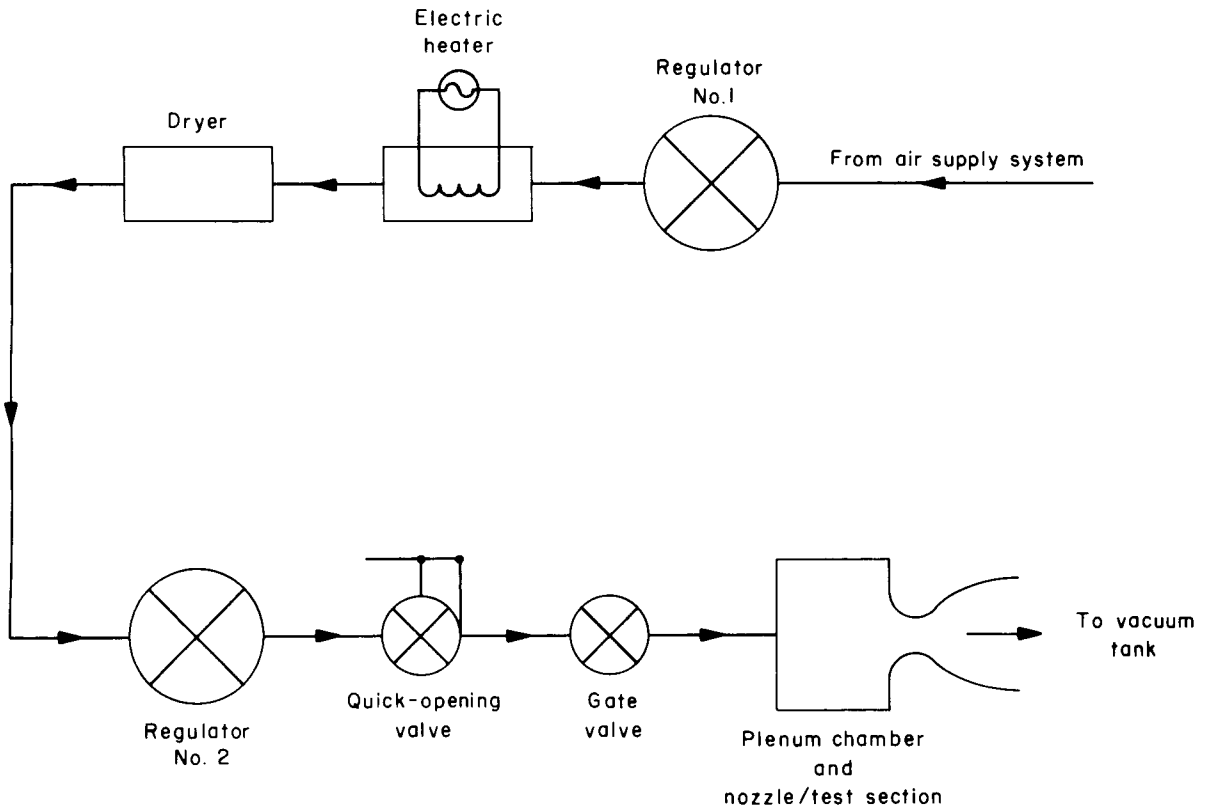

Figure 18.- Line drawing of air flow through experimental apparatus.

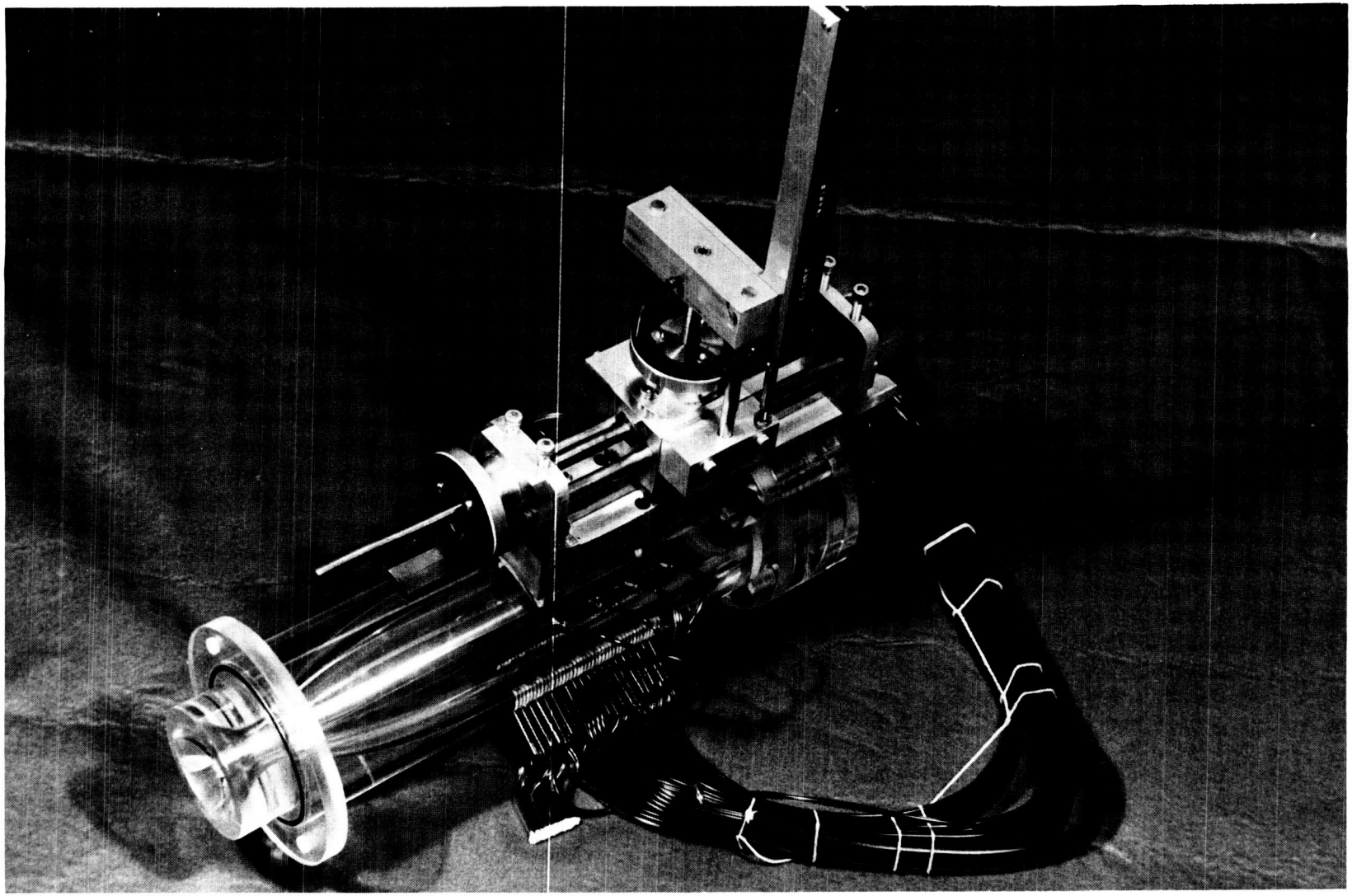

Figure 19.- Plexiglass nozzle/test section and probe drive.

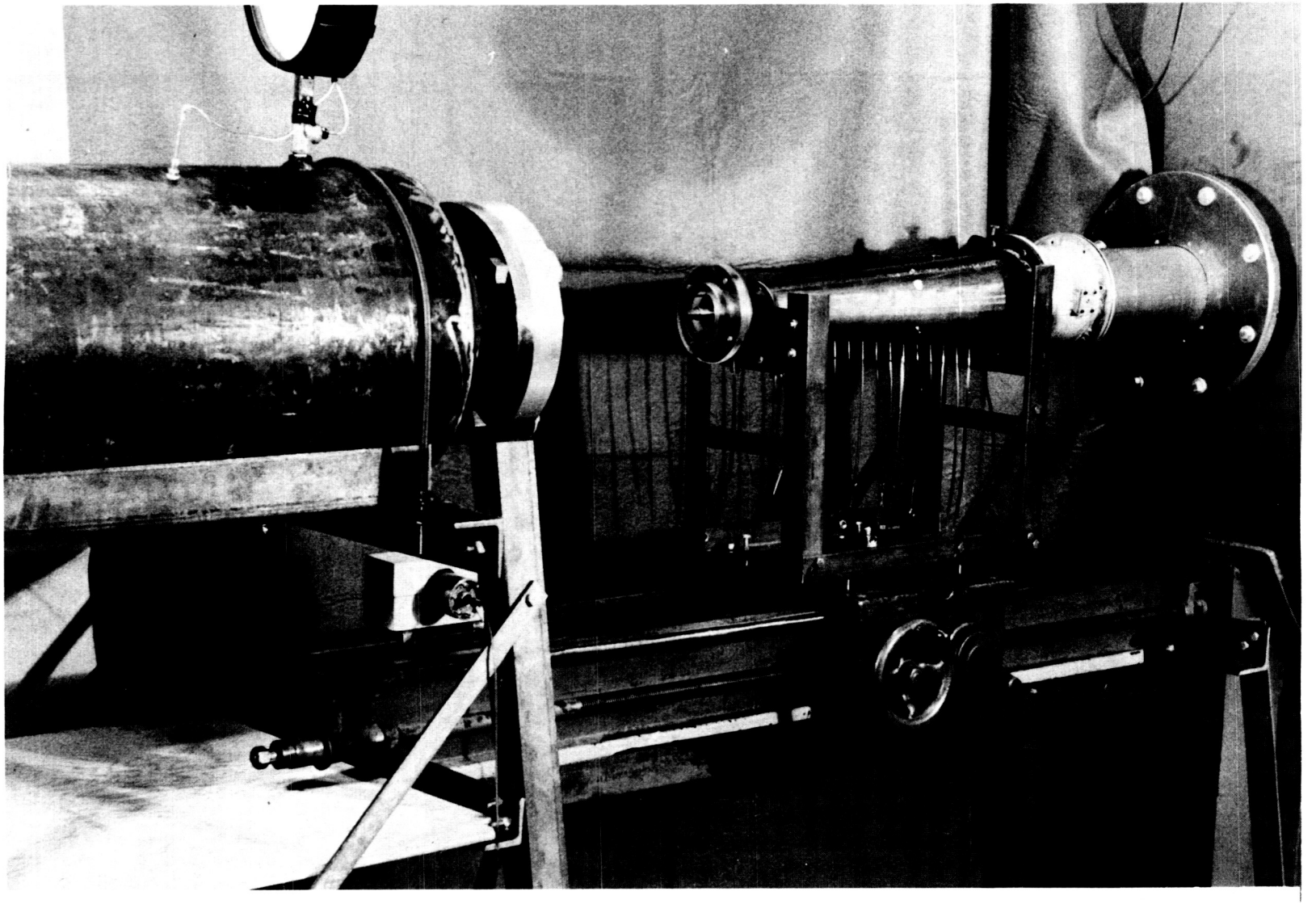

Figure 20.- Experimental test site showing plenum, diffuser, and vacuum tank.

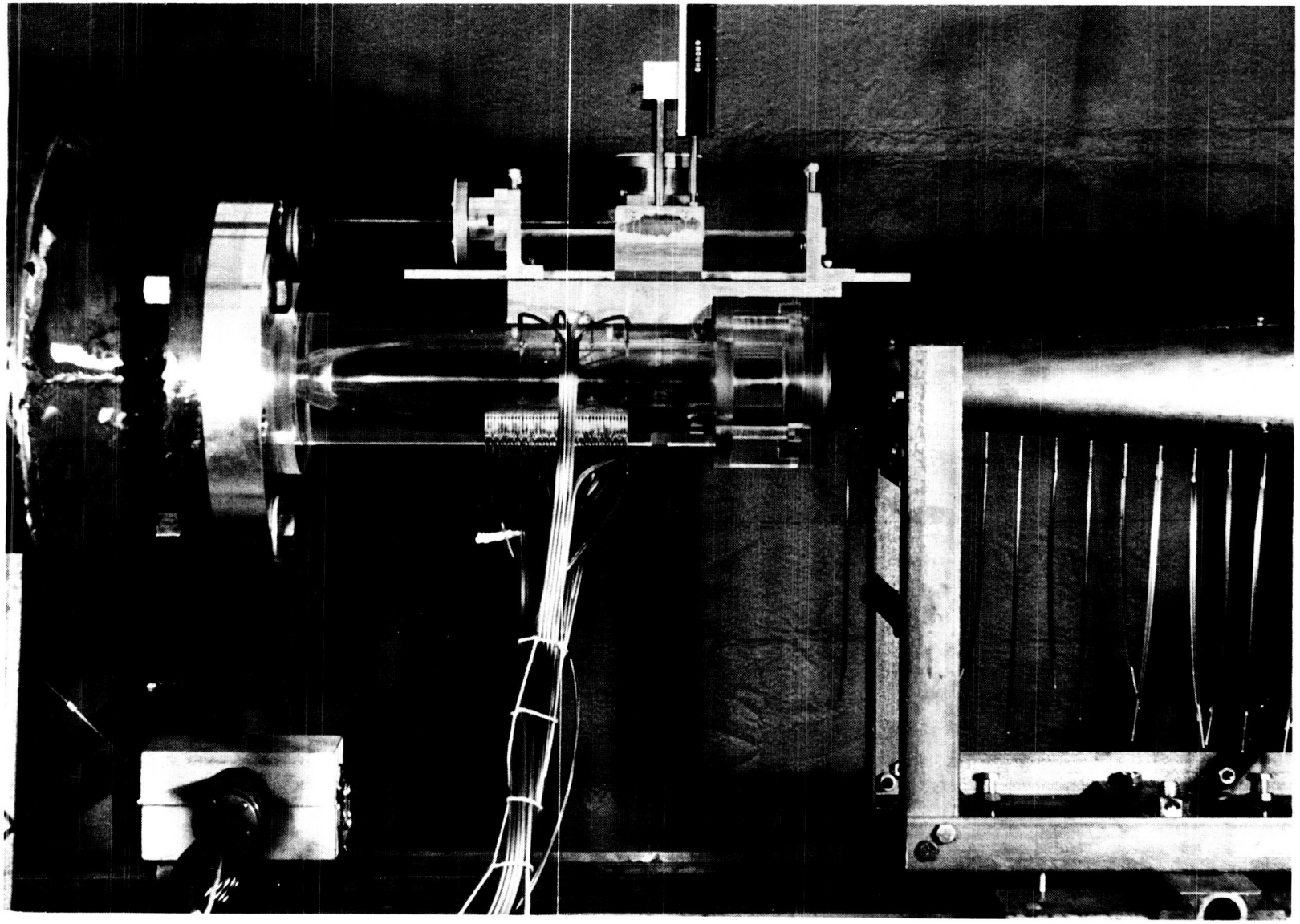

Figure 21.- Experimental facility with nozzle/test section installed.

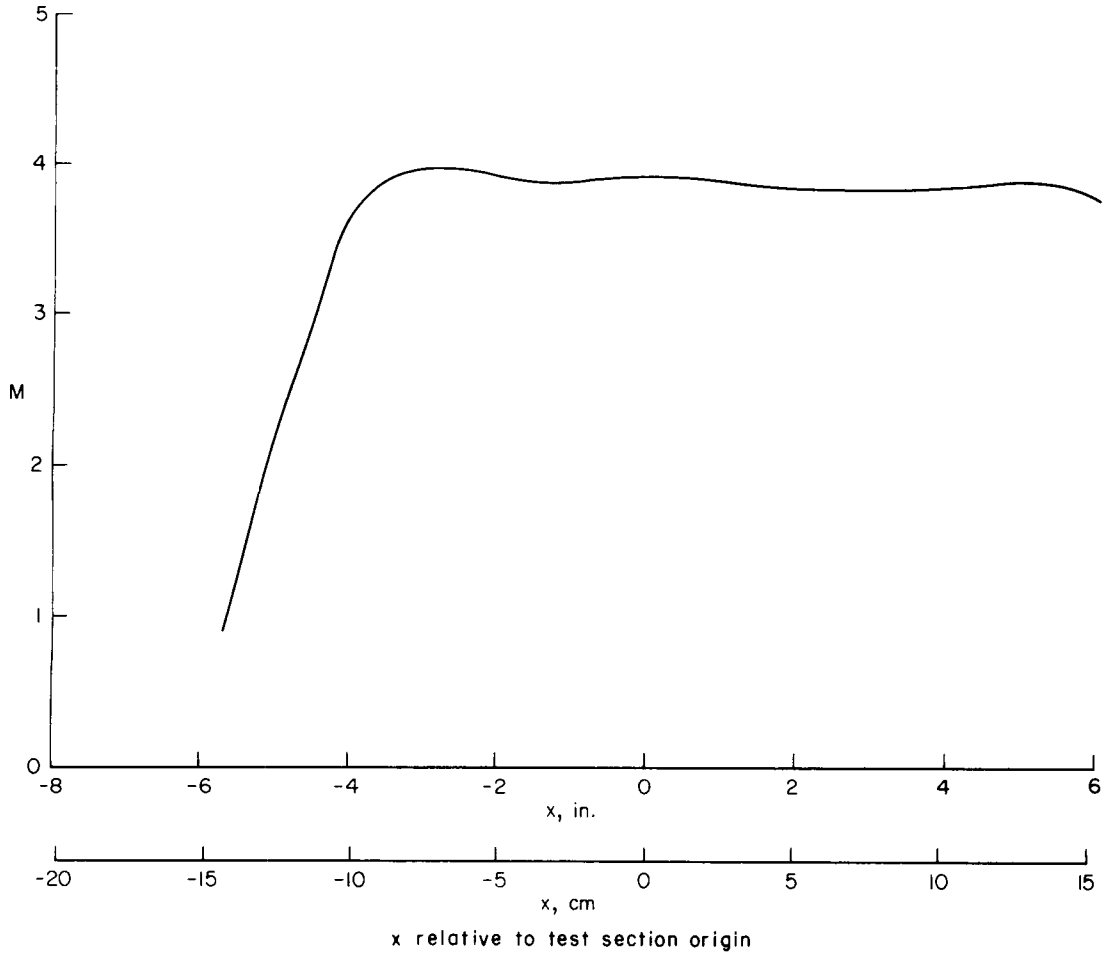

Figure 22.- Distribution of Mach number on nozzle/test section centerline.

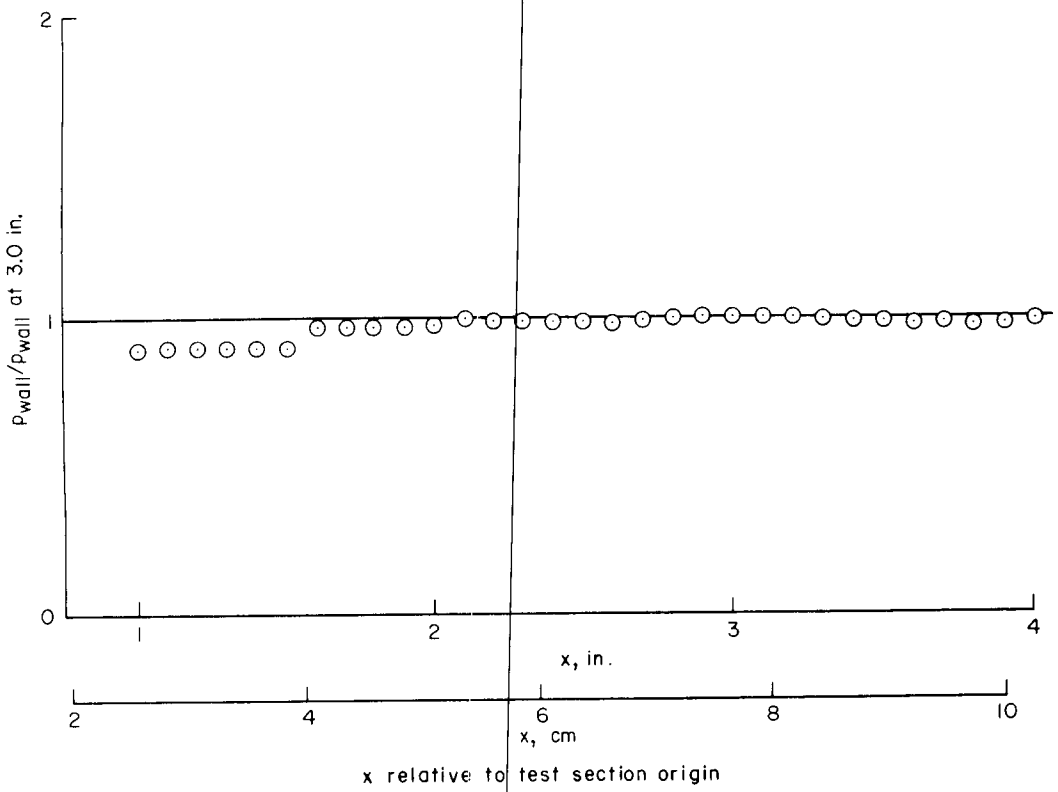

Figure 23.- Tunnel-empty surface-static pressure distribution.

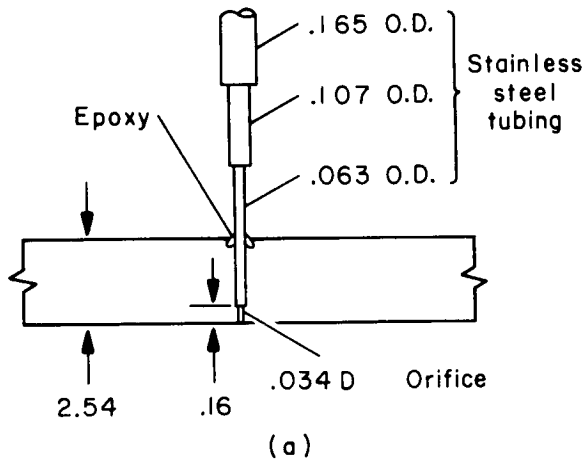

Note: All dimensions are in cm

(a) Typical surface-static pressure instrumentation.

Figure 24.- Pressure instrumentation.

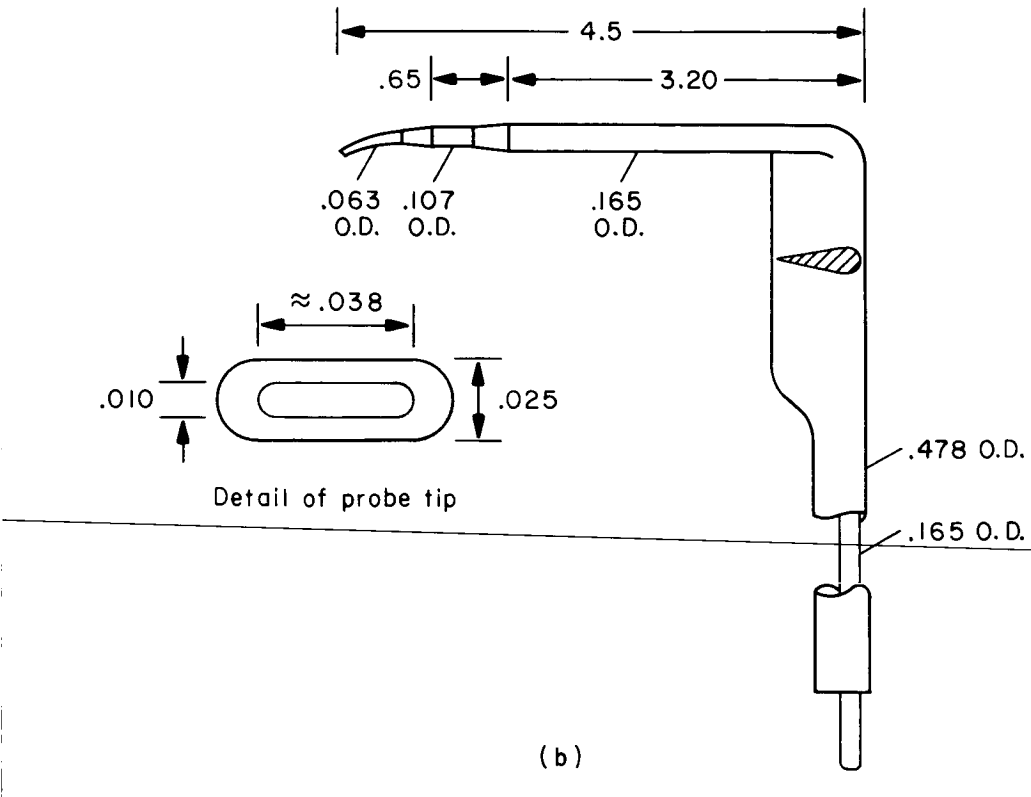

Note: All dimensions are in cm

(b) Pitot-pressure probe.

Figure 24.- Concluded.

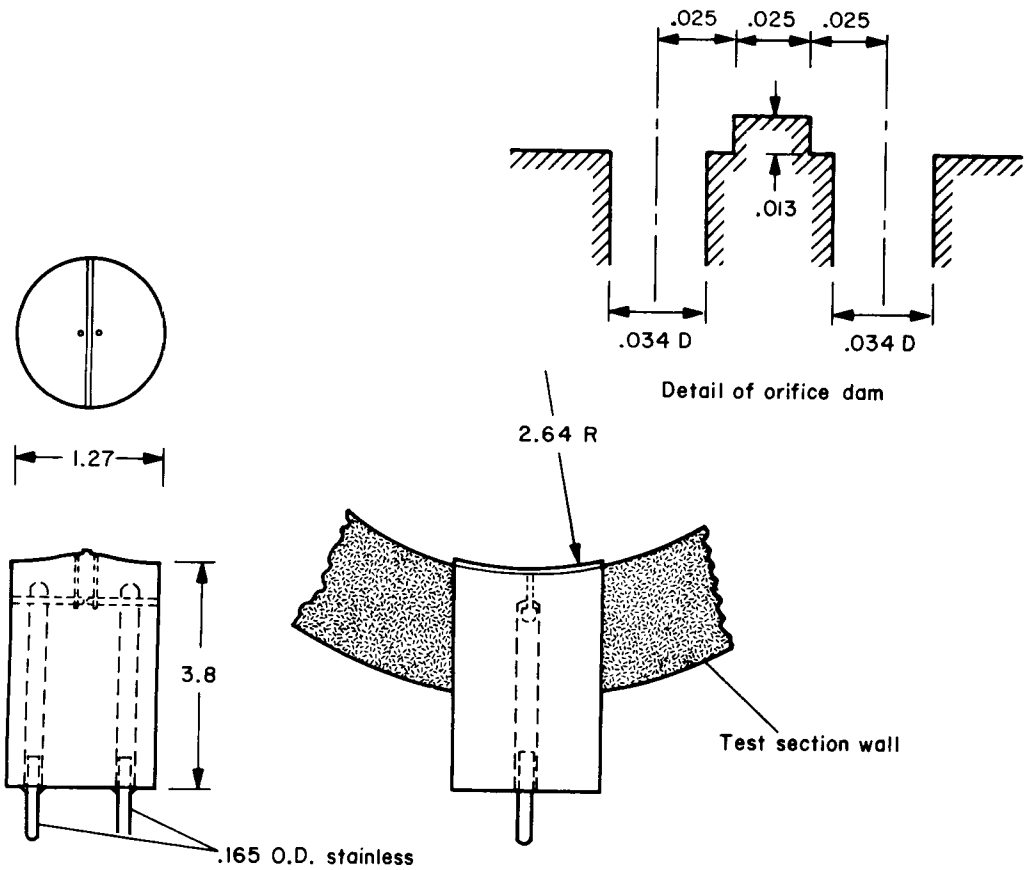

Figure 25.- Orifice dam.

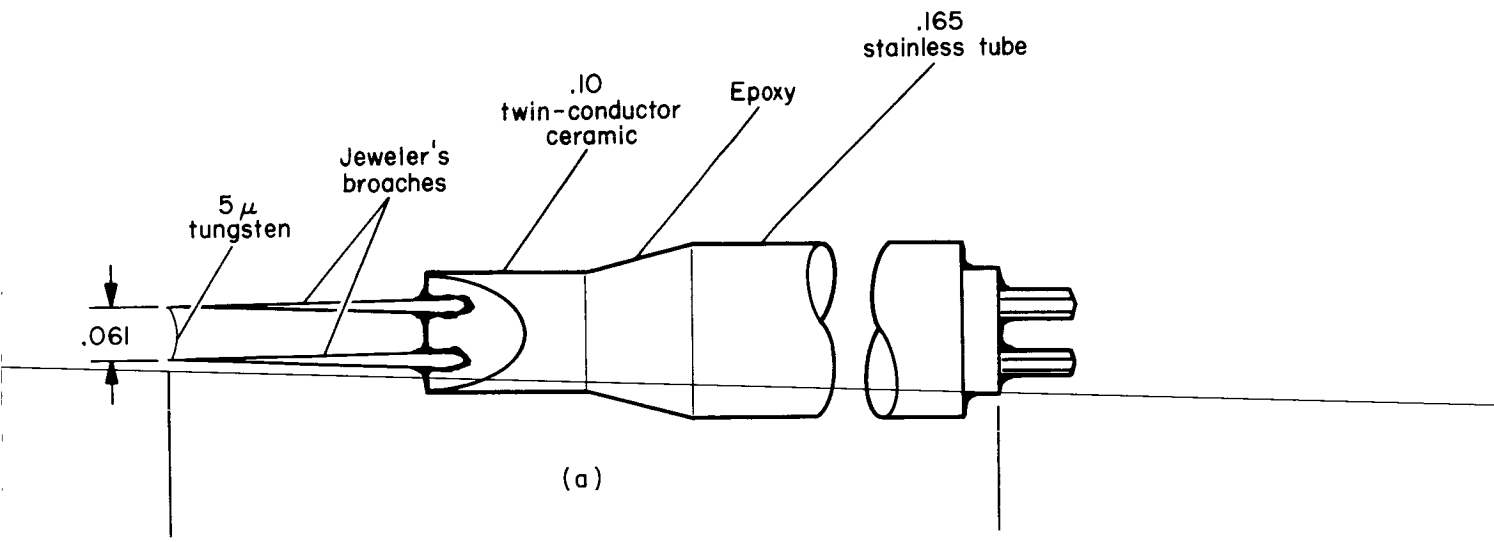

Note: All dimensions are in cm

(a) Normal wire.

Figure 26.- Hot-wire probes.

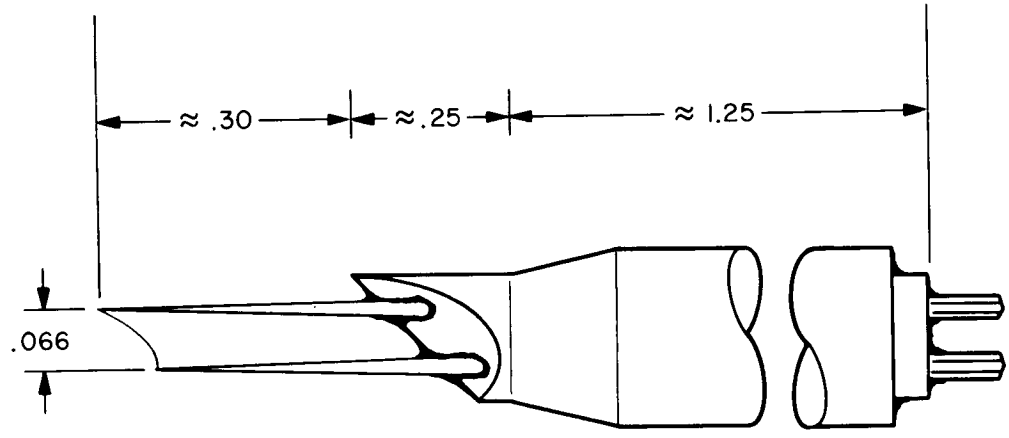

(b)

Note: All dimensions are in cm

(b) Yawed wire.

Figure 26.- Concluded.

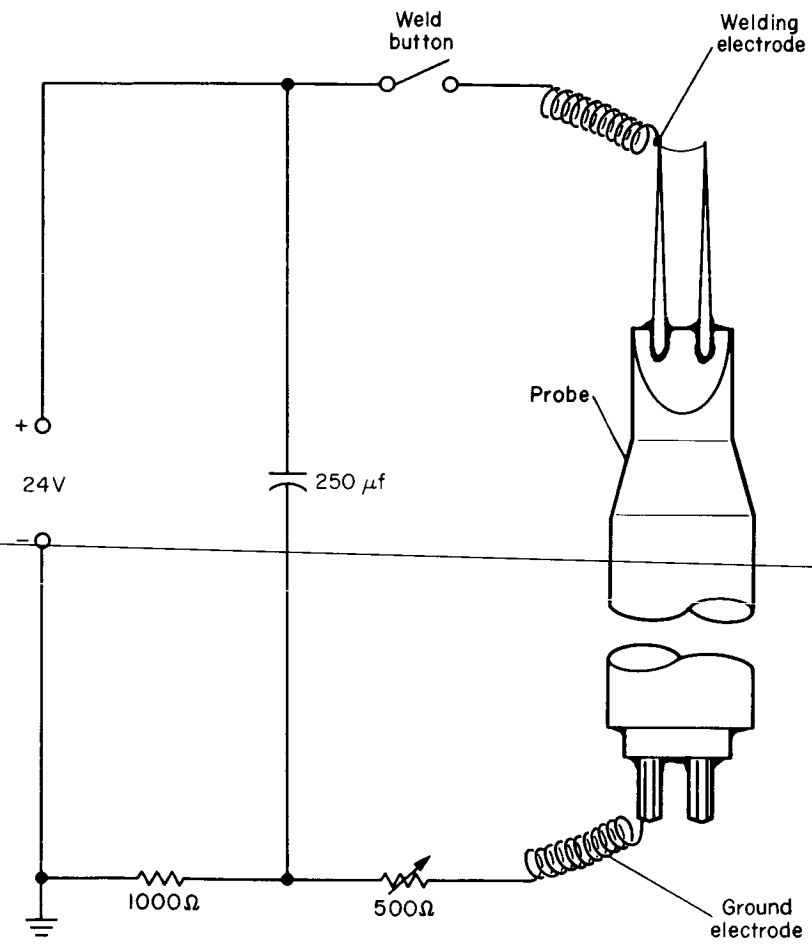

Figure 27.- Micro-arc welder circuit.

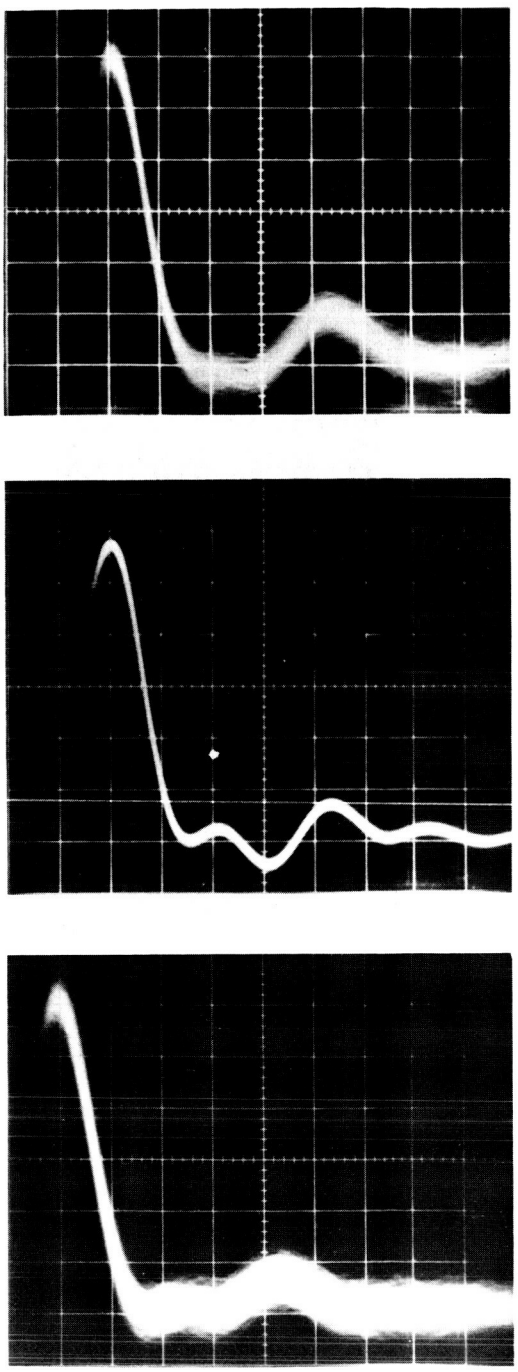

(a) Normal wire; minimum mass flow. $\tau_0 \approx 1\mu s$

(b) Normal wire; maximum mass flow. $\tau_0 \approx .9\mu s$

(c) Yawed wire; minimum mass flow. $\tau_0 \approx 1\mu s$

Figure 28.- Hot-wire anemometer upper frequency response; $a_w = 0.8$; 50 mV/cm, 1 μs/cm.

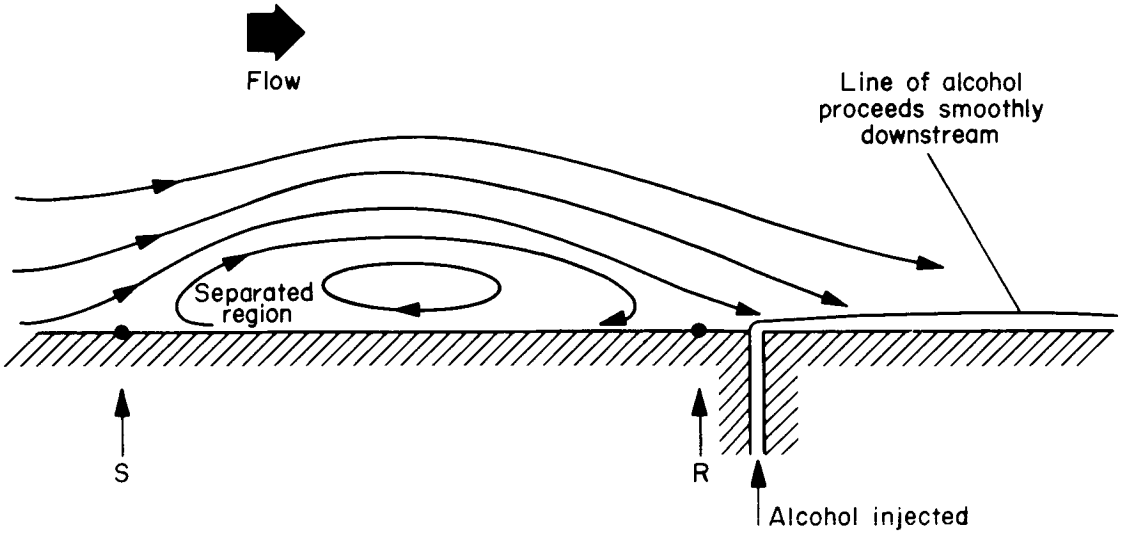

(a) Reattachment just upstream of injection port.

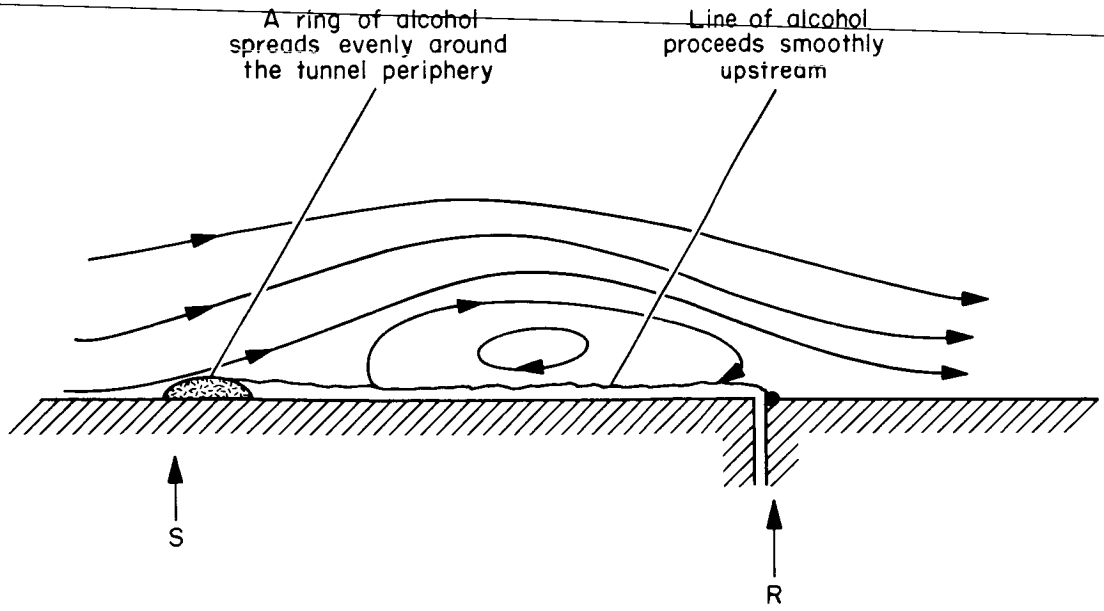

(b) Reattachment just downstream of injection port.

Figure 29.- Alcohol reattachment behavior.

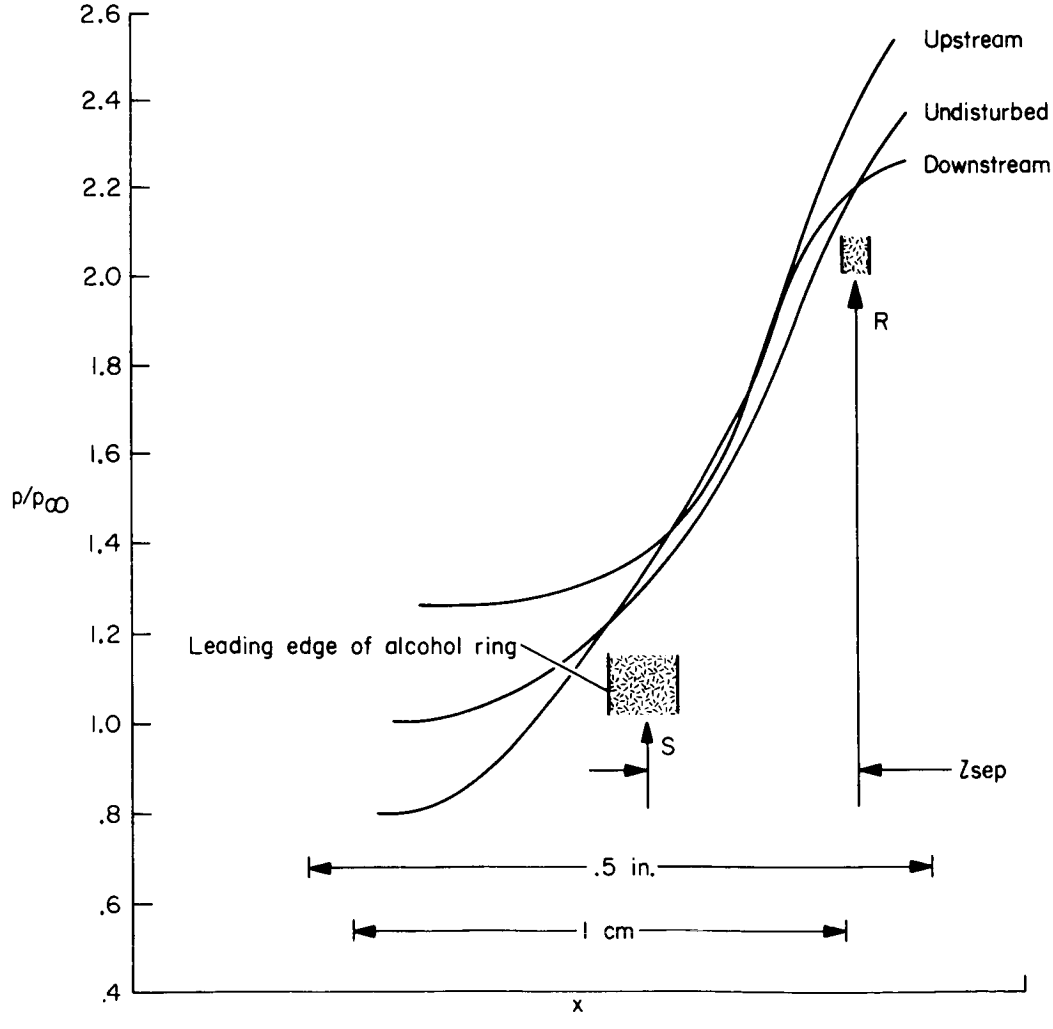

(a) 12° cone.

Figure 30.- Orifice dam pressures.

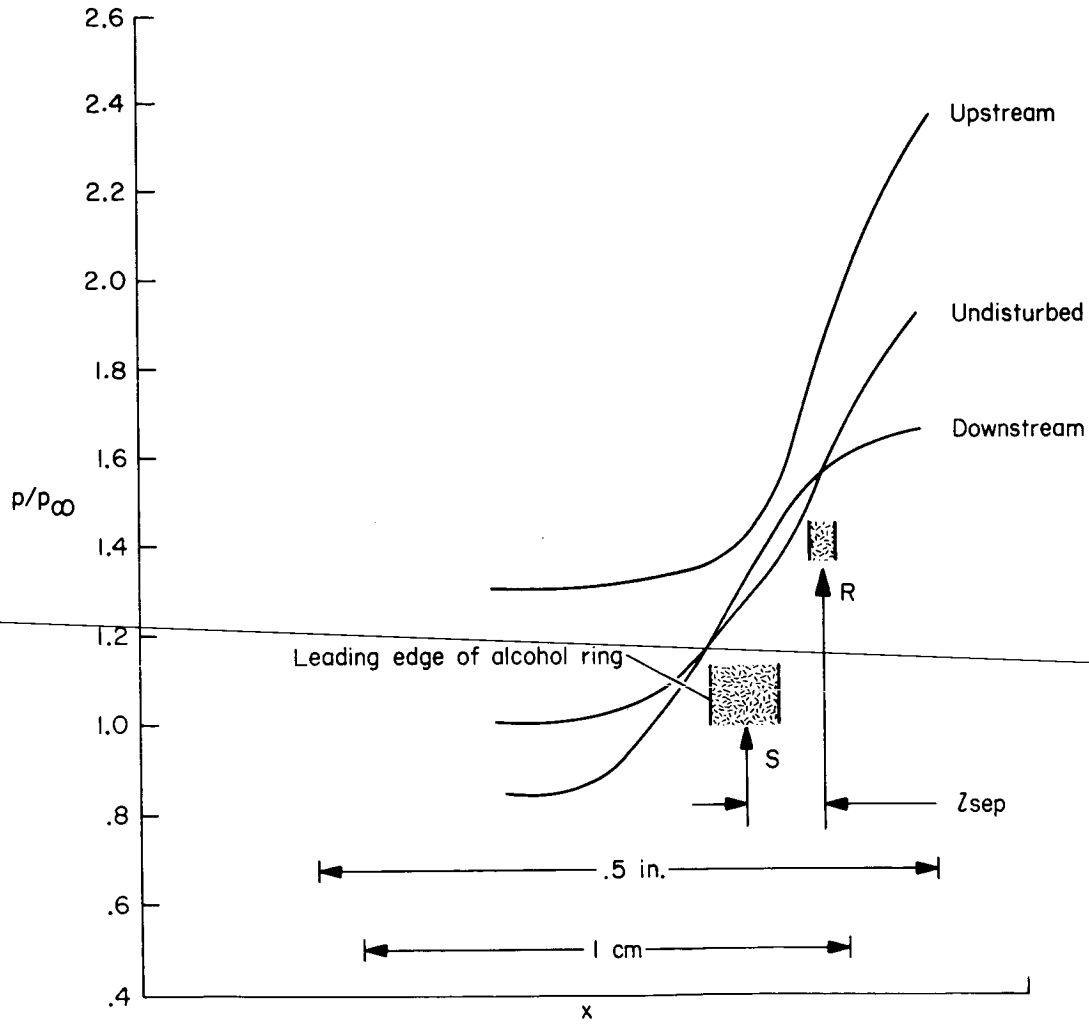

(b) 10° cone.

Figure 30.- Continued.

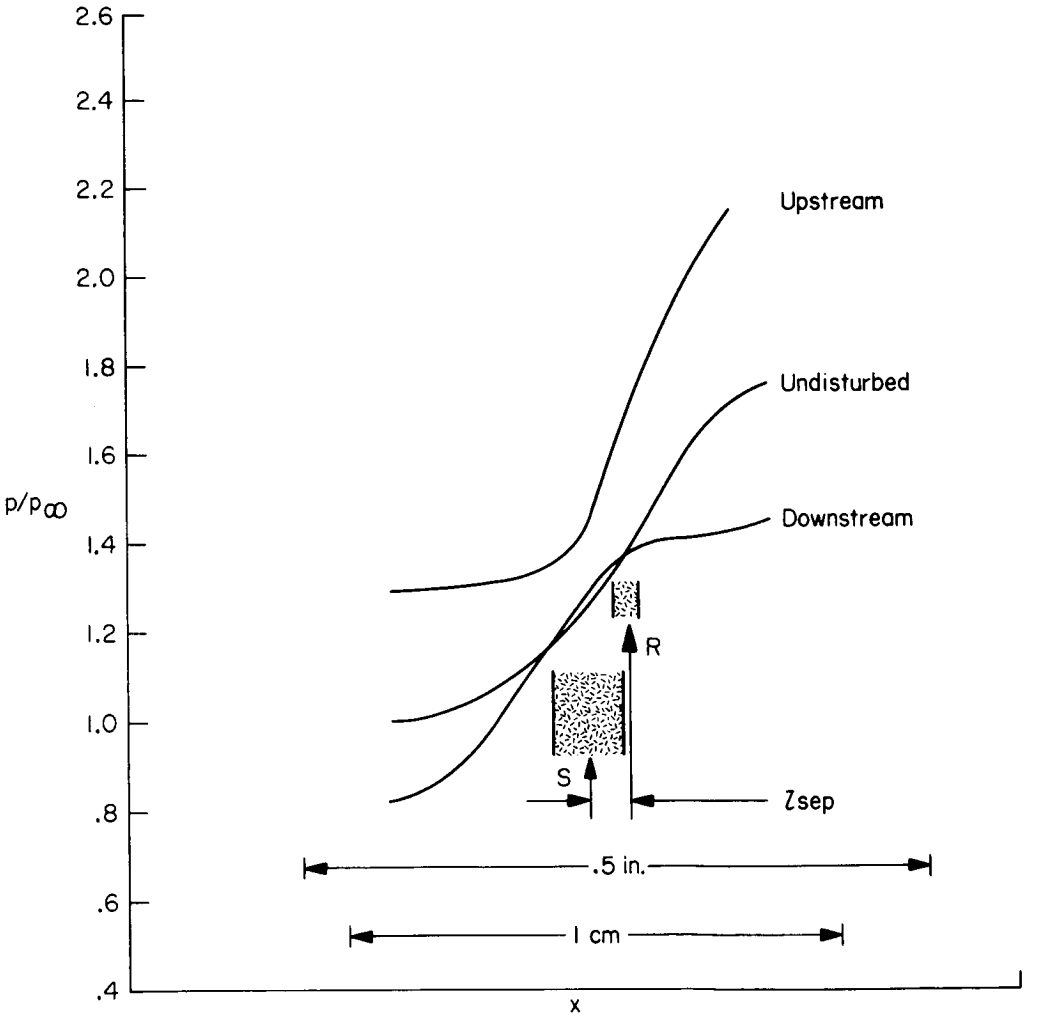

(c) 9° cone.

Figure 30.- Concluded.

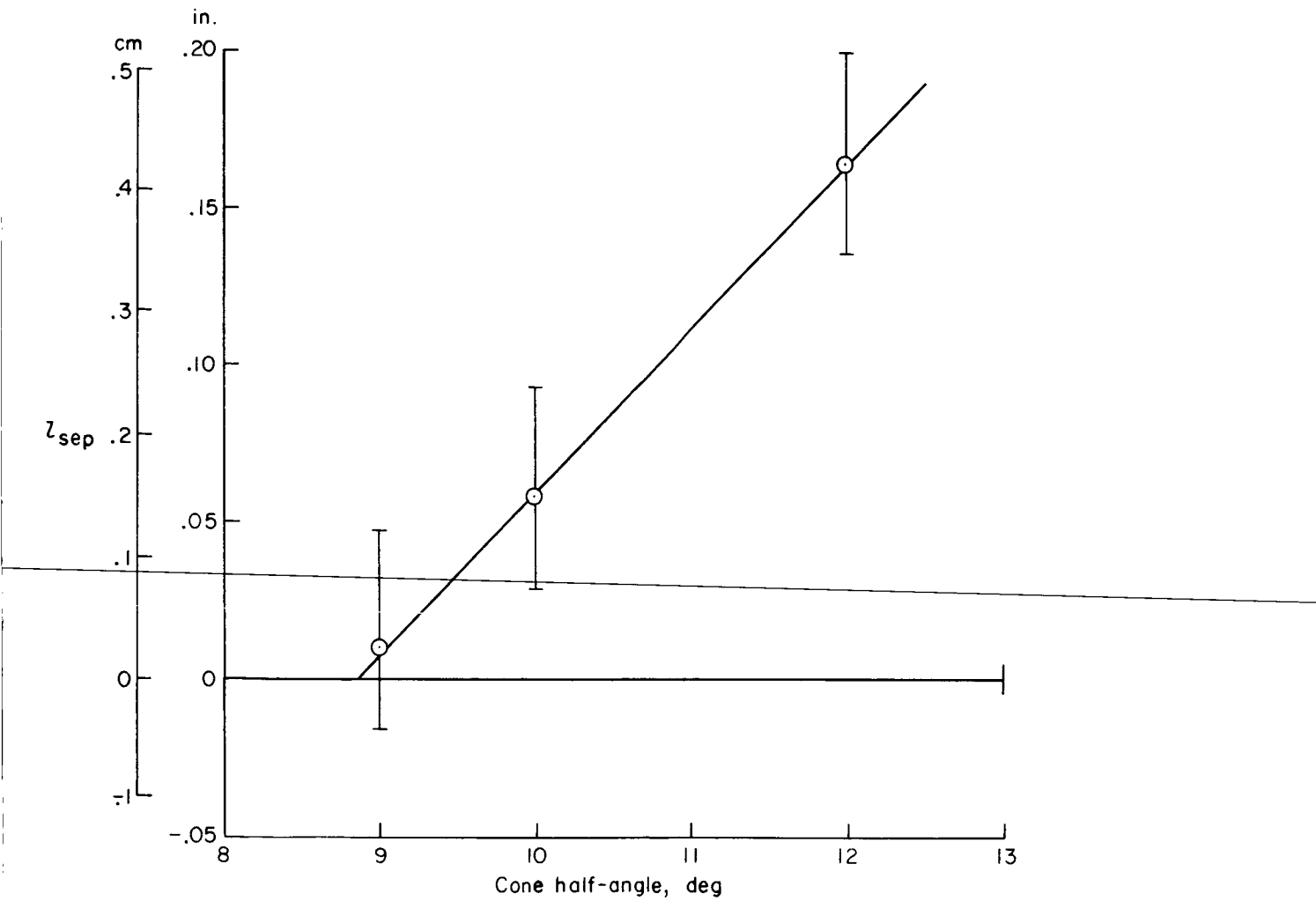

Figure 31.- Incipient separation cone angle.

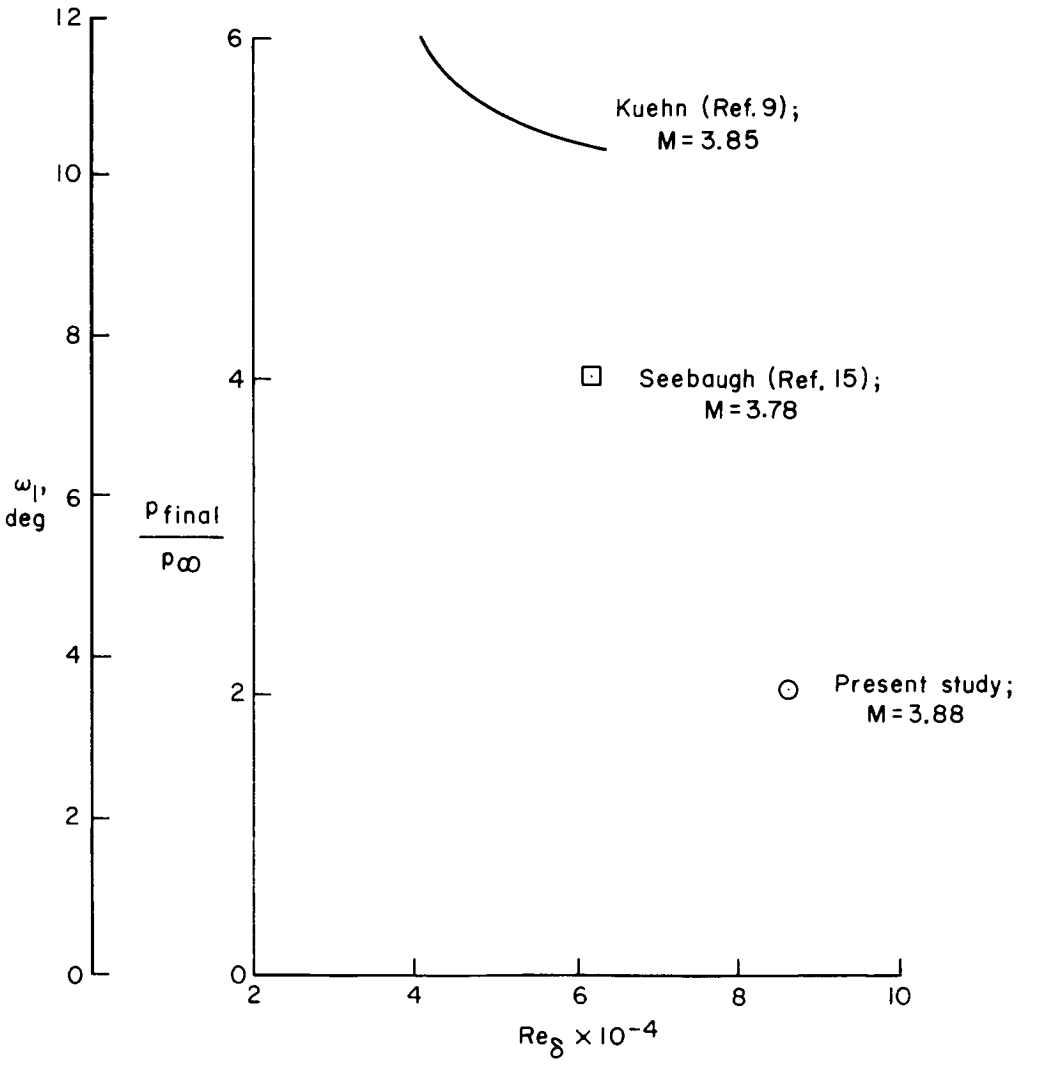

Figure 32.- Conditions for incipient separation.

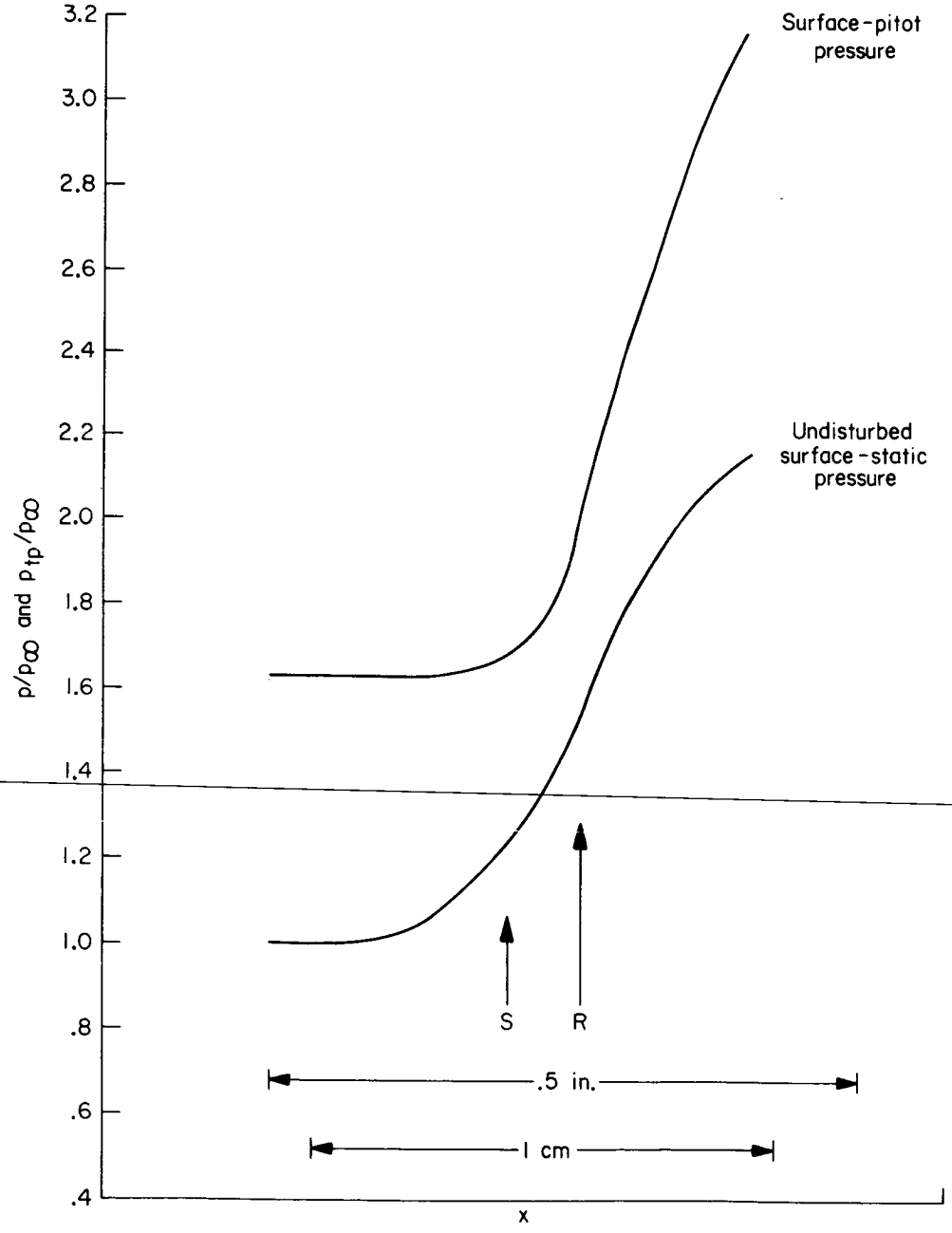

Figure 33.- Surface pitot pressure distribution.

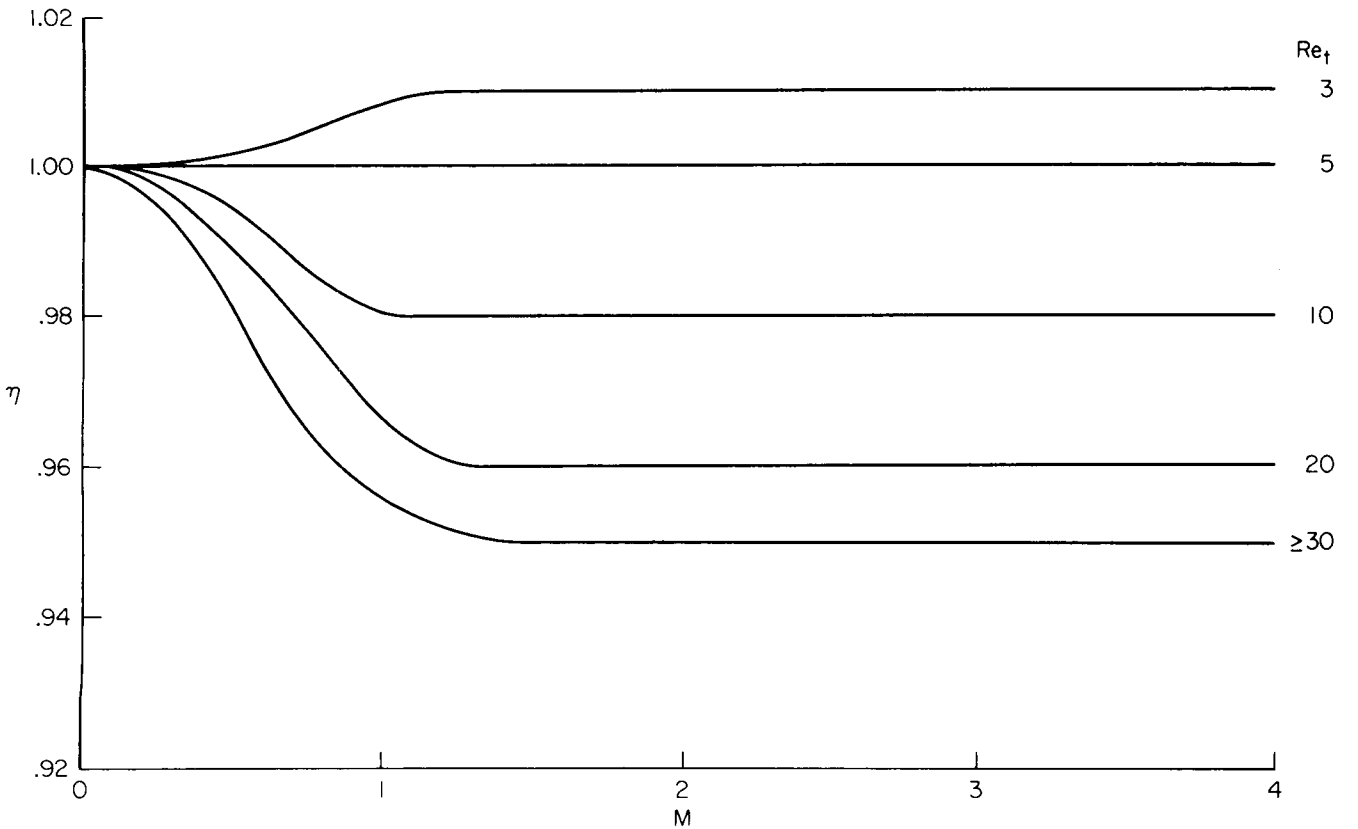

Figure 34.- Wire recovery factor.

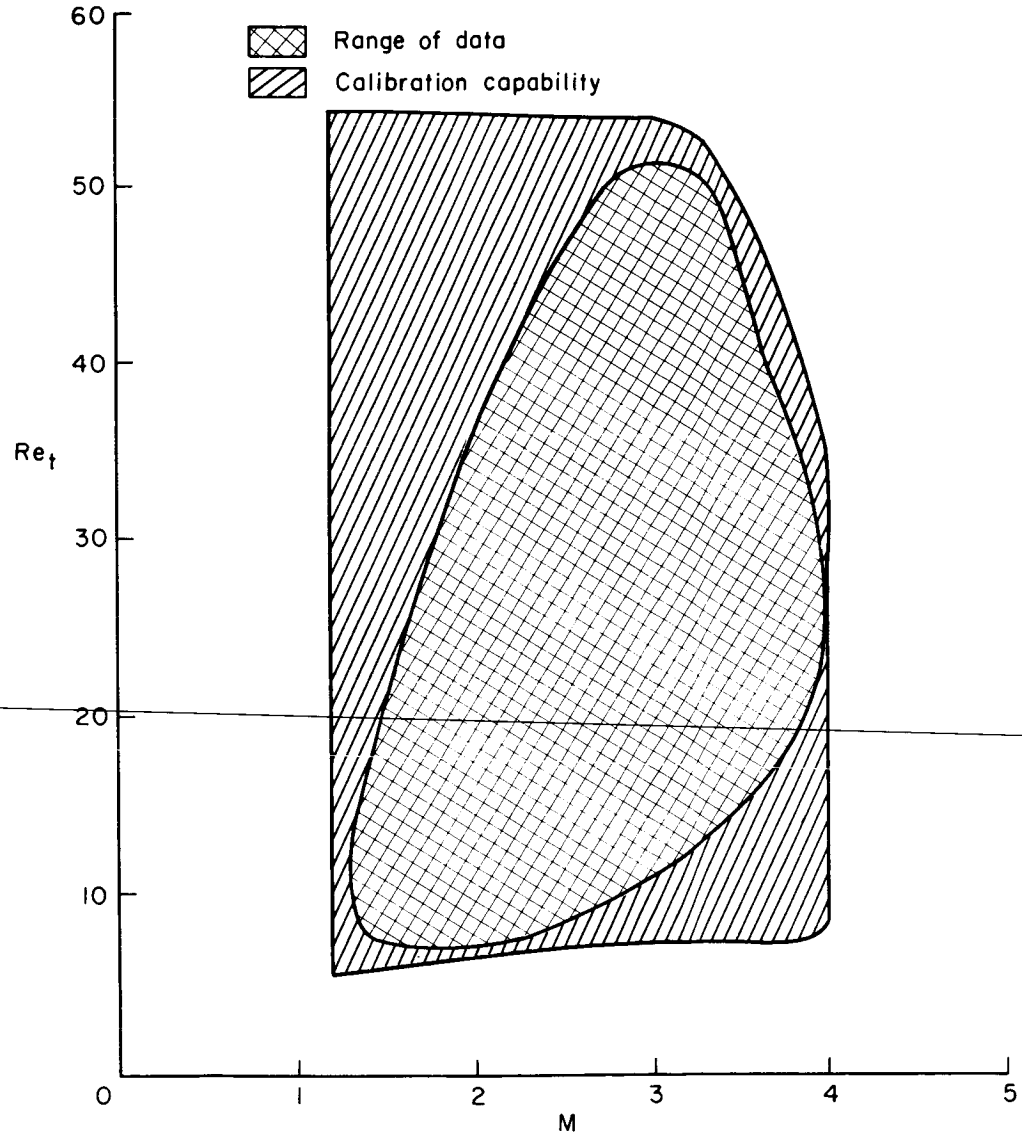

Figure 35.- Range of Mach and Reynolds numbers encountered in the present study.

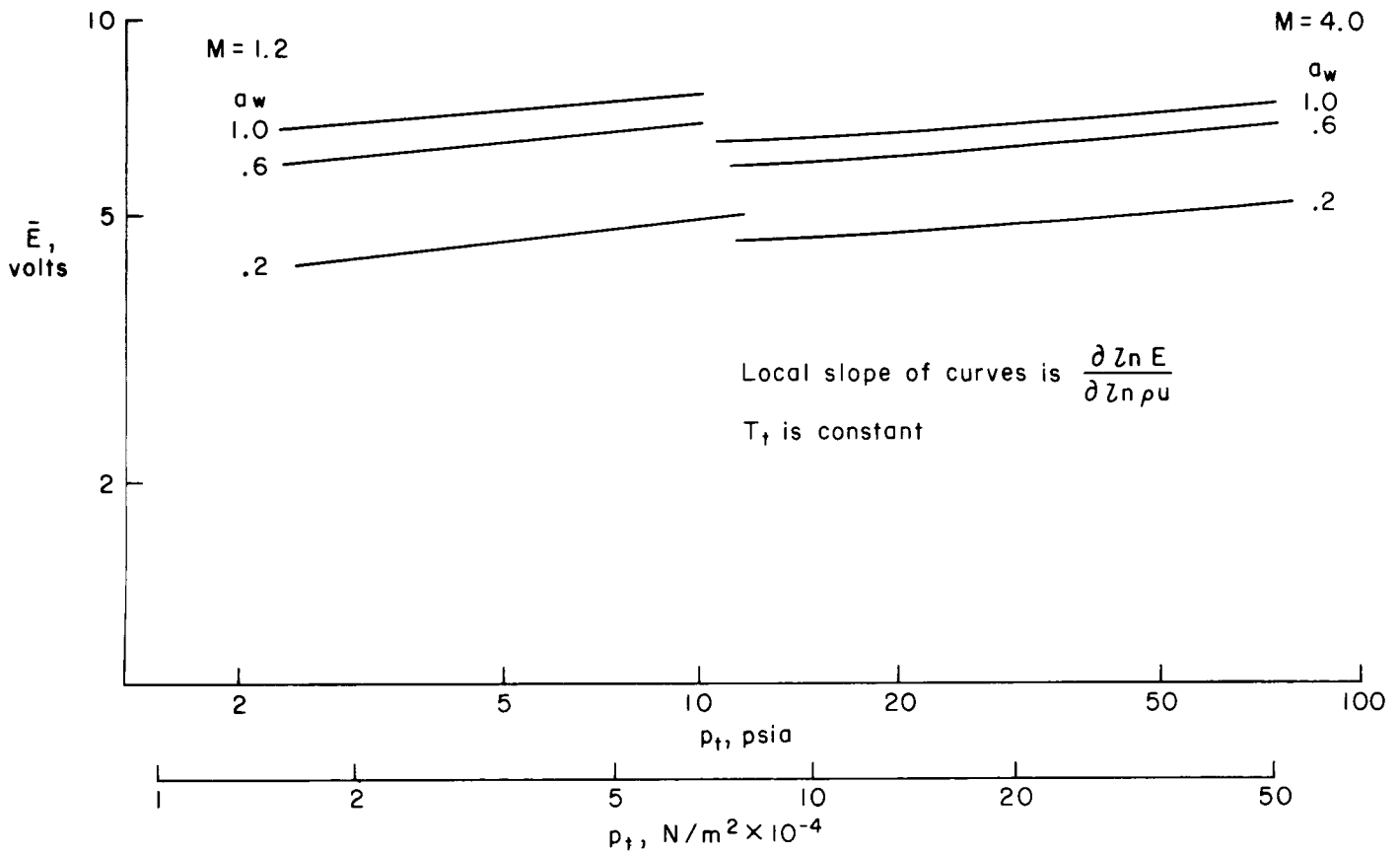

Figure 36.- Calibration technique for $\partial \ln E / \partial \ln \rho u$.

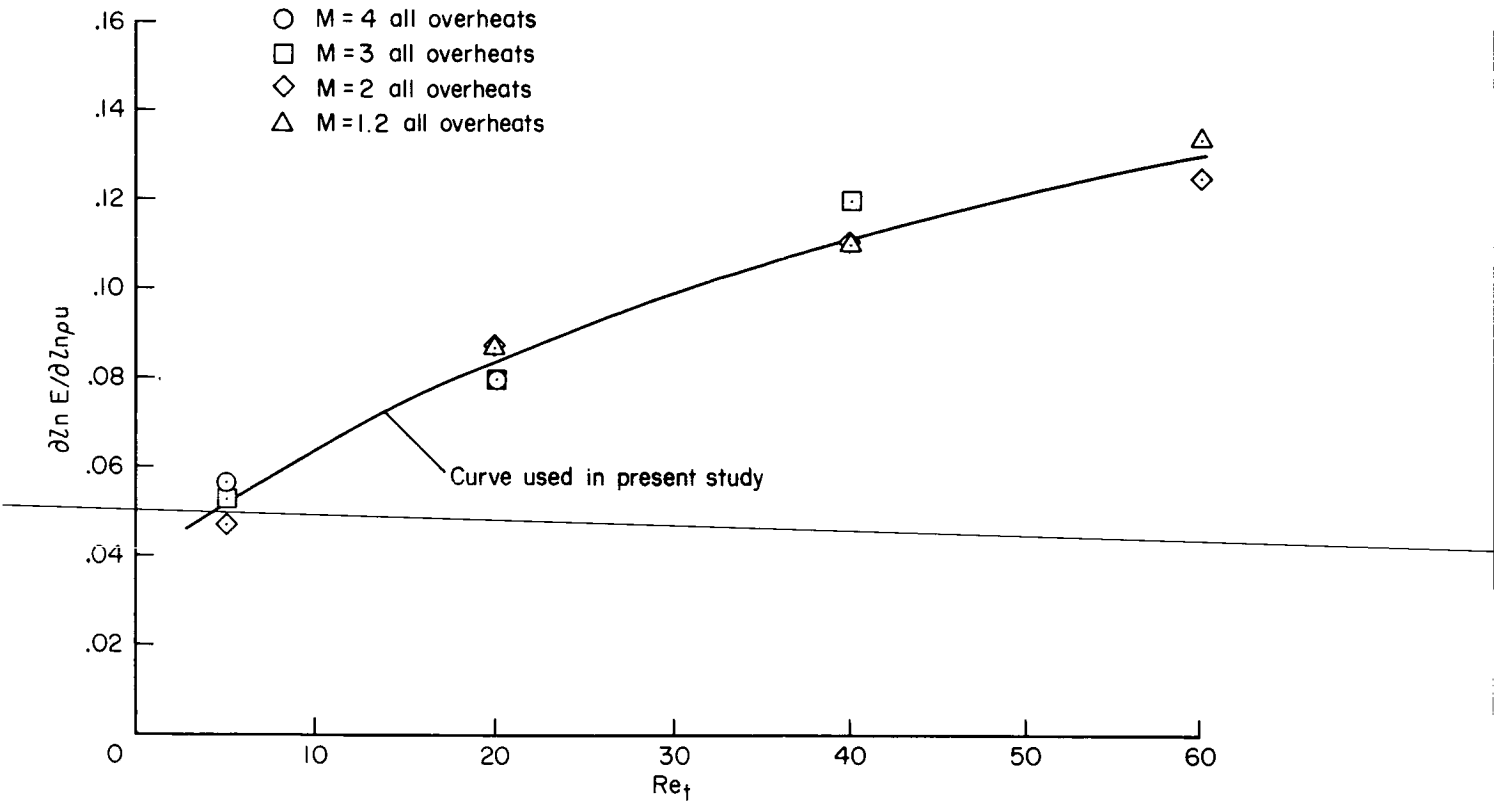

Figure 37.- Calibrated ∂ ℓn E/∂ ℓn ρu for normal wire.

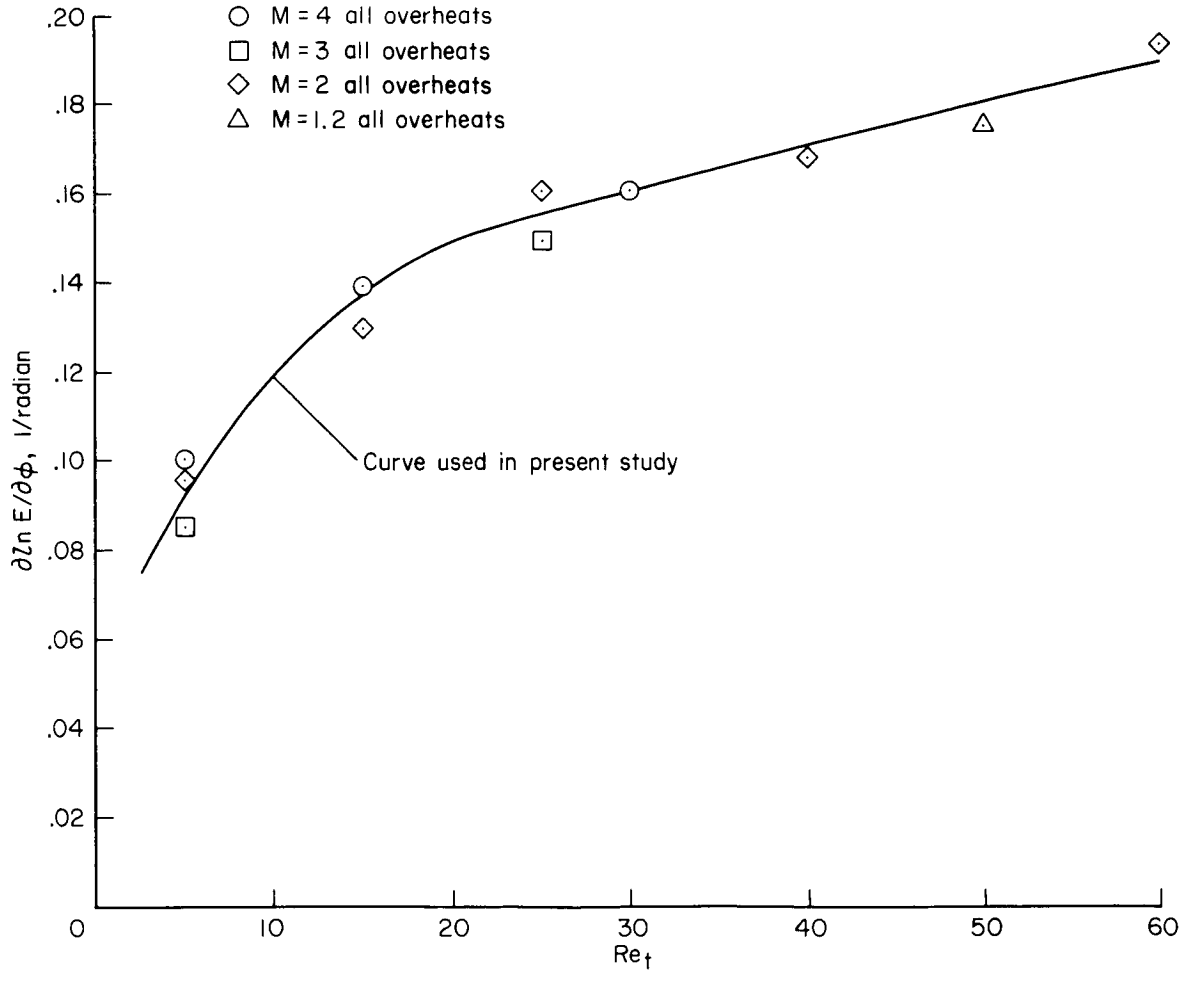

Figure 38.- Calibrated $\partial \ell n E/\partial \phi$ for yawed wire.

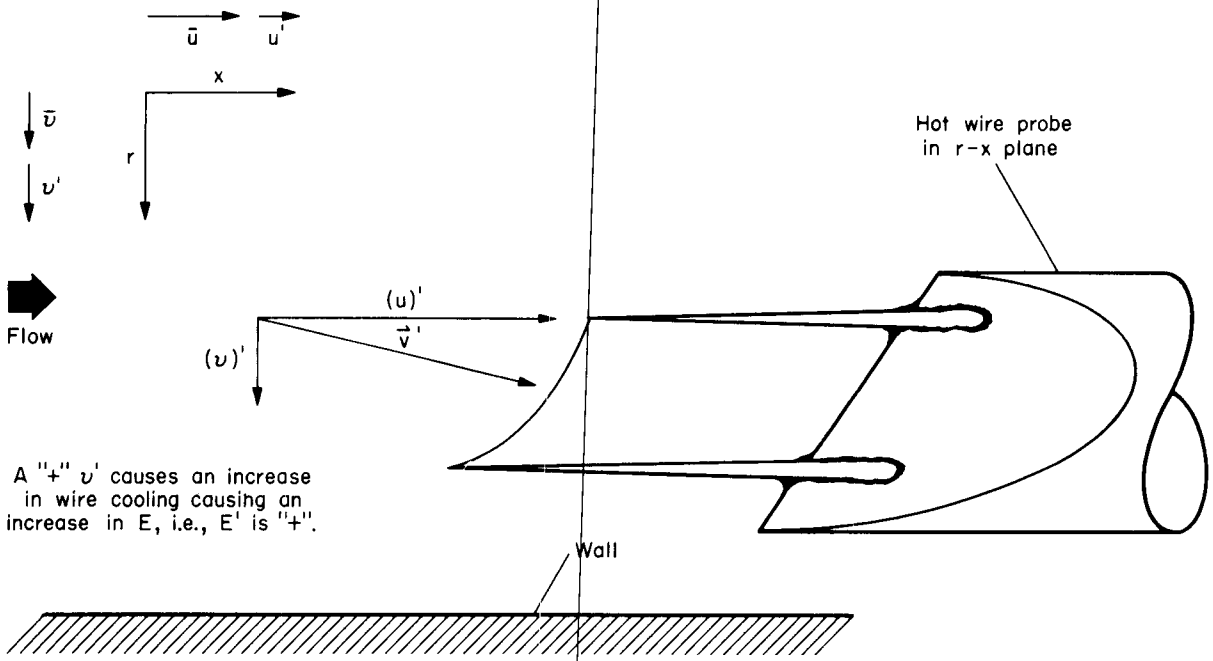

Figure 39.- Wire orientation for + sign convention in equation (D4).